Caractérisation multi-échelle du minéral osseux : apport de l'imagerie structurale par contraste de diffraction des rayons X et d'électrons

Mariana Verezhak

Communauté
UNIVERSITÉ Grenoble Alpes

THÈSE

Pour obtenir le grade de

DOCTEUR DE LA COMMUNAUTÉ UNIVERSITÉ GRENOBLE ALPES

Spécialité : **Physique/Nanophysique**

Arrêté ministériel : 7 août 2006

Présentée par

« Mariana / VEREZHAK »

Thèse dirigée par **« Marie/PLAZANET »** et
codirigée par **« Aurélien/GOURRIER »**

préparée au sein du **Laboratoire Interdisciplinaire de Physique**
dans **l'Ecole Doctorale de Physique de Grenoble**

Caractérisation multi-échelle du minéral osseux: apport de l'imagerie structurale par contraste de diffraction des rayons X et d'électrons

Thèse soutenue publiquement le **« 28 octobre 2016 »**,
devant le jury composé de :

Prof. Franz BRUCKERT
Grenoble INP UGA, Président du jury
Dr. Aurélien GOURRIER
LIPhy, Grenoble, co-Directeur de thèse
Prof. Thomas LAGRANGE
École Polytechnique Fédérale de Lausanne, Examinateur
Dr. Marie PLAZANET
LIPhy, Grenoble, Directrice de thèse
Prof. Sylvain RAVY
Laboratoire de Physique des Solides, Orsay, Rapporteur
Dr. Ina REICHE
LAMS, Paris, Rapporteur

Communauté
UNIVERSITÉ Grenoble Alpes

THESIS

In order to obtain the grade of

DOCTOR OF GRENOBLE ALPES UNIVERSITY

Specialty: **Physics/Nanophysics**

Ministerial order: 7 August 2006

Presented by

« Mariana / VEREZHAK »

Thesis supervised by **« Marie/PLAZANET »** and
co-supervised by **« Aurélien/GOURRIER »**

Prepared at **Laboratory of Interdisciplinary Physics**
at **Doctoral School of Physics of Grenoble**

Multiscale characterization of bone mineral: new perspectives in structural imaging using X-ray and electron diffraction contrast

Thesis is publically defended on **« 28 October 2016 »**,
in front of the jury composed of :

Prof. Franz BRUCKERT
Grenoble INP UGA, President of jury
Dr. Aurélien GOURRIER
LIPhy, Grenoble, co-Director of thesis
Prof. Thomas LAGRANGE
Institute of Technology of Lausanne, Examiner
Dr. Marie PLAZANET
LIPhy, Grenoble, Director of thesis
Prof. Sylvain RAVY
Laboratory of Solid State Physics, Orsay, Referee
Dr. Ina REICHE
LAMS, Paris, Referee

Acknowledgements

I would like to express my thanks to my advisors Dr. Aurelien Gourrier and Dr. Marie Plazanet, you have been great mentors for me. I would like to thank you for allowing me to grow as a research scientist, your help and support in the moments of difficulties and many fruitful discussions during manuscript and defense preparation. Your advice on both research as well as on my career have been priceless.

I would also like to thank my committee members, Dr. Sylvain Ravy, Dr. Ina Reiche, Prof. Thomas LaGrange and Prof. Franz Bruckert for accepting to be part of my PhD defense despite your dense schedules, for your brilliant comments and suggestions.

I would especially like to thank our numerous collaborators, from ESRF, for help during beam-time and advice in data analysis: Dr. Manfred Burghammer and Dr. Britta Weinhausen from ID13, Dr. Yuriy Chushkin and Dr. Federico Zonton from ID10; as well as to our collaborators from SIMaP, for access to transmission electron microscope: Dr. Edgar F. Rauch and Prof. Muriel Veron; and to Dr. Pierre Bordet for the collaboration in bone tissue PDF analysis. Many thanks to Dr. Christine Lancelon-Pin (CERMAV) and Dr. Irina Snigireva (ESRF) for providing advice and instrumentation for sample preparation. Additional thanks to Dr. Delphine Farlay from INSERM (Lyon) for providing the pathological samples.

Additional thanks goes to my colleagues from MOTIV group, and LIPhy in general, for many fruitful discussions and making my life in the lab dynamic and interesting. Special thanks to Rachel Genthial for every day exchange and help in getting familiar with French administration and to Brenna Hogan for help as an English native-speaker.

I also acknowledge the Nanoscience Foundation in Grenoble for financial support of my thesis.

A special thanks to my family. Words cannot express how grateful I am to my mother and father for raising me with a love for science and for all of the sacrifices that you've made on my behalf. Your prayers for me have been heard. I would also like to thank all of my friends

who supported me at all stages. At the end, I would like to express appreciation to my beloved one, Victoric Leroy, who spent sleepless nights with me working and many hours of traveling just to make this opportunity for me possible, for everyday support during these 3 years and, especially, in difficult moments.

List of abbreviations and notations:

ACLAR – copolymer film consisting primarily of chlorotrifluoroethylene;
ACOM – automated crystal orientation mapping;
CAP – collagen-apatite porosity;
CL – cross link;
CXDI – coherent X-ray diffraction imaging;
DDSA – dodecenyl succinic anhydride;
DMP-30 – tris (dimethylaminomethyl) phenol;
EDX – energy dispersive X-ray analysis;
FEG – field emission gun;
FTIR – Fourier transform infra-red;
FWHM – full width half maximum;
HAP – hydroxyapatite;
HPT – hyperparathyroidism;
IR – infra-red;
LM – light microscopy;
MMA – methyl methacrylate;
NMA – nadic methyl anhydride;
OPT – osteopetrosis;
PDF – pair distribution function;
PG – proteoglycan;
PMMA – poly (methyl methacrylate);
PTFE – polytetrafluoroethylene;
PV – Pseudo-Voigt;
SAXS – small angle X-ray scattering;
SEM – scanning electron microscopy;
TEM – transmission electron microscopy;
USAXS – ultra-small angle X-ray Scattering;

UV – ultraviolet;

WAXS – wide angle X-ray scattering;

WSS – weighted sum of squares;

XRD – X-ray diffraction.

Table of content

Introduction

Bone is a biological tissue that is composed of many hierarchical levels of organization of three principal components such as collagen molecules, mineral nanocrystals and water. As most biological materials, bone is self-assembled, in a very complex way that demands fundamental understanding. Furthermore, bone pathologies are an important heath concern. Currently, the most common diagnostic approach for bone pathologies is based on bone mineral density measurements [1,2]. Yet it only explains half of non-vertebral fractures [3]. Therefore, further understanding is required.

The principal components of bone are: collagen molecules (300 nm long, 1.5 nm in diameter), non-stoichiometric hydroxyapatite mineral nanoparticles (3 x 25 x 50 nm^3) and water molecules, self-assembled in a complex hierarchical structure with up to 8 levels of organization. Hereby, the phenomenological understanding of the structure and organization of bone component phases and its relationship between each other at the various levels of hierarchical organization can help us understand the mechanical properties of bone as an organ and may serve one day as an input for the development of new diagnostic and treatment tools.

This thesis will mainly focus on the hierarchical structure of the mineral phase in bone. Indeed, thanks to its larger scattering power in comparison to organic phase for the main scattering techniques, deeper characterization can be performed, still providing indirect information about the collagen organization.

Moreover, it was suggested that not only the amount of mineral that is accessible by bone mineral density measurements, but also the properties of the mineral such as mineral composition, crystal size, shape and crystallinity, organization and orientation, must be considered as factors contributing to bone mechanical strength.

Osteogenesis imperfecta is an example of how crystal properties can affect bone strength. Bone, affected by this pathology, shows not only a defective matrix, but the crystals

are abnormally small, have abnormal compositions, and may be found outside the collagen matrix [4].

Many techniques enable access to mineral crystal properties that have very different spatial resolution (see fig. I.1) and requirements for sample preparation. Not only high spatial resolution is necessary, but also the knowledge of the precise anatomical location at each level of structural hierarchy within the tissue. This can be achieved by combining several position sensitive techniques such as light microscopy (LM), scanning electron microscopy (SEM) and transmission electron microscopy (TEM) with elemental analysis, X-ray diffraction, Raman and infrared spectroscopic imaging.

One of the "gold standards" in bone characterization is X-ray diffraction (XRD). X-ray scattering has two different levels of resolution: the reciprocal space resolution (defined by the X-ray wavelength and the experimental setup) and the real-space resolution (defined by the probe size). Therefore, the obtained high resolution information is averaged over the volume illuminated by the X-rays which makes classical XRD perfectly suitable to study well-ordered crystals and it overall requires the object homogeneity.

Powder XRD had provided averaged information about bone crystal structure [5]. It shows the mineral phase in bone as a poorly crystalline apatite whose particle size and crystallinity increases during the individual's life [6].

A very powerful approach that became widely used with the recent developments of third-generation synchrotron radiation sources with high brilliance is the application of scanning small-angle X-ray scattering (SAXS) and/or wide-angle X-ray scattering (WAXS) in order to map local nanostructural features in spatially heterogeneous systems. Diffraction with synchrotron radiation in the scanning mode currently allows focusing the X-ray beam up to 100 x 100 nm^2 [7]. Applying the scanning SAXS and WAXS on bone has allowed the imaging of fibrils and crystal orientation, position-resolved particle size calculation (T-parameter) and quantitative texture analysis [8,9].

TEM is a second "gold standard" in bone characterization. It offers the nm resolution (or better for high resolution TEM) and combined with selected area diffraction or dark field analysis, it can provide, in addition to high-resolution imaging, the information on crystal phase and crystal orientation [10,11]. Nevertheless, due to the low penetration depth of electrons, the samples must have thickness lower than 100 nm, which limit the 3D

information and require very complex sample preparation that introduces many artifacts (ex. cracks and rehydration issues for ultramicrotomy).

In addition, SEM has also a sub-nm spatial resolution but, as a surface technique, it only allows the imaging of polished or cleaved bone surfaces [12]. Recent development of tomographic electron microscopy gives the promising combination of the advantages of TEM spatial resolution and the 3D information [13]. Yet, the limitations for sample preparation are very strict. Eventually, atomic force microscopy of isolated bone crystals also give 3D information on crystal sizes in good agreement with XRD [14].

Complementary to structural techniques, spectroscopic methods such as infra-red (IR) and Raman have been used for the characterization of bone [15,16]. Although these techniques do not provide the direct phase identification (as does XRD), the spatial resolution (on the micrometer scale) enables testing of hypotheses relating the variation in bone mineral properties to mechanical strength [15]. The advantage of the IR and Raman microspectroscopy is that they provide the information on the mineral crystallinity, composition (ionic substitutions) and organic matrix chemistry (collagen, lipids, proteoglycans) in a nondestructive manner.

Most of these methods, however, still lack the spatial resolution needed to describe the distribution of mineral properties in bones in 3D, therefore, the sub-nm resolution.

The current thesis **objective** is to characterize the bone mineral nanocrystal structure from microscopic scale (fibrils organization and porosity) down to atomic scale (structure-chemistry of the mineral phase).

The **tasks** of this thesis can be stated as follows: 1) to develop a method of sample preparation for multi-probe bone characterization; 2) to establish a protocol for ultra-, nano- and atomic scale study of bone mineral nanocrystals (such as nanoporosity volume fraction and dimensions; mineral nanocrystals size, shape and organization; mineral phase structure and chemical composition); 3) to attribute each of the obtained characteristics to a precise anatomical location of the sample within each of the hierarchical structural levels of bone; 4) to suggest nanostructural pathological markers for bones with different diseases.

Mainly bone of animal origin (bovine femur cortical part) and human iliac crest biopsies (in a control state and affected by osteopetrosis, fluorosis and hyperparathyroidism) were the

main **subject** of the study. However, human dentin samples were used as a simplified case for X-ray imaging.

Coherent X-ray diffraction imaging, TEM with automated crystal orientation mapping, XRD followed by Rietveld and pair distribution function analysis are applied for assessing the bone mineral nanocrystal structure and organization at ultra-, nano- and atomic scale.

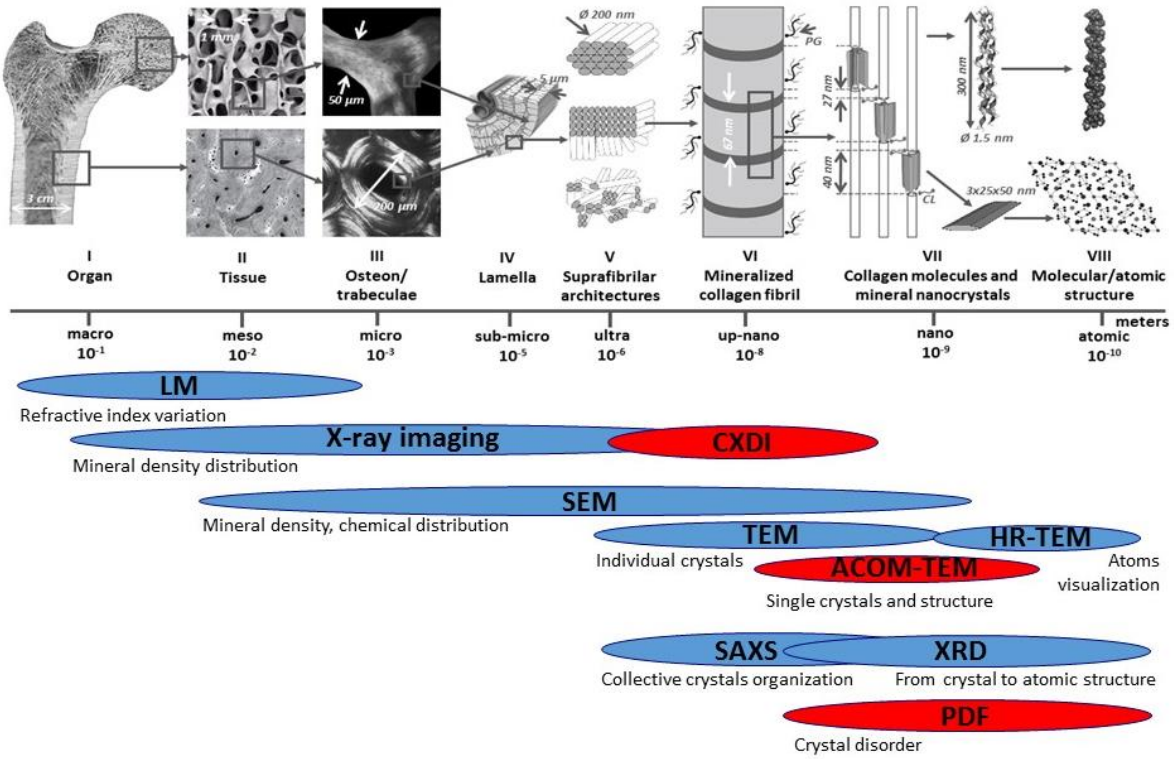

Figure I.1. Schematic representation of commonly used methods for bone tissue characterization at different scales. The methods chosen in current work are show in red.

Chapter 1 gives an insight into the **hierarchical structure of bone tissue**, reviews the state of the art knowledge of specific bone **structure, composition and functions**. Different **animal models** (human vs bovine) are also discussed. The problems associated with bone mineral phase identification and possible substitutions beyond the **heat-treatment** are described. In addition, three **pathological cases** of bone tissue (osteopetrosis, fluorosis and hyperparathyroidism) are illustrated.

A comprehensive work of gathering, testing, adaptation and validation of various sample preparation protocols has resulted in a **generalized multi-probe protocol for bone sample preparation** and is described in the first part of the **Chapter 2**.

It is followed by the **basic terminology** of solid-state physics (crystalline and amorphous solids, short and long-range order, essential crystallographic definitions of unit cell, symmetry, space group and Miller indices). The theoretical background of **scattering** with its properties (elastic/inelastic, coherent/incoherent scattering) and the principal definition of **diffraction** and **imaging** with the discussion on the **resolution limit** and the **choice of probe** are then described.

The following sub-chapters (2.2.2-2.2.3) are divided into two groups based on the use of characterization probe (**X-rays** and **electrons**). In the **X-ray probe group**, the background and the practical implementation for such methods as **Rietveld, pair-distribution function analysis** and **coherent X-ray diffraction imaging** are presented. In the following sub-chapters, the **sources of X-ray radiation** used in the current work are shortly described, including **laboratory source** for powder diffraction and **synchrotron** facility (ESRF), with the illustration of the setup at two **beamlines** (ID10 and ID11). The **electron probe group** contains the basic information about **electron diffraction** and **electron transmission microscopy** (bright and dark field operational modes) followed by the ideas of the **automated crystal orientation mapping** (ACOM) acquisition and data interpretation.

Chapter 3 contains the principal results that are split into three groups according to the characterization method used and the hierarchical scale it probes.

At first, the composite bone structure was studied at microscale in 3D by **coherent X-ray diffraction imaging** with spatial resolution less than 50 nm for the first time. Therefore, the fibrillar organization and nanoscale porosity were visualized.

The phenomenological understanding of the local mineral nanocrystal orientation and phase was achieved by the first-ever application of **ACOM-TEM** on bone. It provided 2D imaging with 2 nm resolution and collection of electron diffraction patterns from individual nanocrystals. It was tested on the set of bone after heat treatment.

PDF analysis allowed going beyond the information obtained by CXDI and TEM by probing the atomic scale of bone tissue. Bone mineral nanocrystal size, phases, interatomic bonds and order/disorder relation was assessed in bone after heat treatment and the pathological bone sample set. This is, to the best of our knowledge, the first PDF analysis on bone.

Finally, the conclusions and future perspectives are drawn by summarizing the current knowledge of multiscale bone structure and the input of this work into it.

Chapter 1. Bone, a multiscale perspective

1.1. Bone hierarchy

A **bone** is a rigid organ that constitutes part of the vertebral skeleton. Bones serve several vital functions: support and protection of the various organs and the soft tissues of the body; assisting in movement (muscle movement results in bone movement by the tendons that are attached to the skeleton); storage of minerals such as calcium and phosphorus, essential minerals for various cellular activities throughout the body; blood cell production (hematopoiesis) which takes place in red bone marrow, within the cavities of certain bones; energy storage (lipids, such as fats, stored in adipose cells of the yellow marrow serve as an energy reservoir). Therefore, bone structure has to fulfill all requirements for mechanical and physical properties of the tissue at every stage of the organism's life in order to properly provide the body with all these functions.

From the structural point of view, bone tissue can be viewed as a **hierarchical biocomposite** material, built from two principle components: collagen molecules and mineral nanocrystals. In any hierarchical material, the structural elements at one length scale are composed of elements, which, themselves, have a structure at smaller length scales. Such a structure plays a major role in determining the bulk mechanical properties of the overall bone that has to be strong, tough, with the given elasticity and, at the same time, light and able to support different levels of stress at the specific locations. Hierarchical structures typically contain less material to achieve a desired strength and can simultaneously provide strength and stiffness.

Mineral nanocrystals play a role of hardening elements that are incorporated into the organic matrix with high elastic modulus to provide sufficient elasticity and lightness. The overall fibrillar bone reinforcement structure allows the stress and strain distribution in the given directions (for example the strain distribution in the femur during standing). The arrangement of fibers is, therefore, different in several types of bone which gives rise to distinct needed mechanical properties (see as example Fig. 1.3b).

Bone composition includes [17]:

- organic phase ~30% by weight (50% by volume):
    - type I collagen molecules ~90% by weight;
    - noncollagenous proteins ~7%;
    - lipids ~1%;
    - cells ~2%;
- mineral phase ~75% by weight (50% by volume):
    - nanocrystals of apatite structure, close to hydroxyapatite;
- water ~10% from total bone mass.

The relative amount of the various components in given bone varies with age [18], site [19], gender [20], ethnicity [21], disease and treatment [22]. Proteins in the extracellular matrix of bone can be divided in: structural proteins (collagen and fibronectin) and proteins with specialized functions (that regulate collagen fibril diameter, serve as signaling molecules, growth factors, enzymes, etc.). Water plays an important role in the bio-mineralization process and serves as a plasticizer, enhancing the toughness of bone.

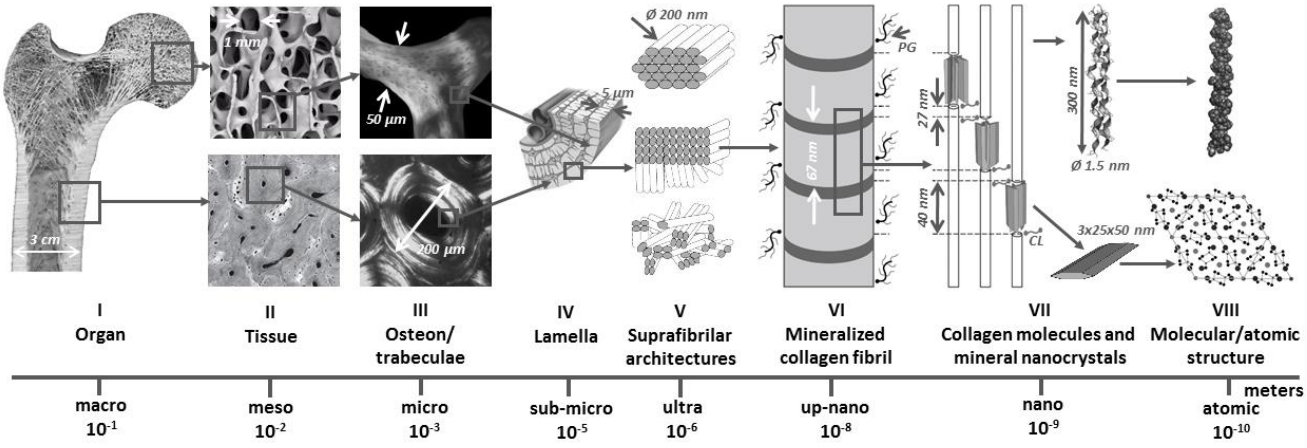

Figure 1.1. Bone hierarchy (example of human femur): I - photo of longitudinally cut femur, II - SEM of trabecular and cortical tissue, III - polarized light optical microscopy of a single trabeculae and osteon, IV - schematic representation of lamella, V - types of suprafibrular organizations [23], VI - collagen fibril with 67 nm periodicity (pg - proteoglycan molecules), VII - collagen molecules and mineral nanocrystals with gap (40 nm) and overlap zones (27 nm), CL - cross-links, VIII - molecular and atomic structure of the principal components.

Bone hierarchy can be described by many levels of structural organization. From 5 to 10 levels were defined by different authors [23–25]. The most known views on bone hierarchy are summarized in review [26] and in Table 1.1. In the current work, we choose 8 hierarchical levels of organization for representation that are drawn in Fig. 1.1. They will be discussed in detail in the following sub-chapters.

Table 1.1. Classification and definition of the hierarchical levels of bone proposed by different authors [26].

Hierarchical Level	Principal Components	Ref.
Macrostructure	Cortical and trabecular bone	(Rho et al., 1998)[25]
Microstructure	Individual osteons and trabeculae	
Sub-microstructure	Layers	
Nanostructure	Fibrilar collagen and mineral components	
Sub-nanostructure	Molecular structure of the different elements	
Level 7	Whole bone	(Weiner and Wagner, 1998)[23]
Level 6	Cortical and trabecular bone	
Level 5	Osteons	
Level 4	Patterns of the fibres (mature bone vs interstitial bone)	
Level 3	Collagen fibres	
Level 2	Fibrils of collagen and minerals	
Level 1	Molecules	
Whole bone level	Whole bone or bone representative of both subtypes	(Hoffler et al., 2000)[27]
Architectural level	Cortical or trabecular and osteons	
Tissue level	Individual trabeculae and osteons	
Laminar level	Layers	
Ultrastructural level	Mineral and molecular components	
Macrostructure	Whole bone or bone representative of both subtypes	(An, 2000)[28]
Architecture	Blocks of cortical or trabecular bone	
Microstructure	Trabeculae and individual osteons	
Sub-microstructure	Layers, large collagen fibers	
Ultra- or nanostructure	Fibrils and molecules of collagen, mineral components	

1.1.1. Level 1. Macrostructure: Organ

Bone as an organ (individual bones of the body) consists of:

- osseous tissue;
- nerves, blood vessels, cells, marrow;
- epithelial tissue.

Bones in human body are often classified based on their macroscopic morphology as: long, short, flat, irregular, and sesamoid. They come in a variety of shapes and sizes. In the human body at birth, there are over 270 bones [29], but many of them fuse together during development, leaving a total of 206 separate bones in the adult [30] (if not considering numerous small sesamoid bones). The largest bone in the human body is the femur and the smallest is the stapes in the middle ear. Bone dimensions range from several millimeters to several hundreds of centimeters or more, depending on species.

In Fig. 1.2a, the components of long bones such as femur or tibia are shown. The **epiphysis** are extreme parts of long bones, at the positions of its joint with adjacent bone(s). **Proximal** and **distal** epiphyses designate two ends of long bones: the first one is the closest to the center of the body and the second one is furthest, respectively.

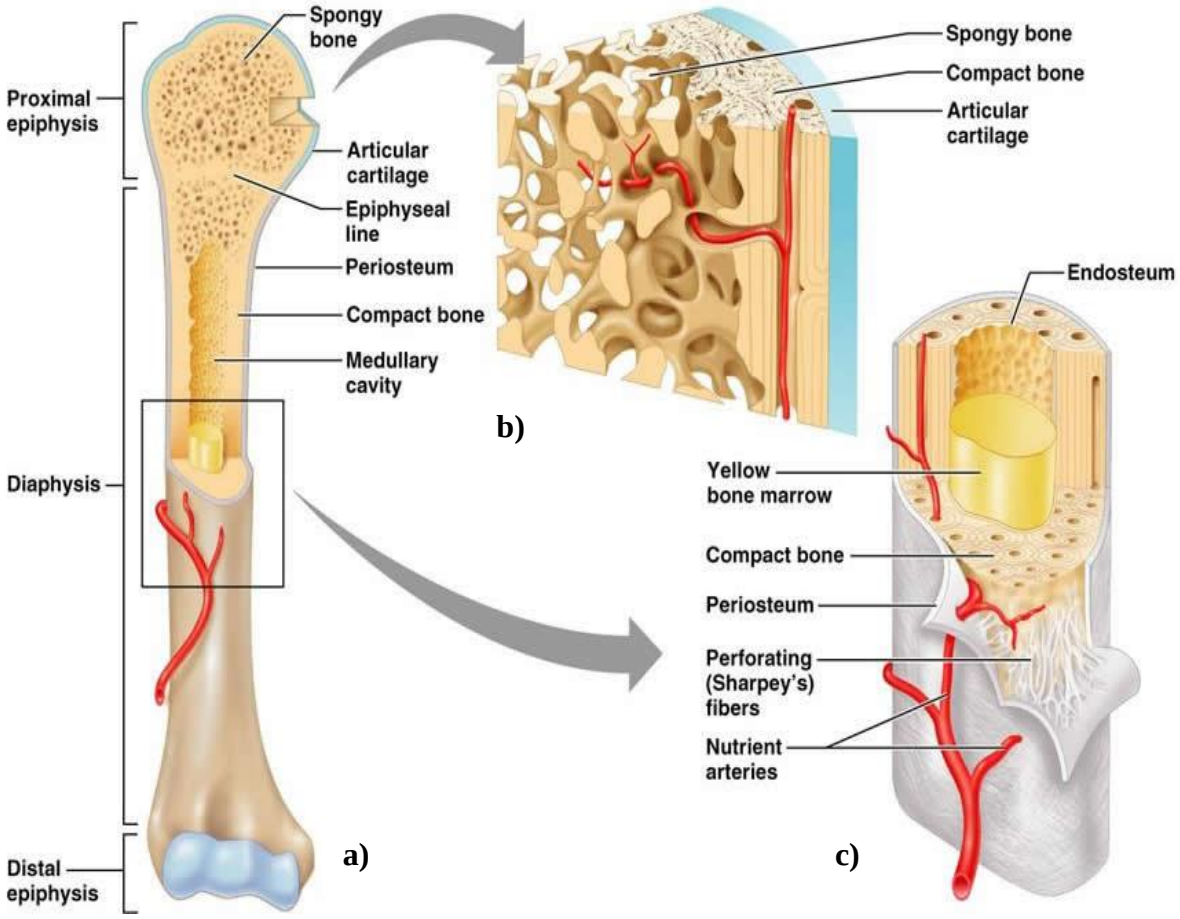

Figure 1.2. Bone hierarchical levels 1 and 2 illustrated for long bone: a) whole bone, b) zoom into epiphysis structure; c) zoom into diaphysis structure.

The **diaphysis** is the middle part of a long bone. It forms a cylinder-like hollow shape with the so-called **medullary cavity** that contains red or yellow marrow and adipose tissue (fat).

Between the epiphysis and diaphysis lies the metaphysis, including the **epiphyseal plate** (growth plate) or **epiphyseal line** - the area where bones grow in length. At the joint, the epiphysis is covered with **articular cartilage**.

Two types of membranes are present in bone: **periosteum** (the membrane that covers the outer surface of all bones, except at the joints of long bones) and **endosteum** (inner surface of all bones).

1.1.2. Level 2. Mesostructure: Tissue

Bone tissue can be divided into two types (see Fig. 1.2) by taking into account its structure, location and properties:

- cortical (or compact);
- trabecular (cancellous or spongy).

Cortical bone constructs around 50-80 % of the human skeleton and trabecular bone - around 20-50 %. **Cortical bone** is a strong and dense tissue. In contrast to cortical bone, **trabecular bone** is a porous, more flexible, reinforcing tissue that frequently contains red bone marrow, where hematopoiesis, the production of blood cells, occurs. It has a higher surface area to mass ratio than cortical bone because of the lower density. Some structural and mechanical properties of cortical and trabecular bone are compared in Table 1.2.

The long bones are composed from a dense cortical shell (that provides the organ with required strength and stiffness) with a porous trabecular interior (that ensures stress reinforcement and lightness). Flat bones such as frontal bone have a sandwich structure: dense cortical layers on the outer surfaces and a thin, reinforcing trabecular structure within. Trabecular bone is also present within the interior of vertebrae.

Normally, both bone types are easily distinguished by their degree of porosity or density but the true differentiation comes from histological evaluation of the tissue's microstructure as it is shown in Fig. 1.3.

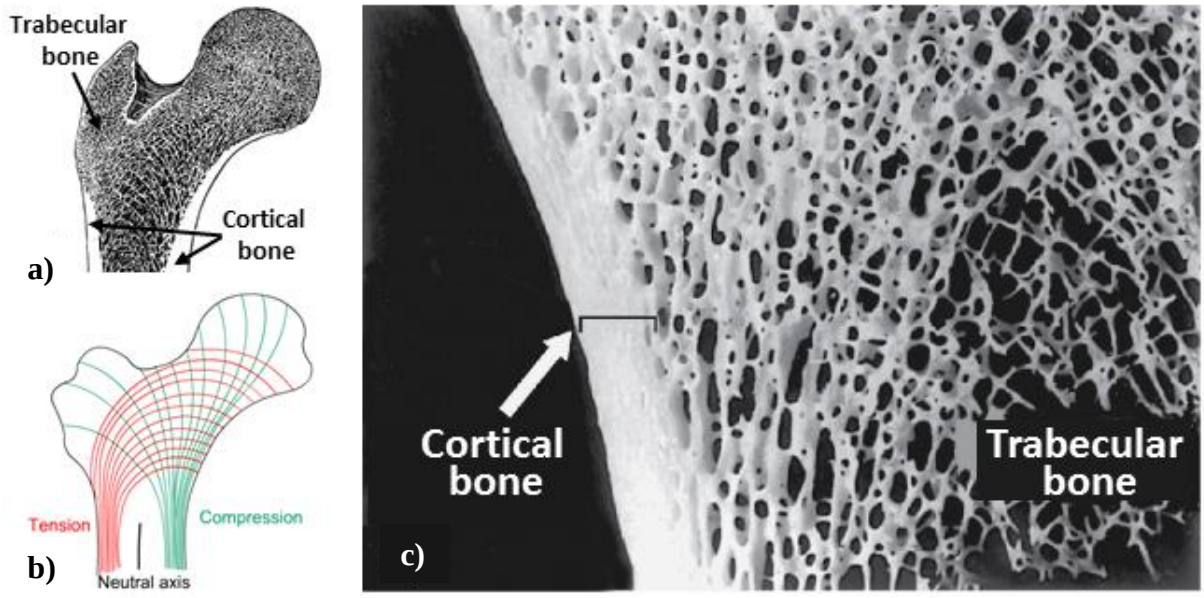

Figure 1.3. Cortical vs trabecular bone: a) human femoral head structure with b) diagram showing computed lines of constant stress and c) scanning electron micrograph of a part of femoral head. Adapted from [31,32].

Table 1.2. Comparison of structural features and mechanical properties of cortical and trabecular bone. Summarized from [33–35].

Tissue type/properties	Cortical	Trabecular
Volume fraction, mm^3/mm^3	0.85 - 0.95	0.05 - 0.60
Surface fraction, mm^2/mm^3	2.5	20
Porosity, %	5-10	50-90
Density, g/cm^3	1.6-2.0	0.03-0.12
Total skeletal mass, %	80	20
Young's modulus, GPa	7-30	0.7-20
Strength, MPa	100-230	1.0-7.0

1.1.3. Level 3. Microstructure: bone units (osteons and trabeculae)

At the microstructure level, cortical bone is arranged in repeating structural units that are called **osteons** (or Haversian systems), see Fig. 1.4c.

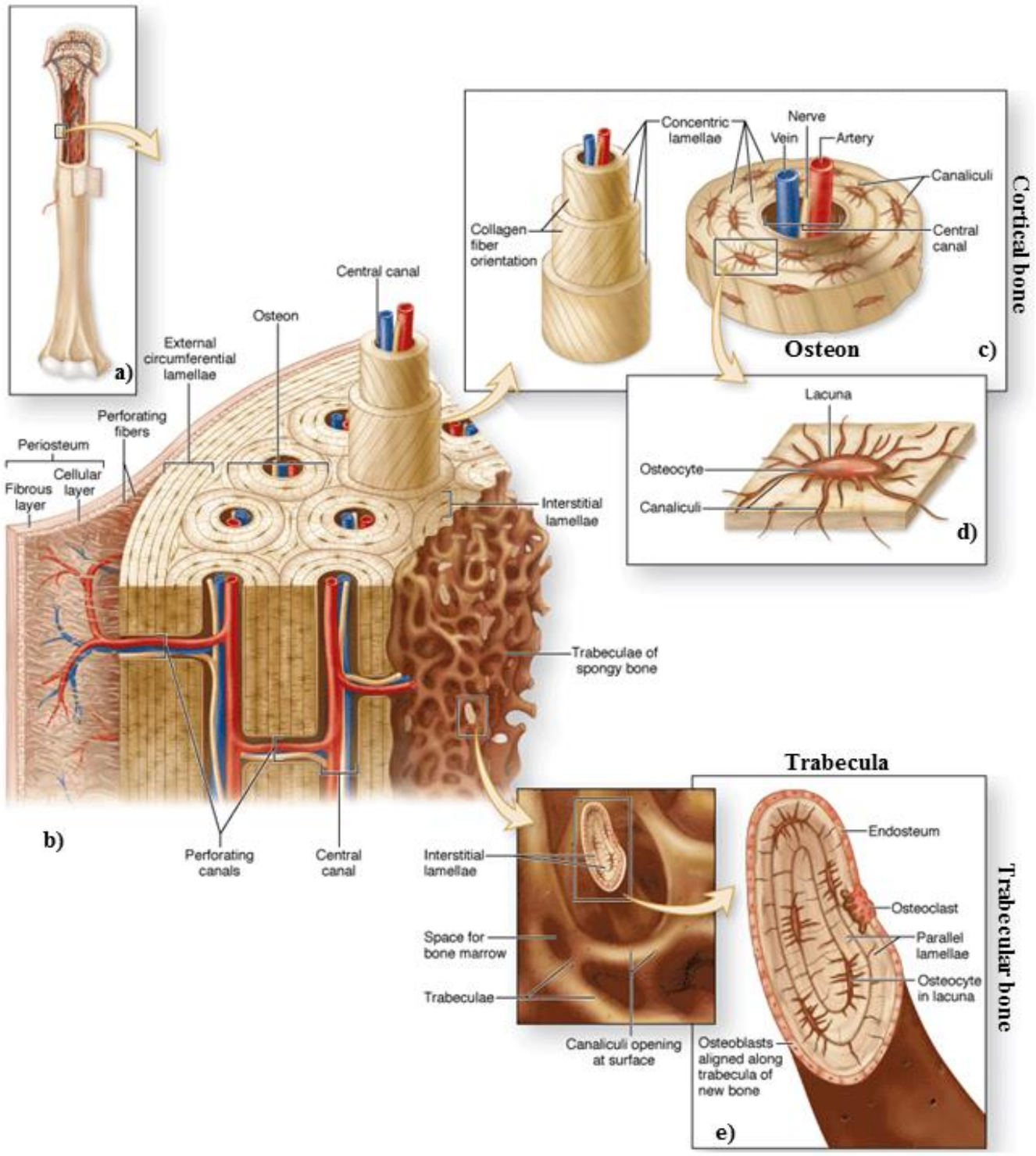

Figure 1.4. Bone hierarchical levels 1-3: a) whole bone; b) section of long bone; c) osteon - cortical bone unit; d), e) lacuna-canaliculi network; e) trabecula - trabecular bone unit. Adapted from [31].

Typical osteon diameters can range from 200-500 μm depending on species and anatomical location. Those cylindrical features have a central canal, also called as **Haversian**

canal (around 50 μm in diameter), where blood vessels (artery, vein) and nerve fibers pass. Haversian canals are connected between each other and to bone marrow by the perforating canals (see Fig. 1.4b). Haversian canals are surrounded by the concentrically arranged **lamellae** (~3-7 μm thick). The mature **bone cells** (osteocytes) in cortical bone are located in lamellae in cavities called **lacunae** (~300-500 μm^3) that are connected to each other by fluid-filled channels, **canaliculi** (~100-500 nm in diameter) (see Fig. 1.4d). This channel system serves cell nutrition and communication functions and is often referred to as the lacuna-canaliculi network.

In contrast to cortical bone, trabecular bone is composed of irregular units of thin bone columns which can be partly flattened, called **trabeculae** (~50 μm in diameter) that form an interconnected network, as shown in Fig. 1.4e. Overall trabeculae are aligned towards the principal direction of mechanical loading that a bone experiences. The porous trabecular tissue with pore size, typically, of the order of 1 mm, are filled with bone marrow, fat and bone cells. A single trabecula is composed of lamellar tissue with osteocytes lying in lacunae with canaliculi network similar to the one of cortical tissue.

Four major **bone cell** types can be found in bone tissue such as:

1) Osteogenic cells (“genic” refers to genesis, the start of something new) - undifferentiated stem cells located in the inner layer of the periosteum and the marrow.

2) Osteoblasts (“blast” from Greek “blastos” - to germinate) – the cells with single nuclei that synthesize bone material. They are located in growing portions of bone at periosteum and synthesize collagen with additional specialized proteins (organic bone matrix) and regulate calcium and phosphate based mineral that is deposited, in a highly regulated manner, into the organic matrix.

3) Osteoclasts (“clast” from Greek “clastos” - broken) - bone material destroyers, the large multinucleated cells responsible for bone resorption. They are located at the surface of the bone (periosteum and endosteum) and at sites of old, injured or unneeded bone.

4) Osteocytes (“cyte” from Greek - cell) - dendritic shaped mature bone cells with a single nuclei that is formed when an osteoblast becomes embedded in the material it has secreted. Osteocytes are located in lacunae of both cortical and trabecular tissues. They perform essential mechanotransduction function (sensing and transferring the information about bone fracture and mechanical load, regulating bone mass and mineral metabolism) and control the activity of osteoblasts and osteoclasts for bone remodeling.

The schematic representation of bone cell types with the example of their location is shown in Fig. 1.5.

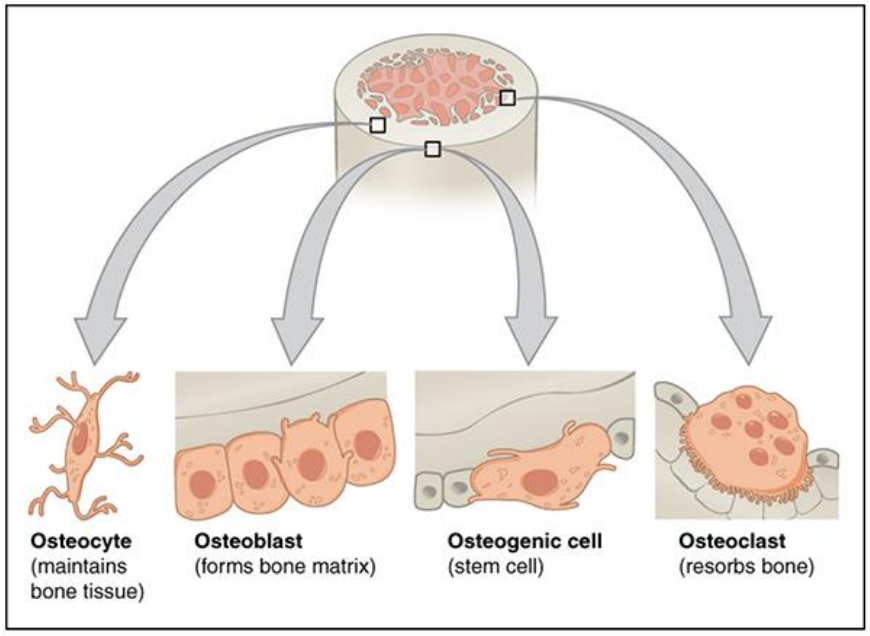

Figure 1.5. Four types of bone cells and their location [36].

1.1.4. Level 4. Submicrostructure: lamella

At this hierarchical level, one can find two distinct states of bone as it matures: woven bone and lamellar bone. **Woven bone** (or primary bone) is formed during bone development or repair of fracture. Woven bone consists of strongly disorganized collagen fibers (see Fig. 1.6). It is found in all tissues formed under fast dynamics, e.g. fetuses, newborns, near a fracture, close to the growth plate of bones, in many animal adult species (bovine, equine, murine etc.) and in certain bone diseases.

For certain species (human, canine, ovine, porcine etc.), in the later stages of body development, bone is being removed by osteoclasts and new **lamellar bone** (or secondary bone) is being formed by osteoblasts. This process is called remodeling. Lamellar bone replaces the woven bone after the remodeling process or the repair of a fracture [37] or micro-damage.

Bone remodeling is a continuous process during life time which occurs only in certain species (human, canine, ovine, porcine etc.). It involves a combination of bone synthesis and removal. In compact bone, remodeling resorbs parts of “old osteons” and produces “new ones”. This process involves the coordinated activity of osteoblasts and osteoclasts. It is

responsible for bone adaptation to changes in stress, especially during the body's growth. Therefore, for those species, adults' bone consist of several generations of osteonal systems (Fig. 1.7). In healthy adults, 5–10% of bone is remodeled annually.

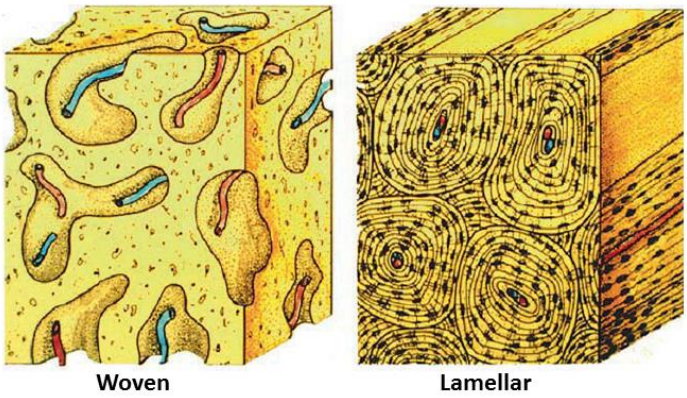

Figure 1.6. Diagram of woven and lamellar bone. In woven bone, the collagen fibers are randomly oriented such that no distinct microscopic scale features can be identified and the cells (osteoblasts and osteocytes) tend to be randomly arranged. In lamellar bone, lamellar Haversian system organization is observed [38].

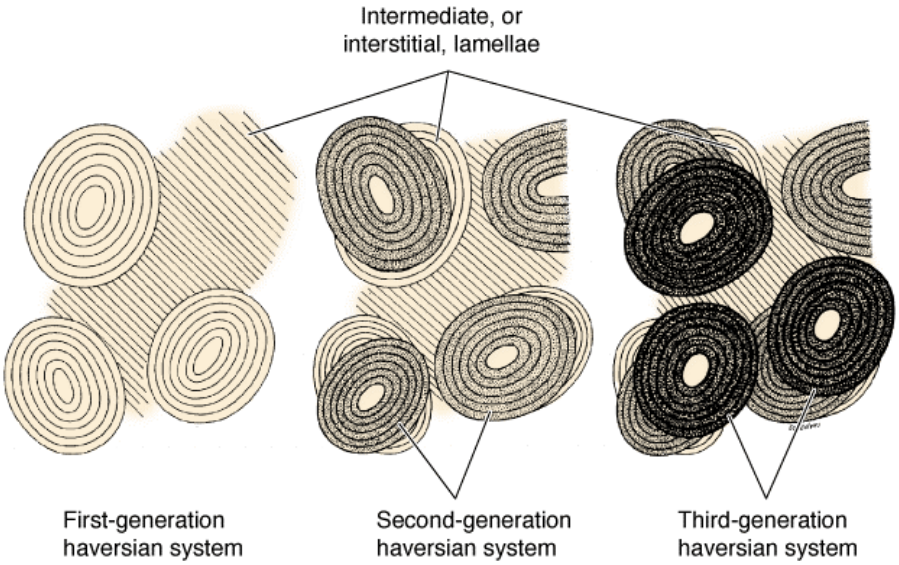

Figure 1.7. Schematic diagram of compact lamellar bone remodeling showing three generations of osteonal systems with the resulting formation of interstitial lamellae [31].

In mature bone, concentric lamellae are arranged around Haversian canals in cortical bone and form well delimited bone volumes in trabecular bone. The remaining tissue in between osteons (filling the gaps between osteons) is known as interstitial bone. Furthermore,

large circumferential lamellae can be found at the outer and inner periphery of the cortex, respectively (as shown in Fig. 1.8).

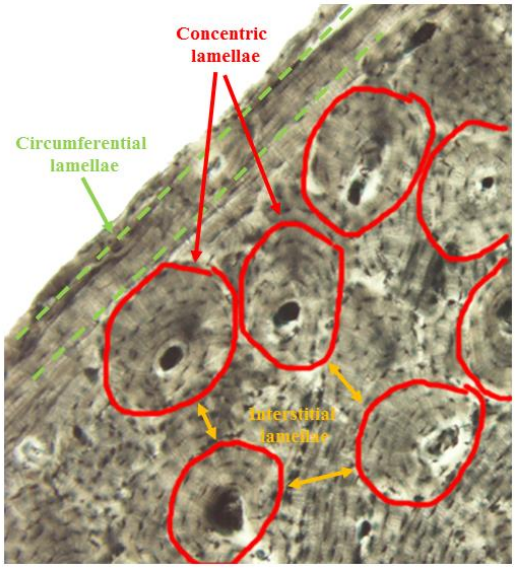

Figure 1.8. Optical micrograph of transverse section of human femur illustrating the location and the microstructure of concentric, interstitial and circumferential lamellae.

Independent of its location, lamellar bone structures are quite similar. In a single lamella, the mineralized collagen fibers are approximately perpendicular to the direction normal to the lamellae and follow a helical course about this direction similar to a twisted plywood structure [39] (see Fig. 1.4c). The pitch of the helix is, however, different for different lamellae, so that at any given point, fibers from adjacent lamellae are related by 60-90°[40]. The specific organization of collagen fibers in successive lamellae of each osteon is has been shown to be a major determinant of the elasticity (and, hence, rigidity) of secondary bone.

1.1.5. Level 5. Ultrastructure: suprafibrilar architectures

This structural level is composed from mineralized collagen fibrils that will be defined in the Level 6 of the hierarchy. However, how these fibrils are organized at the upper scale is a source of debate for a long time. We will call this structural level **suprafibrillar architectures** [41]. A few main concepts existing in the literature will be discussed here.

The most generalized concept, in my point of view, was published by S. Weiner and H.D. Wagner in 1998 [23]. They define this level as “fibril array patterns.” The idea comes

from the fact that four main types of fibril array organization patterns were observed in different bone types such as: parallel, disordered, plywood-like and radial fibril arrays. The scanning electron micrographs of these patterns with corresponding schemes are shown in Fig. 1.9.

Parallel fibrils array pattern (Fig. 1.9a) can be found in mineralized turkey tendon (scale bar: 0.1 mm). Collagen fibrils are packed parallel to each other in bundles. Disordered array is a characteristic pattern for woven type of bone (Fig. 1.9b). Fibrils are arranged in different orientations. Plywood-like structure is present in lamellar bone (Fig. 1.9c). The fibrils in each layer are rotated relative to their neighbors, following the rotated plywood model. And at last, the radial array pattern is observed in dentin tissue (Fig. 1.9d). The tubules (holes) are surrounded by collagen fibrils that are located in one plane (perpendicular to tubules) but with no preferential orientation within the plane.

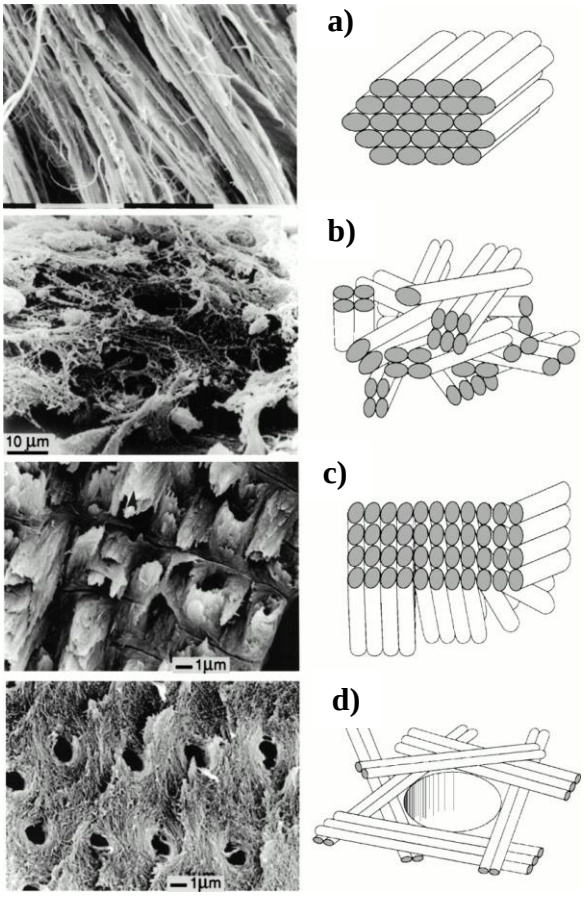

Figure 1.9. Four of the most common patterns of fibrils organization: SEM micrographs of fractured surfaces and schematic illustrations (not drawn to scale) of the basic organizational motifs: a) parallel array pattern (turkey tendon, scale bar: 1 mm), b) disordered array patter (human fetus femur), c) plywood-like lamellar bone (baboon tibia), d) radial array pattern (human dentin) [23].

P. Fratzl and co-workers [42], also shows an existence of different architectures: fibril "bundles" in tendon and ligaments and radial arrays in dentin.

However, the paper of J.-Y. Rho et al. [25] proposes the concept of "collagen fiber" structural level as shown in Fig. 1.10. Collagen fibers that are made of a set of collagen fibrils is believed to be both surrounded and infiltrated by mineral.

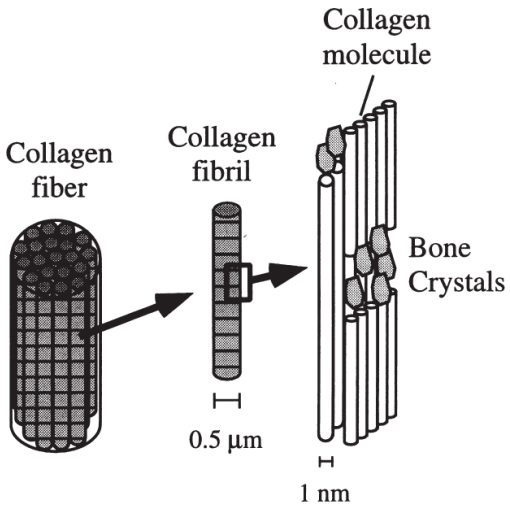

Figure 1.10. Nano- and sub-nanostructure of bone hierarchy by J.-Y. Rho et al. indicating the collagen fibrils assembly into collagen fibers [25].

Eventually, another interesting concept is proposed by the group of F.-Z. Cui [43] where the collagen fibril is surrounded by mineral nanocrystals that define its specific diameter as shown in Fig. 1.11.

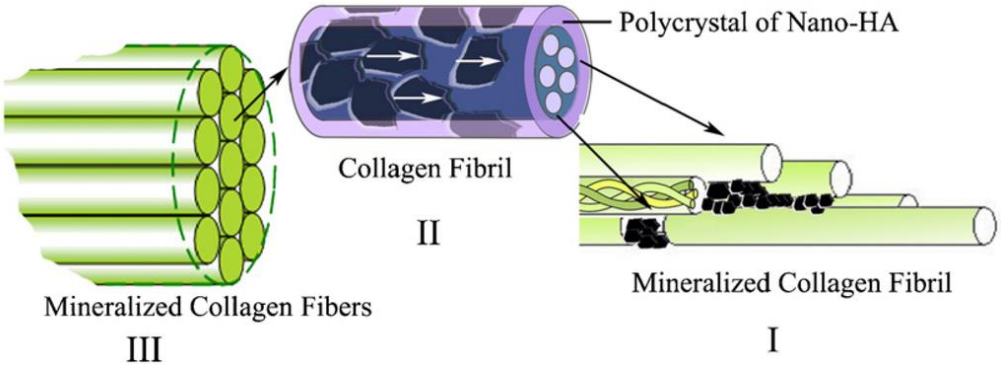

Figure 1.11. The self-assembled hydroxyapatite-collagen composite hierarchical structure [43].

It is possible that the formation of a specific structural unit referred to as "fibers" or "bundles" can be one of specific cases that is observed when the fibrils are packed in parallel manner such as in the case of tendon. But it may be difficult to define some kind of packing unit in other kinds of bone tissues. Therefore, we would call this structural level as "suprafibrilar architectures" and define it as mineralized collagen fibrils organization packing.

1.1.6. Level 6. Up-nanostructure: mineralized collagen fibril

The mineralized collagen fibrils of a diameter of around 200 nm are the basis for various connective tissues such as bone and cartilage. They are cylindrical shaped self-assembled composite bunches of collagen molecules and mineral nanocrystals.

Collagen molecules are shifted by about 67 nm within the fibril, as shown in Fig. 1.12. The three-dimensional organization of collagen molecules will be discussed in the next sub-chapter; however, one important aspect essential to bone mechanical properties and fibrils diameter has to be mentioned: the covalent cross-linking between molecules that develop with the tissue maturation allow the molecules to interconnect within the fibril. These cross-linking, indeed, prevent fibrils from sliding with respect to each other. However, the fibrillar surface is believed to be a complex area which contains a variety of proteoglycans that define the more or less regular diameter of collagen fibrils [42].

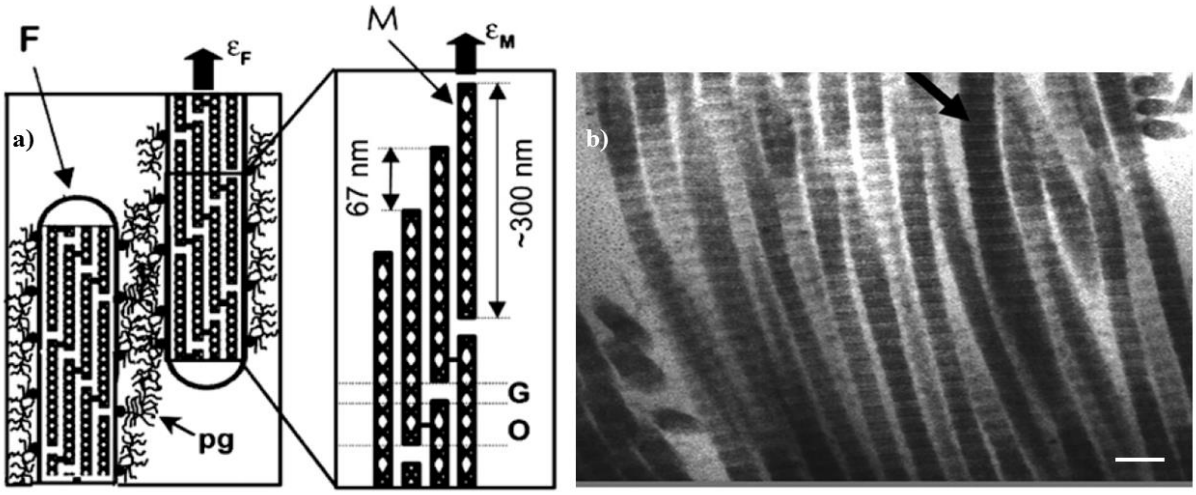

Figure 1.12. Collagen fibril: a) sketch of the inter- and intrafibrillar structure (F - fibril, pg - proteoglycan matrix, M - collagen molecule, G-gap zone, O-overlap zone, ε_F and ε_M are fibrillar and molecular strain, respectively) [44]; b) TEM illustrating the collagen fibrils seen in the longitudinal section [45].

Proteoglycan is a compound consisting of a protein bonded to mucopolysaccharide groups. They have distinct biological functions apart from their hydrodynamic functions (provides hydration and swelling pressure to the tissue enabling it to withstand compression forces) and they may play a role in regulating collagen fibril formation and stability.

1.1.7. Level 7. Nanostructure: collagen and mineral

At this structural level of organization, bone tissue consists of two principal components: collagen molecules and mineral nanocrystals.

Collagen molecules are around 300 nm long and 1.5 nm thick. They are composed of three polypeptide chains that form a right-handed triple-helical structure as show in Fig. 1.13 [46].

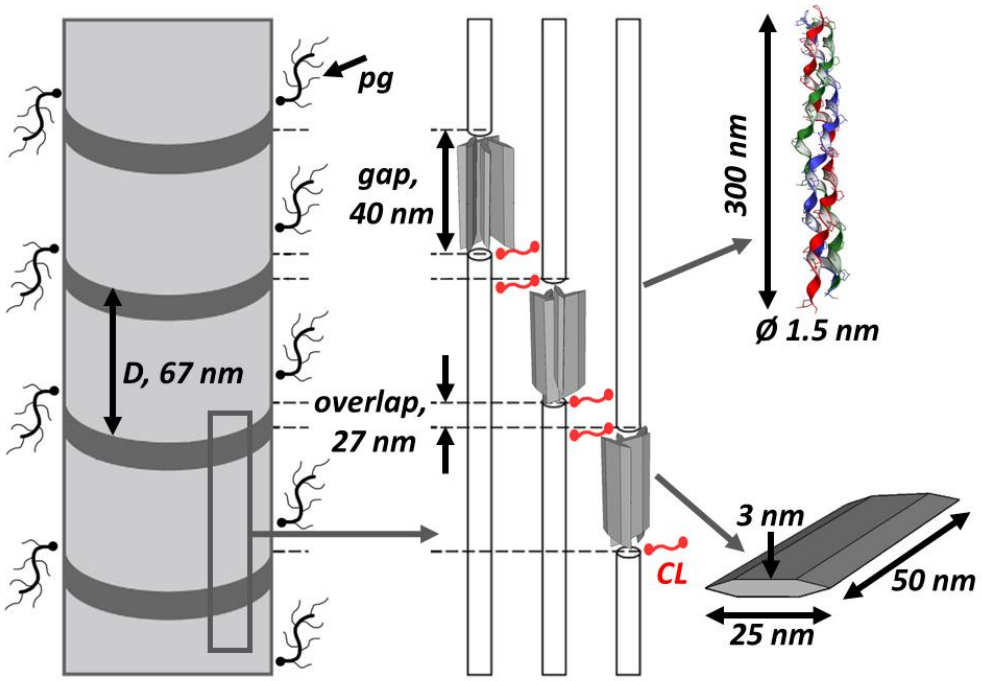

Figure 1.13. Mineralized fibril structure: collagen molecules and mineral nanocrystals organization (D - collagen periodicity). The gap and overlap regions are the source of characteristic 67 nm collagen banding. Mineral nanocrystals that are located within the gap zones are oriented with the c-axis being parallel to the collagen fibrils.

In this structure, three polypeptide chains combine to form an alpha helical strand of **tropocollagen**. Tropocollagen molecules further combine to form collagen fibrils. Due to the space between the ends of the tropocollagen molecules and an offset from row to row, **gap and overlap zones** exist within the fibril and produce an oscillating surface topography with a characteristic axial repeat pattern called the D-periodicity of 67 nm. This periodicity (repetition of gap and overlap zones) produces a characteristic interference pattern that is observed as bands in transmission electron microscopy as illustrated in Fig. 1.12b.

Whereas mineral nanocrystals are platelet-shaped apatite crystals of the size of about 3 x 25 x 50 nm^3 [47] assembled together with collagen molecules with their c-axis (long axis) parallel to the collagen main axis [48]. There are also many evidences of the existence of intra-fibrillar mineral crystals that are equally oriented along the long axis of collagen [43].

The nanocrystals' size can vary depending on different factors such as: the arrangement of the collagen molecules (template for mineral deposition) [49], species, age, anatomical location, diseases, diet, etc. [50]. For example, an increase in crystal length and decrease in thickness in human bone biopsies from newborn to 25 years old as well as slight length decrease over 50 years old was reported in [6] by XRD. Also diet influences trace elements in drinking water that may impact the crystal size and quality. Some trace elements may be incorporated into the lattice of mineral nanocrystals and affect growth of apatite crystal. For example, strontium impurities cause in some cases strontium osteomalacia; fluoride treatment is known to increase bone crystal size [41]. In addition, in diseases such as osteogenesis imperfecta, or brittle bone disease, the collagen molecules have genetically deficient structure. It also affects mineral crystals that are in most cases significantly reduced in size [51].

1.1.8. Level 8. Molecular and crystal structure: bone crystallography

The final lowest level of the bone tissue hierarchical description contains the information about crystal and molecular structure of the two principal components (mineral nanocrystals and collagen molecules). It also includes important discussions on the mineral crystal phases, degree of crystallinity, crystal-chemistry and different possible lattice defects. From the organic point of view, the questions such as how collagen cross-linking, defects, and the functions of non-collagenous proteins can influence the molecular structure are important, but these questions are beyond the current discussion.

As mentioned before, collagen is a long (300-nm), thin (1.5-nm-diameter) protein that consists of three coiled subunits: two α1(I) chains and one α2(I). Each chain contains 1050 amino acids that are wound around each other in a characteristic right-handed triple helix [46,52].

The triple-helical structure of collagen is built of three amino acids: glycine, proline, and hydroxyproline that create the characteristic repeating motif Gly-Y-X, where X, Y can be any amino acid. The first high resolution crystal structure solution of collagen triple helix is shown in Fig. 1.14a,c [53].

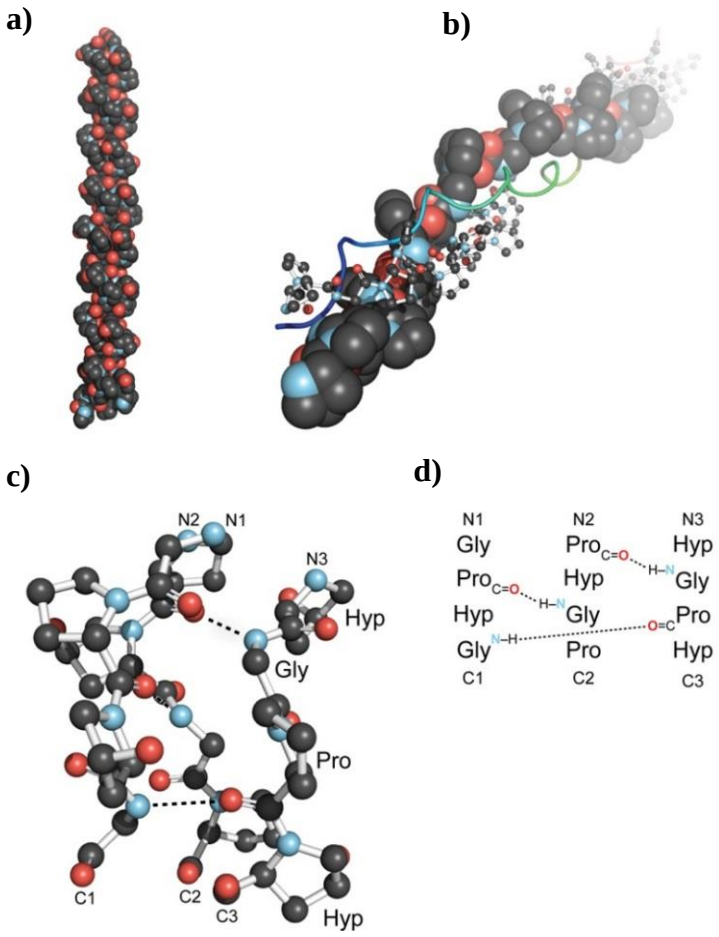

Figure 1.14. Collagen triple helix structure: a) crystal structure of a collagen triple helix, formed from (ProHypGly)4–(ProHypAla)–(ProHypGly)5 [53]; b) view down the axis of a (ProProGly)10 triple helix [54] with the three strands depicted in space-filling, ball-and-stick, and ribbon representation; c) ball-and-stick image of a segment of collagen triple helix [53] highlighting the ladder of hydrogen bonds; d) stagger of the three strands in the segment in panel c. Reprinted from [55].

Each amino acid has a precise function. The side chain of glycine, an H atom, is the only one that can fit into the crowded center of a three-stranded helix. Hydrogen bonds linking the peptide bond NH of a glycine residue with a peptide carbonyl (C═O) group in an adjacent polypeptide help hold the three chains together (see Fig. 1.14c,d). The fixed angle of the peptidyl-proline or peptidyl-hydroxyproline bond enables each polypeptide chain to fold into a helix with a geometry such that three polypeptide chains can twist together to form a three-stranded helix. Interestingly, although the rigid peptidyl- proline linkages disrupt the packing of amino acids in an α helix, they stabilize the rigid three-stranded collagen helix [52].

Mineral nanocrystals have platelet shape with the characteristic length 20-60 nm, width 10-20 nm and thickness of 1.5-5 nm [56]. Such small crystal size has several advantages. First of all, it permits an extended surface area of 100-200 m^2/g that makes bone crystals metabolically active and eligible for numerous interactions with extracellular fluids. Secondly, from the mechanical point of view, small crystals that are ordered in location and orientation within collagen molecules provide high strength and rigidity of the tissue. However, many debates still exist concerning the origin of mineral nanocrystal size limitation: whether it is defined by the collagen molecules organization that acts as a template for mineralization or by the specified cells activity.

Also, the mineral nanocrystals' location with respect to collagen is still an open question of great interest. It is well known that the crystals are oriented with their c-axis aligned to the collagen molecules long axis and that the majority of crystals are located within gap zones of collagen banding pattern. However, it is not yet clear whether the mineral can also be present at additional locations. The volume percentage of mineral phase in the tissue is about 45 %, while the volume of gap zones is 12 %. Therefore, the additional locations may be possible. Some papers had reported the presence of the mineral phase in-between collagen molecules [57] and on the outer part of fibrils [43]; however, such periodicities were not observed with X-ray techniques.

It seems now to be generally believed that crystals initially form within the gap region of the collagen fibrils, further proceed into the overlap region, and occasionally grow into the extrafibrillar space [58]. Consequently, mineral can be found both within and outside the collagen fibrils, but the exact amount in each location is still a matter of discussion.

Several models of the mineralization process include other elements. The group of V.J. Landis had shown their model based on the 3-D TEM tomography [59,60]. The mineral nanocrystals grow preferentially in length along the collagen long axes and in width within the spaces generated by the collagen stacking. After, crystals fuse together and grow 40–170 nm in length and ~40 nm in width beyond the gap and overlap regions. However, the growth in thickness stays limited to 4–6 nm. Therefore, fused mineral crystals form thin parallel sheets throughout the assemblage of collagen fibrils. In a recent study on mineral crystals in embryonic chick bones, V.J. Landis et al. [61] suggested that the mineral sheets may fuse to form a continuous mineral organization. I. Jäger and P. Fratzl [62] have also proposed a model of a staggered arrangement of mineral platelets circumferentially surrounding a concentric structure of the collagen fibrils based on mineralized turkey leg tendon that recalls the model proposed by F.Z. Cui [43]. Thus, there is a fundamental interest in development of imaging techniques with sufficient spatial resolution, especially in 3D, for spreading the light on this question.

Another important aspect involves the chemical composition and mineral nanocrystal structure. For a long time, bone mineral crystallographic structure was assimilated to hydroxyapatite (HA). In 1926 it was defined as "an apatite similar to geological hydroxyapatite" by chemical analysis and X-ray diffraction by W.F. de Jong [5] and confirmed a few years later by H.H. Roseberry [63]. It is interesting to note that now, 90 years after the first report of bone mineral structure, such questions as exact chemical composition, crystallographic symmetry and specific atomic spatial arrangement of bone mineral are still not known in details.

However, it soon became very clear that there are significant structural and compositional differences between hydroxyapatite and bone mineral. X-ray diffraction data shows that the spectrum from bone gives peaks at exact positions of hydroxyapatite, but they are largely broadened (see Fig. 1.15) [50]. Such broadening can come from several factors: very small crystal size, presence of strain, degree of crystallinity and chemical substitutions.

Stoichiometric hydroxyapatite belongs to the general and wide apatitic group, represented by the formula:

$$Me_{10}(XO_4)_6Y_2 \qquad (1\text{-}1)$$

where Me is a divalent metal ($Ca^{2+}, Sr^{2+}, Ba^{2+}, Pb^{2+}$, …), XO_4 is a trivalent anion ($PO_4^{3-}, AsO_4^{3-}, VO_4^{3-}$, …), and Y is a monovalent anion ($F^-, Cl^-, Br^-, I^-, OH^-$, …).

Apatitic crystal structure has usually a hexagonal lattice and is very accommodating to chemical substitutions. The stoichiometric hydroxyapatite has the following chemical formula:

$$Ca_{10}(PO_4)_6(OH)_2 \qquad (1\text{-}2)$$

It constructs the hexagonal space group $P6_3/m$ with 44 atoms per unit cell and lattice parameters of $a = b = 9.417$ Å; $c = 6.875$ Å; $\alpha = \beta = 90°$; $\gamma = 120°$ as is shown in Fig. 1.16. [64]. Stoichiometric hydroxyapatite has a calcium-to-phosphate ratio of 1.6.

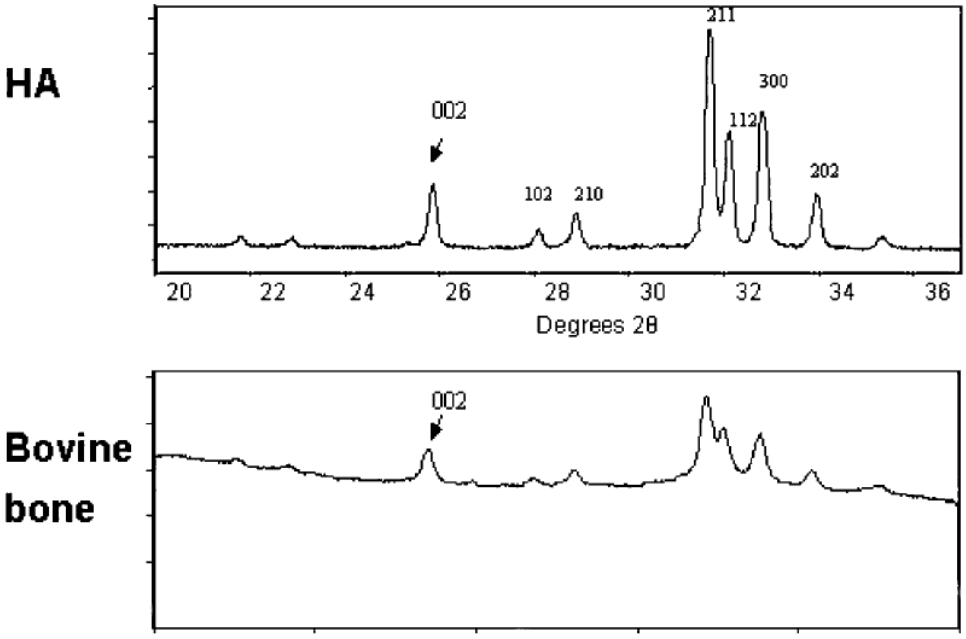

Figure 1.15. Comparison of XDR diagram for stoichiometric hydroxyapatite (HA) and bovine bone showing large broadening of peaks in case of bone [50].

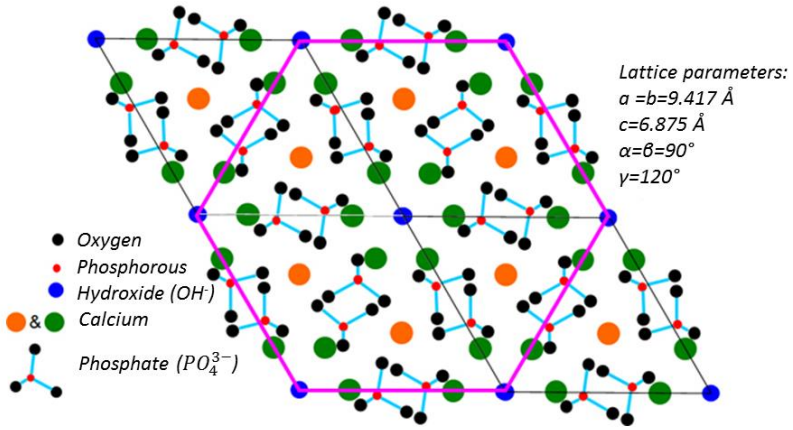

Figure 1.16. Schematic representation of hydroxyapatite crystal structure with its lattice parameters (from American Mineralogist Crystal Structure Database #0001257 [64]).

Some discussions about the existence of bone mineral with monoclinic space group of $P2_1/b$ also took place [65,66]. However, it was mainly predicted by models [67,68], heat treatment on bone [69] and artificial synthesized hydroxyapatite [70,71]. From the theoretical point of view, monoclinic hydroxyapatite structure is thermodynamically more stable than hexagonal; however, the hexagonal phase allows easier exchange of OH-groups with other ions which is necessary for bone [68]. Therefore, it is generally accepted that bone apatite in the native state has a hexagonal phase.

The structure of bone mineral is far different from stoichiometric hydroxyapatite due to numerous substitutions. Geological apatite lattice can accommodate nearly half of the periodic table. Nonetheless, possible ionic substitutions in bone are limited to the number of available elements in the body. Therefore, the ions that are known and/or reported to be present in bone and dentin are: $F^-, Cl^-, Na^+, K^+, Fe^{2+}, Zn^{2+}, Sr^{2+}, Mg^{2+},$ citrate and carbonate (some of them are shown in Fig. 1.17). These minor elements may not only alter the space group, crystallinity, morphology, stability, and mechanical properties of the hydroxyapatite structure, but can also play an important role in the biological responses of bone cells.

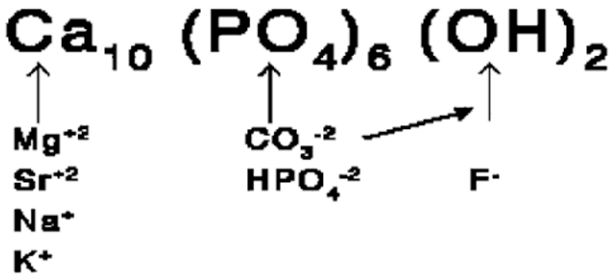

Figure 1.17. Schematic of possible ionic substitutions into hydroxyapatite lattice [50].

Hydroxyapatite lattice has four different sites (crystallographic positions) in the unit cell: 1) P sites with P^{5+} ions in tetrahedral sites with 4-fold coordination with oxygen; 2) Ca(I) sites for four of Ca^{2+} ions; 3) Ca(II) sites for other six Ca^{2+} ions that form a channel along the c-axis; 4) the channel occupied by two monovalent anions such as OH^-, F^- and Cl^- [72]. Therefore, different possible substitutions and vacancies can occupy different characteristic sites. In case that the substitution ion has different electric charge than the lattice ion (for example, CO_3^{2-} substitutes PO_4^{3-}) a vacancy is created in order to maintain electrostatic equilibrium [56].

For example, the fluoride substitution has the following mechanism: fluoride ions (F^-) replace hydroxyl groups (OH^-) in a hydroxyapatite lattice [72]. Fluorapatite is less soluble than hydroxyapatite, even under acidic conditions, which makes it to some extent a desirable substitution in teeth. However, it was shown that large amounts of fluoride substitutions in bone introduces changes in crystallinity, affects bone cells and reduces its mechanical properties [73,74].

Magnesium is the fourth most abundant cation in the body and the second most prevalent intracellular cation. Typical concentration of Mg ions in human bone is 0.55 wt.% [75]. Mg^{2+} substitutions are preferentially incorporated into the Ca(II) positions. It plays a key role in bone metabolism, in particular during the early stages of bone formation where it rapidly increases number of active osteoblasts, and its depletion causes bone fragility and bone loss. The dietary Mg deficiency has also been implicated as a risk factor for osteoporosis [76]. Furthermore, relationships have been suggested between the magnesium content in enamel and the development of dental caries [77].

Despite the fact that Cl^- is abundant in the human body, especially in blood plasma, and its concentration reaches tens of wt.%, Cl^- does not substitute for OH^- in bone and tooth apatite due to its large ionic size [72].

Bone apatite contains approximately 7 wt.% of carbonates [72]. In principle, carbonate ions can substitute in the apatite structure either in the OH-site (A-type substitution) or in the PO_4-site (B-type substitution). The nomenclature A-type and B-type was first introduced by the geologist D. McConnell, who studied apatites that released CO_2 upon dissolution [78]. The principal scheme of A-type and B-type carbonate substitutions is shown in Fig. 1.18 [79]. Carbonates were shown to have a strong influence on the growth of apatite crystals [80].

It was demonstrated by micro-Raman and FTIR studies that B-type carbonate substitution in bone is predominant; however, A-type is also present [81].

Another concern involves the existence of a so-called “hydrated layer” in bone mineral nanocrystals. It was shown that the outer part of bone crystals has varying concentrations of a wide range of mineral ions and constitutes the non-apatitic domain that is very labile and reactive and surrounds the relatively inert and more stable apatite domain of the bone crystal [82,83].

It is believed that the hydrated, highly reactive layer around bone crystals progressively decreases in thickness and leads to the more stable apatite domain (as shown in Fig. 1.19.).

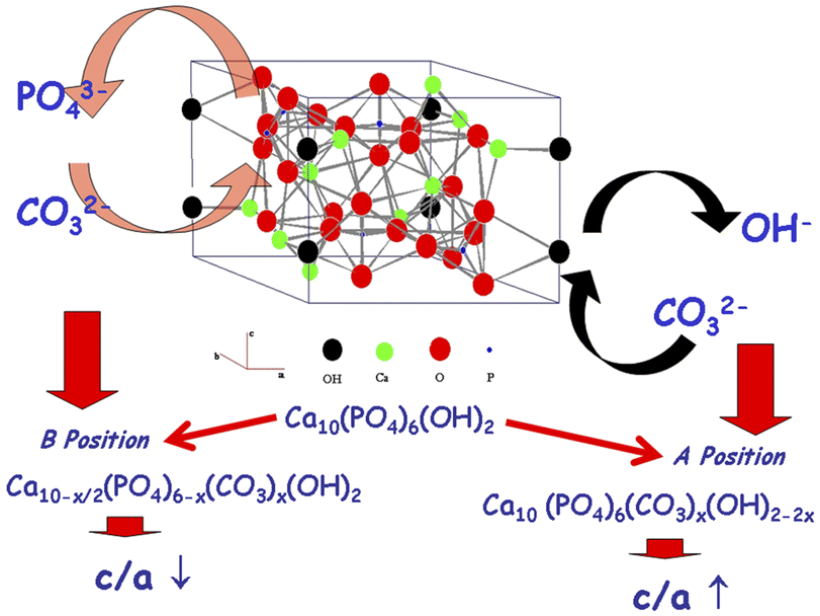

Figure 1.18. The schematic of A-type and B-type carbonate substitutions in hydroxyapatite and its effect of chemical composition and lattice parameters [79].

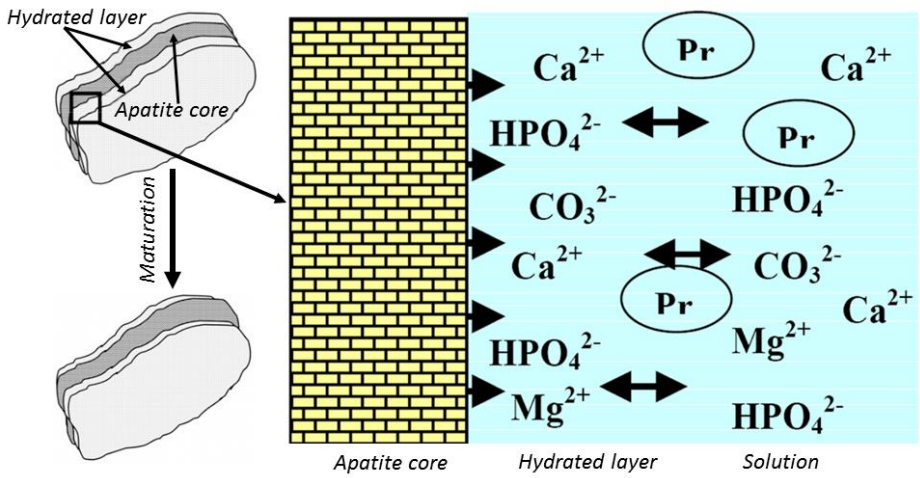

Figure 1.19. The evolution of the hydrated layer around the apatite bone crystal during the maturation and crystal growth. Adapted from [56] and [57].

However, recent studies suggest the existence of a hydrated amorphous coating in addition to the hydrated layer [84,85] as shown in Fig. 1.20. They state that water plays a significant role in orienting bone apatite crystals and that such ordering is mediated by an amorphous mineral coating layer. Even single crystallites may therefore present strong and

relevant structural heterogeneity. The relative amount of the different phases may not be sufficient in order to monitor it with standard averaging techniques. It then requires better spatial resolution than the smallest dimension of bone nanocrystals.

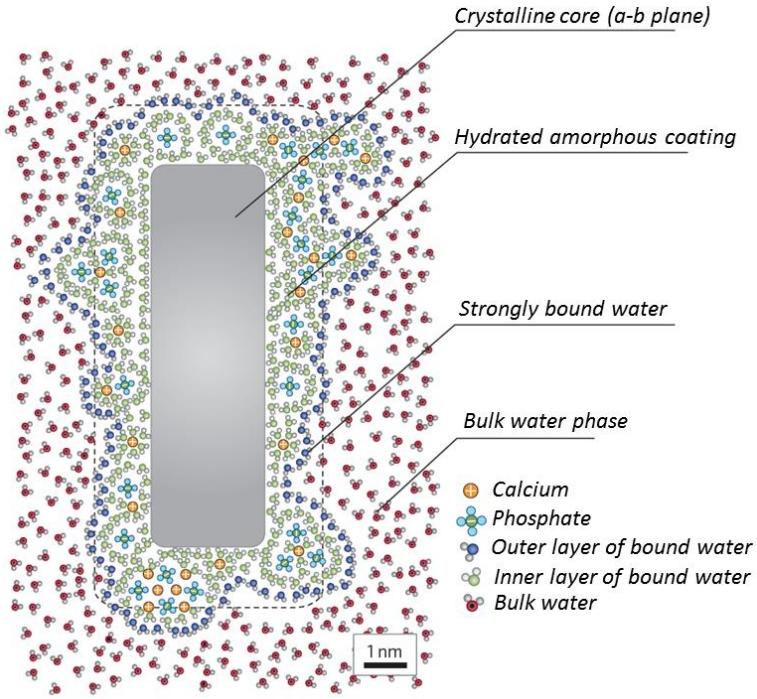

Figure 1.20. Structure and organization of mineral nanoparticles in bone. Bone apatite nanoparticles consist of a crystalline core of a calcium phosphate phase, closely related to hydroxyapatite, surrounded by amorphous coating mainly composed of calcium, phosphate and water. The amorphous hydrophilic layer is enclosed by a thin layer of strongly bound water. The dashed rectangle delineates what is usually considered as the boundary between bulk water and the amorphous calcium phosphate phase [85].

Another important difficulty, which has prevented the basic understanding of chemical composition and structure of bone mineral nanocrystals, is intrinsic to the hierarchical bone structure at all levels of anatomical location. This prevents easy ways of sample preparation. Moreover, the determination of structural parameters has suffered from the lack of consideration of precise anatomical position, type of bone, species, state of maturation etc. leading to data that are difficult to compare. Furthermore, the structural methods that involve summation of some values over the studied volume (such as powder XRD) give only an average understanding of the phenomena, while very high-resolution methods (such as TEM,

scanning nano-beam X-ray methods) are often lacking in field of view, 3D information, and require complex and destructive sample preparation.

Therefore, the instrumentation for the study of such complex and sensitive materials as bone requires the combination of high spatial resolution, large field of view and, the most important, the knowledge of the precise anatomical location of the bone sample at each hierarchical level of the whole organ.

1.2. Bone animal models

As mentioned before, bone structure and chemical composition differs depending on the animal species. Therefore, understanding of such differences in bone construction and remodeling is crucial for comparing existing models for bone multiscale structure. Besides, these different animal models play a key role in the development of biomedical tissue engineering, bone implants and therapeutic methods [86]. In the current thesis, human and bovine bone tissues were investigated. Therefore, a few words about bone structural differences between these tissues must be said. Very good reviews concerning other animal tissues such as dog, pig, sheep, goat and rabbit can be found in the references [87–89].

At the microstructural level, large mammal bones consist of three types of primary bone: circumferential lamellar bone, woven-fibered bone and primary osteons. At birth, the cortical bone consists mainly of woven-fibered bone (a matrix of interwoven coarse collagen fibers with osteocytes more or less randomly distributed as show in Fig. 1.6.) and primary osteons.

Cows bones grow more rapidly compared to humans and their adult cortical bone structure normally consists of the combination of woven and lamellar bone (also called plexiform bone) with a small fraction of osteonal bone [90] where the number of osteons increases with age. However, contrary to humans, bovine do not have bone remodeling processes, such that the secondary osteonal structure found in human mature bone is never found in cows. Moreover, in human adults, the woven-fibered bone is only formed during rapid bone accretion, which can occur due to fracture healing, or pathological conditions such as hyperparathyroidism, or Pagest's disease.

The composition of bovine cortical bone has been studied more extensively than that of human cortical bone [91]. However, investigations of the ash content and composition of the

organic matrix in human bone suggest that the distribution of constituents is essentially the same [92].

1.3. Heated bone

The effect of thermal treatment on the bone tissue leads to significant differences in organic content, mineral nanocrystal size, unit cell dimensions and the amount of lattice defects. The presence of a hexagonal to monoclinic phase transition upon heating is also debated. In addition to the fundamental understanding, the heated bone model provides a significant input into archeology, forensic science, forensic anthropology and crime scene investigation fields.

In recent years, an increasing number of studies have reported the transformation of bone during the heat treatment as shown in the review [93]. The removal of absorbed (up to 200 °C) and lattice incorporated water (up to 400 °C) is first observed [94], while denaturing and combustion of the organic matrix is progressively observed at temperatures up to 550 °C.

Around 700-750 °C, a rapid change in the mineral microstructure, as demonstrated by an increase in both crystallite size and lattice order is well documented [95,96]. With increasing temperature, the crystals continue to grow which is commonly referred to as the recrystallization process. However, some authors still refer to it as simple crystal growth without breaking down of the former structure [97].

The hexagonal to monoclinic phase transition is also proposed as an explanation of the transition that occurs around 700 °C. However, it was, to the best of our knowledge, only shown by the atomistic modeling [67,68] or by the heat treatment of artificially obtained hydroxyapatite [69,70].

Appearance of additional phases such as calcium oxide [97] and tetracalcium phosphates [98] is observed at temperatures above 800 °C due to the thermal decomposition of the apatite structure. However, the possibility of decomposition will strongly depend on the heating conditions (atmosphere, time, sample volume) and the original apatite chemistry. Melting of bone occurs at temperatures exceeding 1600 °C [99].

The concentration of both A and B-type carbonate substitutions is decreasing during heating and, therefore, causes changes in the lattice parameters. The loss of A-type carbonate causes an expansion in the *a* axis and a contraction in the *c* axis. Conversely, the loss of B-

type carbonate results in a contraction in the *a* axis while an expansion in the *c* axis is observed [93].

Other questions involving the lack of OH groups [100], change in concentration of other substitution ions [101], crystal structure ordering [93] and amount of organic phase [102] have been investigated. However, many contradictions in the published data still exist due to differences in treatment conditions and bone mineral composition.

1.4. Pathological bone

Bone tissues with several pathological conditions were analyzed in the current thesis. The pathological group includes osteopetrosis, hyperparathyroidism and fluorosis.

Osteopetrosis (also called “marble bone disease”) is an inherited disorder originated by osteoclast dysfunction (failure of osteoclasts to resorb bone) that was first described H. Albers-Schönberg [103]. As a consequence, bone modeling and remodeling are impaired and bone hardens and becomes denser [104]. The crystals in the hyper-mineralized bones affected by osteopetrosis are reported to be smaller and less perfect than those in age-matched normal tissues [105].

Hyperparathyroidism is a disease characterized by inappropriate overactivity of the parathyroid glandsan providing the abnormally high concentration of parathyroid hormone in the blood that results in weakening of the bones through the loss of calcium [106]. Most studies have reported decreased bone mineral density in hyperparathyroidism mainly located at cortical sites, whereas sites rich in trabecular bone only show a modest reduction or even a slight increase in bone mineral density [107]. However, the nanoscale characteristics of mineral phase affected by this pathology are still not clear.

Fluorosis is a disease caused by excessive accumulation of fluoride in bone or teeth. Fluoride is a cumulative toxin, which can alter accretion and resorption of bone tissue. It also affects the homeostasis of bone mineral metabolism [108]. This process results in increased bone density as reported in [109] but decreased strength. The fluorotic bone contains high amount of mineralization defects, has less organized structure with much smaller degree of crystalline order and larger crystal size compared to healthy bone [73].

Chapter 2. Materials and methods

2.1. Sample preparation

Sample preparation in biophysics is a complex task due to fast degradation and decomposition of material of biological origin and the need of maintaining the object in "as close as possible" to living state. The necessary stages of bone tissue processing prior to being stored and/or investigated will be discussed in this sub-chapter.

Followed by gathering, testing, adaptation and validation of various sample preparation methods, the generalized multi-probe protocol for bone sample preparation was designed. It was designed to be suitable for TEM, scanning XRD/SAXS and CXDI. Moreover, the thin sections of different thickness produced from one sample block can be used for different characterization techniques thus enabling close histological location analysis.

Two animal models were used in the current studies. Human bone tissues (in the form of biopsies) were obtained from the collaboration group of G. Boivin (Inserm, Lyon). They were provided embedded which can, in certain cases (e.g. CXDI), be a limitation. Therefore, bovine animal model was used for the following protocol design, providing the required flexibility (access, repeatability, large volumes of the same sample, etc). Bovine femur was taken at the local butchery (12 days after animal was killed) from which all connective tissues and fat were removed mechanically.

As shown in Fig. 2.1, samples were first cut to smaller pieces by a high precision circular diamond saw (Mecatome T210, PRESI). Full diaphysis femoral sections were cut, from which sticks were cut at precise anatomical locations (proximal or distal, anterior or posterior, medial or lateral). The blocks were then cut for different orientations and fixed, dehydrated and embedded in different resins (PMMA, Epon B, LR-white, Epofix) or left unembedded. Depending on experimental requirements, longitudinal (along the principal bone axis) and transverse (across the principal bone axis) bone sections of varying thickness were obtained from the blocks by cutting and reduced in thickness by polishing for thicknesses larger than

50 µm, or cutting by ultramicrotomy that provided a wide range of thicknesses from 10 µm to ~40 nm.

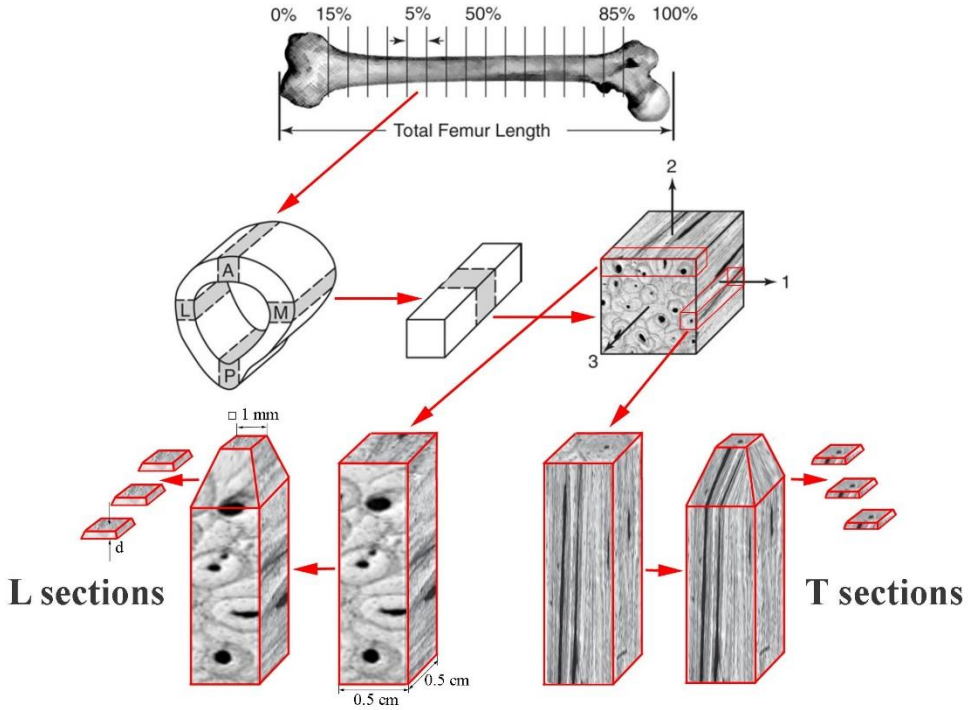

Figure 2.1. Cutting scheme for bone samples preparation.

2.1.1. Fixation, dehydration, impregnation and embedding choice

Fixation and dehydration are important steps for preserving the bone structure and preventing its decay and decomposition. This step needs to be performed as soon as possible following bone extraction from the body. Different protocols of fixation and dehydration can be used depending on the features in bone tissue one wishes to preserve and the same holds for the choice of resin.

Two methods of fixation are used for the described protocols: in ethanol and in glutaraldehyde. Glutaraldehyde is the most standard fixation in TEM used to cross-link cellular structures into a matrix (it minimizes changes in morphology and volume) which protects and stabilizes the cellular structure from changes during subsequent treatment and minimizes irradiation effects during measurements (e.g. by an electron beam). In contrary, the ethanol fixation degreases the samples (gets rid of lipids) but does not preserve the cellular structures, and it is mainly used for structural studies at molecular/atomic scales.

Dehydration of biological materials is a necessary step in sample preparation, especially for electron microscopy. Water that is incorporated within the specimen makes it not resistant to the high vacuum, electron beam and may affect the contrast. Hydrated samples in TEM would, indeed, dehydrate so fast that it would damage the structure. Beam damage is more severe for light elements. The contrast is improved by decreasing the amount of elements with low atomic number such as carbon (cells) and oxygen (water) with respect to heavier ions. In this respect, dehydration will improve it. The dehydration time should be adjusted to size and kind of tissue. The development of cryo-TEM now allows observations of biological samples after vitrification (the sample must be frozen to temperatures <-137 °C extremely rapidly, at a rate of ~10^6 °C/s, so that the water in the specimen is fixed in a vitreous state). However, the formation of crystalline ice may introduce severe changes into the sample structure. In addition, we did not have access to the instrument that combines both cryo-TEM and ACOM-TEM options.

For samples that do not need to be embedded (as for coherent X-ray diffraction imaging and for heated bone pair distribution function analysis) blocks were fixed and dehydrated in the 70 % ethanol solution for around 10 days. The time of ethanol bath depends on the sample volume to be dehydrated. More than 20 days are needed for some massive parts (as for 5-10 μm^3). The success of dehydration is determined by the color of the bone sample: dehydration was achieved when the full volume has turned white, while remaining pink color indicates a need of longer dehydration. After dehydration, the samples were stored in 70% ethanol solution prior to use.

Samples prepared for ACOM-TEM measurements were embedded. Embedding is very important for preserving the structure during subsequent thin sectioning with ultramicrotomy as well as for providing homogeneous section thickness. Sufficient quality electron diffraction patterns (by ACOM-TEM) can also be obtained from unembedded samples, however, sections cannot be sufficiently homogeneous in thickness and the measurement areas that can provide not superposed diffraction patters are limited to small areas near sample edges and comparison between different samples is less reliable. Therefore, the samples for ACOM-TEM investigation were embedded. The embedding protocol may include such steps as substitution, impregnation and inclusion.

Substitution is needed only if the resin is not soluble in ethanol. In this case, ethanol is exchanged with the transition solvent, both mixable in ethanol and resin (such as propylene

oxide). Impregnation is the gradual replacement of ethanol or transition solvent with resin. The goal of impregnation is to penetrate the resin into the specimen porosity. Eventually, the final step of embedding, the inclusion, involves the positioning of the tissue specimen in the desired orientation into a mold with liquid resin and its subsequent polymerization.

Four types of resins were tested: PMMA, Epon, LR white and Epofix.

PMMA embedding media is widely used for bone histology and electron microscopy. PMMA results in hard blocks with a good penetration that provides better support for cortical bone tissues. It is also fully transparent resin (easier manipulations) and provides better cell matrix preservation (such as alkaline and acid phosphatase). PMMA embedding cannot be done in any plastic or silicon molds because methylcyclohexane used in the process dissolves it. It is generally advised to perform embedding in glass bottles with covers. However, if orientation of sample matters, most of the classical flat molds cannot be used. PTFE flat embedding molds and ACLAR film have been tested and provide required properties. For 2 x 2 x 10 mm^3 samples, PMMA embedding protocol took 27 days.

The advantage of Epon resin is its ease in use and good compromise between embedding time and quality. Epon resin hardness can be adjusted by different concentration of hardener and plasticizer. It enables good penetration into the tissue. Epon media results in non-transparent, light brown color. Most plastic and silicon flat embedding molds can be used. For 2 x 2 x 10 mm^3 samples, Epon embedding protocol took 5 days.

LR white is an aromatic acrylic resin mixture. It has a very low viscosity (8 cps), low toxicity is stable to electron beam exposure and is softer than PMMA and Epon. However, it is a hydrophilic embedding medium and the sections of polymerized LR white resin are hydrophilic. During resin curing, embedding molds (eppendorf tubes or gelatin capsules) have to be well sealed, as even one bubble of air can ruin the solidification. For orientation driven embedding, PTFE flat embedding molds with ACLAR film covering can be used. For 2 x 2 x 10 mm^3 samples, LR-white embedding protocol took 8 days.

Epofix is a commercial cold-setting resin based on two fluid epoxy components. Epofix is specially developed for a quick room temperature curing. The solidification time is only 8 hours and no impregnation is required. However, Epofix does not penetrate well into small porosity and it results in low adhesion with samples of regular shape (cut or polished surfaces), which is less critical for irregular shape (trabecular bone, periosteum or endosteum). Therefore,

the use of this resin is advised when no internal penetration is required or for manipulation facilitation.

The complete detailed protocols for the PMMA, Epon, LR white and Epofix embedding can be found in Appendix 1.

2.1.2. Ultramicrotomy cutting

Cutting the bone tissue blocks, embedded or not, into sections from 10 µm to 40 nm (depending on the knife type used) was performed by using ultramicrotome Leica EM UC6 at CERMAV laboratory.

In ultramicrotomy, the sectioning is performed by a vertical movement of the sample [110] over the extremely sharp blade of a fixed glass or diamond knife [111] (Fig. 2.2). Removing the sections directly from the knife blade is difficult due to their small thickness. Therefore, the diamond knife is attached to a water bath and the sections float on the water surface after cutting.

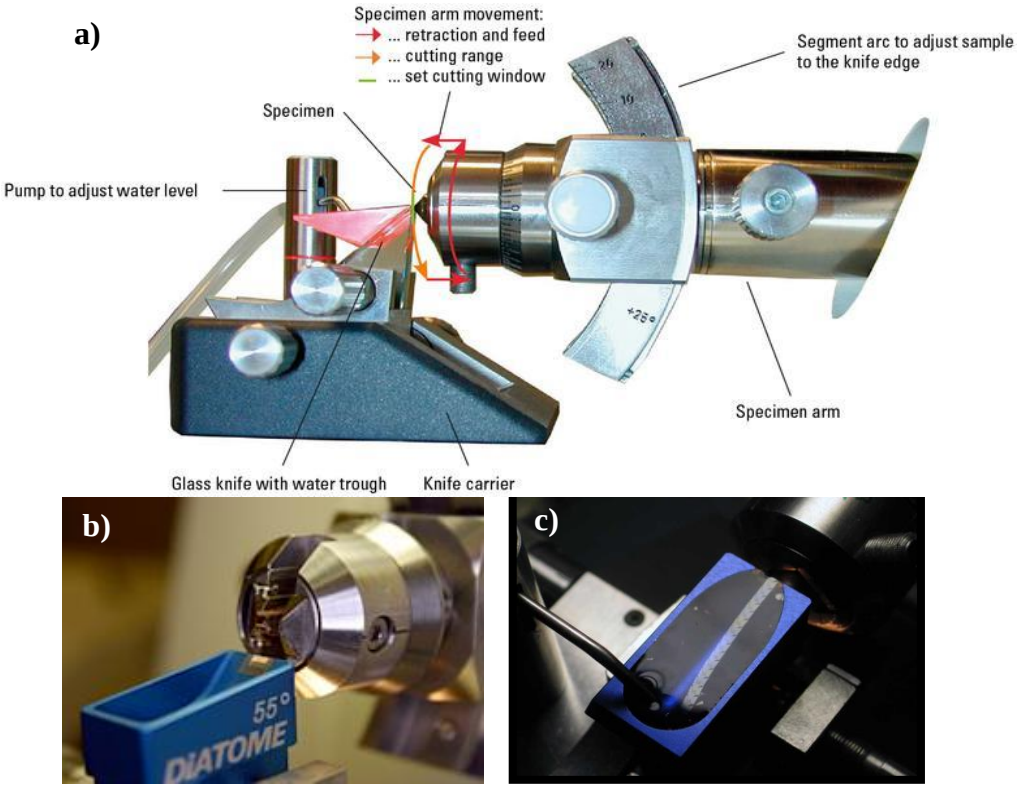

Figure 2.2. Ultramicrotomy cutting: a) principle scheme of ultramicrotome setup, b) example of diamond knife, c) samples floating on the water bath after cutting [110].

Samples must be trimmed into a shape that is suitable for sectioning. The shape most often used is that of a trapezoid block face with sloping sides (a flat pyramid). This shape has several advantages: it makes orientation of the block with respect to the knife easier, minimizes compressive forces on the sample during sectioning, and facilitates serial sectioning (since the trapezoid has sloping sides, the sections become larger as one sections deeper into the sample; therefore, the size of the sections can be used to determine whether they were cut from the top or bottom of the specimen block) [112].

After the desired trimmed surface is achieved, the sample is cut with different knifes, in order to produce thin sections for different experimental characterization techniques. The detailed protocol of sample trimming and cutting is presented in Appendix 1.

In this way, samples for a variety of applications can be prepared:

- 1-8 µm cuts (with histo knife) on glass slides can be used for histological study (with or without staining), determination of the tissue orientation, finding a particular region of interest or/and assessing the quality of tissue preservation.
- 5 µm cuts (with histo knife) on glass slides can be used as a first step for CXDI sample preparation (see Chapter 3.1.).
- 1 µm cuts (with histo knife) on Si_3N_4 membranes can be used for scanning XRD/SAXS measurements with micro-beam.
- 100-200 nm cuts (with histo knife) on Si_3N_4 membranes can be used for scanning XRD/SAXS measurements with nano-beam or 2D ptychography.
- 40-70 nm cuts (with ultra 35 knife) on Si_3N_4 membranes can be used for TEM.

This composite protocol was designed and is advised for cross-correlation use of various techniques with electron and X-ray diffraction where semi-thin and thin sample sections are required. The protocol is developed for bone and dentin tissue preservation but it can be used or adapted to many other biological and non-biological materials.

2.1.3. Heat treatment

For TEM and PDF analysis, samples were heat-treated. Fixed and dehydrated bovine cortical blocks of different geometries depending on the technique requirement (see details in Chapter 3) were heated to 9 temperatures (100, 150, 200, 300, 400, 600, 700, 800, 1000 °C) for 10 min in vacuum (10^{-2} mbar) in an aluminum oxide container inside a quartz tube. Samples

were treated sequentially, such that the next sample was inserted at the heating temperature of the previous one (the first one – at room temperature). This allowed lower overheat than heating them from room temperature (extra time sample is subjected to heat while reaching the given temperature). The temperature precision of the thermocouple was 2-3 °C and the heating rate was around 30-40 °C/min. The overall time for achieving the desired temperature did not exceed 5 min. After the treatment, air was quickly inserted and the samples were cooled down in air.

2.2. Techniques

2.2.1. Basic terminology

2.2.1.1. Structure of the solid body

Solid is one of the four fundamental states of matter (the others being liquid, gas, and plasma). It is characterized by structural rigidity and resistance to changes of shape or volume.

Any solid material can be classified using two groups: crystalline and amorphous. In **crystalline** solid, atoms exhibit short and long-range order whereas in **amorphous** material, atoms have short-range order only.

Long-range order can be defined by the presence of spatial correlation in the structure of the solid at distances that tend to infinity. However, real crystals are far from ideal due to the presence of defects, therefore more realistic long-range order distances are in the order of 10^7 atoms.

Short-range order is the existence of spatial correlation in the distances of first or second coordination spheres (first or second nearest neighbor distances). Thus, both long-range and short-range order are absent in the ideal gas, but liquids and amorphous solids exhibit short-range order — a certain regularity in the arrangement of the neighboring atoms.

Crystalline solid consists of repeating patterns of its components in three dimensions (a crystal lattice) and the entire crystal can be represented by the smallest identical unit that, when stacked together, form the crystal. This basic repeating unit is called the **unit cell**. In three dimensions, only **14 Bravais lattices** exist [113]. These are obtained by combining one of the **7 lattice systems** (triclinic, monoclinic, orthorhombic, tetragonal, rhombohedral, hexagonal, cubic) with one of the **7 lattice types** (primitive (P), body-centered (I), face-centered (F), base-

centered (A, B, or C) and rhombohedral (R)). In general, the lattice systems can be characterized by their shapes according to the relative lattice parameters (a, b, c) and angles (α, β, γ).

32 crystallographic point groups can be defined by their set of symmetry operations, like rotations or reflections. For a periodic crystal (as opposed to a quasicrystal), the group must also be consistent with maintenance of the three-dimensional translational symmetry that defines crystallinity [114].

Therefore, the generalized term **space group** represents a description of the symmetry of a given crystal. The space groups in three dimensions are made of combinations of the 32 crystallographic point groups with the 14 Bravais lattices, each of the latter belonging to one of 7 lattice systems. This results in a space group being a combination of the translational symmetry of the unit cell including lattice centering, the point group symmetry operations of reflection, rotation and improper rotation, and the screw axis and glide plane symmetry operations. The combination of all these symmetry operations results in a total of **230 different space groups** describing all possible crystal symmetries.

The second important feature of the crystal is the **basis** - a group of atoms located at each point in the lattice. **Miller indices** are used as a notation system in crystallography for describing the lattice. In particular, a family of lattice planes is determined by three integers h, k and ℓ [115].

2.2.1.2. Scattering vs diffraction

Scattering is a general physical process where a radiation, such as light, sound, moving particles or waves, are forced to deviate from a straight trajectory due to localized non-uniformities in the medium they are crossing. The types of non-uniformities which can cause scattering, also denominated as scatterers or scattering centers, can be particles, bubbles, droplets, density fluctuations in fluids, grains in polycrystalline solids, defects in monocrystalline solids, surface roughness, cells, etc. The effects of such features on the path of any type of propagating wave or moving particle can be described in the framework of scattering theory. Any particle or matter (electrons, protons, neutrons, etc.), indeed, propagates like a wave for which L. de Broglie defined the wavelength:

$$\lambda = \frac{h}{p} = \frac{h}{mv} \qquad (2\text{-}1)$$

where λ is the wavelength of the particle, h is Planck's constant (6.626 x 10^{-34} J seconds), p is the particle momentum, m is the mass, and v is the particle velocity.

The associated wavevector, k is given by:

$$|\vec{k}| = \frac{2\pi}{\lambda} \tag{2-2}$$

Any scattering event can be characterized using two important concepts: whether the scattering is elastic or inelastic and whether it is coherent or incoherent.

In an **elastic scattering** event, there is no exchange of energy between the scattering particle and the system ($|\vec{k}_i| = |\vec{k}_f|$), in contrary to **inelastic scattering** ($|\vec{k}_i| \neq |\vec{k}_f|$), where $\vec{k}_i, \vec{k}_f$ are incident and scattered wavevectors, respectively. The difference between these two events is shown in Fig. 2.3 ($\vec{Q}$ is momentum transfer) [116].

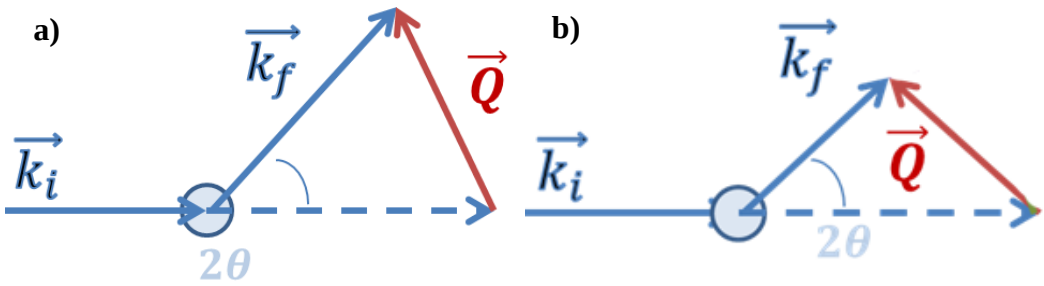

Figure 2.3. The scattering experiment: a) elastic scattering, b) inelastic scattering [116].

The coherence of the scattering refers to whether there is a defined phase relationship between scattered waves allowing them to interfere constructively or destructively [117]. In the case of **coherent scattering**, the waves interfere and the resulting intensity is given by the square of the sum of the wave amplitudes. For example, if there are two scattered waves of amplitude ψ_1 and ψ_2, then $I = |\psi_1 + \psi_2|^2$. In the case of **incoherent scattering,** no defined phase relationship exists between the waves, they do not interfere, and the resulting intensity is simply the sum of the squares of the intensities of the individual waves, i.e. $I = |\psi_1{}^2| + |\psi_2{}^2|$ (see Fig. 2.4). Since structural information comes from the interference effects of scattered waves, it is clear that only coherent scattering contains any structural information.

Coherence is a fundamental property of a radiation source. A simple definition of coherence is that a wave is coherent if it can produce detectable wave-like effects as diffraction and interference.

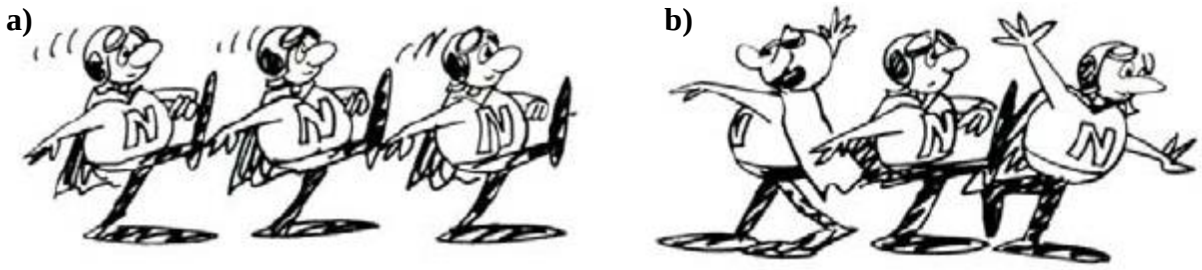

Figure 2.4. Types of scattering experiment: a) coherent - there is phase relationship between scattered particles; b) incoherent - scattered particles do not have a phase relationship [118].

Real sources are neither fully coherent nor fully incoherent, but rather are partially coherent. In Fig. 2.5a, the point source radiates waves that are perfectly phased and thus coherently correlated everywhere. While in Fig. 2.5b, a source of finite size and spectral bandwidth, restricted to radiate over a limited angular extent, generates fields with strong phase and amplitude correlation only over a limited spatial and temporal extent. This brings us to the notions of "regions of coherence" and "coherence time": that is, spatial and temporal measures over which the waves have fixed phase relation.

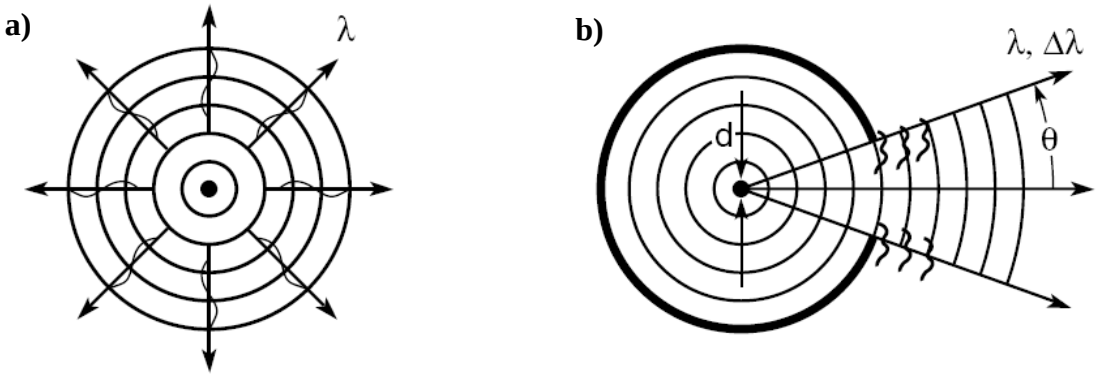

Figure 2.5. Coherence sources: a) fully coherent radiation from a point source oscillator which oscillates for all time; b) partially coherent radiation from a source of finite size, *d*, emission angle, θ, and wavelength, λ [119].

In cases where there is a well-defined direction of propagation, it is convenient to decompose the region of coherence into orthogonal components, one in the direction of propagation and one transverse to it, as illustrated in Fig. 2.6.

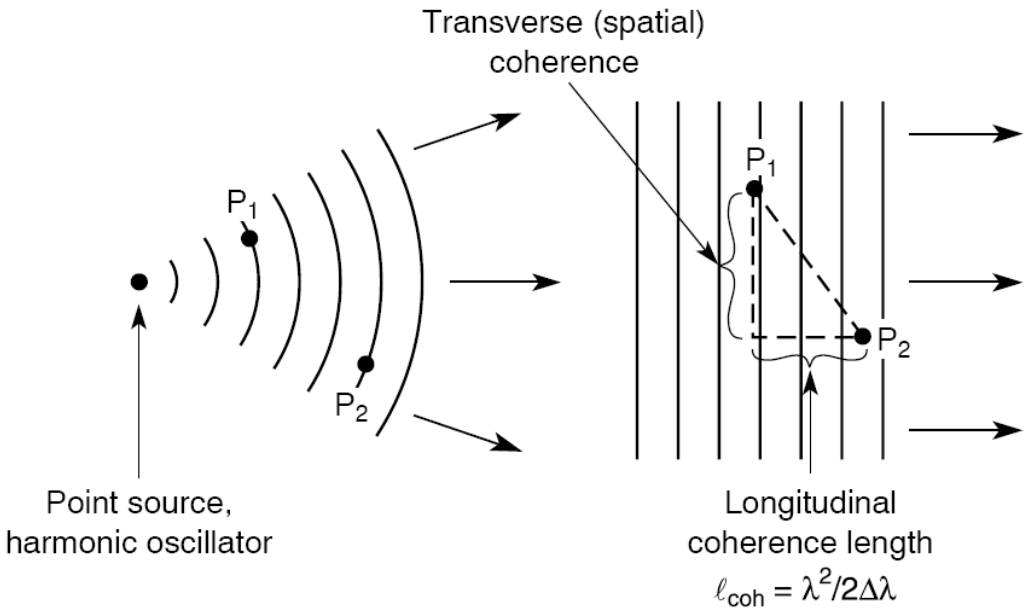

Figure 2.6. Transverse and longitudinal coherence [119].

In the direction of propagation it is common to introduce a **longitudinal, or temporal, coherence** length, l_{coh}, over which phase relationships are maintained. For a source of bandwidth, $\Delta\lambda$, one can define a coherence length as:

$$l_{coh} = \frac{\lambda^2}{2\Delta\lambda} \tag{2-3}$$

where $\Delta\lambda$ is the spectral width (see Fig 2.7).

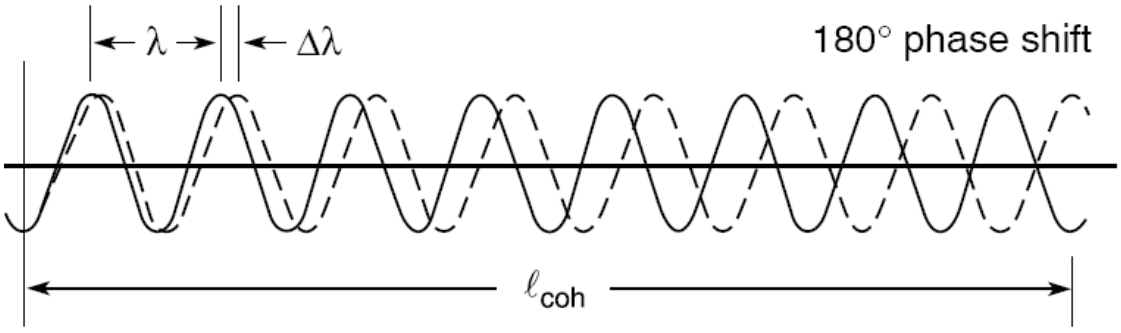

Figure 2.7. Spectral bandwidth and coherence length illustration [119].

Transverse, or spatial, coherence is related to the finite size of the source and the characteristic emission (or observation) angle of the radiation (Fig. 2.6). In this case, one is interested in phase correlation in the plane orthogonal to the direction of propagation (Fig. 2.7). Full spatial coherence is obtained in the situation in which phase is perfectly correlated in every point transverse to the propagation direction and can be achieved with a spherical wave front, which we associate to a point source. Spatial coherence length is then defined as:

$$l_{transverse} = \frac{z\lambda}{2\pi d} \tag{2-4}$$

where *d* is the source diameter and *z* is the distance from the source. Coherent scattering by two objects separated by distance, d, can be observed only if the coherence length of the incident radiation is larger than d.

Typical transverse coherence length for X-rays with λ~1.5 Å is around 10 μm that can be selected with focusing optics by upstream slits. The longitudinal coherence in practice is directly related to the beam monochromaticity (around 0.5 μm with a Si(111) monochromator) [120].

Diffraction arises from the collective interaction of the incident wave with many scattering objects (or an object that causes the wave to have interference with itself). Therefore it is coherent.

Bragg diffraction occurs when radiation with wavelength comparable to atomic spacing is scattered in a specular fashion by the atoms of a crystalline system and undergoes constructive interference. For a crystalline solid, the waves are scattered from lattice planes separated by the inter-planar distance, *d*. When the scattered waves interfere constructively, they remain in phase since the difference between the path lengths of the two waves is equal to an integer multiple of the wavelength as shown in Fig. 2.8. The effect of the constructive or destructive interference intensifies because of the cumulative effect of reflection in successive crystallographic planes of the crystalline lattice (as described by Miller indices). This leads to Bragg's law, which describes the condition on θ for the constructive interference to be at its strongest [121]:

$$2d \sin\theta = n\lambda \tag{2-5}$$

where n is a positive integer, λ is the wavelength of the incident wave and θ is the scattering angle.

A diffraction pattern is recorded by measuring the intensity of scattered waves as a function of the scattering angle. Strong intensities known as Bragg peaks appear at the points where the scattering angles satisfy Bragg's law. Thereby, Bragg diffraction is used to study the internal structure of solids (with structural units of the same order of magnitude or larger than de Broglie wavelength of the probe).

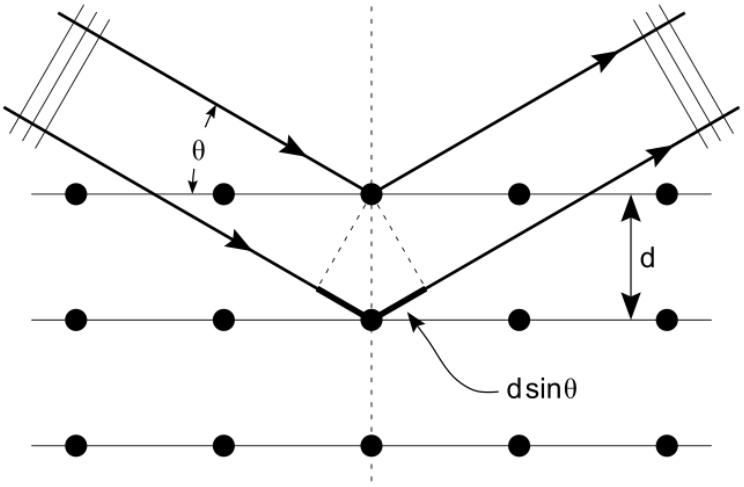

Figure 2.8. Bragg diffraction. Two incident waves with identical wavelength and phase are scattered by two different atoms of the crystalline solid. The lower wave crosses an extra length of *2dsinθ*.

Structure factor is a mathematical description of how a material scatters incident radiation, and its inverse Fourier transform gives the atomic positions. It is a particularly useful tool in the interpretation of interference patterns obtained in X-ray, electron and neutron diffraction experiments. Derivation of the structure factor notation can be found in [121] resulting in the following:

$$F(hkl) = \sum_j f_j e^{-2\pi i(hx_j + ky_j + lz_j)} \tag{2-6}$$

where the sum is taken over all atoms in the unit cell, h, k, l are the Miller indices, x_j, y_j, z_j are the position coordinates of the j-th atom, f_j is the atomic form factor of the j-th atom.

The **atomic form factor** is a measure of the scattering amplitude of a wave by an isolated atom. The atomic form factor depends on the type of scattering, which in turn depends on the nature of the incident radiation, typically X-ray, electron or neutron (scattering length).

The structure factor *F(hkl)* is directly related to the intensity *I(hkl)* of the corresponding reflection as [122]:

$$I_{hkl} \sim |F_{hkl}|^2 \tag{2-7}$$

The constant that relates the two depends on many factors (multiplicity, polarization factor, Lorentz factor, absorption, temperature, etc.).

2.2.1.3. Diffraction vs imaging

What if we would like to obtain not only the structural information of the object of study (by diffraction) but to image it? It is not always discussed in classical optics textbooks but the whole process of imaging involves diffraction. Diffraction pattern is formed by the sample and can be seen at the back focal plane (or diffraction plane) in case the focusing length is place after the sample (see Fig. 2.9). The Fourier transform is, therefore, performed by the lens allowing the magnified object to be visualized in the image plane.

The diffraction pattern acts as a source of light that propagates to the screen where the image is formed. This is called diffraction theory of image formation, and it was first described by E. Abbe in 1873 [123].

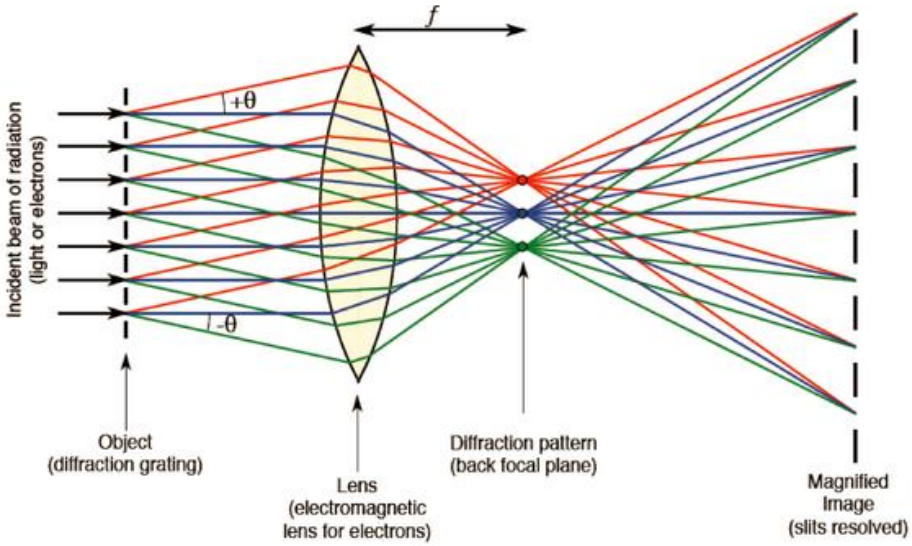

Figure 2.9. Illustration of the physical basis of image formation (example of diffraction grating) where f - focal length, θ - scattering angle [122].

In a paper published in 1906, A.B. Porter built upon Abbe's idea [124]. Porter proposed that Abbe's two planes, the diffraction plane and the image plane, could be interpreted using the **Fourier series**: it turns out that the image on the **image plane is the Fourier transform of the diffraction pattern** on the diffraction plane. The diffraction plane is now often called the "Fourier plane" or "back focal plane" of the lens.

Therefore, the important point to keep in mind is that by using a single probe radiation, one can access both the structural information about the object (from reciprocal space in diffraction plane) and its image (from real space in image plane), and these two planes are related by the Fourier transform. The Fourier transform in optics is usually done by the lens or another approach is used such as in the case of lensless imaging.

2.2.1.4. Resolution limit, wavelength and the choice of probe

Resolution describes the ability of an imaging system to resolve details in the object that is being imaged. It is defined by the smallest distance between two distinguishable radiating points. Resolution in microscopy is limited to about ½ of the wavelength of the illumination source used to image the sample (as shown in eq. 2-5). Because our eyes can only detect photons with wavelengths greater than ~400 nm, the best resolution that can be achieved by light microscopes is about ~200 nm. However, the state-of-art fluorescence based super-resolution optical microscopy can now achieve resolutions of 20 nm [125,126].

One way to overtake the diffraction limit of light is to use an illumination source with a shorter wavelength than visible photons – X-rays or electrons.

X-rays have a wavelength ranging from 0.01 to 10 nm, corresponding to energies in the range of 100 eV to 100 keV according to the relation:

$$E = \frac{hc}{\lambda} \tag{2-8}$$

In case of electron probe, the velocity of electrons is determined by the accelerating voltage, V, or electron potential where:

$$eV = \frac{1}{2}mv^2; v = \sqrt{\frac{2eV}{m}} \tag{2-9}$$

Therefore, the wavelength of propagating electrons at a given accelerating voltage can be determined by:

$$\lambda = \frac{h}{\sqrt{2meV}} \tag{2-10}$$

Moreover, the relativistic effects have to be taken into account because the velocities of electrons in an electron microscope reach about 70 % the speed of light with an accelerating voltage of 200 keV. These effects include significant length contraction, time dilation and an increase in mass. By accounting for these changes,

$$\lambda = \frac{12.25 \cdot 10^{-10}}{\sqrt{V}} \cdot \frac{1}{\sqrt{1 + \frac{eV}{2mc^2}}} \tag{2-11}$$

where *c* is the speed of light, which is ~3 x 108 m/s. Therefore, the wavelength at 100 keV, 200 keV, and 300 keV in electron microscopes is 3.70 pm, 2.51 pm and 1.96 pm, respectively. In practice, the resolution is limited to ~0.1 nm due to the objective lens system in electron microscopes.

Many probes can be used to study the internal structure of the solid (see Fig. 2.10) depending on the required resolution. Therefore, in the current work, X-ray and electron scattering were used to characterize bone mineral structure (reciprocal space information) and organization (real space imaging) in order to achieve better spatial resolution than optical techniques.

So how to build the electron and X-ray microscope? The principal scheme of electron and X-ray microscope looks similar to the optical one, and it is schematically drawn in Fig. 2.17.

The first important difference are the lenses used for focusing the radiation. In TEM, a series of electromagnetic lenses are used, in a similar way to optical lenses, for beam collimation. Focusing for X-rays is not as simple. In the X-ray wavelength region, the refractive index of any material to X-rays is close to 1. The manufacturing of efficient X-ray lenses is, therefore, very difficult. Also, the high-frequency information is often not collected by the lens and the resulting image contains lens imperfections such as aberrations. Instead, the computational phase retrieval algorithm is used and will be described in details later.

The second significant difference is the sample geometry requirements. Electrons have very small penetration depth, therefore, the samples measured in TEM must be electron transparent (with thickness in the range of 50 - 100 nm). Limitation for X-ray microscopy samples is also very strict and depends on setup parameters such as coherence length, detector area, pixel size and sample to detector distance.

Therefore, in transmission optical microscope, visible light is focused on the sample by a condenser lens, the diffraction pattern is generated in Fourier plane and a set of objective and projector lenses is used for Fourier transform for producing the magnified image of the sample in the image plane (see Fig. 2.11).

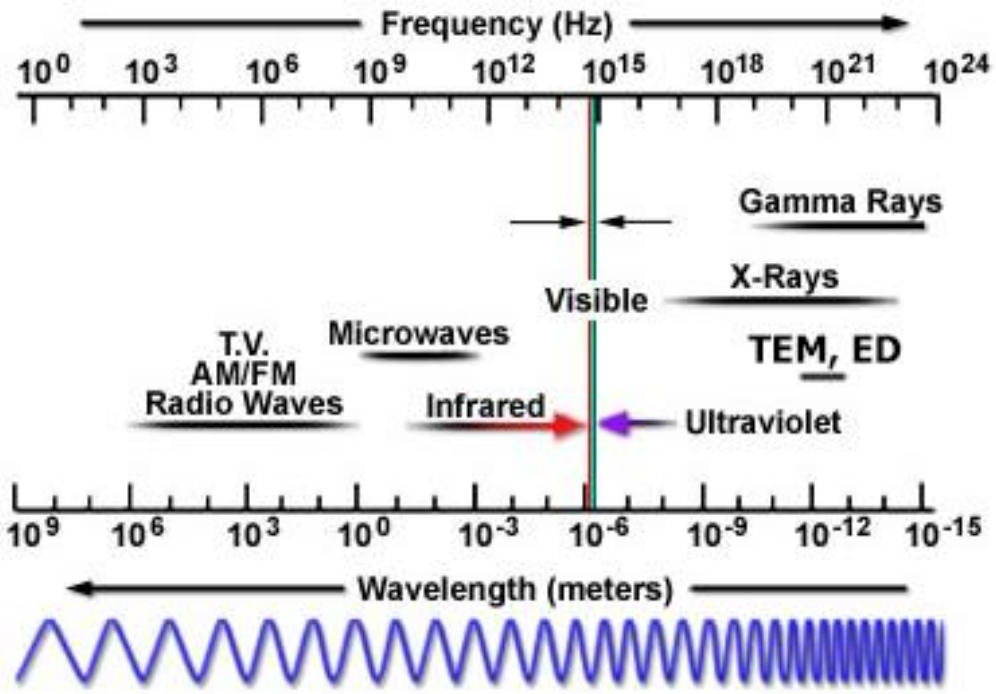

Figure 2.10. Electromagnetic radiation spectrum indicating probe choice.

In TEM, a beam of electrons is focused by electromagnetic lens on an ultra-thin specimen and interacts with the specimen as it passes through. An image is formed by the set of objective and projector lenses, it is magnified and focused onto an imaging device, such as a fluorescent screen or CCD camera. By adjusting the magnetic lenses such that the back focal plane of the lens rather than the imaging plane is placed on the imaging apparatus, a diffraction pattern can also be generated.

In coherent X-ray diffraction microscope (as CXDI), X-ray beam passes through a monochromator, vertical and horizontal slits in order to achieve the required temporal and spatial coherence, respectively. Then it passes through the sample that is rotated and the diffraction patterns are recorded at each angular position on the CCD screen. The image is reconstructed using a computational phase retrieval algorithm.

In the following sub-chapters, these techniques will be described in more details.

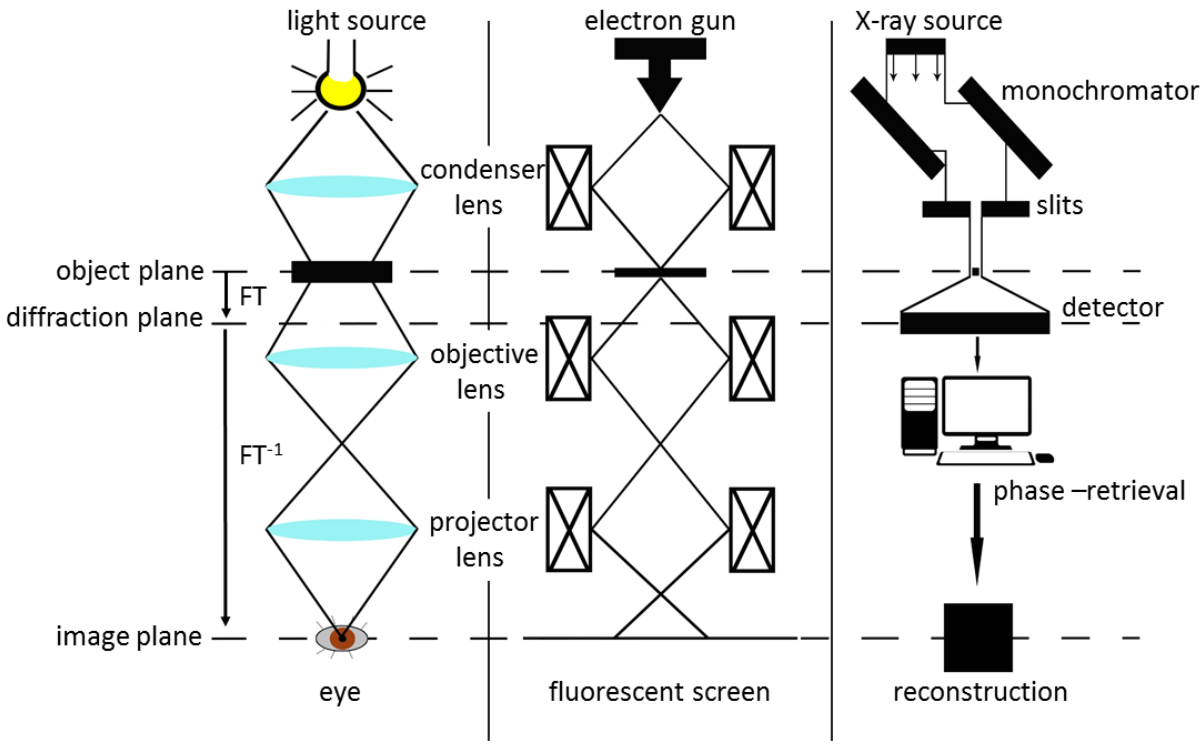

Figure 2.11. Simplified scheme for imaging with different probes.

2.2.2. X-ray radiation based techniques

X-ray scattering is a tool used for identifying repeating domains present in the sample, which can be the atomic and molecular arrangements on the smallest length scale or organization of larger units. By measuring the angles and the intensities of the diffracted radiation, one can produce a three-dimensional picture of the electron density in the crystal. From this electron density, the mean positions of the atoms in the crystal can be determined, as well as crystal size, chemical bonds, and more specific information related to disorder.

Elastic X-ray scattering includes single-crystal diffraction, powder diffraction, small and wide-angle X-ray scattering.

2.2.2.1. Rietveld refinement

Single crystal diffraction, using relatively large crystals of the material, gives a set of data from which the structure can be easily solved.

However, most materials of interest such as bone tissue cannot be grown to large crystals, and exist under the form of polycrystals or composites containing small crystallites. Powder diffraction, therefore, has to be used. The drawback of powder diffraction method is that the diffraction peaks are highly broadened and grossly overlap, thereby preventing proper determination of the structure. This problem is overcome in the Rietveld analysis in creating a virtual separation of these overlapping peaks [127,128].

Rietveld refinement extracts much more information from powder XRD data than classical peaks identification. It also gives access to the characterization of:

- unit cell dimensions;
- phase quantities;
- crystallite sizes / shapes;
- atomic coordinates / bond lengths;
- micro-strain in crystal lattice;
- texture effects;
- substitutions / vacancies, etc.

However, Rietveld does not perform phase identification and structure solution, which has to be given as an input for the refinement.

The Rietveld method is based on the refinement of user-selected parameters to minimize the difference between an experimental pattern (recorded data) and a model based on the hypothesized crystal structure and instrumental parameters (calculated pattern). The refinement principle can be shown with the following formula in which several phases can be accounted for. Calculated intensity, y_{ic}, at the point *i* of the diagram is:

$$y_{ic} = y_{ib} + \sum_{\Phi} S_{\Phi} \sum_{k} G_{\Phi}(2\theta_i - 2\theta_k) I_k \qquad (2\text{-}12)$$

where y_{ib} is the background at the point *i*, *G* the normalized profile shape function, S_{Φ} the scale factor of the phase Φ, I_k the intensity of the *k*-th reflection. The summation is performed over all phases, Φ, and over all reflections, *k*, contributing to the respective point.

Whereas the intensity of Bragg reflections depends on the following parameters:

$$I_k = m_k L_k |F_k|^2 P_k A_k \tag{2-13}$$

where m_k is the multiplicity (or multiple scattering coefficient) of k; L_k the Lorentz polarization factor; F_k the structure factor; P_k the preferred orientation factor; A_k the absorption factor.

Therefore, the calculated intensity for a given phase can be written as:

$$I_i^{calc} = S_\Phi \sum_k L_k |F_k|^2 G_\Phi(2\theta_i - 2\theta_k)\, P_k A_k + bkg_i \tag{2-14}$$

where bkg_i is a value of the background function at the point *i*.

The spectrum is calculated using (2.12) that depends on: phases (crystal structure, microstructure, quantity, cell volume, texture, stress, chemistry, etc.), instrument geometry (beam intensity, Lorentz-Polarization, background, resolution, aberrations, radiation, etc.) and sample (position, shape, orientation and dimensions). The calculated spectrum is compared to the experimentally obtained one and the refinement of structural and experimental parameters is done until the best fit is found [129].

For background, bkg_i, the most commonly used function is a polynomial in 2θ but more complicated functions may be used.

The scale factor, S_Φ, from (2.12) is defined as:

$$S_\Phi = S_F \sum_{j=1}^{Nphases} \frac{f_j}{V_j^2} \tag{2-15}$$

where S_F is the beam intensity; f_j the phase volume fraction; V_j the phase unit cell volume.

The Lorentz polarization factor, L_k, is a measure of the amount of time that a point of reciprocal lattice remains on the sphere of reflection during the measuring process and sample rotation. The Lorentz factor depends on the instrument geometry, monochromator (angle θ), detector, beam size/sample volume and sample angular positioning.

Different profile shape functions, $G_\Phi(2\theta_i - 2\theta_k)$, are available such as Gaussian (the original Rietveld function for neutrons), Cauchy, Voigt and Pseudo-Voigt (PV), Pearson VII, etc.

For modeling the texture (or preferred orientations) factor, P_k, the March distribution function is used for empirical models of preferred orientation effects. This model describes preferred orientation of cylinder or needle shaped crystals. Other functions such as Gauss-like distributions and spherical harmonics can be also used.

The absorption factor, A_k, accounts for the transmission and absorption of the X-rays through the irradiated volume of the sample. It depends on sample geometry: flat, plate or cylindrical; and on the mass absorption coefficient of the sample.

Quality of the refinement is usually defined by the weighted sum of squares (WSS):

$$WSS = \sum_{i=1}^{N} \left[w_i (I_i^{exp} - I_i^{calc}) \right]^2, \qquad w_i = \frac{1}{\sqrt{I_i^{exp}}} \tag{2-16}$$

And the goodness of fit, χ^2, which is often calculated using R-indices (R_{wp} is the weighted pattern):

$$\chi^2 = \frac{R_{wp}}{R_{exp}} \tag{2-17}$$

$$R_{wp} = \sqrt{\frac{\sum_{i=1}^{N} \left[w_i (I_i^{exp} - I_i^{calc}) \right]^2}{\sum_i^N \left[w_i I_i^{exp} \right]^2}} \tag{2-18}$$

$$R_{exp} = \sqrt{\frac{(N-P)}{\sum_i^N \left[w_i I_i^{exp} \right]^2}} \tag{2-19}$$

where N is number of points and P the number of parameters [130].

$R_{wp} < 0.1$ corresponds to an acceptable refinement with a medium complex phase. For a complex phase (monoclinic to triclinic), a value < 0.15 is good. For highly symmetric compounds (cubic) with few peaks, a value < 0.08 start to be acceptable. The R_{exp} is the minimum R_{wp} value reachable using a certain number of refineable parameters. It needs a valid weighting scheme to be reliable [129].

Many software exist that enable Rietveld refinement such as: GSAS, Fullprof, BGMN, DBW, LHPM-Rietica, MAUD, Rietan, Simref, etc.

Rietveld methods fit a multivariable structure-background-profile model to experimental data which is why there is a potential for false minima, diverging solutions, etc. The most

important variables need to be refined first, and then more variables can be added until an adequate solution is obtained.

The R. Young's Refinement Strategy suggests the following refinement scheme:

- scale factor;
- zero shift or specimen displacement (not both);
- linear background;
- lattice parameters;
- background;
- peak width, w;
- atom positions;
- preferred orientation;
- isotropic temperature factors;
- u, v, and other profile parameters;
- anisotropic temperature factors.

More refinement schemes can be found in [131].

2.2.2.2. PDF analysis

The standard tool to study the atomic structure is crystallography which aim is to determine the average atomic positions within a periodic lattice (fully crystalline solid). On the other hand, there are also well-established methods to characterize the structure of fully disordered materials such as liquids and glasses. However, there is a dearth of techniques for the cases in-between, like crystalline solids with internal atomic or nanometer scale disorder. The study of complex hierarchical materials such as bone tissue requires a technique that will be able to determine the deviation from an average crystal structure in the short- or middle-range order.

The pair distribution function (PDF) appears to be a method which is ideal for such cases [117]. It describes a probability of finding any pair of atoms at a given inter-atomic distance (Fig. 2.12). The primary application of PDF analysis was the study of materials that do not show a long-range lattice periodicity, i.e. liquids or glasses. Their PDFs show broad features and do not extend over the short-range of the first few coordination spheres.

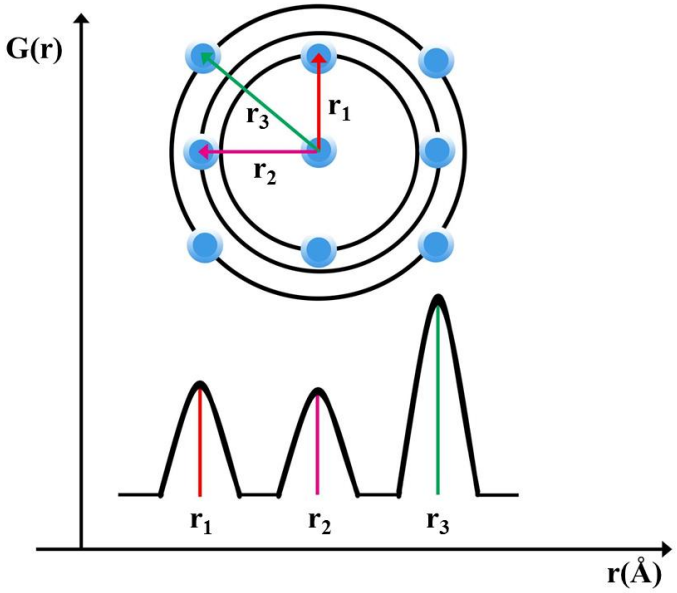

Figure 2.12. The principle of PDF. Inter-atomic distances, r_i, give maxima in the PDF *G(r)*. The area below the peaks corresponds to the number of neighbors, scaled by the scattering power of the respective atoms.

A PDF from crystalline material is much more structured and gives information on a medium-range of inter-atomic distances. This is complementary to the Rietveld method, which models the average crystal structure from the intensities of the Bragg reflections in a diffraction pattern. Thermal vibrations that are always present in crystals and disturb the ideal atomic arrangement are considered in the Rietveld method by the thermal displacement parameters and are treated as random deviations. Other deviations from the ideal symmetry, e.g. short-range order, do not contribute to the Bragg reflections but to the diffuse scattering. They are, therefore, not considered by the Rietveld analysis.

In contrary, PDF takes into account both Bragg and diffuse scattering. PDF can than discriminate between short-range order (represented by finite non-random displacements from the ideal crystal structure) and random displacements of the atoms. Systematic deviations from the ideal structure are, indeed, frequently observed in very small particles and are expected in our system. In other words, PDF analysis does not use the assumption of lattice periodicity but uses information from Bragg reflections and the information buried in-between Bragg peaks in the form of diffuse scattering. It imposes the fact that the structure is non-crystalline even though it has long-range order.

The PDF *G(r)* yields the probability of finding a pair of atoms separated by a distance *r*. Experimentally, the PDF is obtained from a powder diffraction pattern by realizing the Fourier transform as [132]:

$$G(r) = 4\pi r[\rho(r) - \rho_0] = \frac{2}{\pi}\int_0^\infty Q[S(Q) - 1]\sin(Qr)dQ \qquad (2\text{-}20)$$

where $\rho(r)$ is the pair density, *S(q)* the total scattering structure function, i.e. the normalized coherent scattered intensity. It is worth noting that the whole diffraction pattern is used to obtain *G(r),* not just the Bragg peak intensities as for a classical crystallographic analysis. Therefore the contributions of disorder, defects, etc. which contribute to the pattern through diffuse scattering outside of the Bragg peaks, will also be encoded in *G(r).*

A set of corrections has to be applied in order to obtain *S(q)* from diffraction data (same as for Rietveld refinement) by excluding incoherent and inelastic contributions such as Compton scattering, fluorescence (X-rays), Placzcek and incoherent scattering (neutrons), signals coming from the environment (sample holder, cryostat, air scattering, etc.), as well as the effects of absorption, multiple scattering, etc. Then the function *F(q) =q(S(q)−1)* is Fourier transformed according to (2.18) in order to obtain *G(r)*. To calculate the PDF from experimental data, software such as PDFgetX2, PDFgetX2 [133] etc. can be used.

This experimental *G(r)* is further compared to the model in a similar way as is done in the Rietveld refinement. The model usually consists of atomic positions, thermal factors, symmetry elements, experimental and sample corrections, model-dependent parameters for broadening and damping. The PDF profile can be modeled and fit to the experimental data with software such as PDFgui [134], Diffpy-CMI [135], PDFfit [136], DISCUS [137], RMCProfile [138], etc.

Eventually, when the system of interest is composed of more than one kind of atom, it is generally desirable to understand the distinct structure of a particular chemical species. Therefore, we can extract a partial pair distribution function, $G_{\alpha\beta}(r)$, that gives the distribution of atom pairs in the material coming only from atoms of type β around atoms of type α. In this case, the total pair distribution function would be:

$$G(r) = \sum_\alpha \sum_\beta G_{\alpha\beta}(r). \qquad (2\text{-}21)$$

2.2.2.3. CXDI analysis

Imaging techniques such as optical, fluorescence, phase-contrast, confocal, X-ray and electron microscopies are widely used in the field of materials science. These techniques are based on the lens-microscopy and are limited in resolution by both the lenses and the wavelength of the radiation.

X-ray lens-based microscopy was also used for materials characterization due to its ability to study thick and opaque samples with relatively high resolution. Recently, the development of third-generation synchrotron and free-electron laser radiation sources that produce intense X-ray beams with high degree of spatial coherence have enabled, among others, lensless X-ray imaging technique called coherent X-ray diffraction imaging (CXDI) [139].

CXDI is based on measuring the Fraunhofer (far-field) speckle pattern of an object fully illuminated by a highly coherent synchrotron beam and subsequently applying a phase-retrieval algorithm to reconstruct the image, in an attempt to solve the so-called phase problem.

The phase problem is the name given to the loss of information concerning the phase that occurs when making a physical measurement such as X-ray diffraction. Light detectors, such as photographic plates or CCDs, measure only the intensity of the light that hits them. This measurement is incomplete (even when neglecting other degrees of freedom such as polarization) as a light wave has not only an amplitude (related to the intensity), but also a phase, which is systematically lost in a measurement. In diffraction or microscopy experiments, the phase part of the wave often contains valuable information on the studied specimen. The simple illustration of the phase problem is shown in Fig. 2.18. The standard Lena image widely used in the field of image processing will be used as an example. First let us make a Fourier transform of it and separate the magnitude and the phase. Magnitude image is plotted in the log scale to improve the contrast.

To get further insight, let us reconstruct an image from either just its magnitude or its phase component by inverse Fourier transform of each of them. The reconstruction from the phase contains the edge features in the original image, whereas the magnitude image contains most of the coloring from the original image. One can recognize the girl in the phase-reconstructed image, but cannot see anything resembling her in the magnitude-reconstructed image. Thus, knowing the phase information is absolutely crucial for image reconstruction.

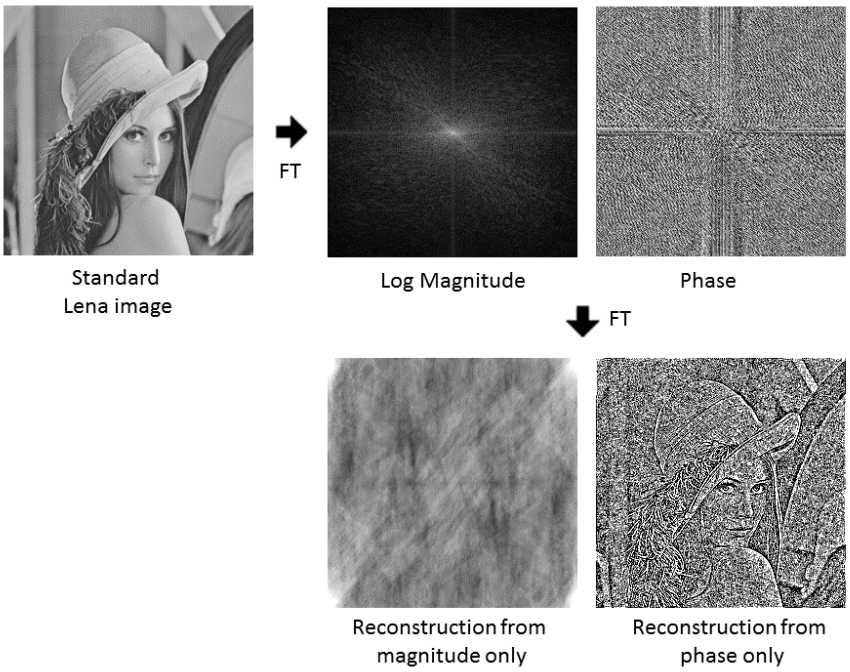

Figure 2.13. Illustration of the phase problem. Separated Fourier transforms of magnitude and phase (calculated with ImageMagick software).

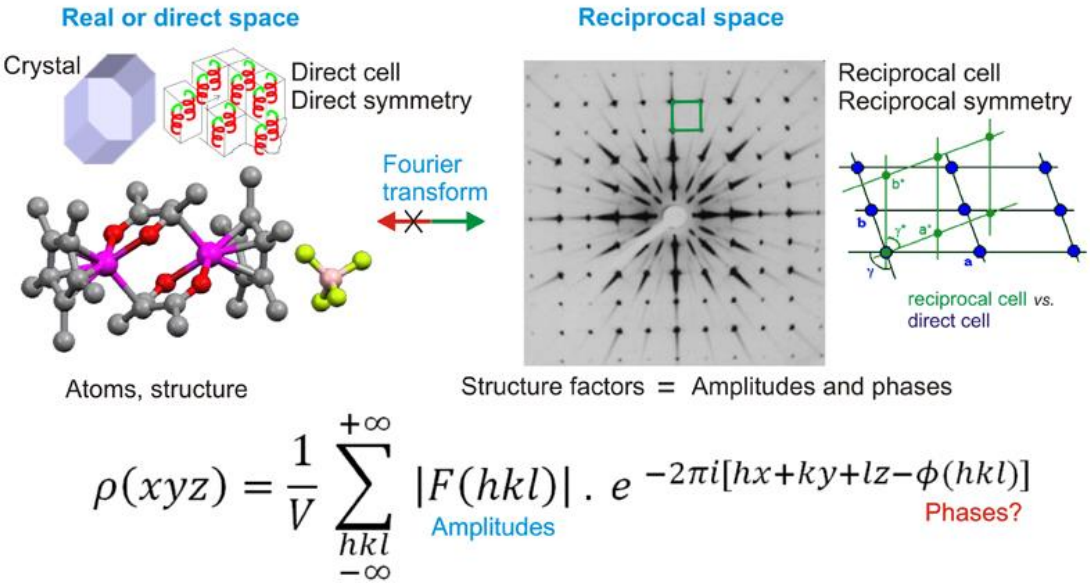

Figure 2.14. Phase problem in X-ray crystallography. Real and reciprocal space information [140].

If we apply this concept to X-rays, one can see that simple Fourier transform of the diffraction pattern that contains the structural information such as structure factor $F(hkl)$ does not recover all the real space information, as is shown in Fig. 2.14. Because in order to calculate the electron density that represents atomic positions in real space, one needs both amplitudes $F(hkl)$ and phases $\phi(hkl)$.

We will then replace the use of the lens by a computational scheme that will allow the reconstruction of the missing phase information (see Fig. 2.15).

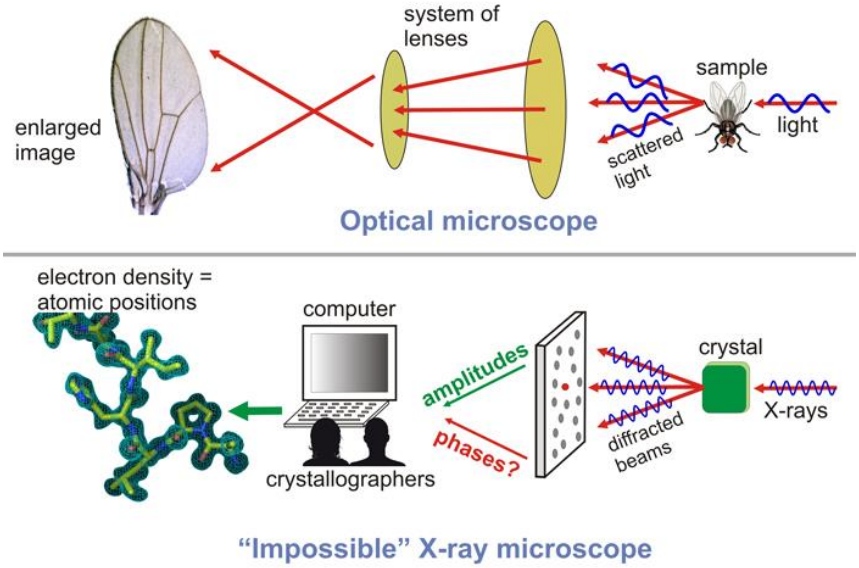

Figure 2.15. Idea of X-ray microscope and its comparison to optical microscope: phase retrieval computational algorithm is used as the lens in optical microscopy [140].

The idea that phase information can be recovered from a diffraction pattern was first proposed by D. Sayre in 1980 [141] and demonstrated for X-rays by J. Miao, D. Sayre, and coworkers in 1999 [141]. In a classical CXDI experiment, the spatially and temporary coherent beam is produced by the monochromator and set of slits. The isolated sample is scanned in rotation within an angular range of ~±70° (the maximum rotational range allowed by the geometrical sample holder limitations) with the sufficient angular step (on the order of 0.25°) to achieve the proper sampling of the reciprocal space [142], see Fig. 2.16. The proper sampling is important in order to recover well enough the reciprocal space of the object for reconstruction. The sample dimensions has to be smaller than the beam coherence length in order to fulfill the isolated object requirement.

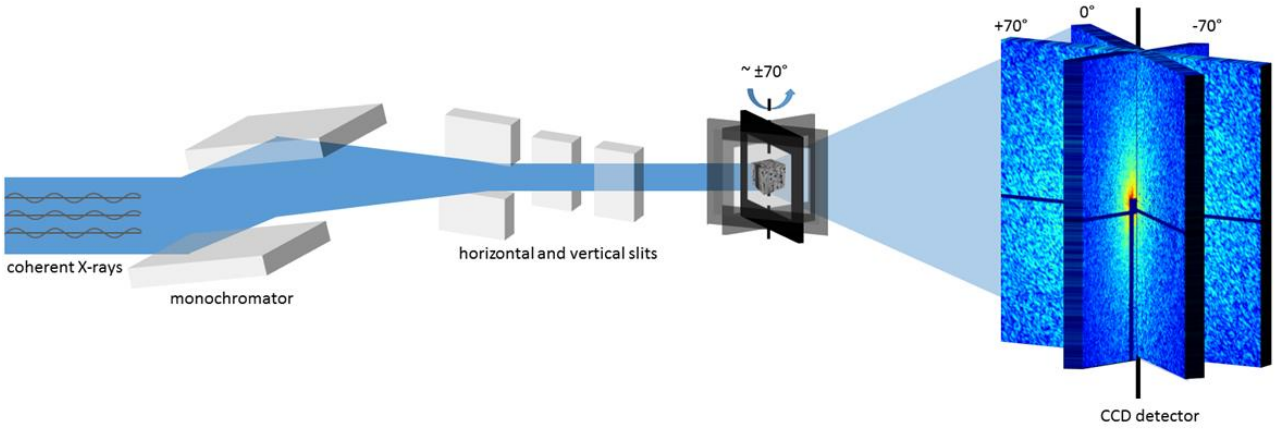

Figure 2.16. General scheme of 3D CXDI acquisition at ID10 (ESRF). Synchrotron beam achieves its temporal and spatial coherence by passing through monochromator and slits; individual isolated sample is being rotated to ±70° degrees; far-field diffraction patterns are recorded by CCD camera.

Collected diffraction patterns need to be corrected for data acquisition geometry and detector characteristics. In practice, this involves flat-field, detector dead-time corrections, background subtraction, masking of the beamstop and detector dead pixels. The final 3D reciprocal space volume is obtained by assembling the individual patterns using linear interpolation.

3D reconstructions are obtained by the use of an iterative phase retrieval algorithm. The combination of Hybrid Input Output (HIO) algorithm (first 70% of iterations) and Error Reduction (ER) algorithm (last 30% of iterations) is used for the object reconstruction.

The ER algorithm developed by J. Fienup [143] is a fast iterative algorithm that uses alternating constraints on a guess solution in real and reciprocal space (schematically show in Fig. 2.17). At the first step of phase retrieval, we take an initial object (in real space) of spherical shape filled with random numbers, referred to an initial estimate. A Fourier transform, $\Phi[]$, of this initial estimate is then calculated resulting in reciprocal space representation, i.e. structure factor, F. Data constraints are then introduced by substitution of the structure factor amplitudes with the measured intensity from diffraction patterns. The inverse Fourier transform, $\Phi^{-1}[]$, of the updated structure factor, F', provides a new real space object estimate, f'. The sample constrains are then introduced to obtain an updated object estimate, f. This assumes that the dimensions of the shape or object are known so solutions outside of the dimensions are set to

zero and the solutions within the object are kept to form the new trial solution. The calculation continues in an iterative way until it does not produce any new information.

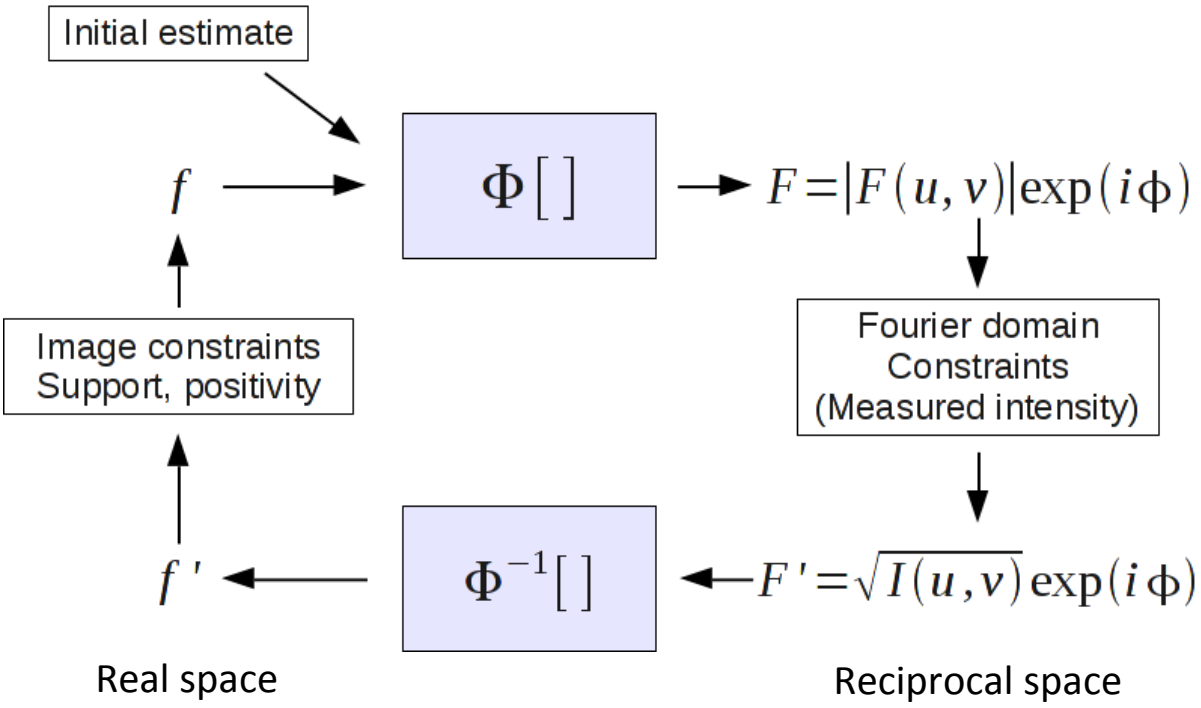

Figure 2.17. Simplified scheme of CXDI iterative phase-retrieval algorithm. Initial: random phases and amplitudes. Input parameters: amplitudes from experimental data.

The data constraint represents a non-unique operator; if this was the only constraint applied the reconstruction could converge on any number of possible solutions and not the at the object phase. The sample constraint drives the algorithm towards the object phase solution because this is the only solution that has the sharp defined edges of the shape dimensions. The ER algorithm is also known as a local minimizer algorithm as it reduces the error from the previous solution. Reconstructing the phase of objects often involves many local minima, so depending on the starting guess of the magnitude and phase it can stuck in a local minimum rather than the global minimum [144] or stagnate. This means that only using ER the program may not converge to the correct solution. This increases the program run time and computer power needed.

HIO is one of many algorithms that were created in order to overcome the stagnation and local minima problem of ER. It was proposed by J. Fienup in 1986 [145]. HIO uses the same

basic iteration process as ER except for a slight difference in the sample space constraint. Unlike ER, where the solutions inside the dimensions of the object are kept, in HIO the solutions outside of the given dimensions are allowed to vary and are not set to zero. This works by subtracting the previous iteration output multiplied by a real parameter from the current iteration output, all done in the frame outside of the object dimensions. This forms a sort of weighted average between the previous iteration and the current iteration with the real parameter, often known as β, within the typical range of 0.5 to 1.0 [144]. Starting with random trial solutions or guess shapes HIO consistently reconstructs the same structure and so it is considered a reliable algorithm [146]. The solutions being allowed to vary outside of the sample constraint makes this more powerful than ER as it is much better at avoiding both stagnation and local minima. However, as it is a weighted average technique it can only reach its full potential when used in combination with ER.

2.2.2.4. Sources of X-ray radiation

2.2.2.4.1. Powder X-ray diffraction at the laboratory source

In the laboratory source, X-rays are produced by bombarding a metal target (Cu, Mo, Ag usually) with a beam of electrons emitted from a hot filament (often tungsten). The incident beam will ionize electrons from the K-shell (1s) of the target atom and X-rays are emitted as the resultant vacancies are filled by electrons dropping down from energetically higher levels. The specific wavelengths are characteristic of the target material (Cu, Fe, Mo, Cr, etc.). In our case, AgKα radiation with λ=0.5608 Å and E=22.1086 keV was chosen.

The sample was placed on the goniometer that was mounted on a diffractometer (BRUKER-AXS KappaCCD) equipped with a CCD camera (Apex II) and an X-ray microsource (Incoatec Ag-IμS) as shown in Fig. 2.18. A beam of 150 μm diameter was focused on the sample. The angular coverage of the detector was 2θ=20°. 36 images were recorded while sample rotation with the step size of 3° with increasing 2θ, allowing for a large angular overlap between images and reaching a maximum at $2\theta_{max}=120°$ ($q_{max}=19.4$ Å^{-1}). In practice, the statistic on the largest angles was too low and the last few angles were not used. The exposure time was 40 min/image; therefore, 24 hours per sample. The background is also recorded in the same conditions.

Figure 2.18. Laboratory XRD setup (Institute Neel).

Standard corrections and azimuthal averaging was performed with the Powderize module of the evalCCD software. An intensity evaluation method EVAL-14 is described in the reference [147]. Diffraction patterns were further averaged with a homemade Matlab script. PDF profiles are calculated with PDFGetX2.

2.2.2.4.2. Synchrotron source

The other part of X-ray measurements was done with a synchrotron source. The description of its functioning, components and focusing optics is discussed in detail in Appendix 2. The experiments were performed on three different beamlines as described below.

ID11 beamline for PDF analysis. ID11 is a multipurpose beamline, concentrating on 3D grain mapping, diffraction and PDF experiments in the area of materials science. It has high flux (~10^{14} photons/s for white beam and ~$1x10^{7}$ photons/s for monochromatic beam) and high energy (18-140 keV, in our case 78 keV was used). X-ray beam dimensions can be tuned from a few mm down to 100 nm.

ID11 is located at the output of an undulator source. The monochromator is made of a double bent crystal (operating in horizontal Laue geometry) and focusing system that consist of a transfocator of 8 cylinders with Be lenses, Al lenses, and a pinhole [148]. It is equipped

with the goniometer (situated 94 m from the source) and Frelon detector of 2048x2048 pix^2 and 45.85x45.85 μm^2 (see Fig. 2.19). In Fig. 2.20, the ID11 setup is shown. We use it in the high resolution diffractometer configuration in scanning mode.

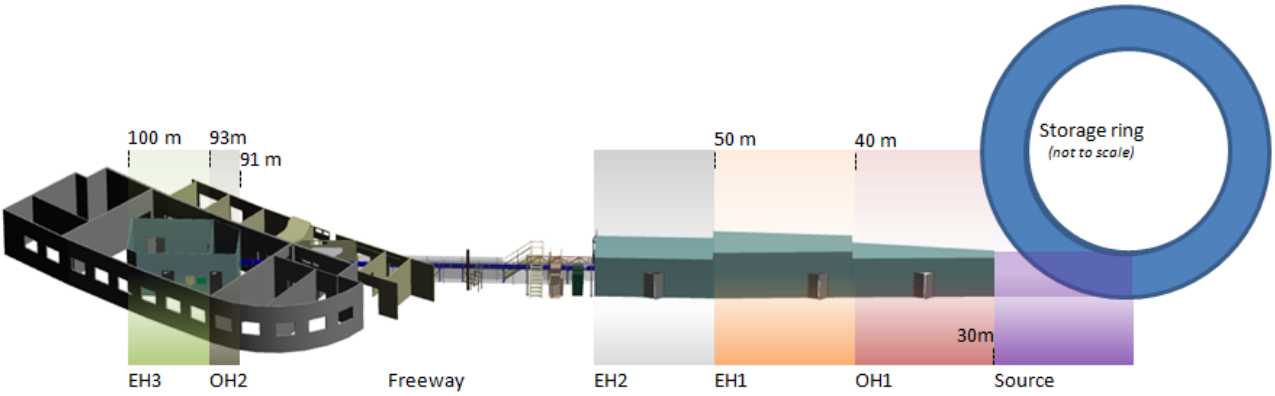

Figure 2.19. ID11 map schematic showing the locations of the Experimental Hutch 3 (EH3) [148].

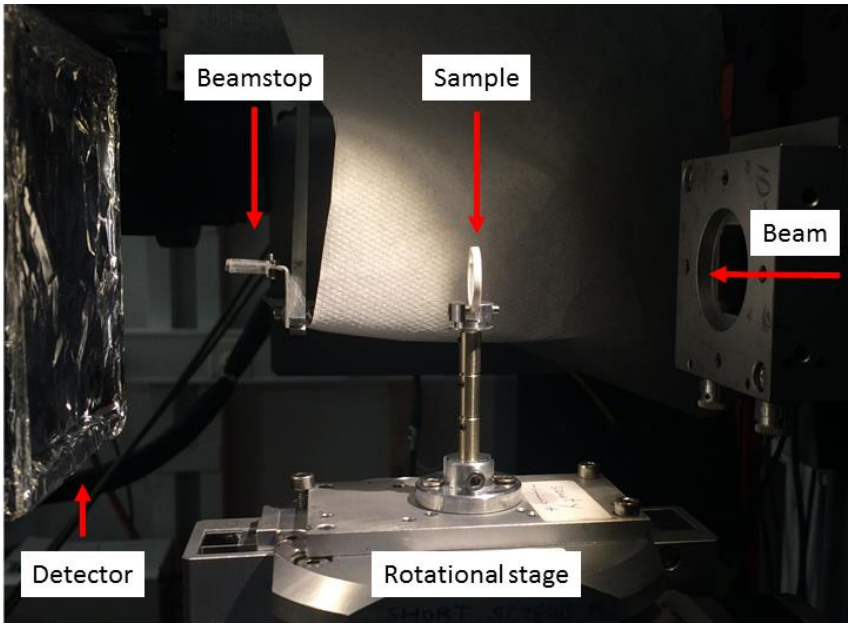

Figure 2.20. Photograph of the ID11 setup indicating the principle components.

Diffraction patterns for PDF analysis were recorded at EH3 hutch with energy of 78.25 keV (λ= 0.158 Å) and beam size of 10x10 μm^2 (HxV, FWHM). Samples were scanned with the step size of 10 µm and the background was recorded before each scan at the empty position (hole in the sample).

ID10 beamline for CXDI. ID10 is a multi-purpose, high-brilliance undulator beamline. Endstation EH1 is dedicated to high-resolution X-ray scattering and surface diffraction on liquid and solid interfaces, combining multiple techniques in a single instrument. Endstation EH2 is adapted for coherent SAXS, X-ray photon correlation spectroscopy and CXDI.

EH2 station was used for CXDI experiments. It has high coherent flux with 10x10 μm^2 beamsize, and intrinsic energy resolution of $\Delta E/E = 1.4\ 10^{-4}$. It uses water cooled silicon (111) crystal pseudo channel cut monochromators (Fig. 2.21).

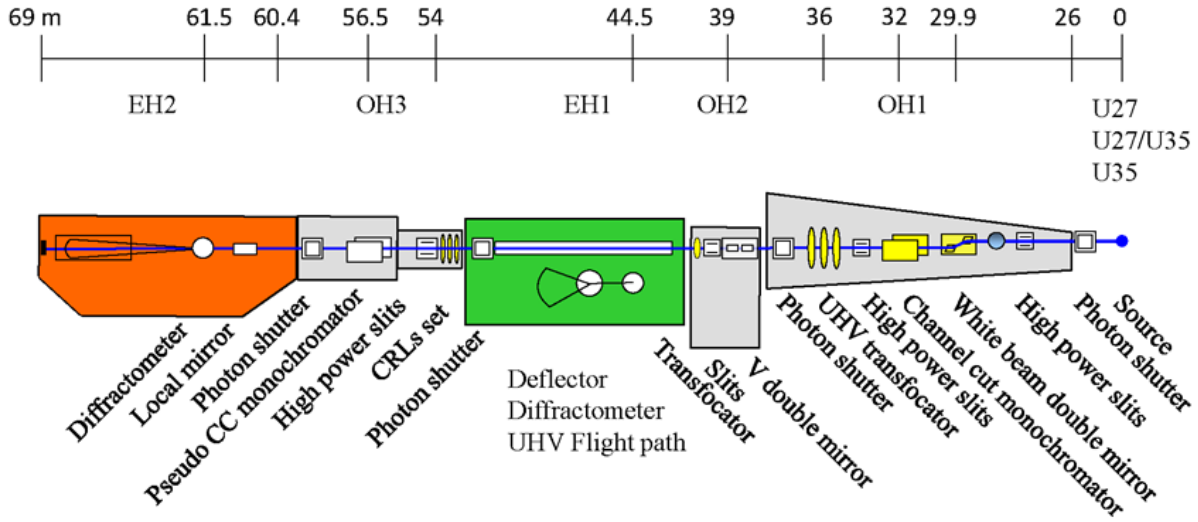

Figure 2.21. ID10 beamline layout [148].

The station is equipped with high resolution goniometer with an on-axis microscope and MAXIPIX 516×516 pix^2, 55×55 μm^2 pixel size detector. 3D reconstructions can be obtained with an in-house software.

CXDI was performed with a highly coherent source at the energy of *7* keV ($2.5\ 10^{10}$ ph/s) and *8* keV ($8.3\ 10^{10}$ ph/s). A coherent X-ray beam was produced by beam defining roller-blade slits opened to 10 x 10 μm^2 and placed 0.5 m upstream of the sample. The diffraction from the slits was cleaned by a second set of roller-blade slits placed 0.25 m upstream of the sample and finally by guard slits with Si blades situated 0.08 m upstream of the sample. Samples of interest were selected and imaged by an in-line microscope.

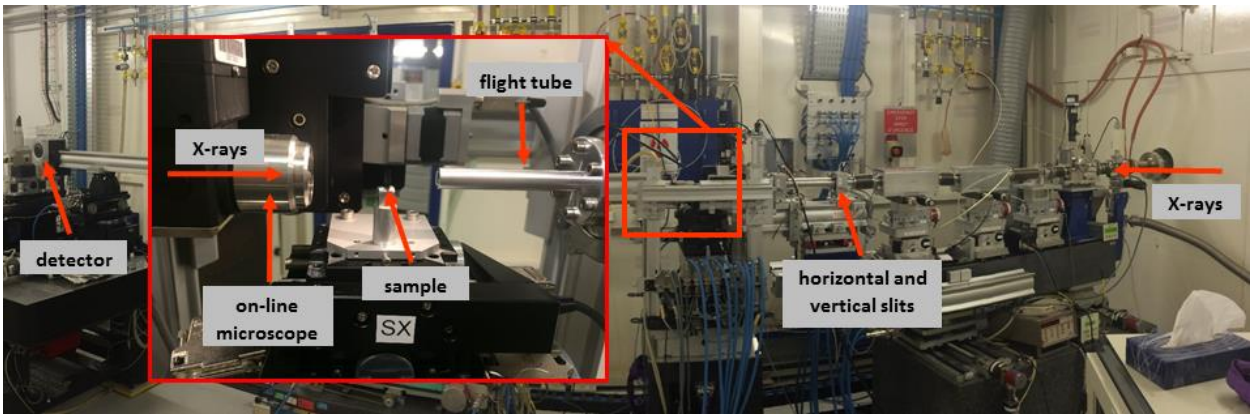

Figure 2.22. Experimental setup for CXDI experiment at ID10.

Samples were rotated to ±70° with the 0.25° step size and 25 ms exposure time as shown in Fig. 2.29 and their far-field diffraction patterns and background was recorded at each rotational step with MAXIPIX 2 x 2 chip detector with 516 x 516 pix^2 and a pixel size of 55 x 55 μm^2, placed 5.27 m downstream from the sample (as shown in Fig.2.22). Rotational range is chosen to be maximal in order to better oversample the reciprocal space excluding angles that give rise to saturation.

Phase retrieval was done by the use of ID10 in-house software (Y. Chushkin). 80 individual reconstructions are done with 1000 iterations each and 30 best in terms of the square root of normalized error metrics value (invariant error metrics for image reconstruction is defined in [149]) are aligned and averaged with sub-pixel interpolation of 1:2.

2.2.3. Electron radiation based techniques

2.2.3.1. Electron diffraction and TEM

The principal scheme of TEM is shown in Fig. 2.11. A TEM is composed of several components, which include a vacuum system in which the electrons travel, an electron emission source for generation of the electron stream, a series of electromagnetic lenses, as well as electrostatic plates. The last two allow the operator to guide and manipulate the beam as required. Imaging devices are subsequently used to create an image from the electrons that exit the system.

Contrast formation in TEM depends greatly on the mode of operation. This stems from the unique ability to change the electro-magnetic lenses characteristics or to deactivate them, which allow many operating modes. A few **operation modes** such as bright field, dark field and diffraction that were used in this study will be described.

The most common mode of operation for TEM is the **bright field** imaging mode. In this mode, the contrast, when considered classically, is formed directly by occlusion and absorption of electrons in the sample. Thicker regions of the sample, or regions with a higher atomic number will absorb more strongly and, hence, appear dark, whilst regions with no sample in the beam path will appear bright – this is where the term "bright field" comes from.

By adjusting the magnetic lenses such that the back focal plane of the lens (rather than the imaging plane) is placed on the imaging apparatus, a **diffraction pattern** can be generated. For thin crystalline samples, this produces an image that consists of a pattern of dots in the case of a single crystal, a series of sharp rings in the case of a polycrystalline or broad rings for an amorphous solid material. In the single crystal case, the diffraction pattern is dependent on the orientation of the specimen and the structure of the sample. This image provides information about the space group symmetries of the crystal and its relative orientation with respect to the beam path. This is typically obtained without using any other information but the position at which the diffraction spots appear and the observed image symmetries.

Analysis of diffraction patterns can be complex, as the image is sensitive to a number of factors such as specimen thickness, objective lens defocus, spherical and chromatic aberrations and, most importantly, due to multiple scattering which occurs when a diffracted photon is diffracted again by another part of the sample. This changes the relative intensities measured on the detector, such that crystal structure analysis becomes more complex.

If the reflections that are selected do not include the direct beam, then the image formed in the image plane will appear dark. This is known as a **dark-field** image. It involves tilting the incident illumination until a diffracted, rather than the incident, beam passes through an objective aperture in the objective lens back focal plane. Dark-field images, under these conditions, allow mapping the diffracted intensity coming from a single collection of diffracting planes. It can be used, for example, to highlight all the crystals in the field of view that produce the given diffraction spot.

Energy dispersive X-ray analysis (EDX) is another modality available in many modern electron microscopes equipped with an energy sensitive X-ray detector. It is a technique used for the elemental analysis or chemical characterization of a sample. Since each element has a unique atomic structure, EDX allows collecting a unique set of peaks corresponding to its X-ray emission spectrum. To stimulate the emission of characteristic X-rays from a specimen, a high-energy beam of electrons is focused into the sample. In its lowest energy state, an atom in the sample contains ground state electrons in discrete energy levels or electron shells bound to the nucleus. The incident beam may excite an electron in an inner shell, ejecting it from the shell while creating an electron hole where the electron was located. An electron from an outer, higher-energy shell then fills the hole, and the difference in energy between the higher and the lower-energy shells may be released in the form of an X-ray, collected by the detector. As the energies of the X-rays are characteristic of the difference in energy between the two shells and of the atomic structure of the emitting element, EDX allows the elemental composition of the specimen to be measured [150].

TEM setup. The TEM used was a high-resolution transmission electron microscope JEOL 2100F with a field emission gun as show in Fig. 2.23.

Figure 2.23. The JEOL 2100F transmission electron microscope.

The instrument has the following specifications:

- 200 kV accelerating voltage;
- Schottky FEG Emission-Zr/W;
- Image Resolution: 1.5 nm with HTP (Bright Field STEM at 200 kV);
- Low Mag: 100x to 15,000x;
- High Mag: 20,000x to 15,000,000x;
- JEOL bright field detector;
- ACOM setup.

2.2.3.2. Automated Crystal Orientation Mapping

The Automated Crystal Orientation Mapping (ACOM–TEM) tool is an extension technique to the classical TEM approach that allows automated crystal orientation and phase mapping. It is based on the collection of diffraction patterns with a fast CCD camera while the beam is scanning the thin film. The data analysis relies on the comparison between the electron diffraction patterns collected at every scan position and the simulated patterns calculated for a given crystal structure in all possible orientations [151,152]. This allows reconstructing crystal orientation maps. The method can be equally applied for the spatially resolved phase identification problem by using several structural templates (models).

Currently, the integrated TEM cameras for direct diffraction pattern acquisition usually do not fulfill the requirements for ACOM in terms of speed. These cameras are better optimized for resolution and sensitivity than for speed. A reasonable orientation map contains typically 100,000 pixels, all being related to a given diffraction pattern. A collecting rate of a few frames per second would require hours for gathering the complete set of pictures, with potential beam drift and radiation damage problems. An alternative solution consists in using an external dedicated high speed, high sensitivity and low resolution camera focused on the phosphorous screen through the TEM front window [153]. A typical acquisition runs at 100 frame par second with a step size that may range between 0.5 and 50 nm. Consequently a 200×200 pixel scan will take less than 10 min.

The requirement on the probe beam size depends on the materials' crystal size. In order to properly resolve the bone structure, we used the minimum available beam size of 2 nm.

Acquisition scheme and data interpretation. After selecting an area of interest using bright field imaging, it then scanned in diffraction mode by the fast camera (Fig. 2.24). Distortion and camera length corrections are applied and the virtual bright field image is constructed numerically by selecting only the transmitted beam intensities (as shown in Fig. 2.25). The structure template is used in order to create a set of calculated diffraction patterns for all possible orientations of the given phase (bank). For bone samples, the hydroxyapatite structure file was used [64]. Each diffraction pattern is compared to the generated bank of templates for all possible orientations and the best fit is chosen and displayed in the fitting window and in stereographic projection. The darkest color code corresponds to the best fit. Therefore, the orientation map is obtained with the corresponding inverse pole figure color map. In order to judge the quality of fit, two parameters are calculated for every template match: index and reliability.

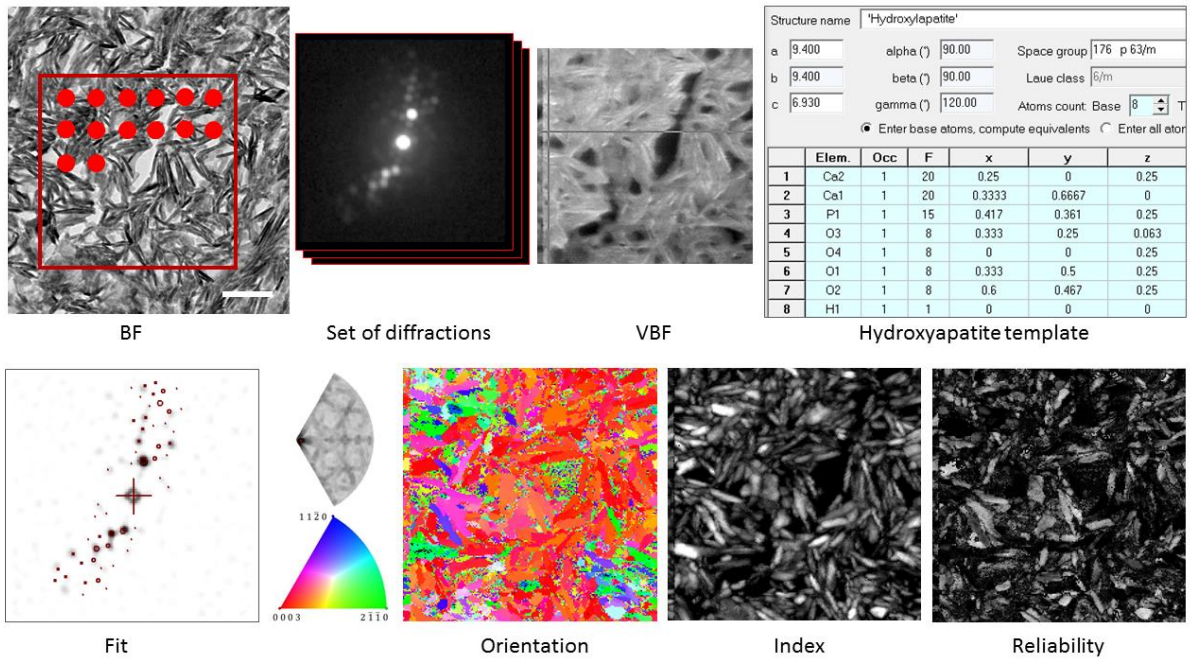

Figure 2.24. General scheme of ACOM-TEM acquisition and data interpretation: bright field image of bone with shown scanning area, set of diffraction patterns, virtual bright field image, structure template for hydroxyapatite, example of fit with stereographic projection, orientation map with inverse pole figure color map, index and reliability maps, which are explained in the following.

In order to obtain orientation maps, the structure templates are calculated for every possible orientation and expected phase (bank). For a known phase, it is straightforward to

calculate the reciprocal lattice. The theoretical diffraction pattern, called template, is the intersection of the reciprocal lattice – oriented according to the chosen set of Eulers angles – and the Ewald sphere whose radius scales with the inverse of the electron wavelength.

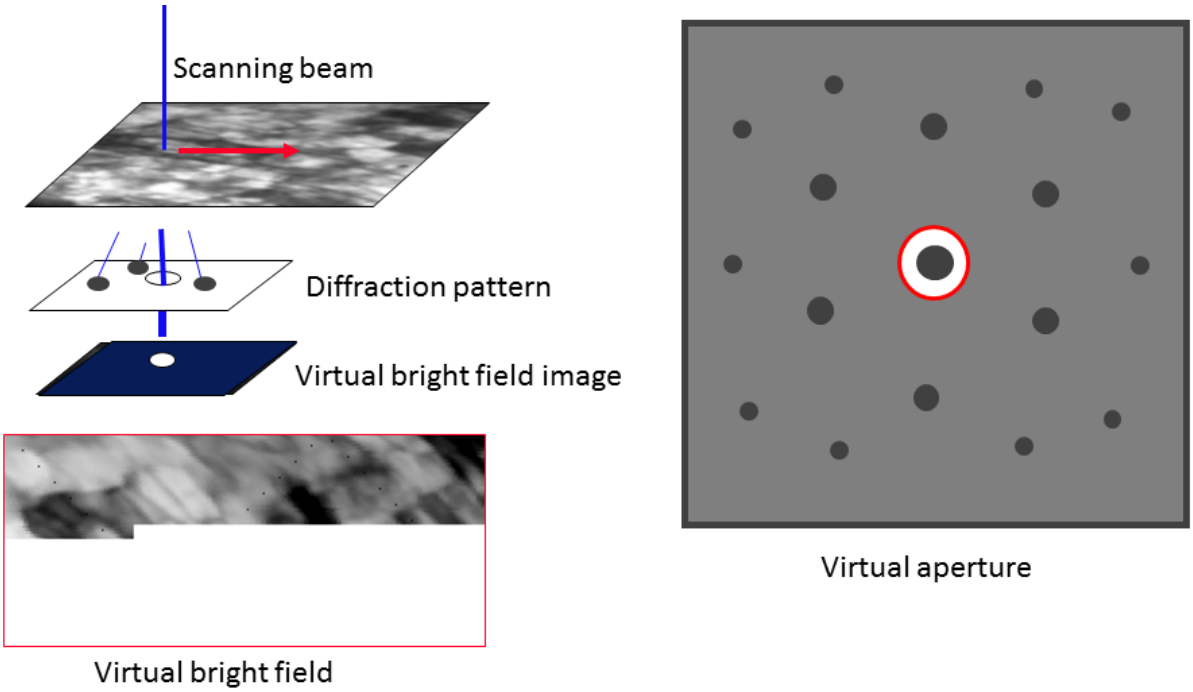

Figure 2.25. Schematic representation of virtual bright field reconstruction. A virtual aperture is used to select only the transmitted beam and then plotted on the image. This is equivalent to introducing an aperture in the beam path.

The image correlation Index is calculated for every template match (Fig. 2.26). In the index equation, the diffraction pattern is represented by the intensity function $P(x,y)$ and every template, i, is given by the function $Ti(x,y)$. The highest Q value corresponds to the best fit of a single template diffraction pattern (in the given orientation) to the data that we will further refer to a solution [152].

In particular, the Index map is a plot of the matching index at every location. This parameter measures the degree of correlation and may be understood as the quantity of information that is filtered out of the successive diffraction patterns (the at the measured diffraction pattern intensities that are not described by the template).

Plotting its value in grey levels provides a contrasted map that highlights dark areas related to structural features like grain or interphase boundaries, as well as non-considered phases (e.g.: precipitates) for which the matching cannot be good.

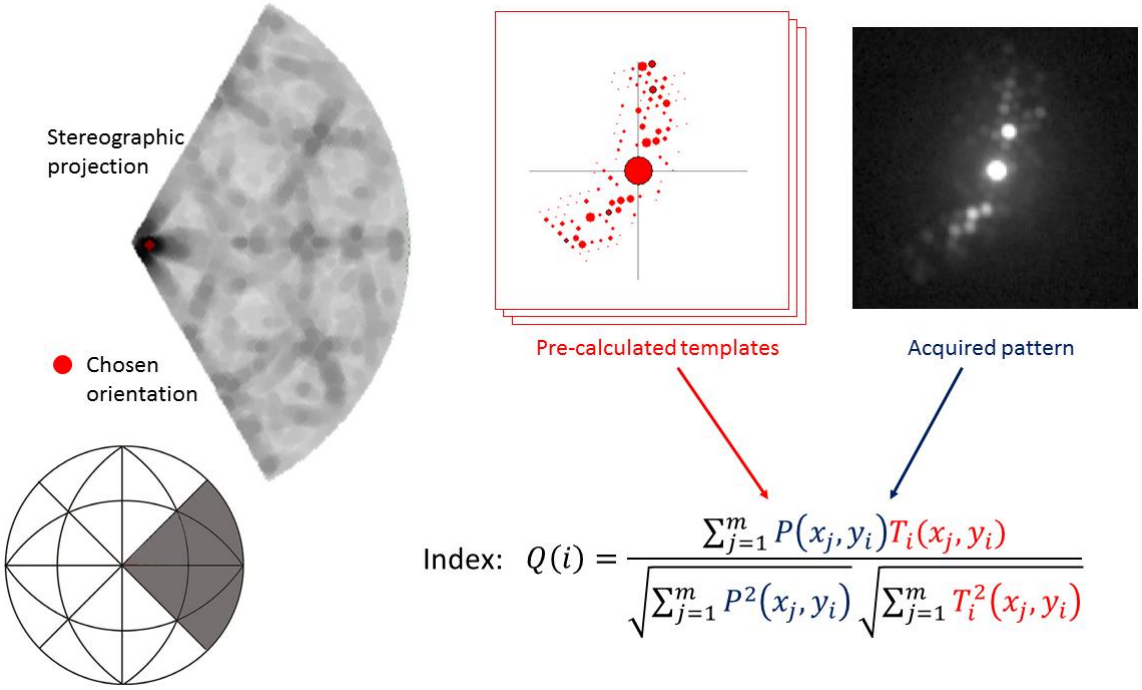

Figure 2.26. Template matching scheme and the definition of index. Each acquired diffraction pattern is compared to the template with all possible orientations for the given phase. The best solution is found by the method described in [151]; the solution is shown as darkest point in a stereographic projection and the Index calculation (the degree of correlation) is done.

It is worth emphasizing that the template matching strategy always provides a solution. Therefore, the validity of the proposed phase/orientation is questionable in particular for overlapping grains (crystals). A further parameter was designed to address this point, Reliability (Fig. 2.27).

This parameter indicates how safe the indexing is. It is set proportional to the ratio of the matching indexes for the two best solutions. Reliability is intimately related to the indexing quality. Its value ranges between zero (unsafe/black) and 100 (unique solution/white). Practically speaking, a value above 15 is sufficient to ascertain the validity of the matching, at least when the diffraction patterns are of good quality [151].

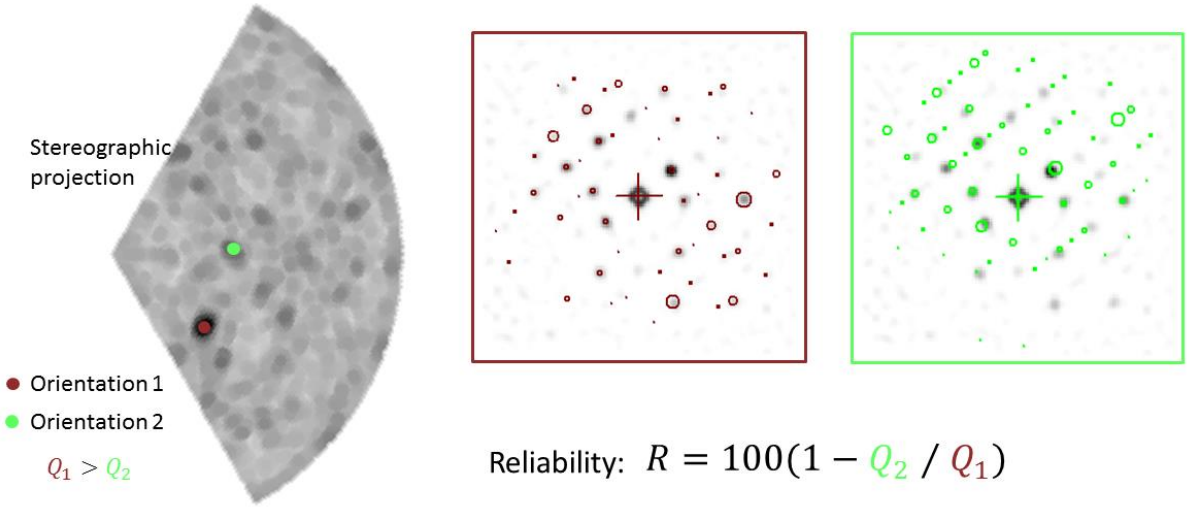

Figure 2.27. The reliability definition [151]. If there are two best orientations in a single template that give the single phase indexes (Q_1 and Q_2) with $Q_1 > Q_2$, then the reliability will be calculated as shown.

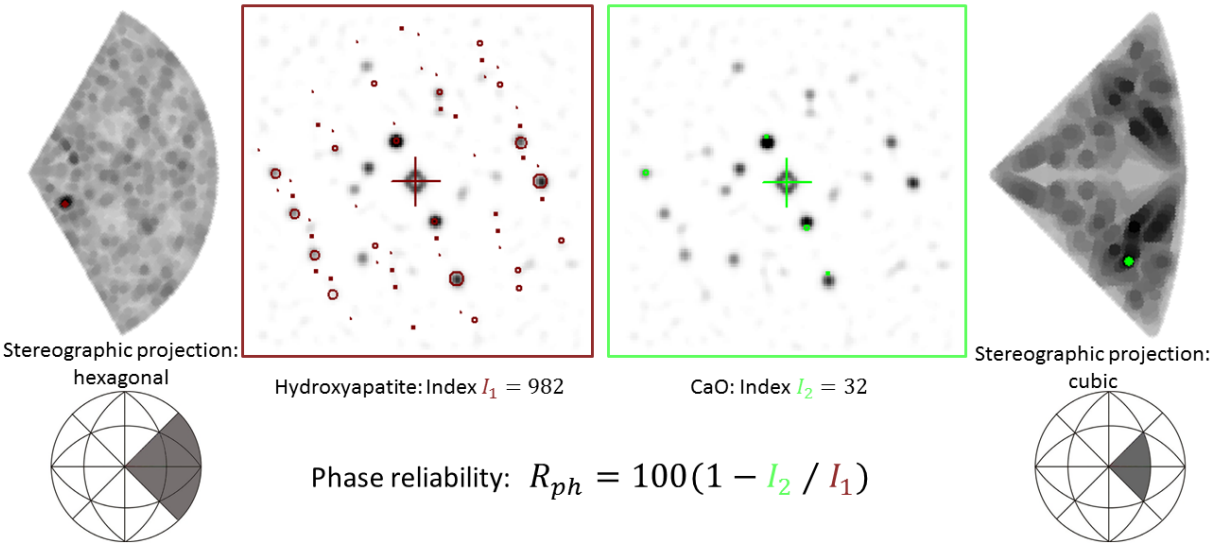

Figure 2.28. Phase identification scheme. The same bone diffraction pattern is compared to two phase templates (hydroxyapatite and CaO) with the corresponding indexes for two phases (I_1 and I_2; not to confuse with single phase indexes Q_1 and Q_2 in Fig. 2.27). Then the phase reliability will be calculated as shown.

It is often required to have access to coupled information such as chemical data (phase identification) and structural data (crystal structure and orientation, grain boundary characteristics). ACOM-TEM may also be used for phase identification. Templates of several phases that are expected to be present in the sample can be fit simultaneously and in addition to orientation, index and reliability, the phase map can be built (Fig. 2.28).

Since templates are calculated for kinematical conditions, the matching would be better if dynamical effects in recorded patterns are minimized. This is made possible by precessing the incident beam [154] using the deflection coils located above the sample (Fig. 2.29). The dynamical signals are smoothed out leaving the less sensitive kinematical signal enhanced. The matching with templates is far better, leading to improved orientation and phase mapping [155].

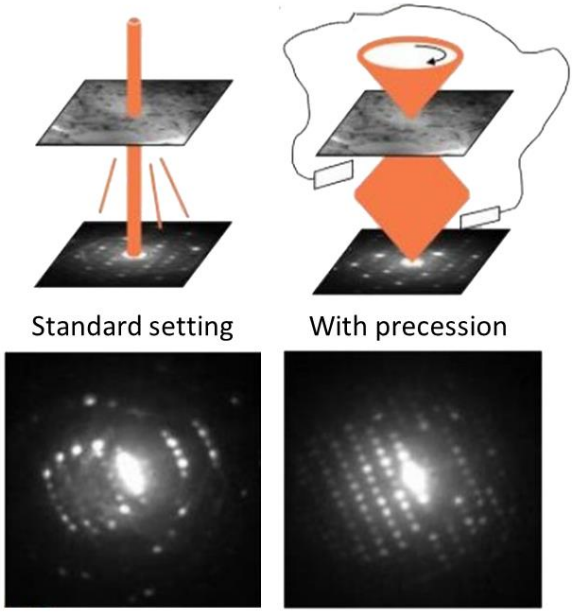

Figure 2.29. An illustration of diffraction pattern quality improvement with precession compared to standard setting.

Chapter 3. Results

3.1. Coherent X-ray Diffraction imaging of dentin and bone ultrastructure

3.1.1. Motivation

As seen from the complex structure of bone, the first step in the multiscale characterization should provide a microscopic field of view with the best achievable spatial resolution, which for bone offers histological information. With the recent progress in third-generation synchrotron radiation sources with high degree of coherence, CXDI is becoming a powerful tool that allows 3D imaging of microscopic samples with a spatial resolution better than 50 nm. Therefore, CXDI was the first step of bone characterization providing the 3D visualization of microscopic arrangements of bone components. The initial goal was to study the fluctuations of the mineral phase at the nanoscale and to test whether CXDI could allow visualizing individual crystallites which requires a spatial resolution of <1 nm. Although this was not achieved, we were able to visualize the collagen organization and, more strikingly, we found that this technique was able to clearly image the nanoscale porosity, whose existence is a matter of debates.

Previous studies [156,157] have shown the importance of understanding multiscale porosity in bone materials in relation to its biological functions: vascular (Haversian channels, 20-40 µm diameter) [158], cellular (lacuna-canaliculi system, down to 150 nm) [158–160] and collagen-apatite porosity [161,162] (CAP, less than 10 nm). Higher scale porosity, up to cellular, had been well defined by fluid characterization methods, such as mercury porosimetry, that are not based on any kind of visualization, but rather on pressure/volume changes of the fluid. While most studies at the level lower are based on confocal fluid transport methods [163,164] that require assumptions on the structure of the fully interconnected multiscale network and ultimate bonding of staining molecules to any surface of porosity. Currently, the term nanoporosity mostly appears in studies focused on the structural-mechanical role and was mainly used in the field of artificial bone materials such as implants, synthetic hydroxyapatite and scaffold construction [165–168]. In this manuscript, we will refer to nanoscale porosity to

designate porosity of the order of 50 nm or below and we will try to give hypothesis on its functions.

Because of its simpler hierarchy of porous network [169], dentin was chosen as a model for the first CXDI investigation. Dentin is similar to bone up to the fibrillar organization. It is formed by odontoblast cells that mineralize the collagen matrix during the tooth growth by moving from the outer side to the pulp leaving behind the dental tubules (1-2 μm in diameter in human). Unlike bone, adult dentin tissue does not contain living cells, so it does not remodel nor does it heal as other tissues do. Due to its structure, in a localized dentin volume, porosity can be assumed to be essentially oriented along one main direction (the tubules main axis, which is related to the tissue growth). It is, therefore, easier to orient the sample by visualizing the porosity at the microscale and, consequently, to visualize the tissue (and eventually the nanoporosity) with respect to the microscopic orientation. This is much more difficult to do with bone. The successful reconstructions of dentin samples provided a proof of concept for the feasibility of such studies and their future application to bone tissues.

With the recent development of high brilliance sources, the application of X-ray microscopy to biological tissues is gradually gaining scientific interest. Extracted collagen fibers from the rat tail tendon were analyzed by CXDI indicating the feasibility of collagen repetition pattern observation [170,171]. The group of J. Miao first applied CXDI to bone fish bone samples of 2 μm diameter [172] with different degree of mineralization imaging with voxel size of 12 nm. However, except for collagen repetition, no rich internal structure such as nanoporosity or individual mineral crystal organization was observed. Whereas, dentin was well described by micro-CT with μm-resolution but, to the best of our knowledge, was not visualized by CXDI [169]

Therefore, in this subchapter, we will discuss bone and dentin nanoscale porosity that was visualized and characterized with the spatial resolution better than 50 nm. The observation of the collagen banding pattern enabled assumptions to be made about the fibrils orientation.

3.1.2. Sample preparation peculiarities

The sample size was chosen based on the ID10 beamline characteristics. It was limited to 5 x 5 x 5 μm^3 in order to provide sufficient sampling of reciprocal space with the given beam

size, detector pixel size/area and resulting spatial resolution in real space (see Chapter 2). Furthermore, the samples needed to be fully illuminated by the beam during the full scan.

Therefore, dehydrated non-embedded human dentin and bovine bone blocks were cut by ultramicrotomy into 5 µm thick sections (see Chapter 2.1.6.) as shown in Fig. 3.1a. The following step had to provide the final cubes of 5 x 5 x 5 μm^3 by cutting the 5 x 5 μm^2 squares from the sections. Due to the difficulty to control precisely the resulting size and/or damage of the samples, we tried three different ways to produce the required geometry that are discussed below.

Focused ion-beam (FIB) milling was used on a first group of dentin samples. The 5 µm thick section previously obtained was covered with a conductive gold layer of 2 nm in order to avoid electron charge accumulation during SEM observation. On the SEM images, one can clearly observe dentin tubules (Fig. 3.1b,c) of around 2 µm diameter running horizontally. Fig. 3.1d shows dentin pieces after FIB sectioning that were mechanically deposited on Si_3N_4 membranes.

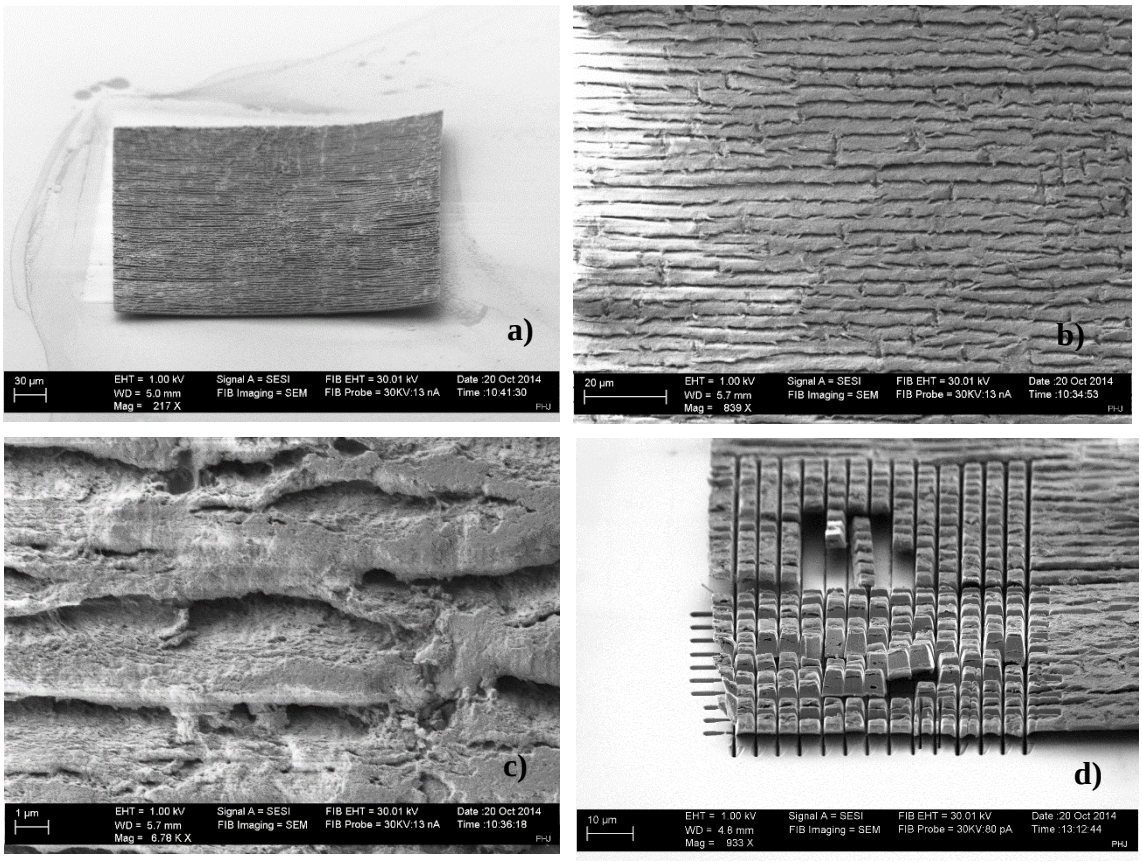

Figure 3.1. FIB/SEM sectioning of dentin tissue: a) a full view of ultramicrotomy slice, b) and c) zoom in on dental tubules, d) cutting of 5 x 5 x 5 μm^3 geometry objects.

The second technique that was used to produce the 5 x 5 x 5 μm^3 separated cubes was UV laser microdissection. By tuning the laser energy, the focus and the cutting speed, one can achieve the smallest beam size (in our case around 0.5 µm in diameter).

The ultramicrotomy slice was deposited on a TEM grid (to provide a flat sample surface and its fixation by electrostatic force) which was positioned on the frame of the Si_3N_4 holder that is approximately 1 mm higher than the membrane as shown in Fig. 3.2. In this configuration, the samples fall directly on the membrane by gravity and optical forces, without use of any liquids or micromanipulators (Fig. 3.3). However, the position of the samples on the membrane cannot be controlled and requires further characterization.

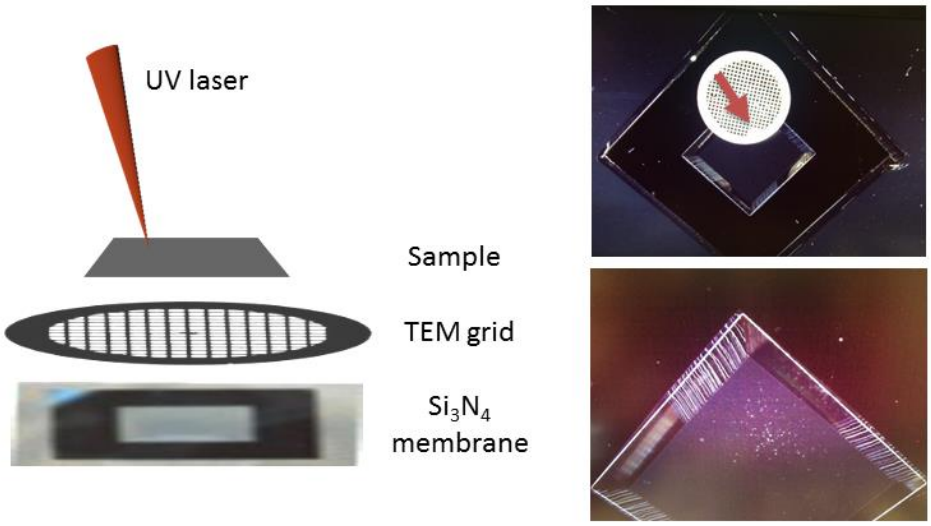

Figure 3.2. Scheme of the UV laser cutting process (left) and photographs (right) of the setup prior and after cutting where the sample section is indicated by the red arrow.

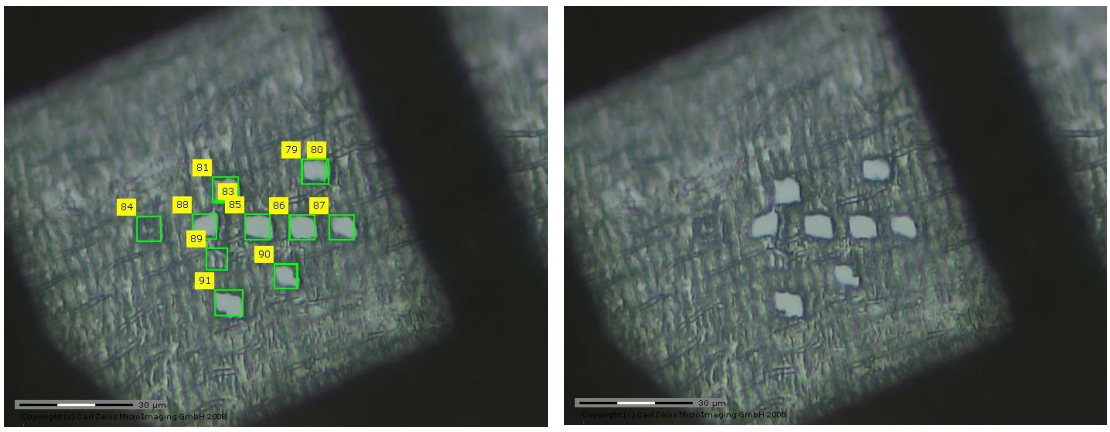

Figure 3.3. UV laser microdissection system in-line microscope view on the cutting process: left) programmed and right) resulting cuts.

The third group of dentin samples was prepared by grinding. The grinded powder was mixed with water filtered with 0.2 µm mesh solid filters and one drop of the final solution was deposited on the Si_3N_4 membrane.

The choice of the Si_3N_4 membrane is important for CXDI. First of all, the thinner the membrane is the larger angular range for tomography is accessible (50 nm is optimal). Secondly, in the case of UV laser cutting, the membrane window size (the distance between the opposite borders) should be 3 cm or smaller in order to position the TEM grid.

3.1.3. Acquisition and reconstruction features

Human dentin and bovine bone samples were investigated by CXDI at ID10 beamline, ESRF [173]. The samples were imaged using the online microscope of ID10 and selected based on the speckle size, separation and diffraction pattern extension criteria which define data quality and are important for the success of reconstruction.

The speckle pattern is generated by the interference between the diffracted beams from different inhomogeneities in the sample. When the sample is fully illuminated by the beam, the speckle size is inversely proportional to the sample size. The extension of the speckle pattern (q_{max}) on the detector is proportional to the flux and sample scattering power and inversely proportional to the inhomogeneities size. As for the last factor, the speckle separation, it comes from the experimental setup (the detector area and pixel size and sample to detector distance).

Fig. 3.4 illustrates how the visualization of a test pattern can guide the choice of sample size and experimental setup parameters. Fig. 3.4a provides optimal conditions, because the speckle size is large enough to be sampled correctly (with at least 3 pixels) and they appear up to the border of the detector (high *q*). Fig. 3.4b and Fig. 3.5c represent a poor choice: b) the speckle size is large but they do not extend to high *q*, c) speckles appear in all the detector area but they are too small and not sufficiently separated from each other to ensure the success of the reconstruction.

The diffraction patterns of isolated samples were recorded in the far-field region with highly coherent synchrotron beam of *7* keV and *8* keV for dentin and bone, respectively. The samples were rotated to ±*70*° with the *0.25*° step size and *25* ms exposure time, and background scattering was recorded at each rotational step. The rotational range was chosen to be maximal in order to better sample the reciprocal space, excluding the angles where the membrane border

or neighboring sample gave additional scattering [142]. No sign of radiation damage was observed with this energy and exposure time.

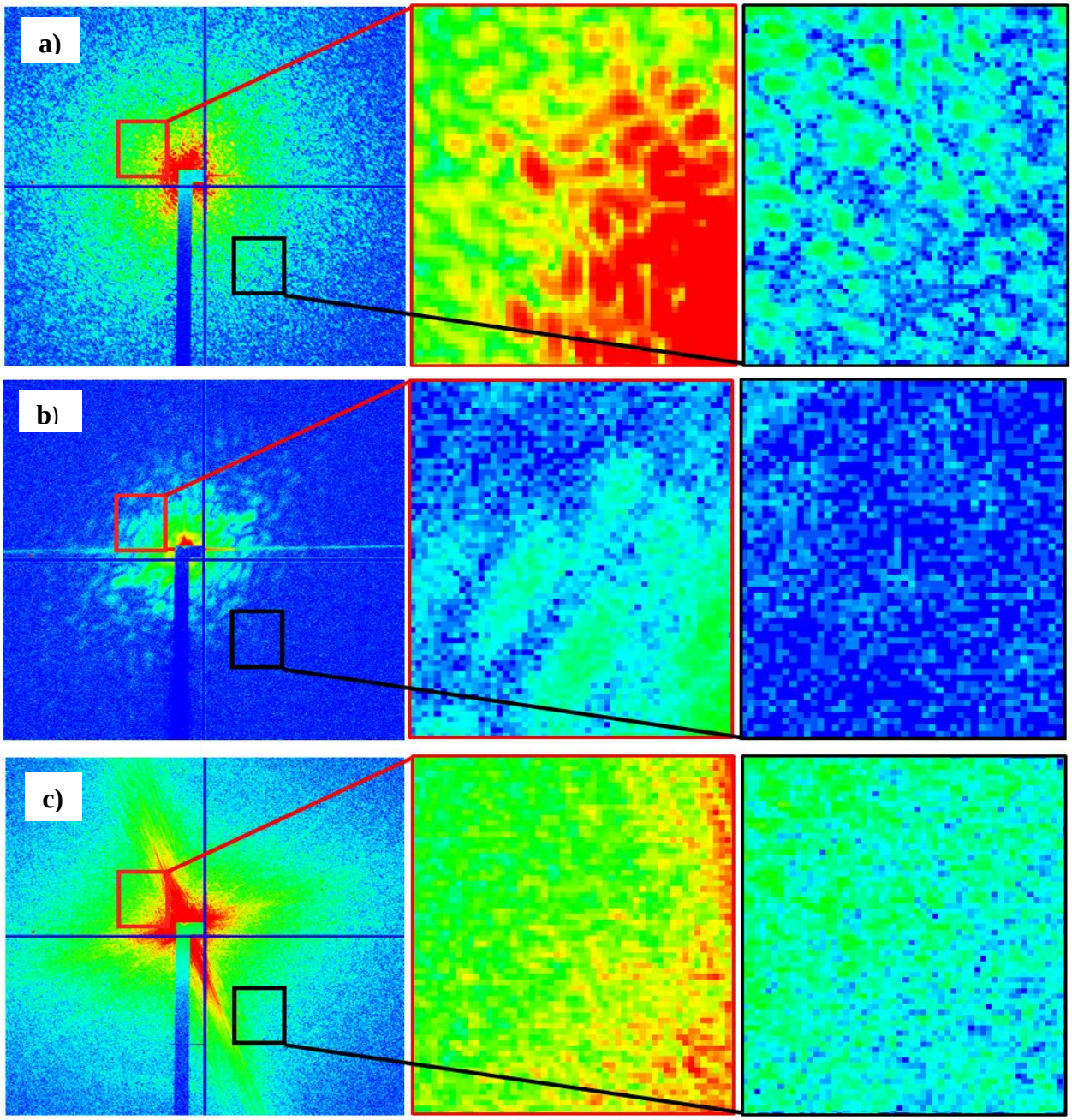

Figure 3.4. Choice of sample size and experimental conditions: a) good choice - separated speckles, in majority bigger in size than 3 pixels; b) and c) bad choice - small *q*-range and small speckles, respectively.

Different sample orientations give rise to characteristic diffraction patterns that contain principal structural information of sample ultrastructure such as border fringes, classical bone-

like tissue diffraction and weak collagen ring (Fig. 3.5, top). Rotation to ±*70*° is sufficient to sample reciprocal space and to assemble 3D reciprocal space volume (Fig. 3.5, bottom-left) [142].

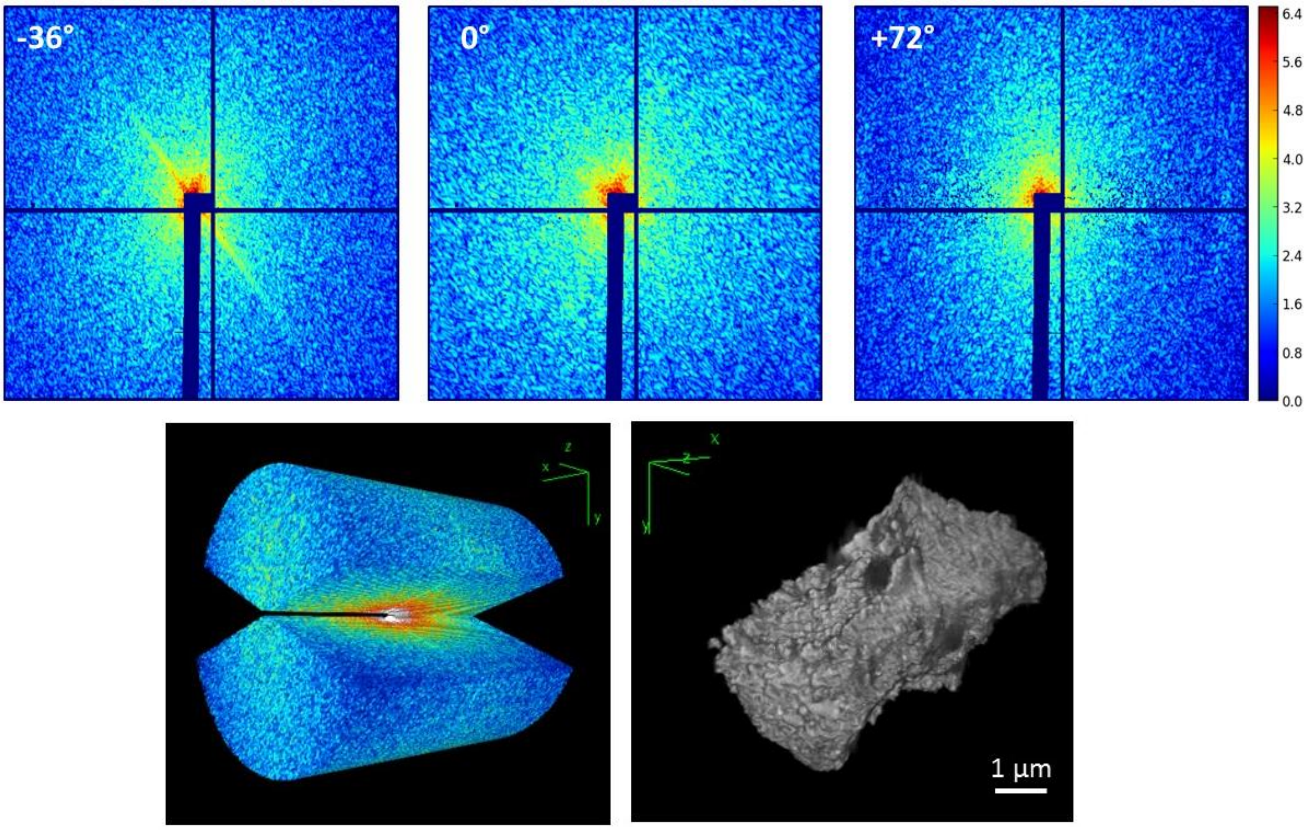

Figure 3.5. Reciprocal vs real space of dentin. Top: Speckle patterns from dentin sample rotated to -36°, 0° and +72° showing characteristic patterns (border, homogeneous speckles distribution, collagen ring). Bottom-left: 3D reciprocal space volume. Bottom-right: 3D real space reconstructed object volume. Scale bar 1 µm.

Speckle patterns of nine different angular positions are presented in Fig. 3.6, showing the reciprocal space information evolution during the data acquisition.

Collected diffraction patterns require several experimental corrections, background subtraction, beamstop and detector dead pixels masking. The final 3D reciprocal space volume is obtained by assembling the individual patterns using centro-symmetry and natural neighbor interpolation (Fig. 3.5, bottom-left). The 3D reconstructions were done using the code available at ID10 (Y. Chushkin) based on an iterative phase retrieval algorithm described in detail in Chapter 2. The resulting voxel size of the reconstructions is 28 nm for dentin and 31 nm for bone.

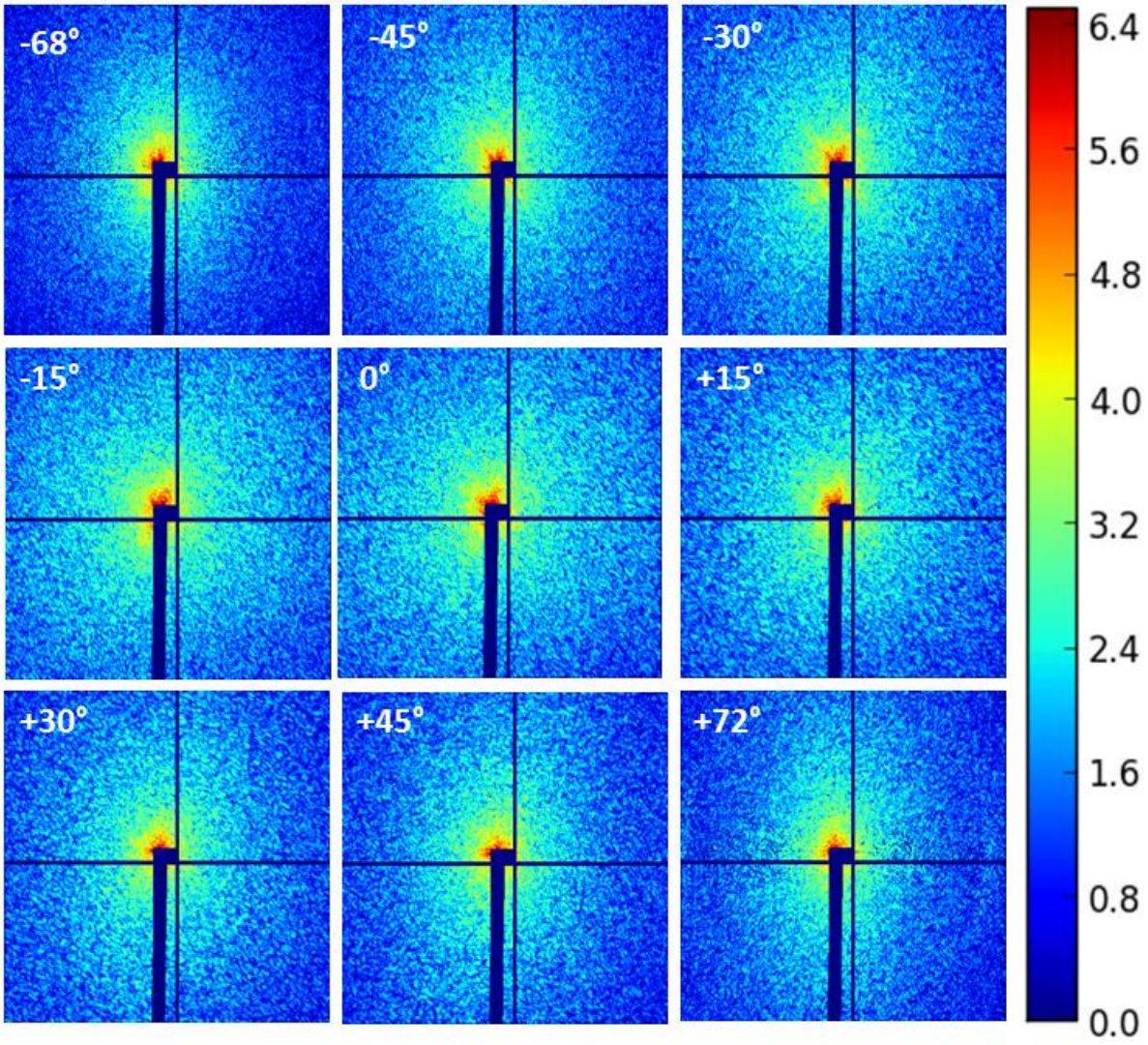

Figure 3.6. Evolution of reciprocal space information during data acquisition (crystal rotation from -68° to +70°).

For each sample, 80 successful individual reconstructions are obtained with 1000 iterations each and 30 best (in terms of error metrics) are aligned and averaged with sub-pixel interpolation of 1:2 [142]. Therefore the final image voxel size is 14 nm and 15.5 nm for dentin and bone, respectively. It is important to mention that if the sample of correct size was chosen (smaller than 5 x 5 x 5 μm^3) for the described experimental conditions and it has a heterogeneous internal structure (not amorphous and with electron density contrast from the constituent elements) the reconstructions end with the same solution in 90 % of cases or more independent from the starting conditions (in case that reasonable sample related constraint is

chosen). The reason why the error metrics selection was applied to average 30 reconstructions is purely for visualization purpose and it was not used for further nanoporosity analysis.

3.1.4. Bone and dentin by CXDI

At first, the decision had to be made concerning the optimal sample preparation method for future experiments. The main criterion was the success of the reconstruction as well as the damage that a particular technique induces to the sample. In Fig. 3.7, the result of a reconstruction and the characteristic speckle pattern at 0 ° is shown.

FIB prepared samples have very regular shape of 4.5 x 4.5 x 5 μm^3 that allows the histological orientation within the tissue. The central hole of 1 x 2 μm^2 corresponds to the dental tubule as shown with SEM in Fig. 3.1d. A thin layer of matter of about 120 nm surrounds the sample. It is believed to be attributed to Si re-deposition that came from the Si wafer used as a substrate for FIB cutting. The reconstructed images have rich internal structure but many artefacts are also visible.

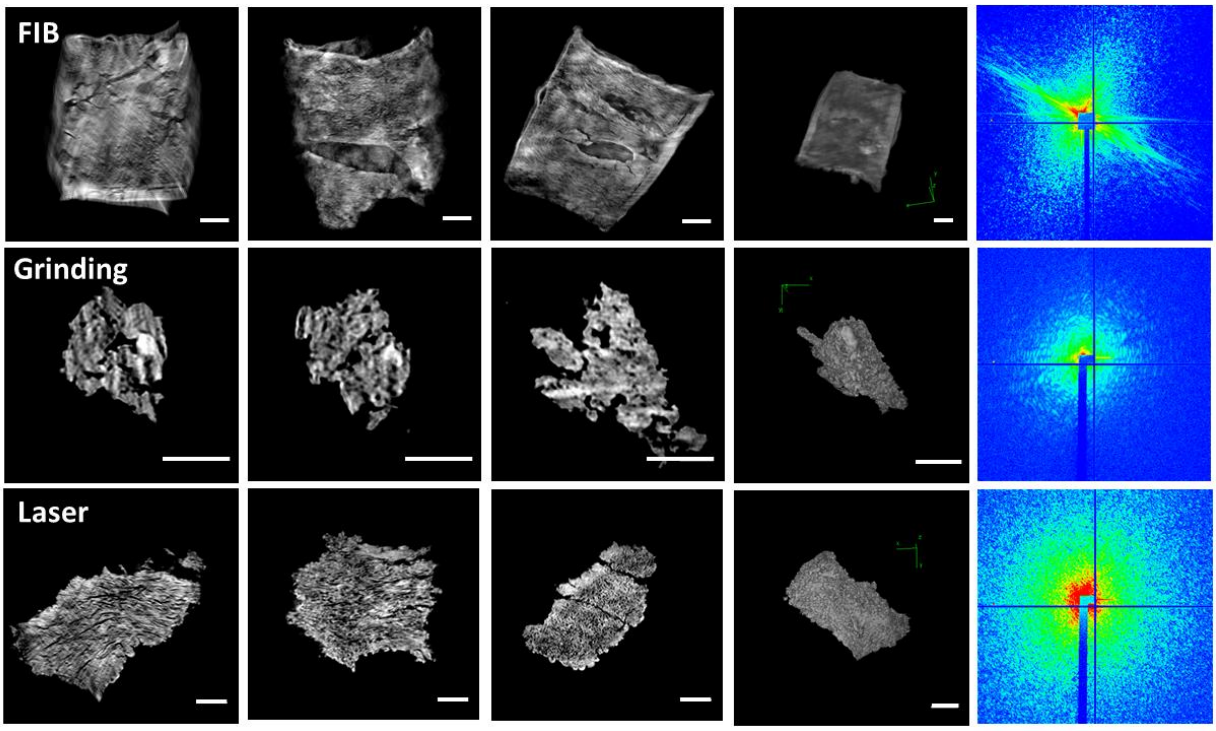

Figure 3.7. Human dentin samples prepared by FIB, grinding and UV microdissection. From left to right: the three orthogonal cuts of reconstructions, 3D volume rendering and characteristic scattering pattern. Scale bar: 1 µm.

The sample obtained by grinding exhibited well separated speckles that allowed a detailed reconstruction. However, in general, grinded samples had a broad size distribution, they were highly damaged and no information about prior histological positions within the tissue could be derived.

The UV laser allowed preparation of well-shaped ~5 x 5 x 5 μm^3 sample that provided a rich scattering pattern. The reconstruction was successful for all samples prepared by this method that allows the internal dentin structure preservation. Therefore, UV microdissection is advised as a well-suited technique to prepare sensitive specimens for CXDI, such as biological materials. Our future analysis will concentrate on dentin and bone samples cut by UV laser.

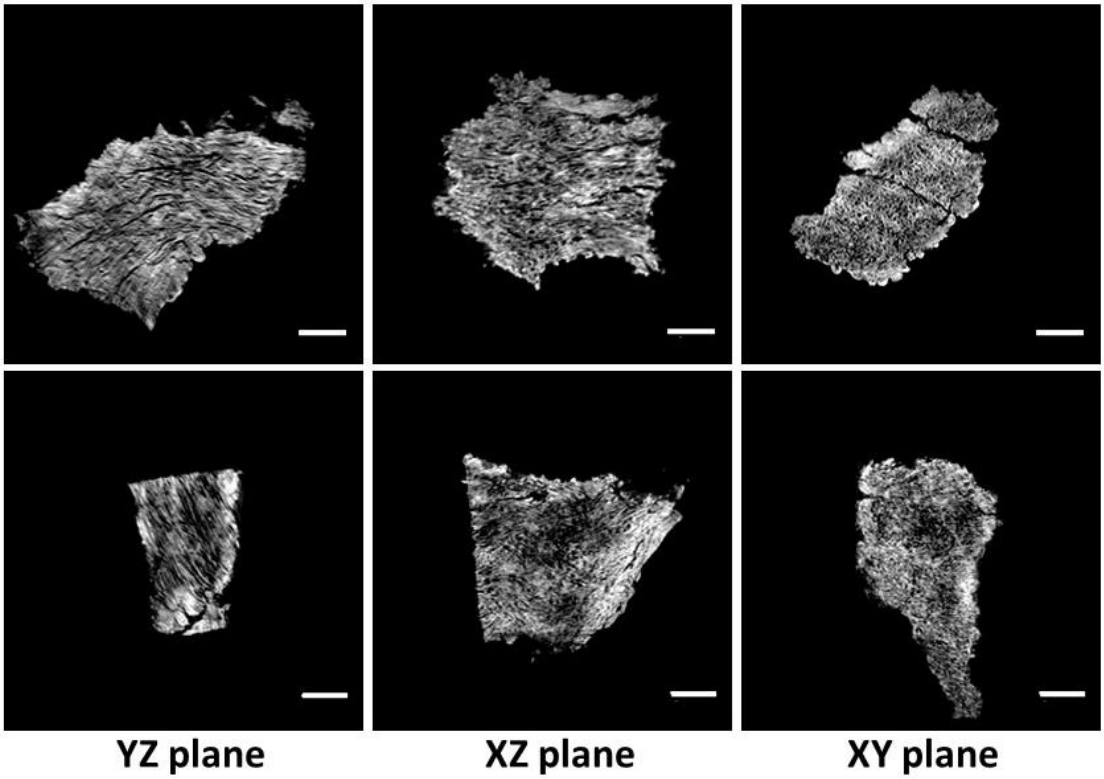

Figure 3.8. Three orthogonal cuts of dentin (top) and bone (bottom) reconstructions. Scale bar: 1 µm.

Orthogonal cuts of samples reconstructions of human dentin and bovine bone are shown in Fig. 3.8. The nanoscale porosity is observed in both cases. On yz-plane, the nanoscale porosity is shown in longitudinal direction and, on xy-plane, – transversally.

The nanoscale porosity appears to be strongly oriented and highly interconnected. To analyze the nanoscale porosity in 3D, real space volumes were resliced in orthogonal and non-

orthogonal directions and shown in longitudinal and transverse planes (Fig. 3.9). 20 longitudinal and transverse intensity line profiles of nanoscale porosity show average values of 50 nm. Another, more automatic way to extract porosity diameter was used to obtain the histogram of diameter distribution [174] that confirms our 50 nm average size (Fig. 3.10).

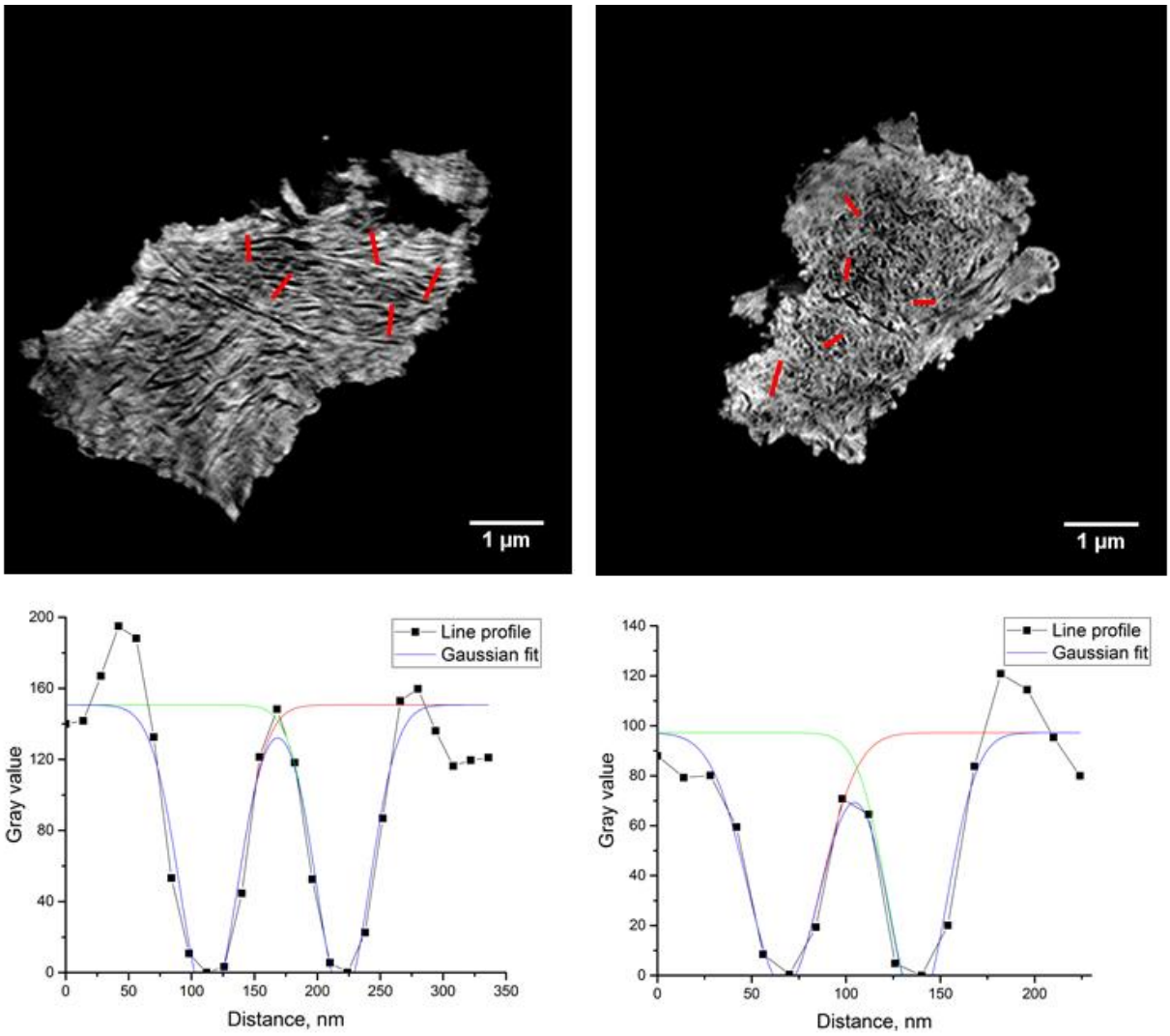

Figure 3.9. Nanoscale porosity in dentin. Left: longitudinal slice with one of its characteristic profile. Right: transversal slice with the one of the corresponding profile. Line intensity profiles were measured along red lines drawn in top figures. Scale bar: 1 µm.

For 3D visualization purpose, the nanoscale 3D porosity was segmented by combining adaptive and interactive thresholding and visualized by Avizo software package (Fig. 3.11a,b).

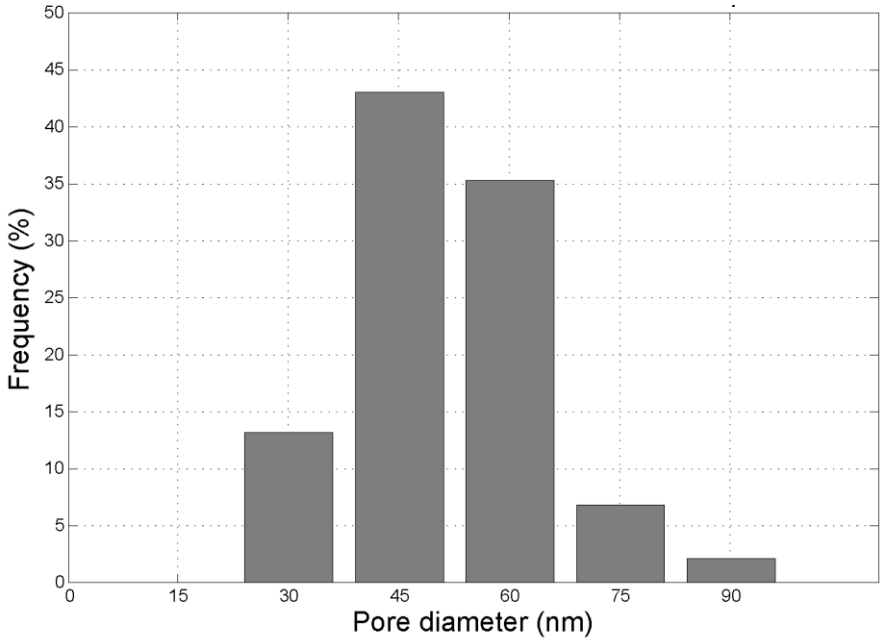

Figure 3.10. Porosity diameter distribution in human dentin sample.

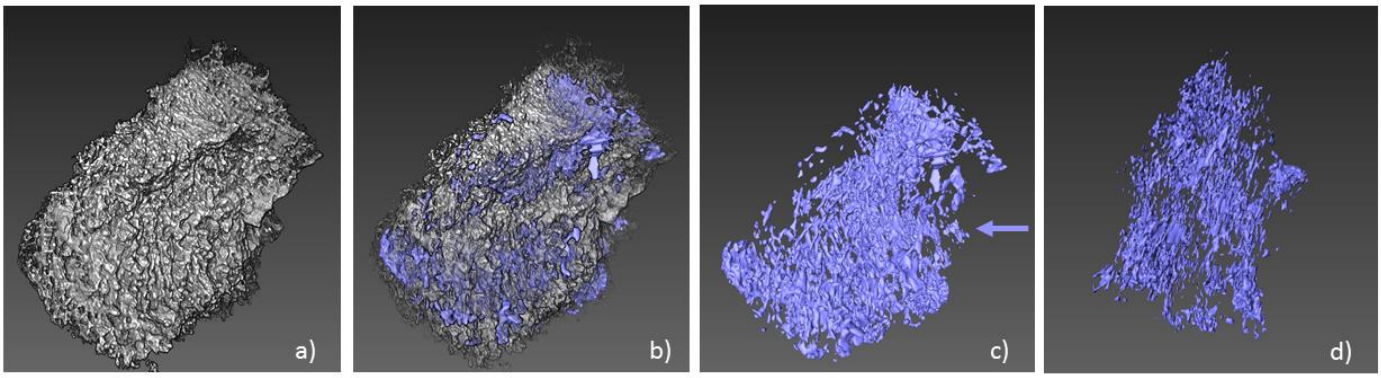

Figure 3.11. Nanoporosity segmentation and visualization: a) volume rendering of dentin reconstruction; b) nanoporosity segmentation; c) nanoporosity network; d) view, shown with the arrow in c, representing longitudinal orientation of nanoporosity.

3.1.5. Collagen repetition by CXDI

Unexpectedly, the spatial resolution achieved by CXDI allowed not only to see the internal structure of bone/dentin but also to visualize the collagen repetition at the single fibril level.

By looking at diffraction patterns at -65-70 angles (Fig. 3.12a), one can mention the appearance of a relatively weak ring that corresponds to the 1st order collagen peak (Fig. 3.12b). Part of the diffraction pattern was radially integrated within the cake drawn in Fig. 3.12a and

the integration profile was fitted with a Gaussian function that showed the periodicity of 64.7 nm (Fig. 3.12c). After re-slicing of the obtained reconstructed object using a plane of 70 ° rotation, we could also see the collagen repetition in reconstructed images (following red arrows in Fig. 3.12c). On the basis of 20 line profiles of dotty-like collagen banding patterns, the average periodicity value of 67.1 nm was found (Fig. 3.12b,d) for both bone and dentin samples that is in agreement with [46].

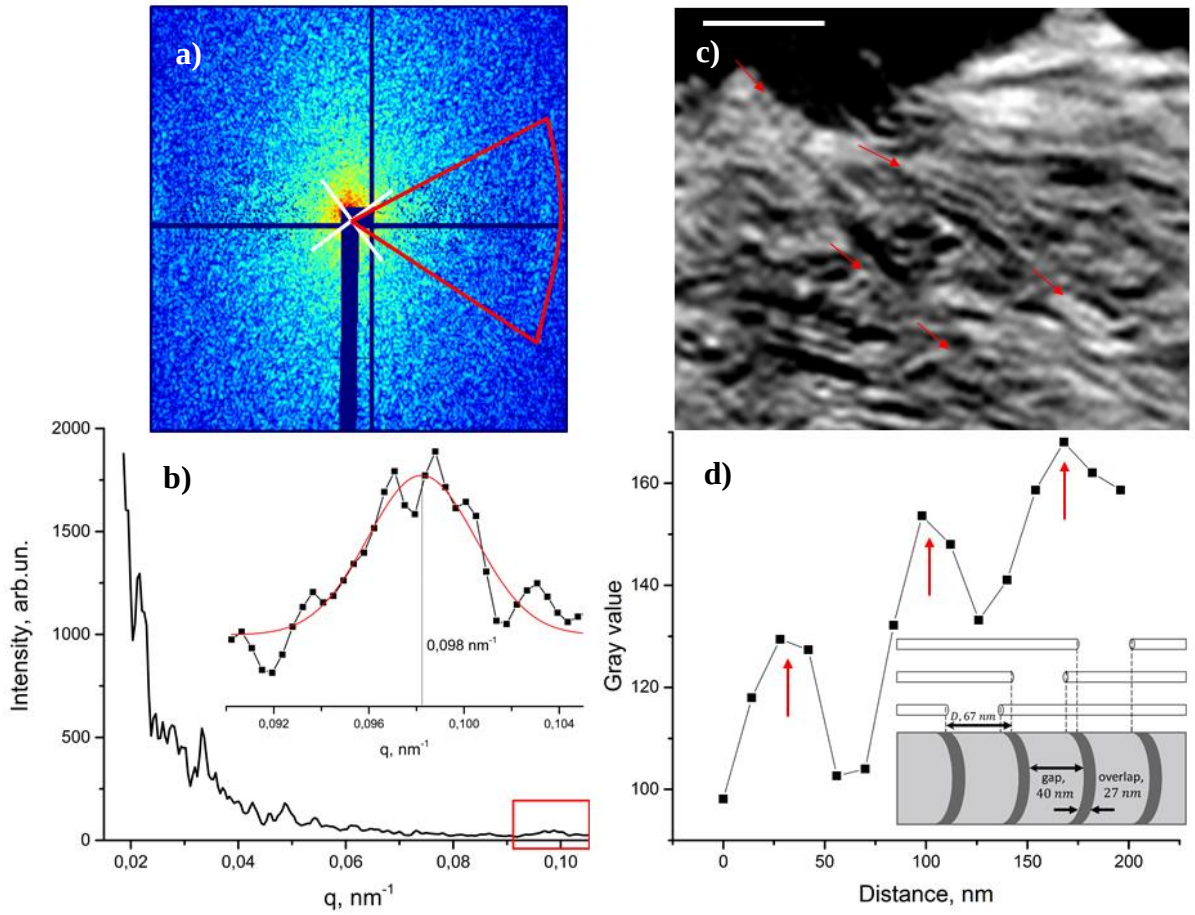

Figure 3.12. Collagen banding pattern: a) diffraction at +71° with radial integration cake for 1st order collagen ring shown in red, b) integrated profile showing a weak peak at 64.7 nm, c) slice of reconstructed volume with collagen repetition shown as light spots following the red arrows directions, scale bar 500 nm, d) intensity profile along one of the arrows from (c) showing mean repetition of 67.1 nm with principal scheme of collagen gap-overlap zones arrangement.

3.1.6. CXDI of heated bone

The last attempt was dedicated to the heated cortical bovine bone model evaluation with CXDI. It would allow primary higher scale examination of heated samples micro- and

ultrasructure prior to individual nanocrystal and crystallographic phase study with ACOM-TEM and PDF analysis.

The samples were prepared as described in sub-chapter 2.1.3 at the same time as the one used for PDF analysis (see sub-chapter 3.3.2) followed by UV laser microdissection.

The final reconstructions of 600 °C, 800 °C heated and control bovine bone samples are show in Fig. 3.13. The control sample looks very similar to the one show in Fig. 3.8: rich internal nanoporosity structure with strong preferential orientation. The 600 °C heated sample loses its continuity while 800 °C sample appears as number of fused regular clusters with homogeneously distributed porosity. This is in a good agreement with ACOM-TEM results as will be show in the following.

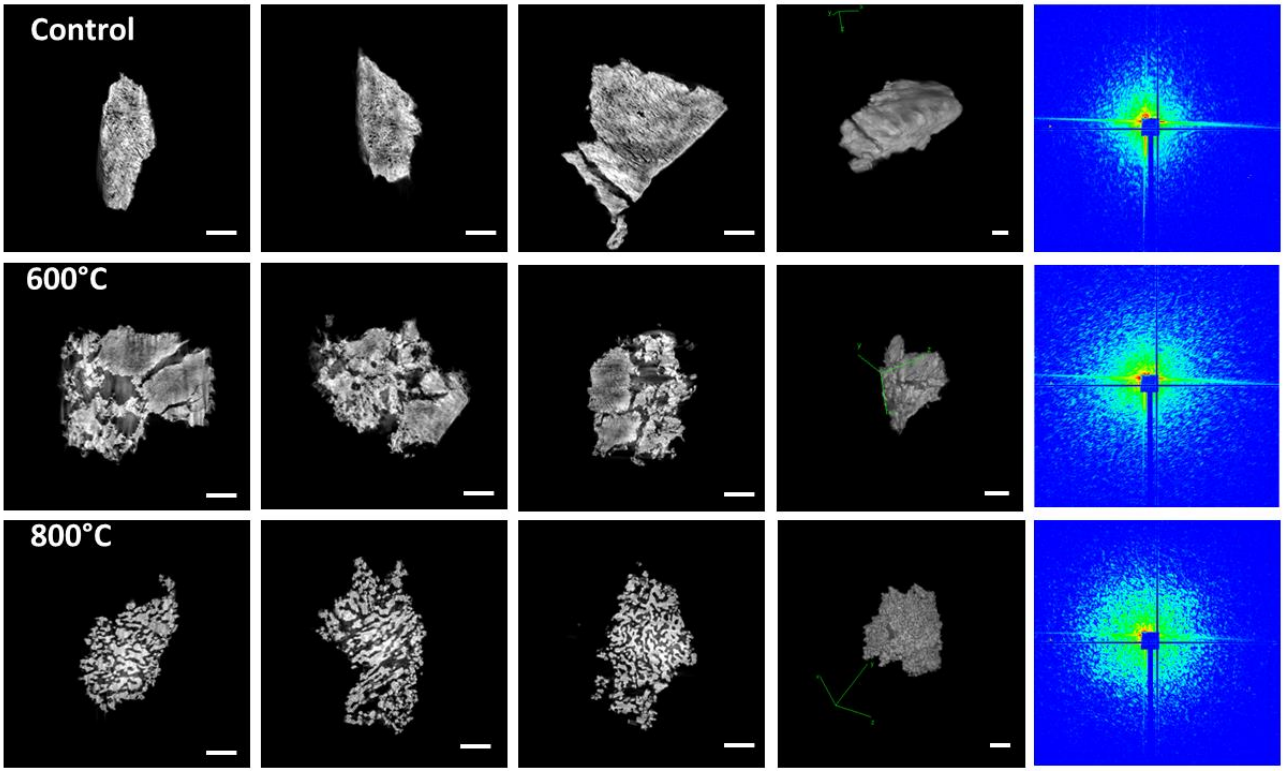

Figure 3.13. Cortical bovine bone samples heated to 600 °C, 800 °C and in reference state prepared by UV laser microdissection. From left to right: the three orthogonal cuts of reconstructions, 3D volume rendering and its characteristic scattering pattern. Scale bar: 1 µm.

3.2. ACOM-TEM of heated cortical bovine bone

3.2.1. Motivation

A general problem of imaging is that the increase in spatial resolution generally leads to a reduction of the field of view. This is a typical problem for TEM studies of bone structure. However, mapping the specimen with a 2 nm electron beam size with diffraction contrast allows investigating the orientation, organization and the structure of individual crystallites of apatite. Moreover, the mineral nanocrystalline phase and possible ionic substitutions can be accessed.

The main difficulty stands in the necessity of analyzing both the nanocrystals morphology and organization as well as crystal structure, which, generally, requires using a combination of methods. Electron microscopy is the most widely used technique to visualize the nanocrystals in real space, while X-ray diffraction is generally used to analyze the crystal structure in reciprocal space, thus giving information on the crystal structure as well as on the crystal-chemistry disorder. The ideal method, therefore, should provide both insights. Automated Crystal Orientation Mapping with TEM (ACOM-TEM, also known as ASTAR^{TM} tool from NanoMEGAS) [155] allows such complex study as described in sub-chapter 2.2.3.

However, a difficulty was encountered in analyzing bone samples in the native state with ACOM-TEM. The available beam size at the FEG-TEM (JEOL 2100F) is limited to 2 nm and the smallest dimension of the mineral nanocrystals may range between 3-5 nm. Therefore, we were at the limit of the spatial resolution required to resolve the individual nanocrystals.

For this reason, a set of heat treated bone samples was prepared and analyzed. The mean crystal size is expected to increase dramatically upon heating; therefore, enabling to test the instrumentation limit. In other words, this should allow answering the question: to what extent in crystal size one can apply the ACOM-TEM on bone to study individual nanocrystals?

Moreover, the study of the effect of heating on bone is a question of particular interest since the presence of phase-transition beyond heating and the co-existence of different phases at high temperature is a subject of many debates (as shown in Chapter 1). The amount of ionic substitutions was also reported to change. However, the first and most important motivation in the study of heated bone comes from archeology, paleo-anthropology and forensic science. Archaeological bone remains contain a considerable amount of information, which can be altered by heating (e.g. radiocarbon dating). Traces of heating are often observed on bone fragments, but it becomes quite difficult to distinguish its effect, particularly at temperatures

below 600 °C. Below this temperature, macroscopic structural parameters become inadequate to characterize the effect of heating and the nanoscale resolution needs to be achieved [175].

The ACOM-TEM, therefore, provides detailed information about orientation, size, phase and structure that is obtained on the individual crystallites.

3.2.2. Sample preparation peculiarities

The requirements in sample thickness for studying bone tissue with ACOM-TEM are strongly dependent on mineral crystal sizes. Since ACOM-TEM is based on recording diffraction patterns in scanning mode and its subsequent fitting with the structure template that allows finding only one best orientation (see sub-chapter 2.2.3), one has to avoid having crystal superposition in illuminated volume. In other words, since bone mineral nanocrystals in a reference state are about 3 x 25 x 50 nm^3 in size we had to prepare ultramicrotomy sections of 50 nm in thickness or less. Even in this case, we often had crystal superposition, depending on crystal orientation, in native bone tissue.

In order to test the limits of the method applied to bone and its sensitivity, we investigated the heat treated bone sample set. Heated bone is known to be a good model for crystal size and orientation evolution study since mineral nanocrystals grow significantly upon heating after 600 °C as discussed in Chapter 1.

Therefore, fixed and dehydrated bovine cortical blocks of ~2 x2 x10 mm^3 volume (see Fig. 3.14) were first prepared. Samples were heat treated to nine temperatures (100, 150, 200, 300, 400, 600, 700, 800, 1000 °C) for 10 min in vacuum and cooled in air.

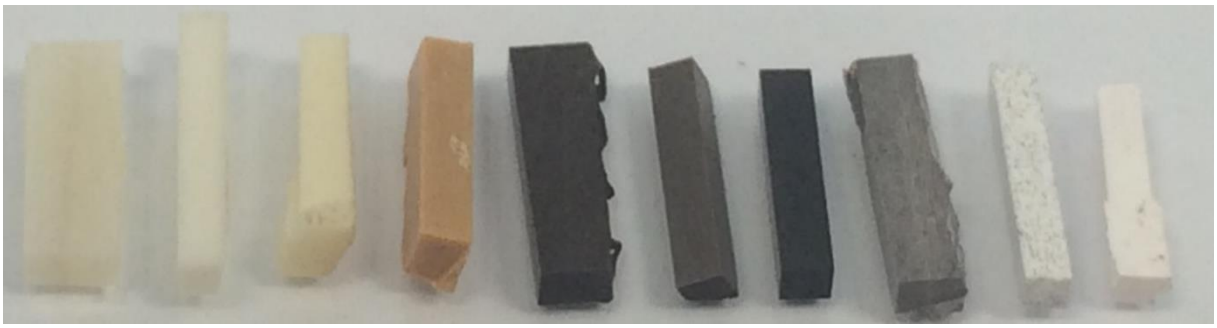

Figure 3.14. Heat treated bovine cortical bone samples for ACOM-TEM. From right to left: control, 100, 150, 200, 300, 400, 600, 700, 800, 1000 °C.

After cooling, the samples were embedded in PMMA, trimmed and cut with an ultramicrotome to 50 nm in thickness in the transverse direction and positioned onto TEM grids (see Chapter 2). The 200 mesh Cu grids with lacey carbon stabilized by formvar were chosen. The formvar layer was removed and grids were plasma-cleaned prior to use. The carbon layer is important for studying bone tissue because it prevents sample charging and therefore movement under the electron beam. Nevertheless, a continuous carbon layer would drastically decreases the contrast. This is why lacey carbon was the best choice since it has a thin spider net-like structure with large holes in which the measurements could be done, thus minimizing the overall charge effect.

3.2.3. Mineral nanocrystals orientation

The general acquisition and data treatment scheme we followed is shown in Fig. 2.24 (Chapter 2). The heat treated bone sample set was scanned with ACOM-TEM with a beam size of 2 nm and a field of view of 400 x 400 nm^2, 10 ms acquisition time and 2 nm step size. A camera length of 30 cm was chosen, except for the 800 and 1000°C heat-treated samples, for which camera length was 40 cm and electron precession was used with a precession angle of 1.2° and a precession frequency of 100 Hz.

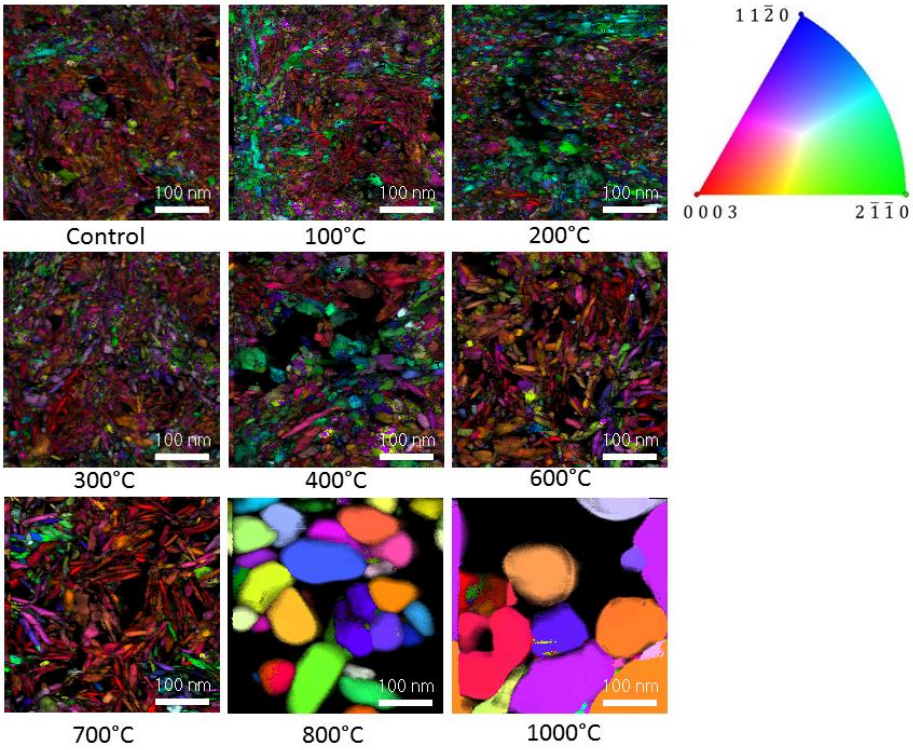

Figure 3.15. ACOM-TEM orientation maps of heated bone (control-1000 °C) mineral crystals.

From the various experimentally determined structures of hydroxyapatite available in the literature, the structure refined by X-ray diffraction from J.M. Hughes [64] was chosen as the construction template due to its reliable composition, stoichiometry and absence of substitutions. The orientation maps were combined with index maps in order to get rid of noise, resin and unreliable points (Fig. 3.15). It is important to notice that one should compare sizes of crystals that have the same color-code due to platelet-shape crystals geometry. For example, crystals that are displayed in red are oriented close to the zone axis, in other words, with *c* axis perpendicular to scanning plane. Moreover, the crystals that are oriented in this manner have their longest axis perpendicular to the section surface. The overlap of several crystals in this configuration is, therefore, mostly improbable. The crystals displayed in green and blue have 60 ° missorientation from the "red" ones.

One can notice the difference between the ratio of red color vs green and blue for different temperatures. This is not a sign of structural changes with temperature but heterogeneities from one area to another within a particular sample. To confirm this hypothesis, larger field of view scans were acquired for each sample in the temperature series (Fig. 3.16) that show local color (orientation) variations on the larger scale.

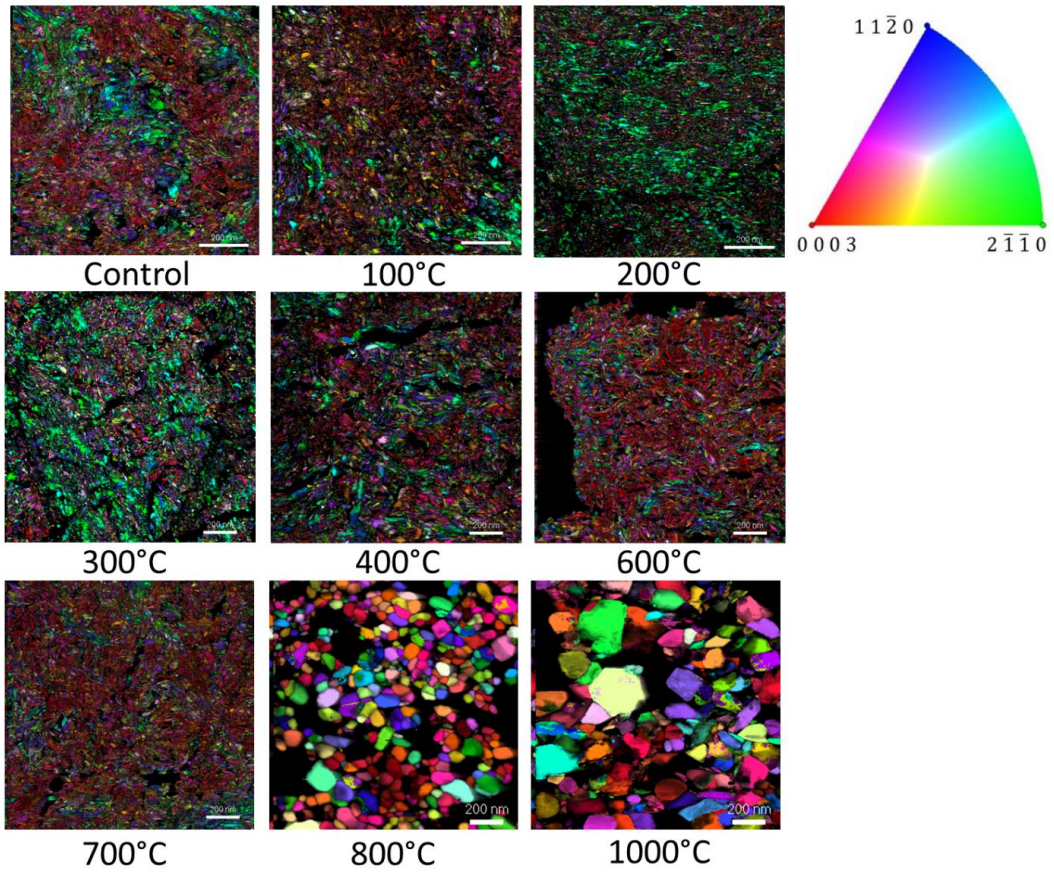

Figure 3.16. ACOM-TEM large field of view orientation maps of heated bone (control-1000 °C) mineral crystals. Scale bar: 200 nm.

The step size and, consequently, the field of view were optimized in order to avoid unnecessary sampling. The field of view for the control, 100 and 200 °C samples was 1x1 μm^2 with the step size of 2 nm. For 300-700 °C the field of view was 1.5 x 1.5 μm^2 and the step size of 2 nm. Eventually, for 800 °C and 1000 °C, the field of view was 1.5 x 1.5 μm^2 and the step size of 5 nm.

Mineral crystals orientation is very heterogeneous even on the level of 100 nm scale for temperatures lower than 800 °C and new orientations, revealed by new color-codes, appear at temperatures of 800 °C and 1000 °C, which is a usual indication of recrystallization. However, the discrimination between crystal growth and recrystallization may still be questionable. These are phase transitions of different order that are characterized by different speed and dynamics and only in-situ investigation may address this question.

3.2.4. Mineral nanocrystals size

Our data show that the crystals grow slowly at low temperatures and are subjected to rapid growth after 700 °C, where polyhedron shaped crystals are observed. In order to analyze the crystals growth in more detail, the sizes of red color-coded crystals (smallest platelet dimension) were measured with line profiling for temperatures below 800 °C. As we previously mentioned, red color-coded crystals are oriented across the section and are the most reliable for the size evaluation.

On the basis of 63 grey level intensity profiles that were measured and fit with Gaussian function, the FWHM gives the measure of the particle size (Fig. 3.17). The smallest particle size increases from 3.5-4 nm for low temperatures to 5 nm at 700 °C.

For the temperatures of 800 °C and 1000 °C, the crystal size was determined by using grain boundaries and grain size distribution calculations with the ACOM software. Grain boundaries are defined as locations where the disorientation is higher than a threshold value (Tolerance = 5 °). These data are used as an input for an additional module called “Grain size distribution”. It allows plotting the grain size distribution as a bar chart with a chosen number of bars and the interval dimension (in our case 20 bars were used). An average grain size is estimated using a spherical approximation either with respect to the total number of grains or weighted by the grains area. The last value is less sensitive to the numerous small “grains” appearing in the map and resulting from orientation misindexing (in particular, a given grain will appear fragmented in small volumes if the orientation is affected by the 180 ° ambiguity).

Ambiguity filter of 15 ° was used for data cleaning. Minimum grain size of three times higher than the pixel size is advised to be chosen, which is 15 nm^3, in our case.

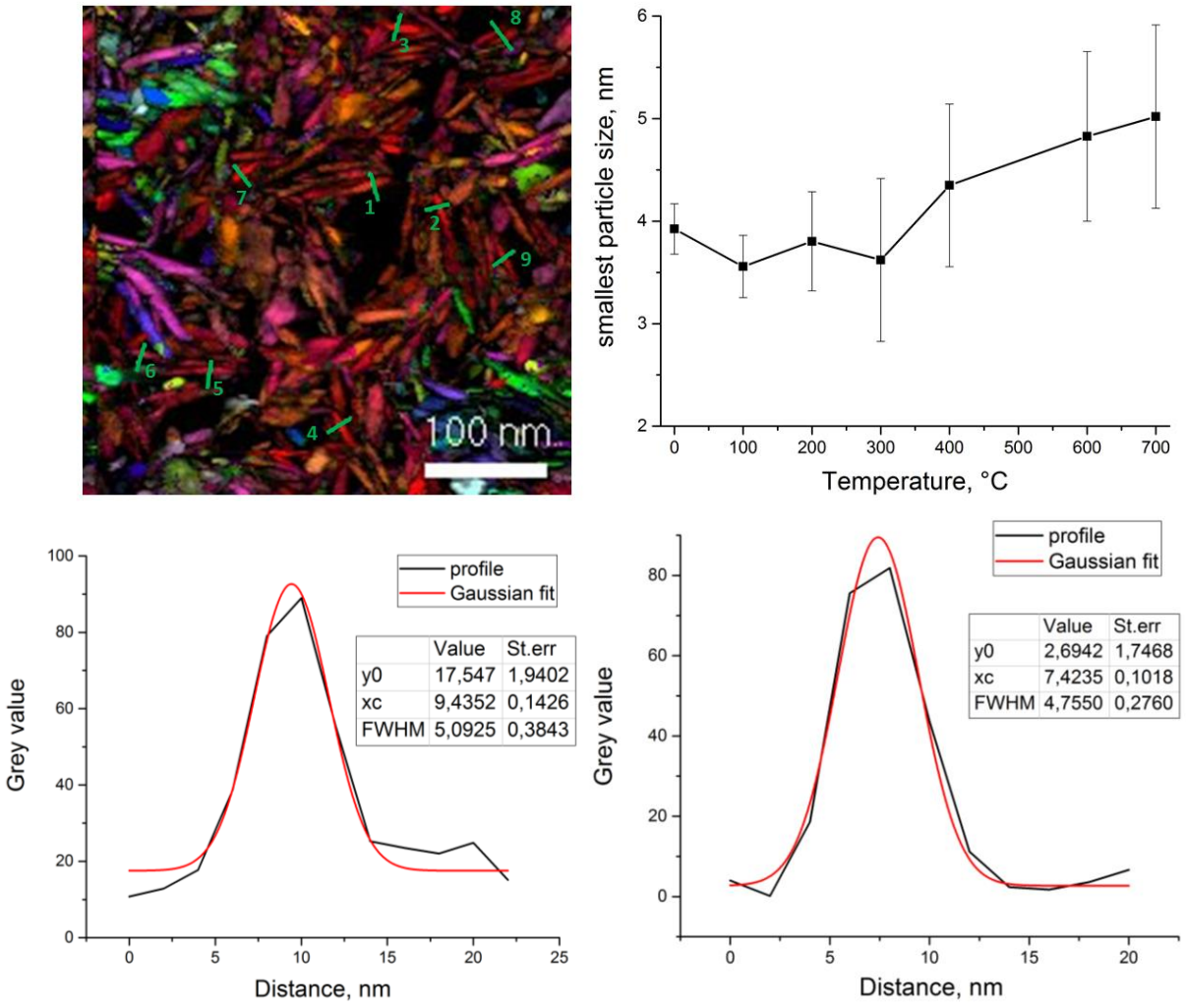

Figure 3.17. Particle size evaluation. Top: example of orientation map for the 700 °C sample with indication for line profiles and smallest particle size distribution with temperature. Bottom: examples of line profiles fit with Gaussian function.

In Fig. 3.18a,b, the orientation and index maps of the 800 °C sample is shown. Fig. 3.18c shows the result of grain boundaries calculation and Fig. 3.18d is the crystal size distribution histogram weighted by the grains area. The average crystal diameter for the 800 °C heated sample was found to be 70 nm and a maximum of 189 nm. Analysis is based on 529 crystals in the field of view.

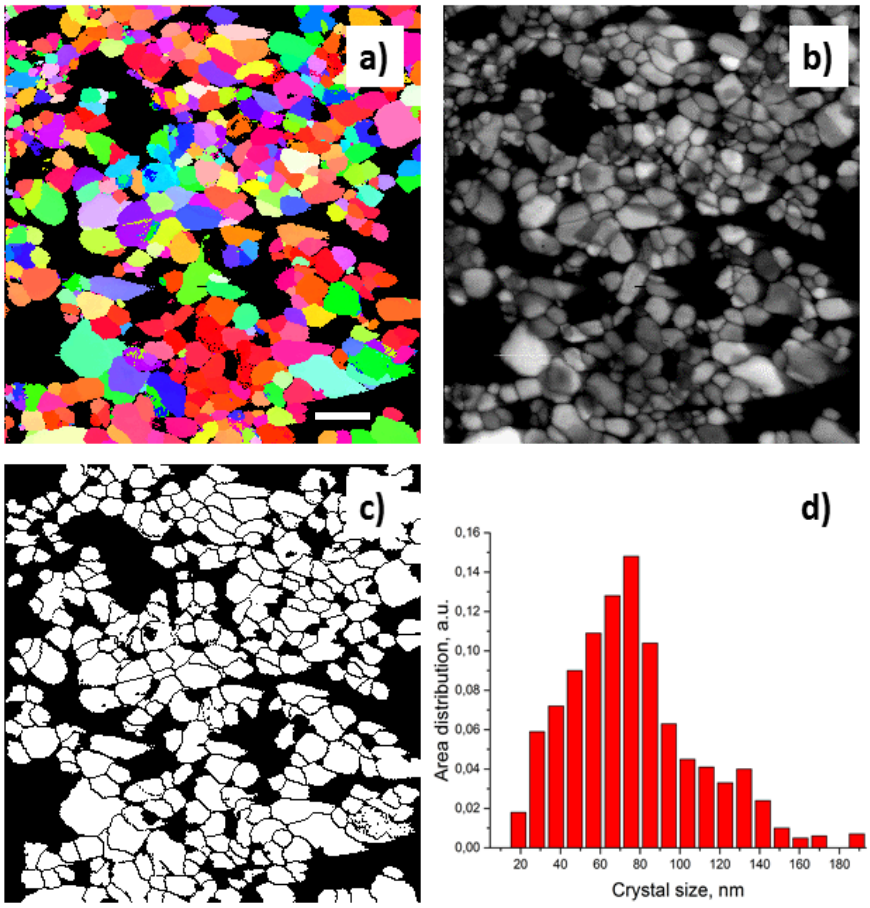

Figure 3.18. Crystal size distribution for the 800 °C sample: a) orientation map; b) index map; c) grain boundaries map; d) grain size distribution histogram. Scale bar: 200 nm.

For 1000 °C heated sample, the equivalent analysis is shown in Fig. 3.19. The average crystal diameter is 94 nm and the maximum is 312 nm. Analysis is based on 411 crystals in the field of view. Despite the fact that the average crystal size of the 1000 °C case is higher compared to 800 °C, there is much broader size distribution and higher content of small crystals. This is due to the fact that these measurements are very position dependent and cannot be used to describe the bone tissue behavior as a whole. However, it is a very straightforward and useful method for crystal size determination.

Thus, the average crystal size for the 800 °C and 1000 °C samples can be added to the chart of crystal size evolution with temperature as shown in Fig. 3.20. However, care must be taken in comparing those values, since we compare small crystal size of platelet (low temperatures) with the diameter in spherical approximation to the polyhedrons (high temperatures).

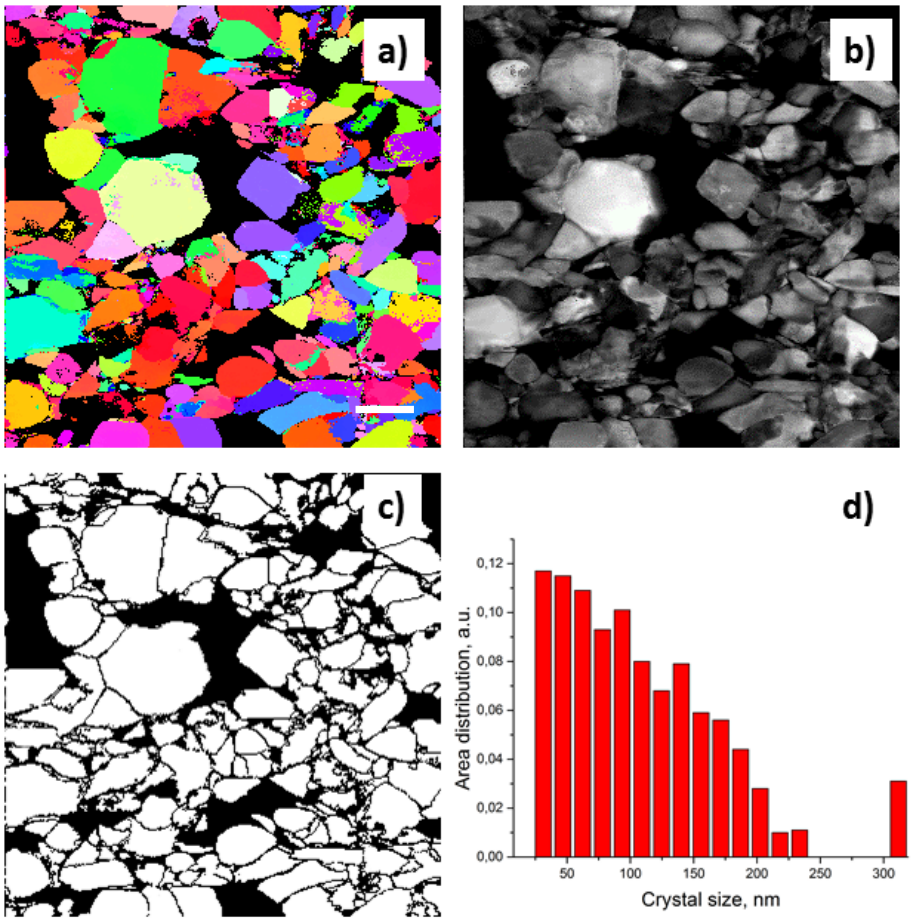

Figure 3.19. Crystal size distribution for the 1000 °C sample: a) orientation map; b) index map; c) grain boundaries map; d) grain size distribution histogram. Scale bar: 200 nm.

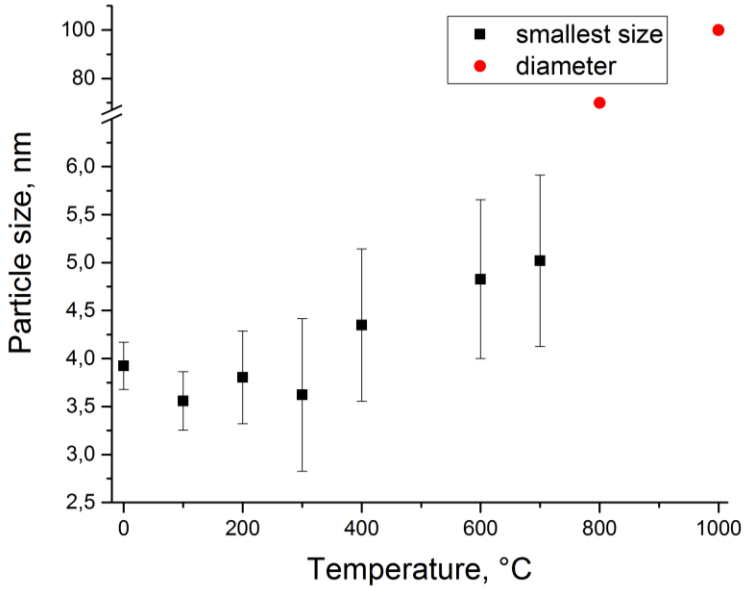

Figure 3.20. Bone mineral crystal size growth with temperature. The smallest particle size measurements for temperature range from control to 700 °C is shown in black. Crystal diameter (spherical approximation) for temperatures of 800 °C – 1000 °C represented in red.

3.2.5. Phase identification

The mineral bone content is considered to be an apatite structure often called "hydroxyapatite", even if it is known for several decades, especially from the XRD diffraction data, that the real bone mineral structure shows modifications with respect to stoichiometric hydroxyapatite crystals in crystalline chemistry as well as nanocrystal size and strain. The XRD profiles of bone show broadening of the diffraction peaks as compared to model hydroxyapatite patterns which can be explained by different reasons, including small crystal size, crystal strain, presence of substitutions and vacancies, degree of crystallinity (order/disorder), etc.

Therefore, we wanted to see whether subtle differences in crystal structure could be picked up by the ACOM-TEM method and what could we add to the heat treated bone model in terms of crystal structure and phase identification. To address these questions, we based the analysis on the scan of bone heated to 1000 °C due to its best diffraction patterns quality and high signal to noise ratio.

Natural apatite minerals. First of all, the acquired diffraction data were analyzed with structures that may have large structural differences from the hydroxyapatite standard model. Different apatite minerals existing in nature with elemental composition compatible with bone biochemistry such as brushite, monetite, tuite and whitlockite were chosen [176–179]. The structure, chemistry and symmetry of the mineral can be compared in Table 3.1.

Table 3.1. Chemical and structural data for minerals used for template matching and phase identification.

Mineral name	Chemical formula	a, Å	b, Å	c, Å	Space group
Hydroxylapatite	$Ca_5P_3O_{13}H$	9.4166		6.8745	P 63/m hexagonal
Brushite	$CaPO_6H_5$	5.7990	15.1255	6.1839	I 1 a 1 monoclinic
Monetite	$Ca_4P_4O_{16}H_4$	6.910	6.627	6.998	P -1 triclinic
Tuite	$Ca_3P_2O_8$	5.2487		18.6735	R -3 m trigonal
Whitlockite	$(Mg_{.587}Fe_{.413})Ca_{9.095}P_7O_{28}$	10.330		37.103	R 3 c trigonal

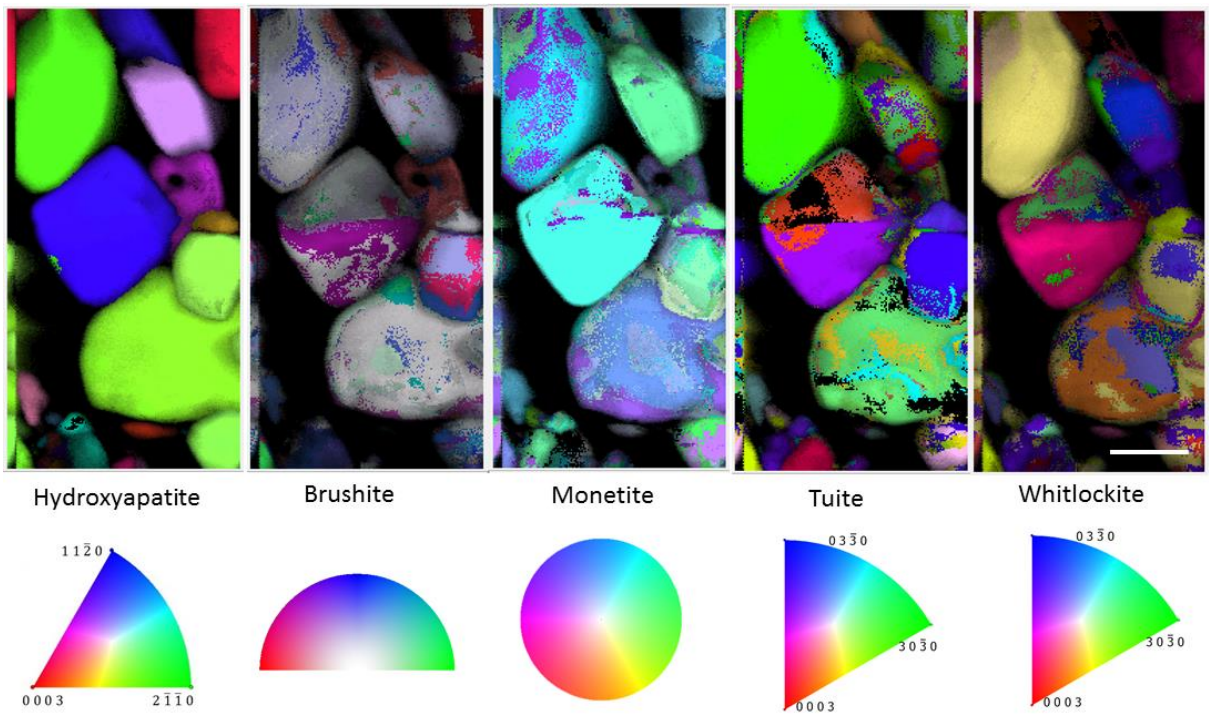

Figure 3.21. Combined orientation and index maps for data fitted with five apatite minerals whose elemental composition is compatible with bone biochemistry with corresponding inverse pole figure color maps. Scale bar: 50 nm.

The result of the fits is shown in Fig. 3.21, where orientation maps combined with index maps of five minerals are shown with corresponding inverse pole figure color maps.

The color map shape varies (triangle, circle or half circle) with the space group. It represents the minimum number of crystal orientations allowed by the symmetry (excluding equivalent ones) that corresponds to the fraction of the stereographic projection so that all possible orientations for the higher symmetry crystals can be limited to smaller number of possibilities. On the contrary, the lower symmetry crystals have larger stereographic range of possible orientations.

One way of deciding which structure fits better to the recorded diffraction set is a comparison of corresponding indexes and reliabilities, presented in Table 3.2. The higher is the maximum index and reliability value – the better the template matching was. It is clear from the table that hydroxyapatite template fits best.

Table 3.2. Minimum and maximum of index and reliability values for five apatite mineral structures for the 1000 °C heated bone sample.

Mineral	Index (min and max)	Reliability (min and max)
Hydroxylapatite	59-1092	0-45
Brushite	65-650	0-25
Monetite	43-669	0-32
Tuite	51-568	0-28
Whitlockite	33-560	0-30

The other complementary way for deciding which structure template fit is better is to look at orientation maps. Normally, a single crystal has to be fit with a uniform (or very close) orientation (color) unless dislocations or mirror planes are present. We will refer to it as single crystallinity criterion. This criterion is fulfilled for hydroxyapatite but not for other apatite minerals (Fig. 3.21).

In Fig. 3.22, the phase map using all five templates simultaneously, based on the phase reliability values (as explained in Chapter 2, fig. 2.28), is shown with its structures along the *c*-axis. Red atoms are oxygens, green - calcium, orange - phosphorous, white - hydrogen. From the phase map, one can safely conclude that the structure is better described by hydroxyapatite mineral and that ACOM-TEM can easily distinguish between different symmetry phases of close chemical composition.

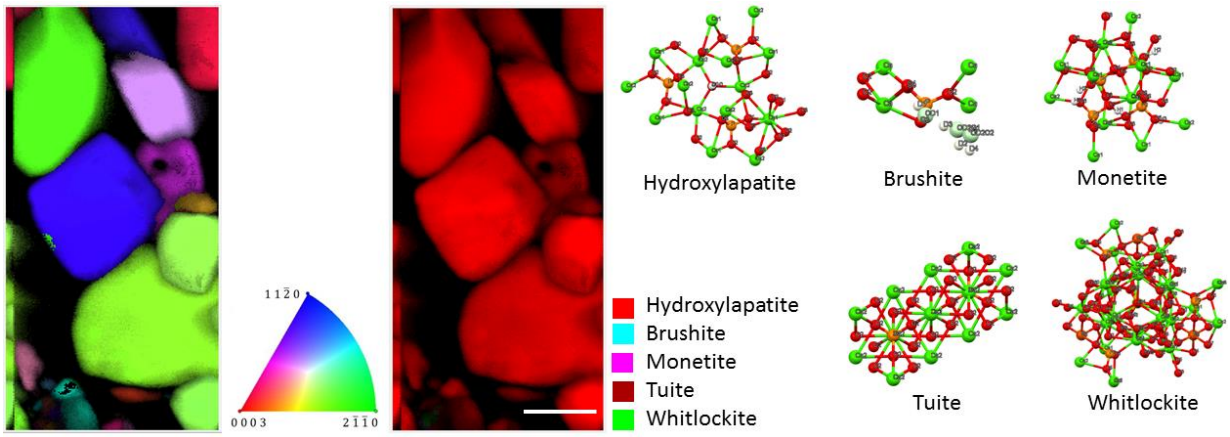

Figure 3.22. Orientation (left) and phase map (middle) of the 1000 °C sample with five apatite mineral structures (right). Scale bar: 50 nm.

Monoclinic vs hexagonal. Another debate in the literature is wherever at high temperature, a hexagonal to monoclinic phase transition takes place [71]. This issue was tested by a hexagonal [64] and a monoclinic [65] hydroxyapatite templates matching (Fig. 3.23). It was shown that the high temperature phase has a hexagonal structure. This excludes the possibility of hexagonal to monoclinic phase transition upon heating.

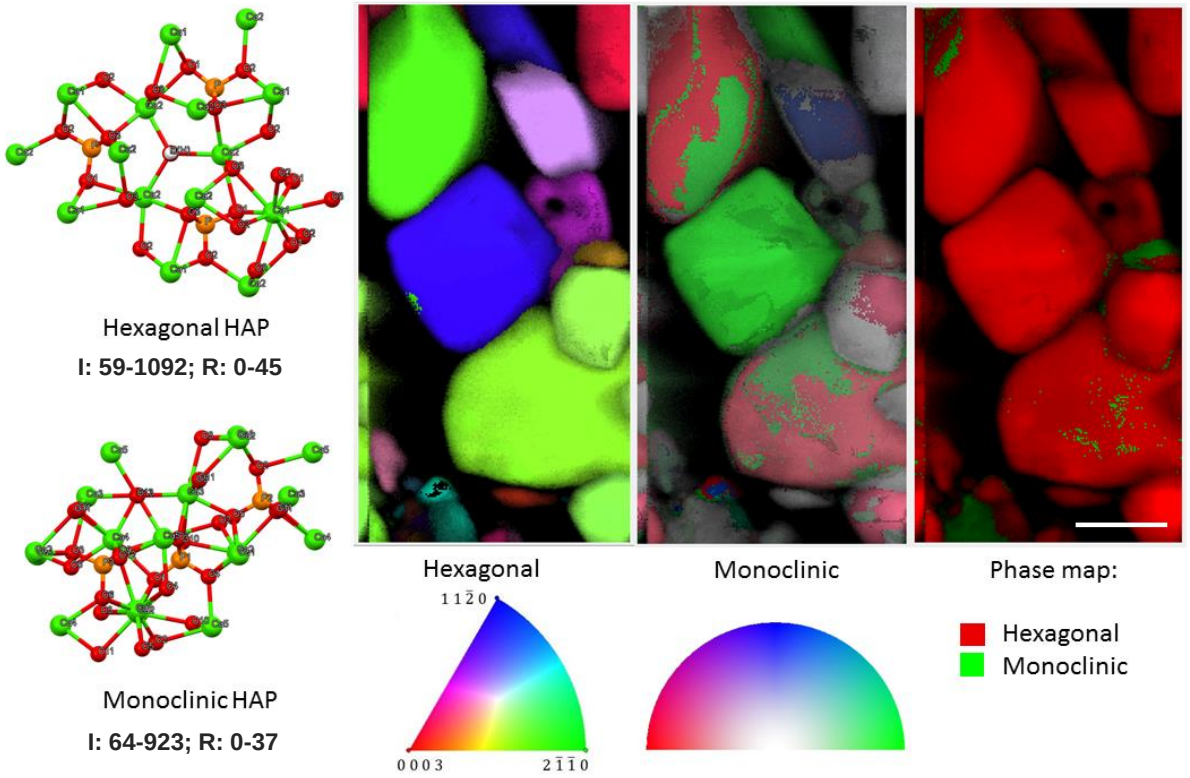

Figure 3.23. Crystal structure of hexagonal and monoclinic hydroxyapatite (along *c*-axis), corresponding orientation maps for the 1000 °C sample with color code and the phase map showing mainly presence of hexagonal phase. Index (I) and Reliability (R) values will be noted for each structure for all following images in this section. Scale bar: 50 nm.

CaO formation. Some authors had shown the formation of CaO [97] appearing while bone heating from 800 °C coexisting with hydroxyapatite. According to reconstructed phase map (Fig. 3.24), the CaO phase was not detected, at least in the scanning field of view. The matching of CaO shows grains with not uniform color and lower values of index and reliability in comparison to hydroxyapatite. Moreover, matching with two phases only shows the presence of hydroxyapatite (Fig. 3.24, right).

This can be explained by the fact that CaO formation is stated for heat treatment in air. In vacuum, oxides formation rate is usually much lower.

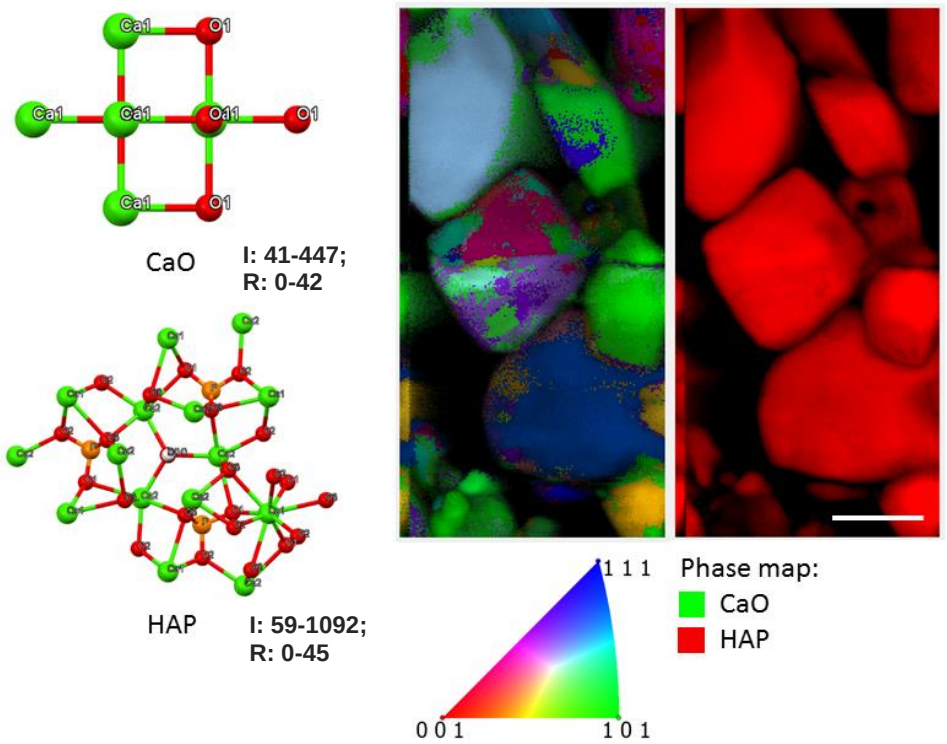

Figure 3.24. CaO vs HAP: crystal structures (along *c*-axis), CaO orientation map for the 1000 °C sample with cubic color map, phase map stating only hydroxyapatite presence. Scale bar: 50 nm.

Carbonates. Bone apatite contains approximately 7 wt. % of carbonate. In principle, carbonate ions can substitute in the apatite structure either in the OH-site (A-type substitution) or in the PO_4-site (B-type substitution). It seems now to be generally accepted that CO_3^{2-} dominantly replaces PO_4^{3-} in biological apatite [72]. However, discussions still exist about how carbonate ions are incorporated into the apatite lattice [180,181].

Template matching with two phases, the A-type and B-type substituted hydroxyapatite, was performed. B-type carbonate substitution in hydroxyapatite gives cleaner orientation maps (Fig. 3.25) in terms of single crystallinity criterion (color uniformity). The phase map was constructed using three templates: hydroxyapatite without carbonate substitution, A-type and B-type substituted hydroxyapatites. Hydroxyapatite phase dominates, the B-type appears but A-type is negligible. Thus, according to our results, particularly the phase reliability, B-type substitution is more probable in bone tissue. The reason for that may lie in the incorporation mechanism. Synthetically, A-type carbonate apatite can be produced only at very high

temperature (solid-state reactions at 1000 °C), whereas synthetic B-type carbonated apatite precipitates from solutions in the temperature range of 50–100 °C [182–184]. It is also possible to synthetically produce mixed A-type/B-type carbonated apatites [185]. However, many results show that B-type carbonates are dominantly present in bone [186,187] that is confirmed by our results.

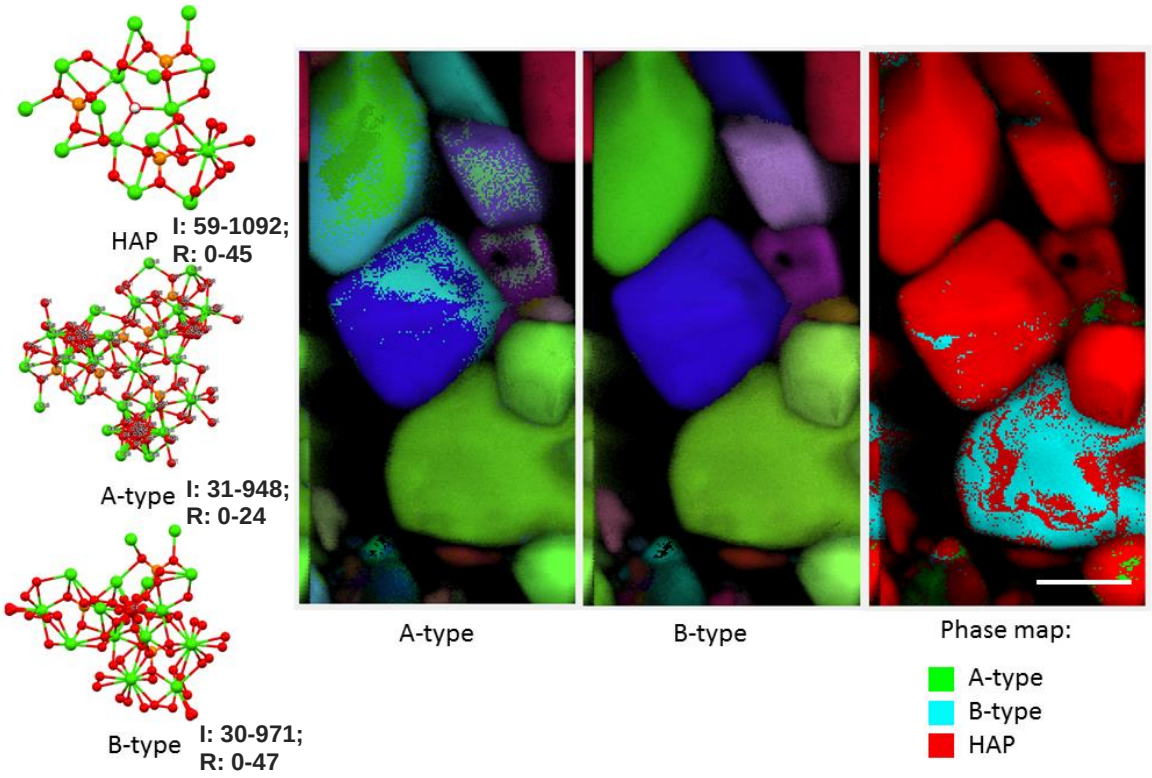

Figure 3.25. Carbonate substitutions in hydroxyapatite: crystal structure of model hydroxyapatite together with A and B-type substitutions; corresponding orientation maps and phase map for the 1000 °C sample showing B-type to be the preferential substitution type. Scale bar: 50 nm.

Other ionic substitutions. The number of ionic substitutions possible in biological apatite is vast, in principle, but limited to the available elements in the body. The substituting ions that are known and/or reported in bone and tooth mineral are F^-, Cl^-, Na^+, K^+, Fe^{2+}, Zn^{2+}, Sr^{2+}, Mg^{2+}, citrate, and carbonate. The effect of several ionic substitutions such as Na^+, Cl^-, F^-, Sr^{2+} [188–191] on the structural analysis were tested (Fig. 3.34).

From orientation maps (Fig. 3.26), one can conclude that Na^+, F^- and Sr^{2+} can be present in the hydroxyapatite lattice, while Cl^- cannot, despite the fact that it is abundant in the human body (the Cl^- concentration in blood plasma is on the order of tenths of wt. %). It is in a good

agreement with [72]. However, Sr^{2+} is not detected in the phase map. Please note that the phase map as it is defined in ACOM (see sub-chapter 2.2.3) does not show the substitution elements distribution in hydroxyapatite but only refers to the crystalline phase with the highest index among others. It is only possible, therefore, to notify which substitution element has the highest probability (in absolute scale) of being incorporated into the lattice. A better indicator, as for example, the relative phase probability, would be more suitable to our case and should be implemented in the ACOM routine.

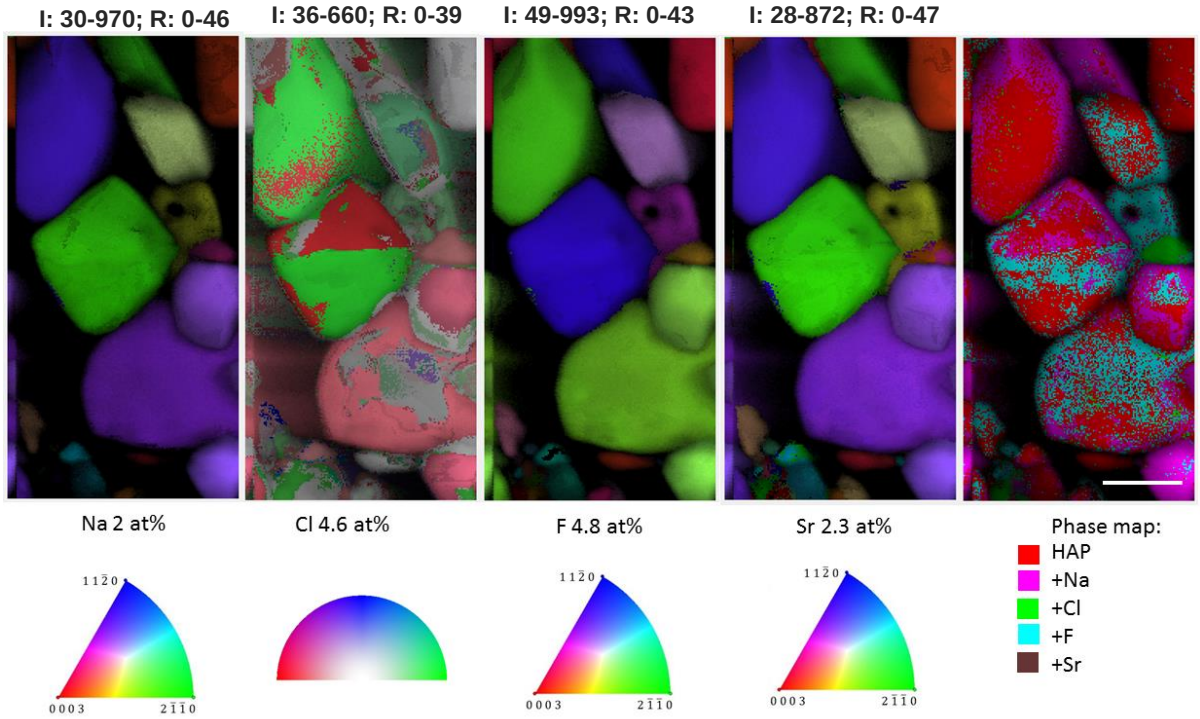

Figure 3.26. Orientation maps for the 1000 °C sample with corresponding color-code and the phase map of hydroxyapatites with different ionic substitutions. Scale bar: 50 nm.

Sensitivity to lattice parameters. Another way to test the ACOM-TEM method sensitivity is to verify how subtle lattice parameters differences can be picked up. Thus, the same data set was fitted with a set of structure templates for hydroxyapatite in which the lattice parameters (*a*, *b* and *c*) were gradually changed with 0.1 Å step higher and lower than the experimental value in [64]. More precisely, *a*=*b* and *c* lattice parameters were changed leading to the variation in the *a*/*c* ratio. A constant *a*/*c* ratio would be compensated by the camera length refinement and therefore useless for the sensitivity test. It is shown (Fig. 3.27) that the acquired data can be well fitted by the structures with lattice parameters that differ by -0.1 Å to +0.1 Å from the experimental value. This implies that the precision on the lattice parameters in ACOM-TEM is around 0.2 Å, which represents 2 % of the *a*=*b* lattice spacing.

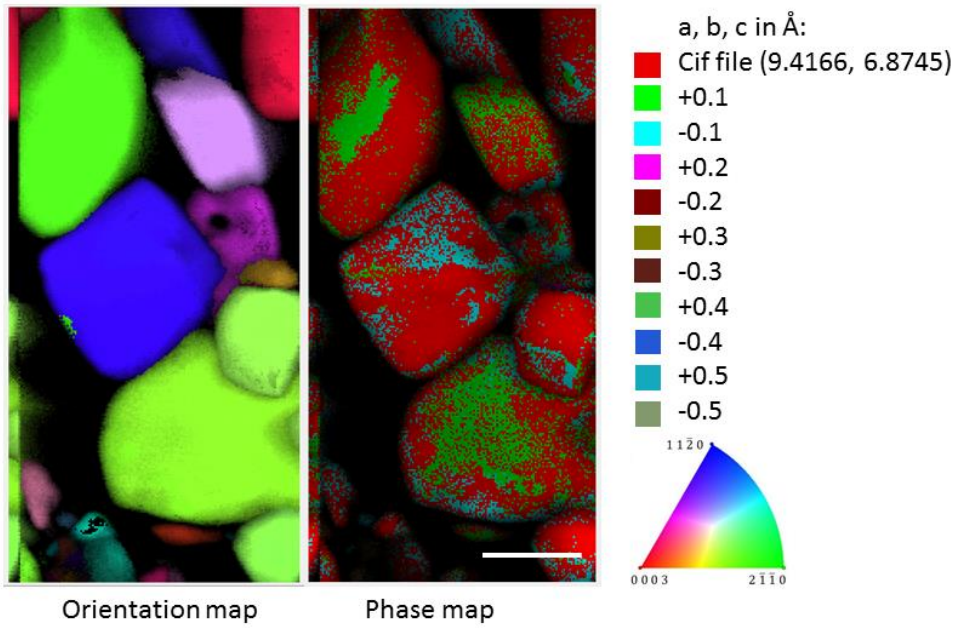

Figure 3.27. Orientation and phase map for lattice parameters refinement in the 1000 °C sample. The data can be fitted with three templates that correspond to 0.2 Å cell parameter precision. Scale bar: 50 nm.

3.2.6. Temperature series

All the phase identification was done for the bone sample treated at 1000 °C in order to test sensitivity of the ACOM-TEM method. But the question remains: what is happening with bone during heating? Are we able to work on phase identification with diffraction patterns of worse quality such as recorded from the control sample?

In order to answer these questions, analysis such as ionic substitution and lattice spacing were also performed for five temperatures: control, 200 °C, 400 °C, 700 °C and 1000 °C.

First of all, the structure is better described by the hexagonal space group P63/m over the whole temperature range, contrary to results in the literature pointing to a monoclinic to hexagonal phase transition.

Then, the carbonate substitutions were investigated. In Fig. 3.28, the phase maps of the temperature series are shown. The maps are constructed with two phases: the hydroxyapatite without carbonate substitutions and the B-type substituted hydroxyapatite. As was shown earlier, this method does not give any quantitative information. Nevertheless, it is clear that the probability of finding carbonate substitutions decreases with temperature (see Fig. 3.28) which

is in agreement with [72]. For lower temperatures, the structure with carbonate substitutions gives higher index values than hydroxyapatite without substitutions close to grain boundaries and does not define full crystals. This may reflects the inhomogeneous carbon content on the level of 100 nm scale.

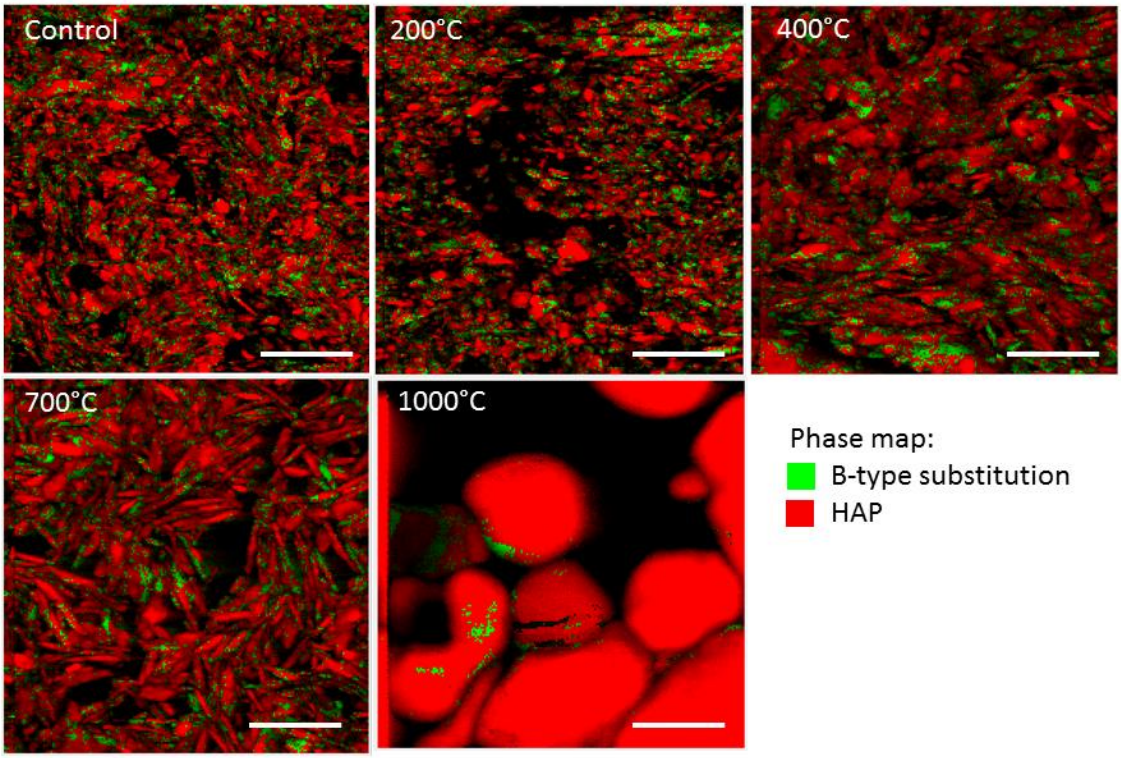

Figure 3.28. Temperature series phase maps of hydroxyapatite with B-type carbonate substitutions. Scale bar: 100 nm.

The next question was to verify whether Na^+ and F^- substitutions are present in the treated samples within the whole temperature range. In Fig. 3.29, the phase maps of various samples are present showing that Na^+ and F^- substitutions do not disappear during heating. Please note that these maps cannot show simultaneous Na^+ and F^- substitutions at the same point. Due to the method limitation, only single orientation of the single phase is considered to be "best" on the basis of index value. So we can only discuss the fact of different areas with different probabilities of finding Na^+ and F^- substitutions.

The last attempt was performed in order to understand the lattice spacing precision and, possibly, its evolution upon heating. From the temperature series phase maps (Fig. 3.30), it is clear that the data is always fit with three structure (colors) which means that the accuracy of cell parameter verification by ACOM-TEM does not depend on the crystals size or diffraction quality and is still equal to 0.2 Å.

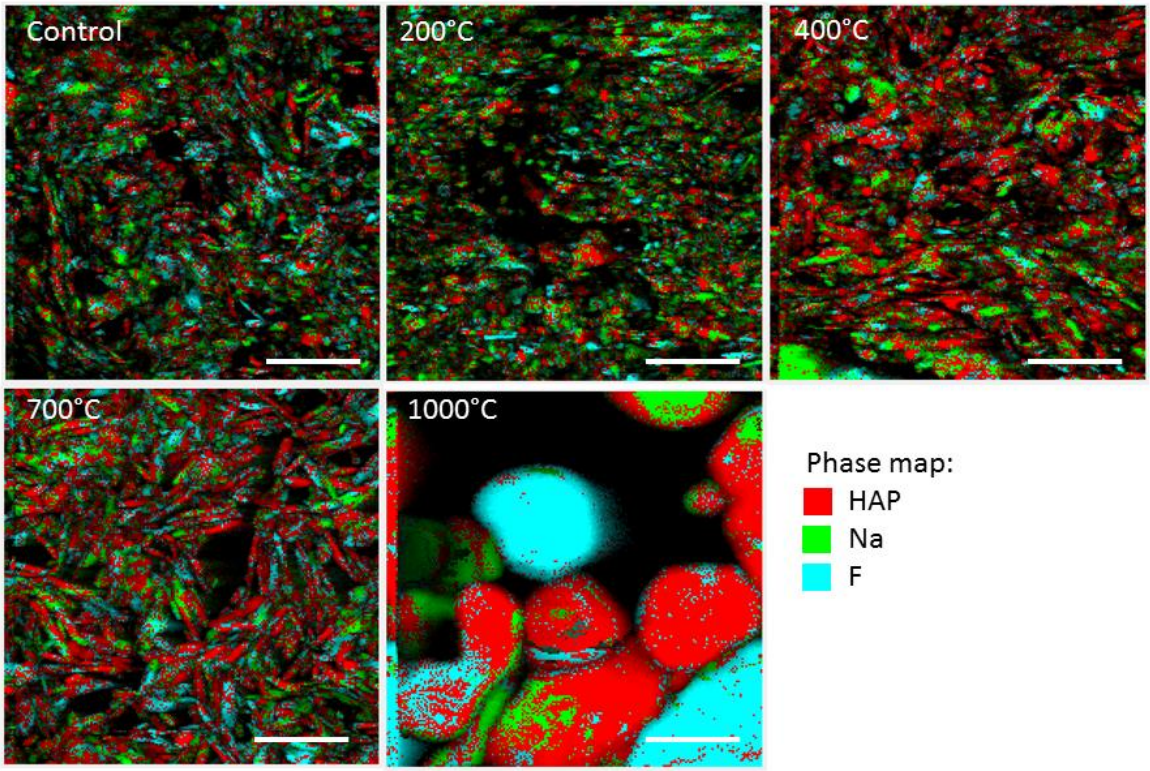

Figure 3.29. Temperature series phase maps of hydroxyapatite with Na^+ and F^- substitutions. Scale bar: 100 nm.

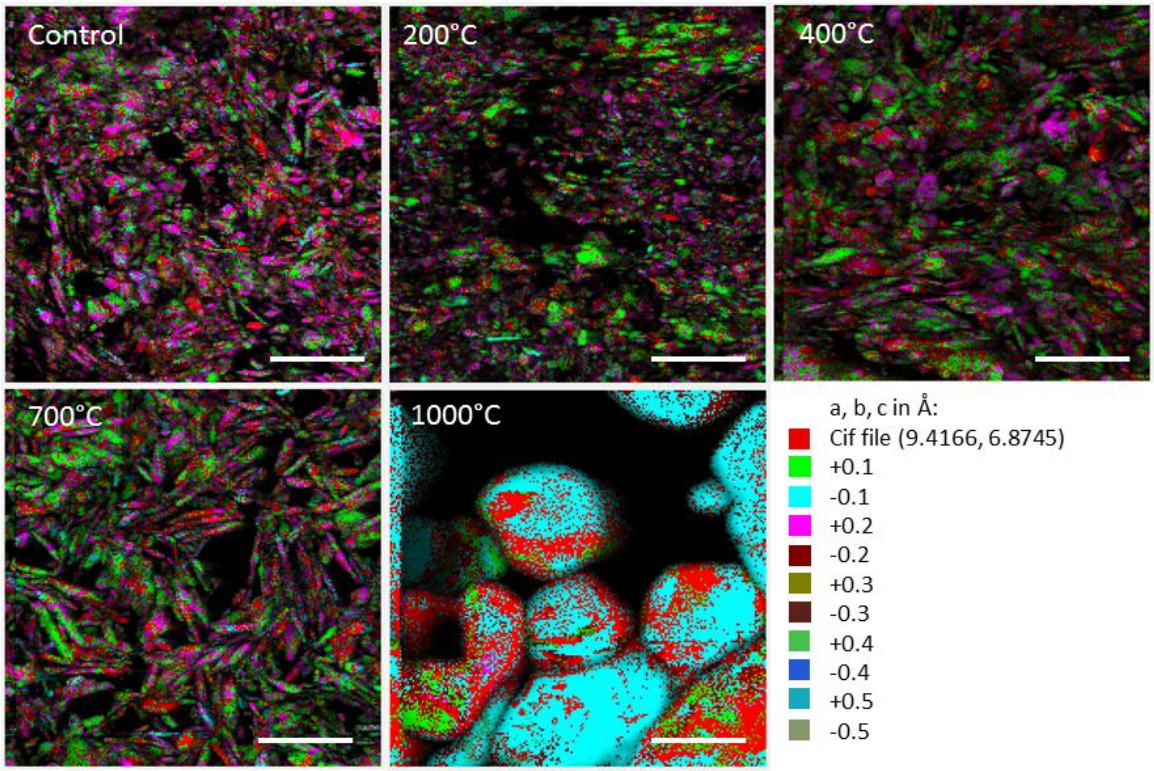

Figure 3.30. Temperature series phase maps of hydroxyapatite with different cell parameters. Scale bar: 100 nm.

However, the surface fraction of colors present in the data set is changing and gives an idea about the average lattice parameter for each temperature. Thus, in the control sample, pink color is dominant (+0.2 Å), followed by green (+0.1 Å) and then red (+0 Å). For temperatures of 200 °C, 400 °C and 700°C, the dominant color is green (+0.1 Å), followed by pink (+0.2 Å) and then red (+0 Å). At last, for the 1000 °C heated sample, most of the image appears in blue (-0.1 Å), followed by red (+0 Å) and then green (+0.1 Å). This trend indicates the slight lattice parameter decrease (cell shrinkage) during the heat treatment, which is in good agreement with [102].

Therefore, TEM is a powerful tool that allows individual nanocrystals visualization and size determination and, with ACOM setup, orientation mapping construction, contrary to X-ray diffraction techniques that provide averaged information over the illuminated sample volume (that even in scanning mode is limited to the probe size of around 150 nm in diameter). The sample thickness in ACOM-TEM is the remaining source of averaging in the case when crystallites are much smaller than the standard TEM sample thickness. Moreover, it is sensitive to subtle structure-chemistry changes offering the information about substitution content and lattice parameter variations.

In principle, electron tomography enables the 3D position and elemental resolved data acquisition, as has been shown for the dentin-implant interface [102], but the sample preparation requires very sophisticated techniques and specific expertise.

.63.2.7. EDX analysis

In order to analyze the chemical composition of bone and its possible modifications in the temperature series, an EDX analysis was performed in a scanning mode with spot size of 0.7 nm in the region close to the one scanned by ACOM-TEM for each heat-treatment temperature.

The field of view had to be adapted to the crystal size present in the structure. Therefore, the 1000 °C and 800 °C samples were scanned with a magnification of x 50k while rest of samples were analyzed at x 200k. In order to achieve good statistics, 25 frames were summed for each sample. A bright field image was recorded before every frame and the probe tracking was performed after every 10 ms in order to correct for the sample charging and moving effects. Elemental maps of O, C, P and Ca were constructed. The scanning area and elemental maps for

the 1000 °C and control samples are shown in Fig. 3.31 and Fig. 3.32, while the rest of the samples information can be found in Appendix 3.

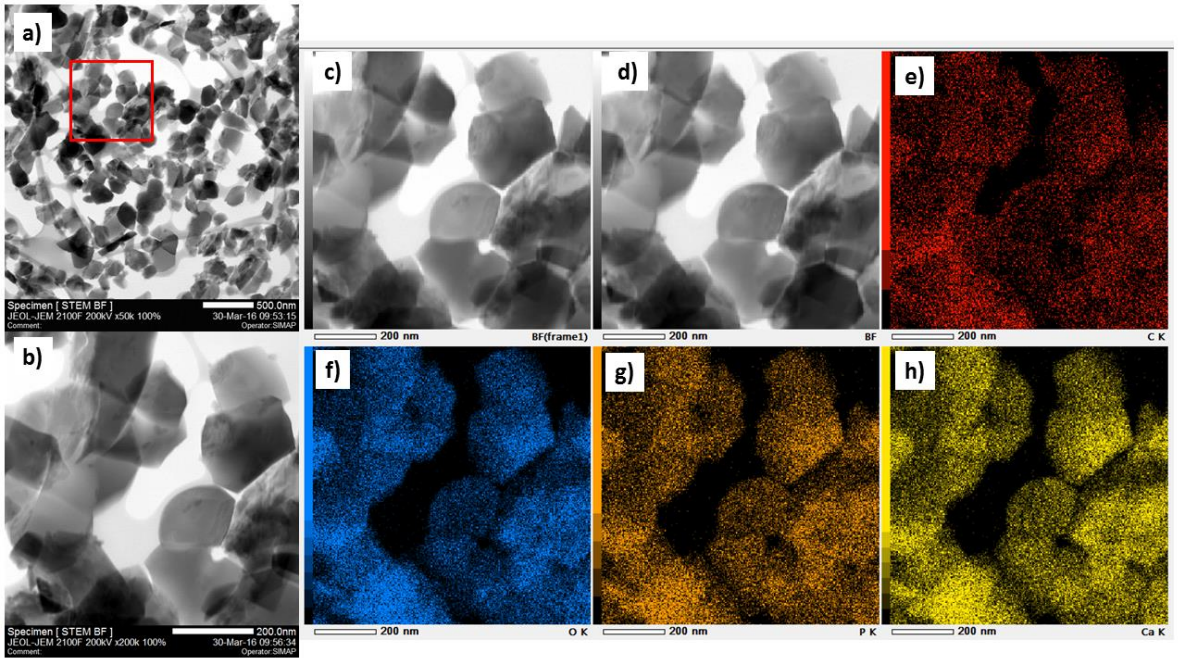

Figure 3.31. Scanning EDX of the 1000 °C bone sample: a), b) bright field images of the scan position; c), d) bright field images before the first and the last scanning frame; e), f), g), h) elemental maps of C, O, P and Ca, respectively.

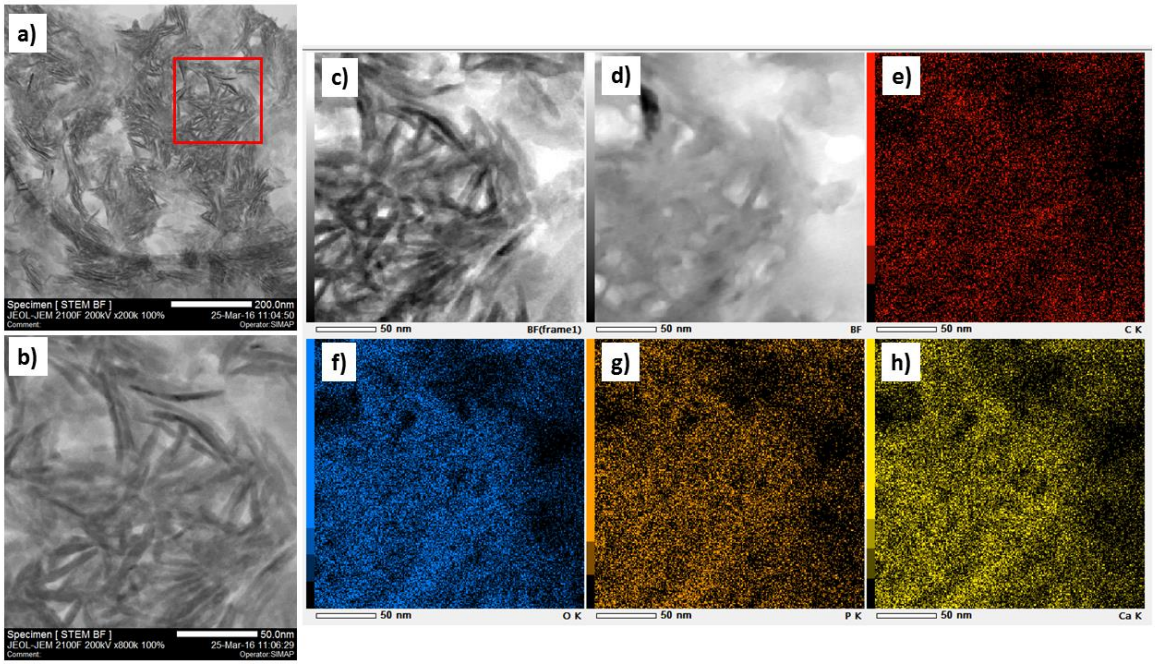

Figure 3.32. Scanning EDX of the control bone sample: a), b) bright field images of the scan position; c), d) bright field images before the first and the last scanning frame; e), f), g), h) elemental maps of C, O, P and Ca, respectively.

Elements are homogeneously distributed over the scan area. However, differences in content may be found for crystals of different thickness. No sign of radiation damage was observed for 1000 °C, while for the control sample, a clear radiation damage is visible if one compares bright field before first and last scanning frame.

The characteristic EDX spectra with its identification (except for contamination elements) for control and 1000 °C samples are presented in Fig. 3.33. Spectra for all temperature series are shown in Appendix 3. Instrumental contaminations from the following elements: Be, C (membrane), Cr, Cu (grid), Co, Fe, Au are present and have not been identified in the spectra.

Mass concentration of all elements detected within the temperature series is summarized in Table 3.3. Beyond the elements that built the hydroxyapatite lattice such as Ca, P and O, minor traces of substitution atoms of F, Na and Mg were found (in some cases at the limit of method sensitivity, but showing a clear peak in the spectra). Presence of N (also close to the limit of sensitivity) for low temperatures (control and 100 °C) and its absence for higher temperatures is an interesting feature that may reflect the denaturation and the disappearance of collagen molecules during heating.

The presence of Si is more difficult to explain despite the fact that it was often reported. It may come from sample preparation contamination or could be originally incorporated within hydroxyapatite lattice. Another possibility is that Si contamination comes from the heat treatment stage due to the use of quarts sample holder during heating.

The carbon content in the samples cannot be verified since the TEM grids had carbon coating and due to overall carbon contamination of the chamber.

Overall, Ca, P and O concentration is increasing with temperature (Fig. 3.34, left) with a decay of substitution elements concentration such as F, Na, Mg (Fig. 3.34, right). This can be expected in the case of recrystallization. N content becomes zero after 200 °C. Ca/P ratio is oscillating around an average value of 1.95 ± 0.2 over the whole temperature range.

Increased mineral crystal size for the 800 °C and 1000 °C cases gave the possibility to do single crystal EDX scanning in order to correct for the crystal thickness differences described above. In Fig. 3.35, four scan positions are shown for both temperatures with corresponding single crystal main elements distribution.

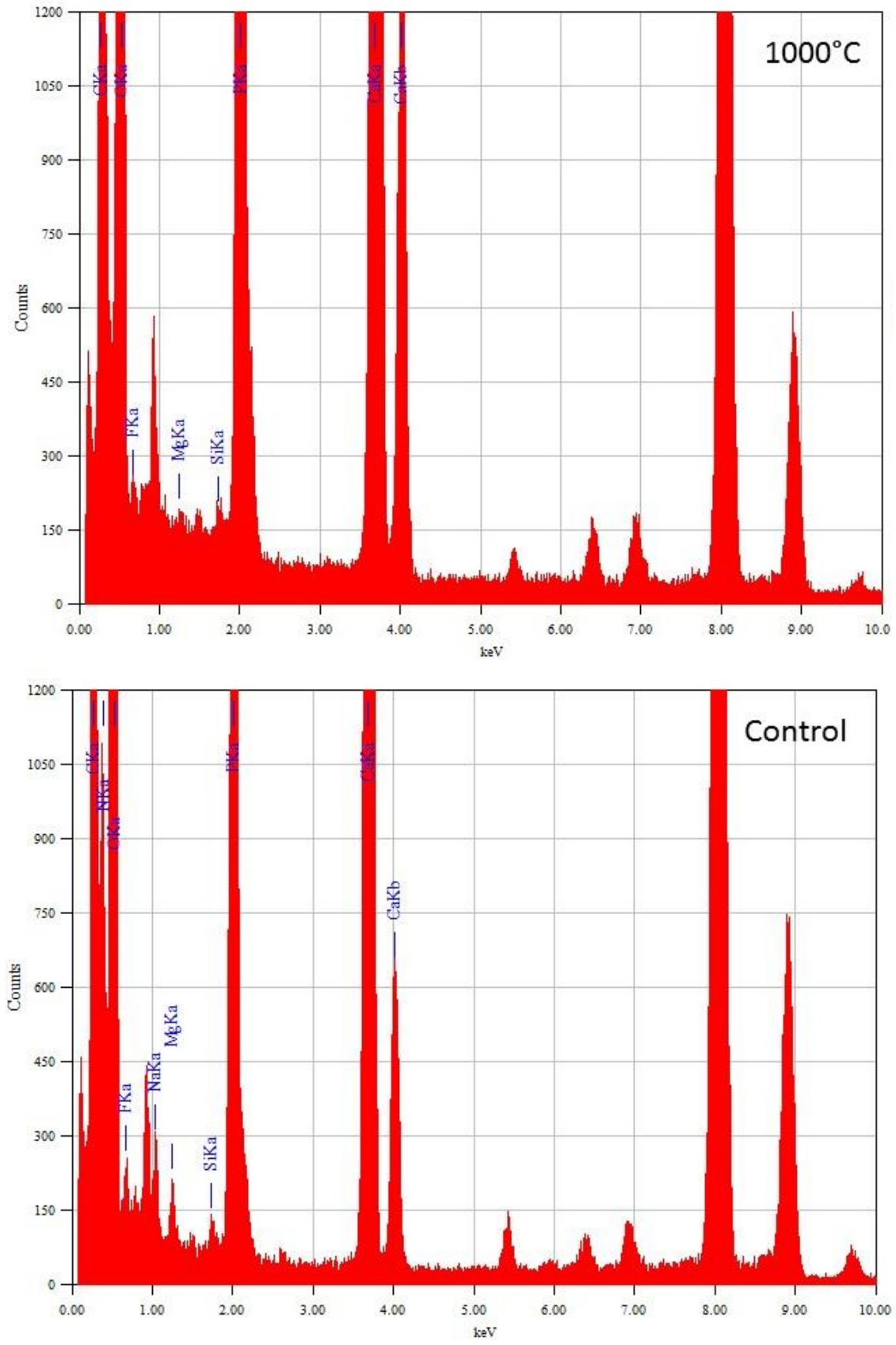

Figure 3.33. EDX spectra for the 1000 °C and control samples. Non identified elements correspond to contamination from the setup including Be, Cr, Cu (grid), Co, Fe, Au.

Table 3.3. EDX atomic concentration (in mass %) of detected elements vs heat treatment temperature.

Mass% / T,°C	C	N	O	F	Na	Mg	Si	P	Ca
1000	6.22	0	38.71	0.3	0	0.06	0.04	18.83	35.84
800	11.41	0	36.77	0.24	0.05	0.15	0.31	17.84	33.23
700	14.08	0	34.76	0.26	0.36	0.47	0.55	15.61	33.91
600	11.63	0	35.91	0.1	0.03	0.55	2.17	14.82	34.90
400	11.41	0	37.11	0.44	0.60	0.47	2.93	16.23	30.82
200	14.11	0	34.74	0.74	0.16	0.52	0.96	15.45	33.30
100	14.78	6.65	29.83	0.37	0.10	0.19	0.10	11.73	36.25
0	13.54	6.82	32.47	0.85	0.62	0.5	0.17	15.41	29.63

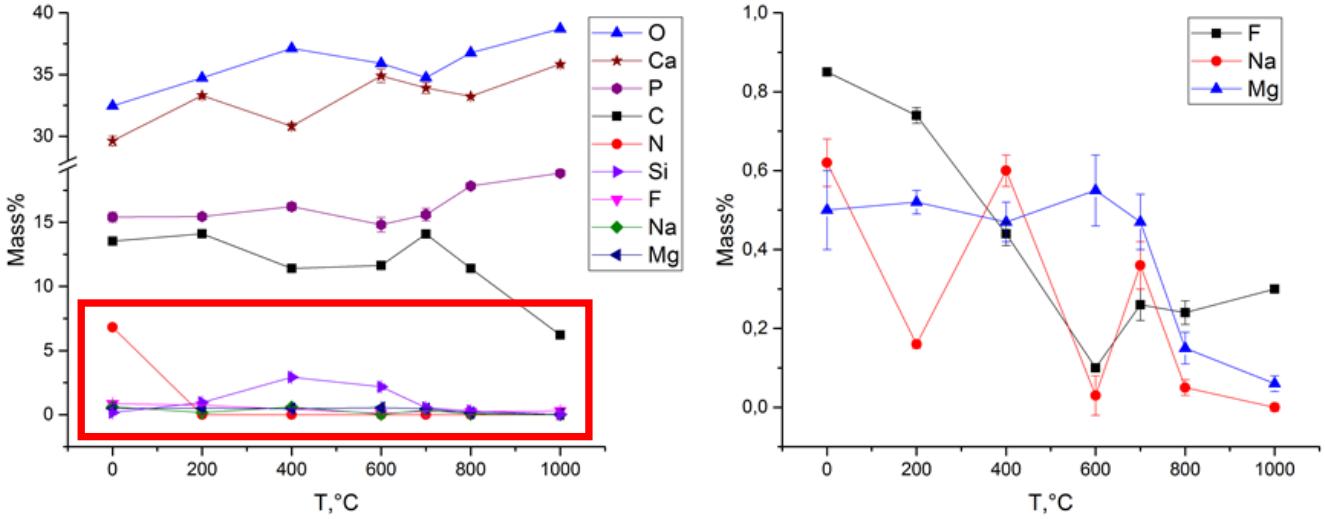

Figure 3.34. Evolution of atomic concentration (in mass %) of detected elements with temperature. Left: full scale. Right: zoom in red box for showing low concentration elements.

Single crystal EDX analysis allows determination of the Ca/P ratio variations between individual crystals. As was stated in Chapter 1, the Ca/P ratio of stoichiometric hydroxyapatite is 1.67, therefore, the deviation from this value will give us the estimation of the degree of substitutions at Ca and P positions. Most of the values we record are higher than for the stoichiometric case that may indicate the presence of B-type carbonate substitutions that replace PO_4^{3-} by CO_3^{2-} and consequently increases the Ca/P ratio.

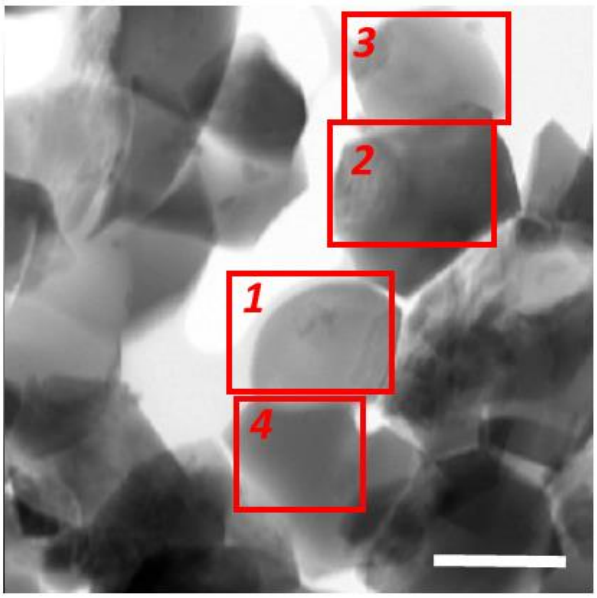

pos / el.	1	2	3	4	average
Ca	35.88	36.68	37.80	36.54	36.73
P	18.83	19.38	17.96	19.29	18.87
O	38.64	39.67	38.28	39.50	39.02
Ca/P	1.90	1.89	2.10	1.89	1.95

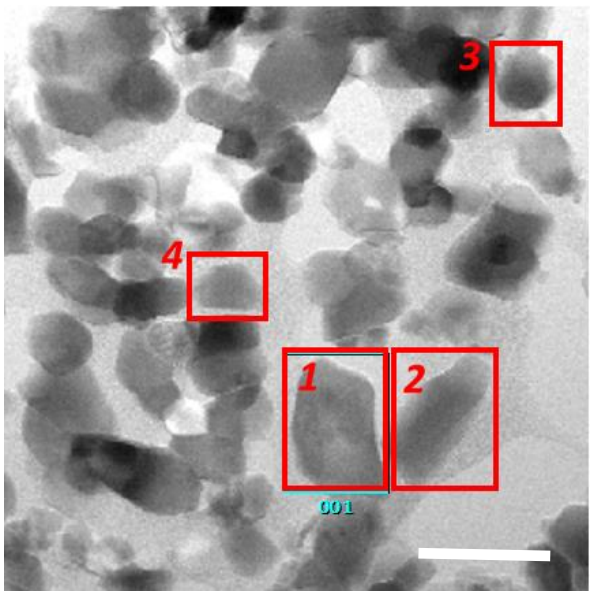

pos / el.	1	2	3	4	average
Ca	33.42	31.26	30.95	32.83	32.12
P	18.57	17.62	17.16	15.32	17.17
O	37.32	35.24	34.51	32.89	34.99
Ca/P	1.80	1.77	1.80	2.14	1.87

Figure 3.35. Single crystal EDX analysis. Bright field images showing scan positions with corresponding elemental mass concentration (in %) and Ca/P ratio for 1000 °C (left) and 800 °C (right).

In order to summarize the EDX data, the overall decay in minor elements concentration and rise in Ca and P concentration are observed along with the collagen denaturation (N disappearance) after 200°C. However, the radiation damage may play an important role for the organic phase modifications present at samples heated below 300°C, and data interpretation, therefore, have to be taken with care.

3.3. PDF analysis of bone

3.3.1. Motivation

Following the ACOM-TEM investigations that provided the individual crystals organization, orientation as well as structural and chemical phase, we are now interested in the atomic local disorder in bone tissue. Therefore, such questions as local deviations from the ideal structure, amorphous phase and nanocrystallinity will be discussed in this sub-chapter.

XRD is widely used for bone structure characterization, joint to TEM, providing an average information over statistically representative sample volumes when TEM allows obtaining real-space pictures of thin samples. However, XRD still presents a number of problems mostly due to peak broadening resulting in strong overlapping in some spectra regions which can be explained by different reasons, including small crystal size, crystal strain, presence of substitutions and vacancies, degree of crystallinity (order/disorder), existence of amorphous phase, etc. [192].

PDF analysis, as an alternative method of analyzing diffraction data without the assumption of lattice periodicity, will be used for characterizing the bone tissue. A periodic lattice is a prerequisite for standard crystallographic study. However, small randomness and local deviations from perfect periodicity often characterize complex materials such as bone. Thus, determining these deviations is an essential part of structural characterization. While crystallographic analysis takes into account only the Bragg peaks, the PDF method utilizes information hidden in-between the Bragg peaks in the form of diffuse scattering, in addition to the Bragg peaks [117].

PDF analysis is an ideal method for our purposes since the structural information can be used to analyze amorphous and disordered crystalline materials including particle size effects but, to the best of our knowledge, was never applied to bone studies of crystallographic disorder. It allows going beyond the information obtained by TEM in probing the atomic scale of bone tissue: bone nanocrystal size, phases, interatomic bonds, existence of amorphous phase and order/disorder relation can be assessed.

The possibility of having an amorphous phase and/or amorphous layer surrounding mineral nanocrystals can be addressed with PDF analysis. In case of heated bone, many studies [95,193] pointed out no differences in crystal structure for temperatures below 600 °C. Our hypothesis is that the differences are subtle and may be attributed to the local structural disorder,

atomic substitutions and vacancies and may simply not be accessible by using simple XRD analysis schemes due to peaks broadening.

3.3.2. Sample preparation peculiarities

Two key experiments were carried out for bone tissue PDF analysis and will be presented in this sub-chapter.

The first one was performed on heat treated unembedded bovine cortical samples with laboratory source Ag Kα radiation four-circle diffractometer (λ=0.5608 Å; E=22.1086 keV) with mosaic monochromator (dspacing=20.0 Å). Fixed and dehydrated bovine cortical blocks of ~0.3 x 0.3 x 10 mm^3 volume were first prepared. In the next step, samples were heat treated in exactly the same conditions and at the same time as samples used for ACOM-TEM analysis (see Chapter 2) to nine temperatures (100, 150, 200, 300, 400, 600, 700, 800, 1000 °C) for 10 min in vacuum and then air cooled (Fig. 3.44). Samples were measured in an unembedded state.

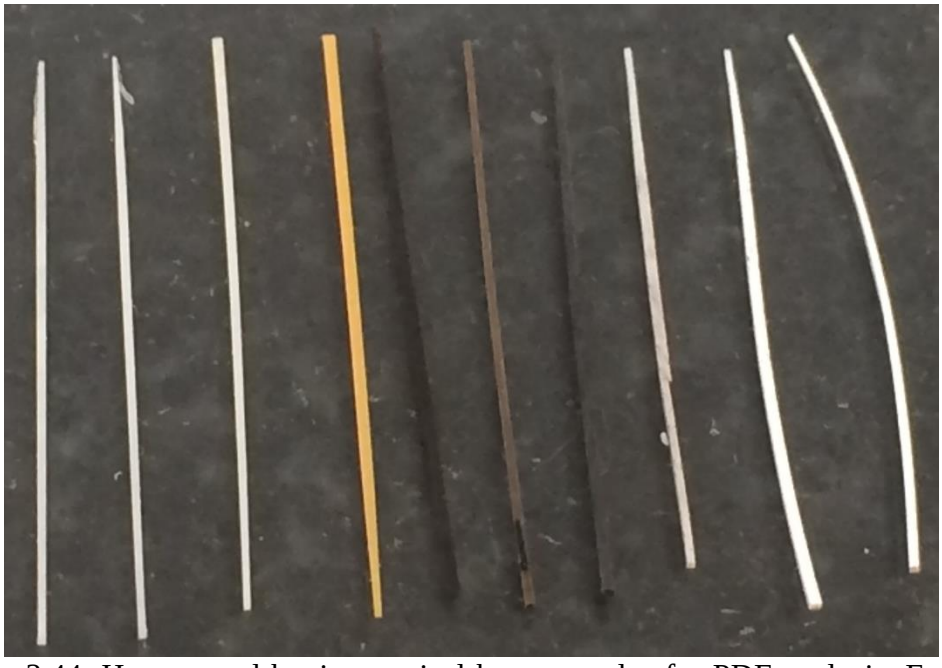

Figure 3.44. Heat treated bovine cortical bone samples for PDF analysis. From left to right: control, 100, 150, 200, 300, 400, 600, 700, 800, 1000 °C.

The second experiment was carried out using synchrotron radiation at ID11 beamline (ESRF, Grenoble) with E=78.2578 keV (λ=0.1584 Å) and sample to detector distance of 101 mm. Specimens were prepared from two sets of available human iliac bone biopsies:

1) control group : healthy women, before menopause, with normal bone mineral density and mass;

2) pathological group: Osteopetrosis (samples with high mineral content), Hyperparathyroidism (low mineral content) and Fluorosis (excessive accumulation of fluoride in the bones) representing a wide range of pathological mineralization conditions.

Samples were embedded in PMMA and the regions of interest were selected based on histological examination and polarized light microscopy measurements (see Chapter 3). Samples were then cut in sections of ~ 300 µm in thickness and reduced by polishing to 100 µm in thickness. The resulting sample geometry was ~2 cm x 2 cm x 100 μm^3 (Fig. 3.45). The sections were glued onto the teflon rings (2 mm thin). One of them (HPT1) was not flat enough and was additionally mounted in between two kapton foils.

Sample names were devoted in the following manner and will be referred to by abbreviations later:

- control transverse section #1 - CT1;
- control transverse section #1 - CT2;
- control longitudinal section #1 - CL1;
- Fluorosis - Fluo1;
- Hyperparathyroidism #1 - HPT1;
- Hyperparathyroidism #2 - HPT2;
- Osteopetrosis - OPT1.

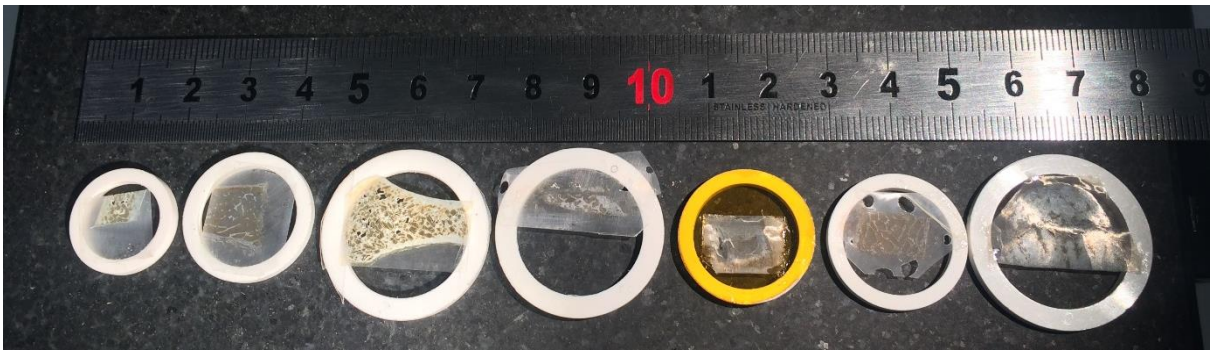

Figure 3.45. Photo of the pathological sample set used for XRD at ID11. From left to right: CT1, CT2, CL1, Fluo1, HPT1, HPT2, OPT1.

3.3.3. Rietveld refinement for heated bone

XRD patterns were collected with 0.025 s acquisition time in 2θ range from 0 to 123 ° for each temperature and the background was measured in the same conditions. *I (2θ)* and *I (q)* dependencies are presented in Fig. 3.46. One can mention that the profiles are offset in intensity due to differences in illuminated volume of the samples (because of precision of the cutting machine and shape change after heating).

As a first step of data treatment, Rietveld analysis was performed using FullProf tool [194] for the samples in the temperature series. Peak shape for fitting was chosen as Thompson-Cox-Hastings pseudo-Voigt function, the background was fit linearly using 4-point fit. Hydroxyapatite structure was used for the refinement [64]. The scale factor, overall B-factor, lattice spacing and γ angle, background, shape parameters (*x, y, sz*) and instrumental displacement were refined subsequently. Ten cycles fit was used to refine each parameter.

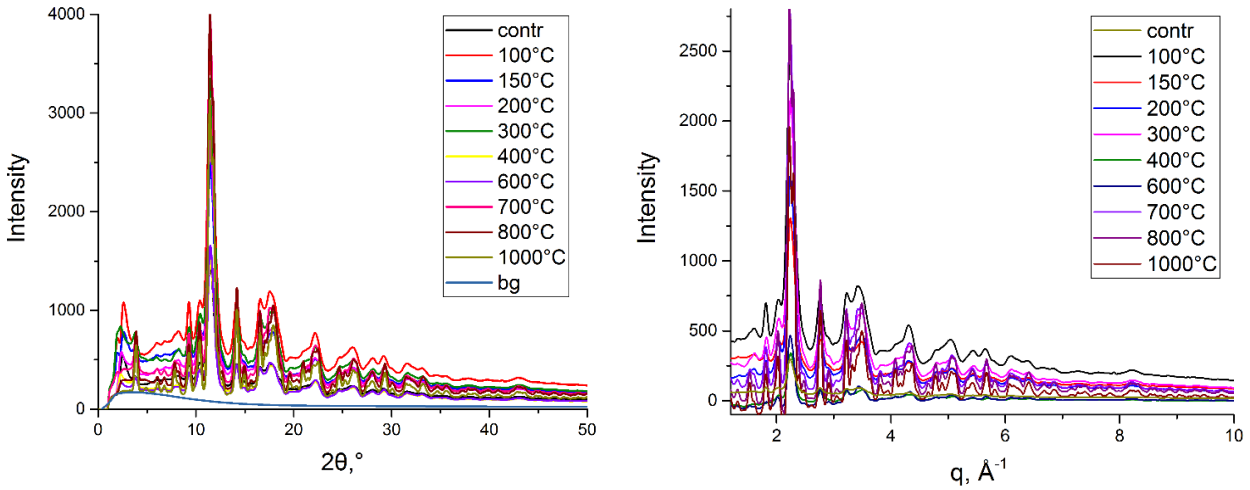

Figure 3.46. XRD spectra for heated bone. Left: *I (2θ). R*ight: *I (q).*

The result of refinement is shown in Fig. 3.47 for the control and 1000 °C samples. The rest of the profiles can be seen in Appendix 4.

Based on the Rietveld refinement, hydroxyapatite cell parameters and volume were obtained and are drawn in Fig. 3.48. An overall decrease of the cell volume (lattice shrinkage) as well as *a* and *c* parameters is observed. This appears to be in good agreement with our expectations from ACOM-TEM analysis (Fig. 3.38). The curves for *a* and *c* lattice parameters seems to follow an exponential decay until 300 °C with the a subsequent rise with the maximum at 400 °C for *a* parameter and at 600 °C for *c*. After 600 °C, decreasing of both values is

observed. The volume increase in the range between 300 and 600 °C and rapid decay after can be explained by pre-transition state with high inter-lattice strain which takes place at this temperature (Fig. 3.48, right).

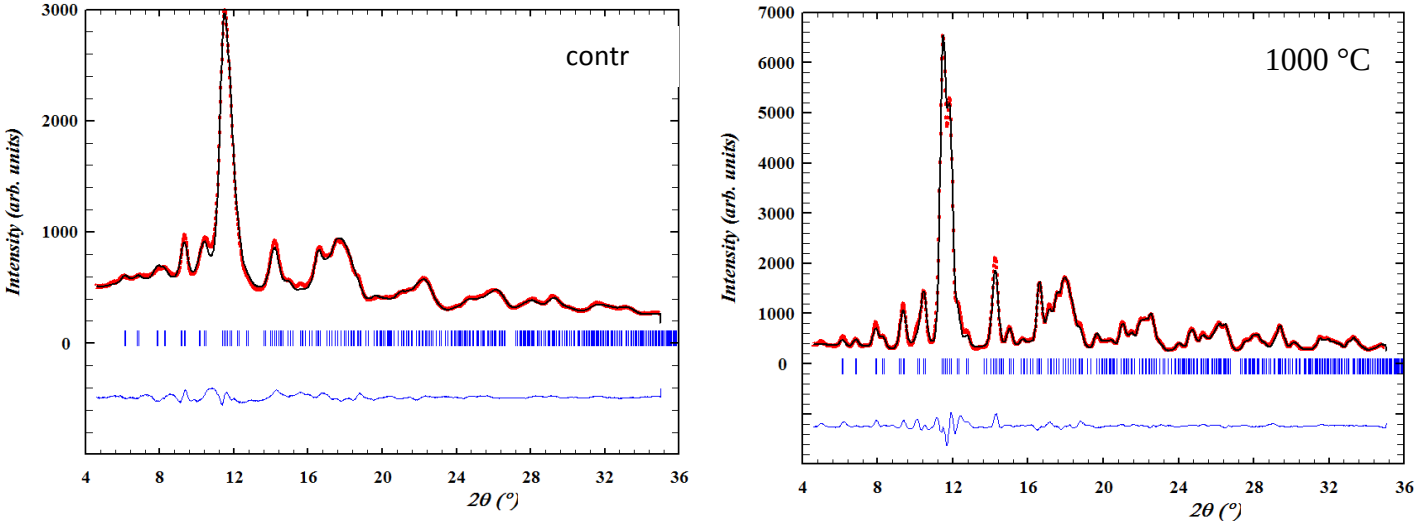

Figure 3.47. Rietveld-refined diffraction patterns for the control and 1000 °C samples. Black - experimental data, red - fit result, blue - misfit function.

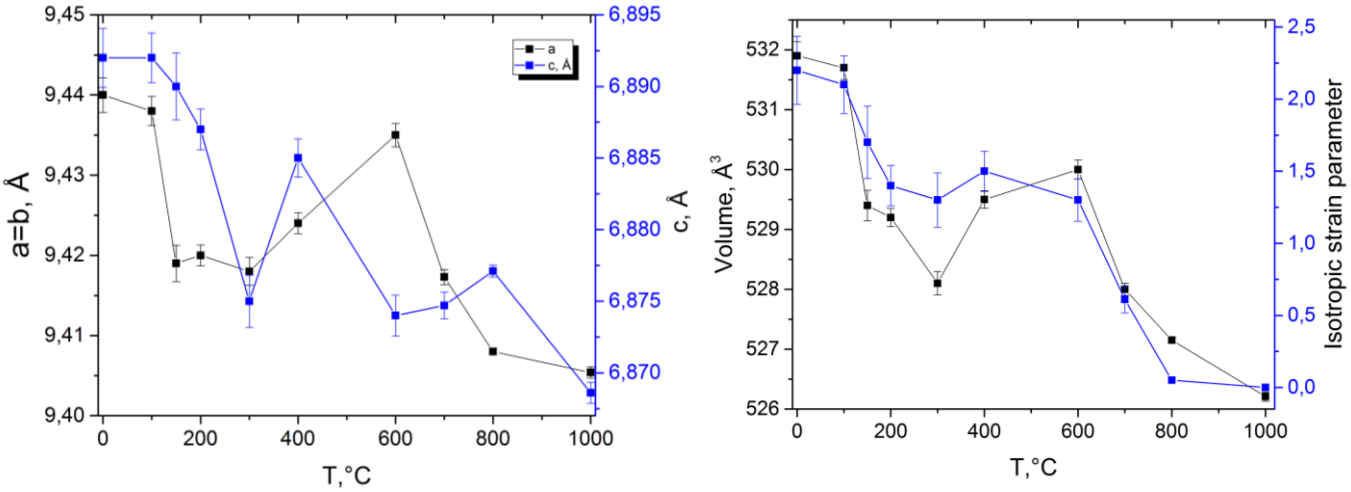

Figure 3.48. Refined bone lattice parameters vs heat treatment temperature. Left: *a*=*b* and *c* lattice distances. Right: cell volume and isotropic strain parameter.

The smallest crystallites size (*100* orientation) changes from 27 nm for the control sample to 33 nm for the 600 °C and then goes to infinity (due to the method limitation, high domain sizes appear as infinity after refinement) as shown in Fig. 3.49, left. Furthermore, the largest particle size (*001* orientation) varies from 28 nm at control state to 300 nm at 800 °C and then rises to infinity. The fact that at control state the domains have very close dimensions goes

against the TEM observations and the literature and is related to disability of Rietveld method to describe materials with small domain sizes. PDF analysis is therefore necessary to address such a question.

Goodness of the fit (χ^2 parameter) is in the range of 0.5 to 2.2 (Fig. 3.49, right) which is satisfactory.

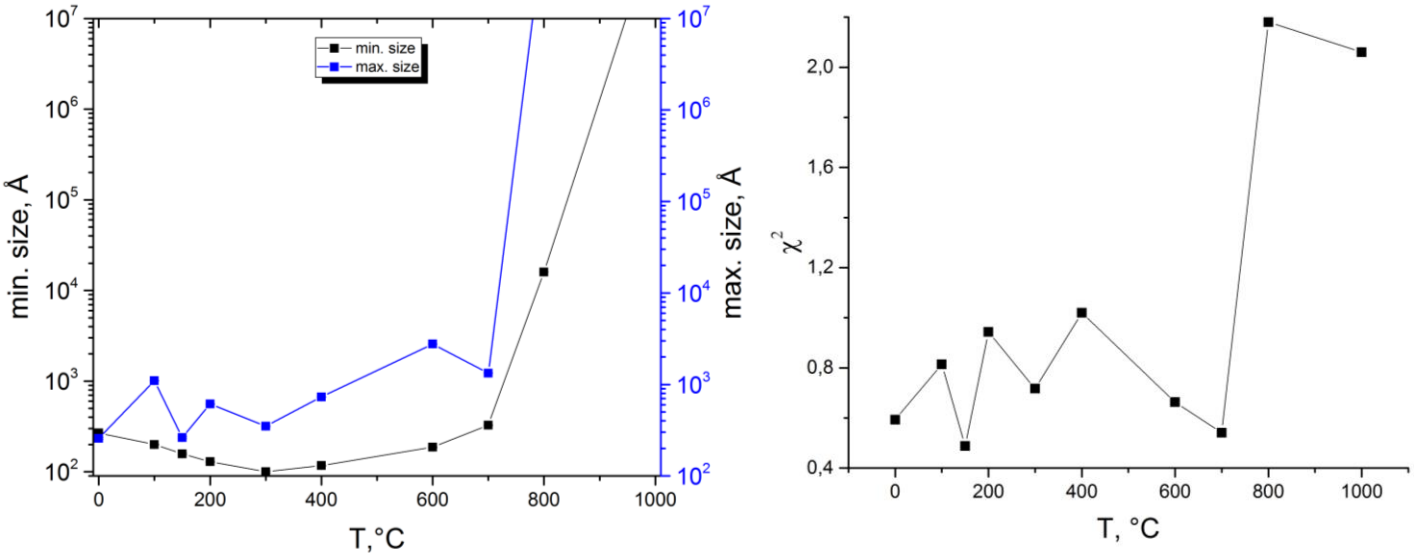

Figure 3.49. Left: smallest and largest particle size. Right: goodness of the fit.

3.3.4. PDF analysis for heated cortical bovine bone

In the next step of data interpretation, PDF analysis was applied to the acquired data set. PDF analysis appears to be a good tool for verifying amorphous phase component and local disorder as it is treating the data as an amorphous compound.

The corrections used for *S(q)* and *G(r)* calculations were the following using PDFgetX2 software [133].

- Sample corrections: geometry (cylindrical capillary), chemical content, lattice number density (number of atoms per lattice unit volume): 0.06, packing fraction: 0.6, sample thickness: 0.3 mm, attenuation coefficient: 0.34.
- *S(q)* corrections: sample self-absorption, multiple scattering (2^{nd} only), X-ray polarization, Compton scattering (energy dependent fit with *1/E* quadr. function), Laue diffuse scattering, weighting function (<asf>^{2}), Q_{min} extrapolation to 0.
- *F(q)* corrections: damping with Lorch function was used.
- *G(r)* optimization: using *S(Q)<=>1* in a *Q*-range from 12 to 18 Å^{-1}.

The *S(q)* were constructed from q_{min}=0.7 Å^{-1} to q_{max}=18 Å^{-1}, *G(r)* were calculated using r_{min}=0.1 Å, r_{max}=250 Å and r_{grid}=0.01 Å.

As a standard procedure, *S(q)* dependencies for each temperature were first calculated (Fig. 3.50, left). *S(q)* were optimized in order to achieve the oscillations around a line for high *q*-s (12-18 Å^{-1}) which is a criteria for correct *G(r)* calculation.

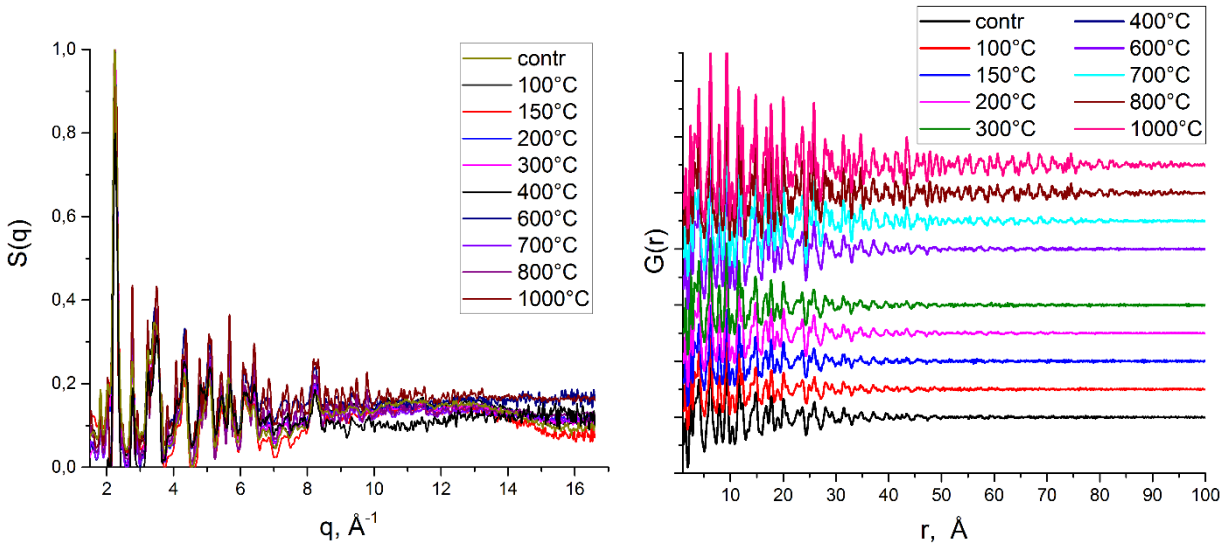

Figure 3.50. *S(q)* and *G(r)* for heated bone. Each curve in *G(r)* is offset by +1 for better comparison.

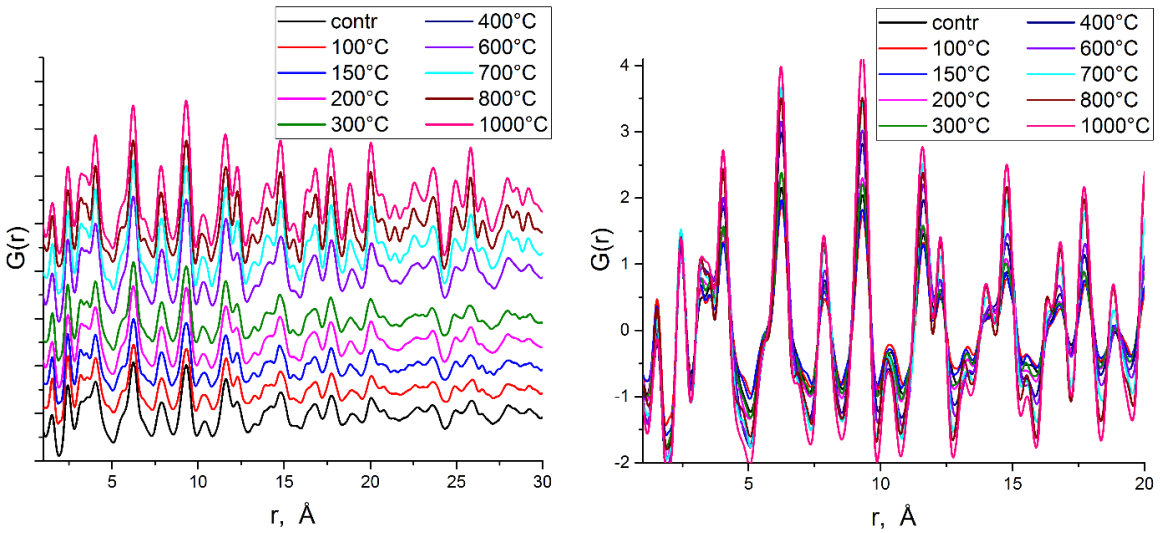

Figure 3.51. *G(r)* for heated bone with different zoom. Left - offset, right - no offset.

Calculated *G(r)* for the temperature series are shown in a full scale in Fig. 3.50, right; and with zoom in first 30 and 20 Å^{-1} in Fig. 3.51. One can clearly see that the oscillations around

zero of *G(r)* extend to much higher *q* starting from 700 °C which indicates considerable domain size growth. Also the intensity of peaks (Fig. 3.51, right) is increasing with temperature, pointing out the improvement in crystallinity.

In order to extract qualitative information about the local structure disorder, modeling of PDF profiles and its fit to experimental ones were done using PDFgui software [134]. The initial model structure was chosen as hydroxyapatite [64], the same one used for ACOM-TEM and Rietveld refinement.

The parameters refinement and fit was done in the following scheme for a control sample. The refinement range was chosen to be from 1 to 30 $Å^{-1}$ with the spacing of 0.01 $Å^{-1}$, q_{max}=18 $Å^{-1}$ (Finite data range used in the Fourier transform step), q_{damp}=0.035 $Å^{-1}$ (Gaussian damping envelope due to limited *q*-resolution, experimentally verified), q_{broad}=0.02 $Å^{-1}$ (peak broadening from increased intensity noise at high *q*, often only significant for wide *r*-ranges).

The refined parameters were fit one by one in the following order and refined values accepted after every cycle. Refinement parameters were:

1) scale factor (data set scale factor);
2) delta1 (*1/r* contribution to peak sharpening);
3) lattice parameters (*a*, *b*);
4) lattice parameter *c*;
5) spdiameter (particle diameter for PDF shape damping function, Å);
6) u11, u22, u33 (isotropic thermal parameters for all atoms except two oxygens that are bound to water);
7) u11, u22, u33 of two oxygens that are bound to water.

After the successful fit was achieved with *rw*=0.17 (goodness of the fit) for a control sample (see Fig. 3.52), the sequential fitting of each sample of the temperature series was performed following the scheme described above. More PDF profiles for the temperature series with their fits can be accessed in Appendix 4. The *rw* evolution for the T-series is presented in Fig. 3.53, left, and always falls within an acceptable range.

The scale factor (Fig. 3.53, right) was found to be close to one which is a good indication of the fit quality.

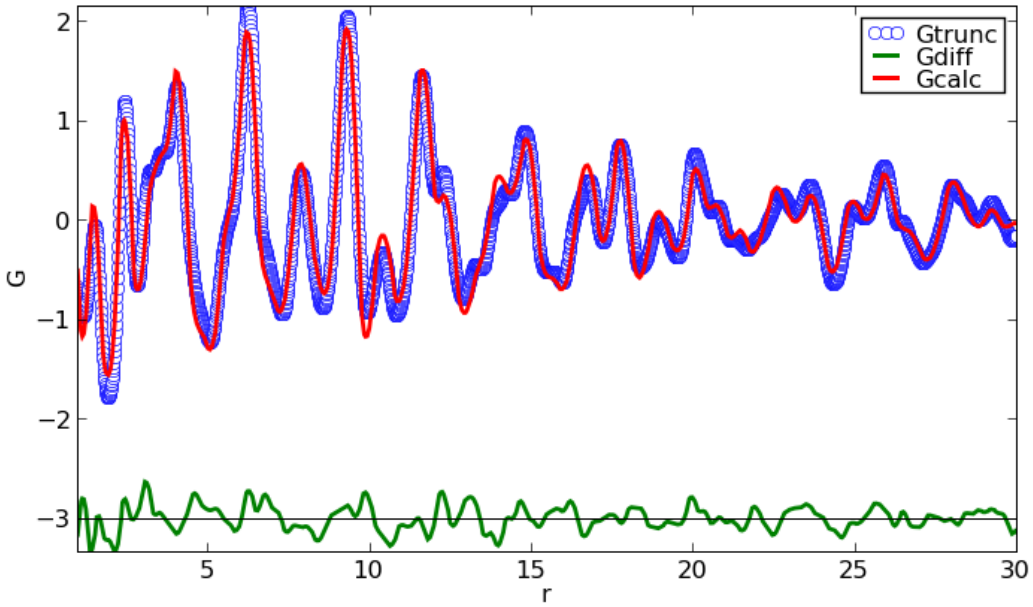

Figure 3.52. PDFgui fit for a control sample. Blue circles: experimental PDF; red curve: modelled PDF; green: misfit function.

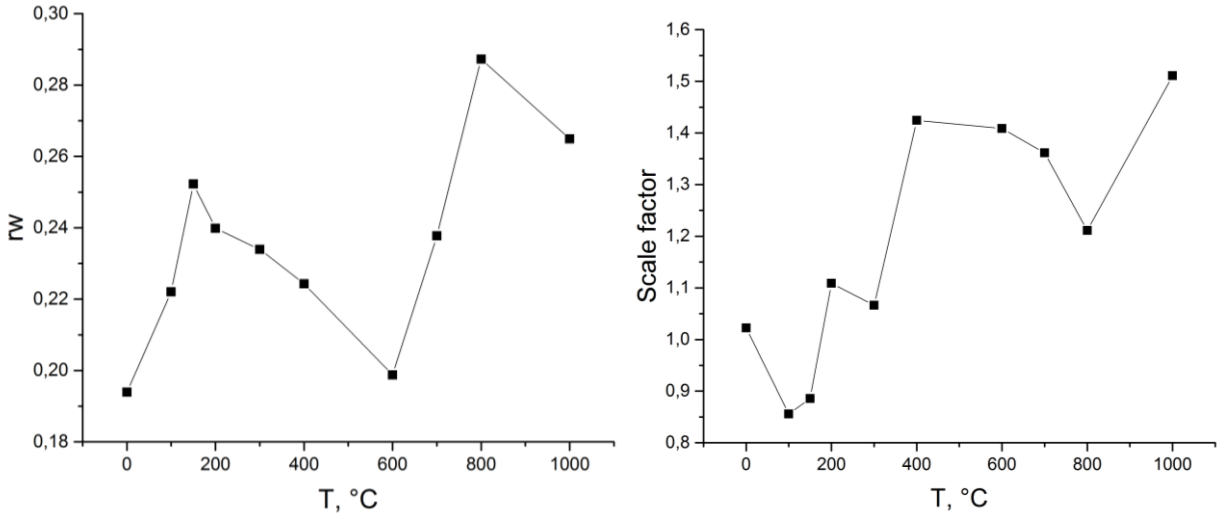

Figure 3.53. Left: the *rw* - parameter (goodness of the fit) evolution with the heat treatment temperature. Right: Scale factor.

The spdiameter value that describes the particle diameter (with spherical approximation) is increasing from 70 Å for the control sample up to 15000 Å for the 800 °C case and then goes to infinity for the 1000 °C, which is in a good agreement (note that spherical approximation is applied here) with ACOM-TEM analysis (4 nm min size for control), unlike the Rietveld refinement results.

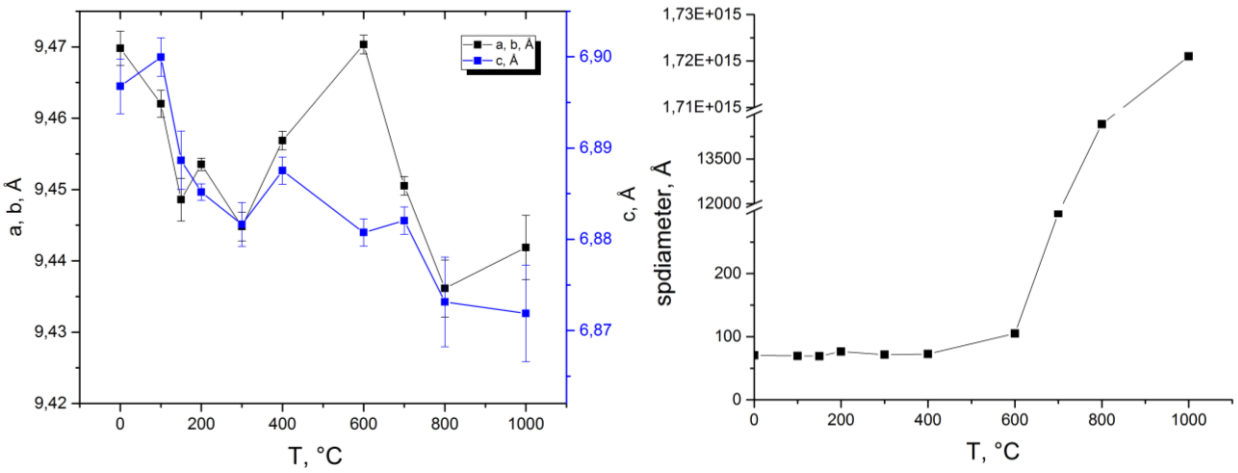

Figure 3.54. Left: lattice parameters vs temperature. Right: spdiameter vs temperature (errors are of the order of 10^{-2} $Å^{-1}$).

3.3.4.1. Partial pair distribution functions

Partial pair distribution function analysis allows the study of individual atomic pair contribution into *G(r)*. Once the resulting model is refined, it is used to calculate the theoretical contribution $G_{ij}(r)$ from each atomic pairs (Ca-Ca, P-P, O-O, Ca-O, P-O and Ca-P pairs) to the total *G(r)* as it is described in eq. 2.21.

As it can be seen in Fig. 3.55, the result of the simulation shows that the PDF technique is mostly sensitive to the relative positions of Ca and O atoms. The P-P contribution to the total PDF is very low.

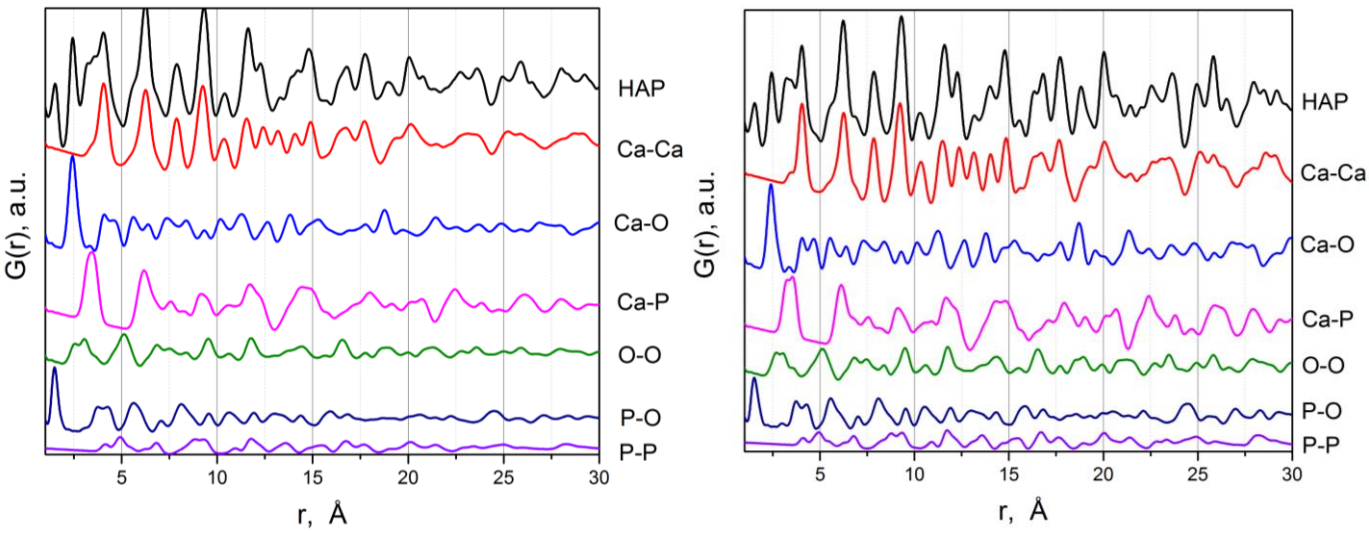

Figure 3.55. Partial pair distribution functions effect of total *G(r)* for control (left) and 1000 °C. All curves are offset for clarity.

The two first peaks in total *G(r)* reflect P-O and Ca-O bonds only, and the following peaks are already a superposition of many bond length contributions.

By looking at the plots of partial PDFs for the temperature series, it is very difficult to see some particular changes with temperature except the increase of crystallinity (as in example of P-O bond shown in Fig. 3.56, left) that give rise to overall intensity raise and peaks sharpening and separations from the broad superimposed maxima. Thus, the bond lengths were calculated from the resulting model structures (as in Fig. 3.56, right). The plots for all six atomic bonds partial PDFs (Ca-Ca, Ca-O, Ca-P, P-O, O-O and P-P) and their bond length evolution with temperature are shown in Appendix 4.

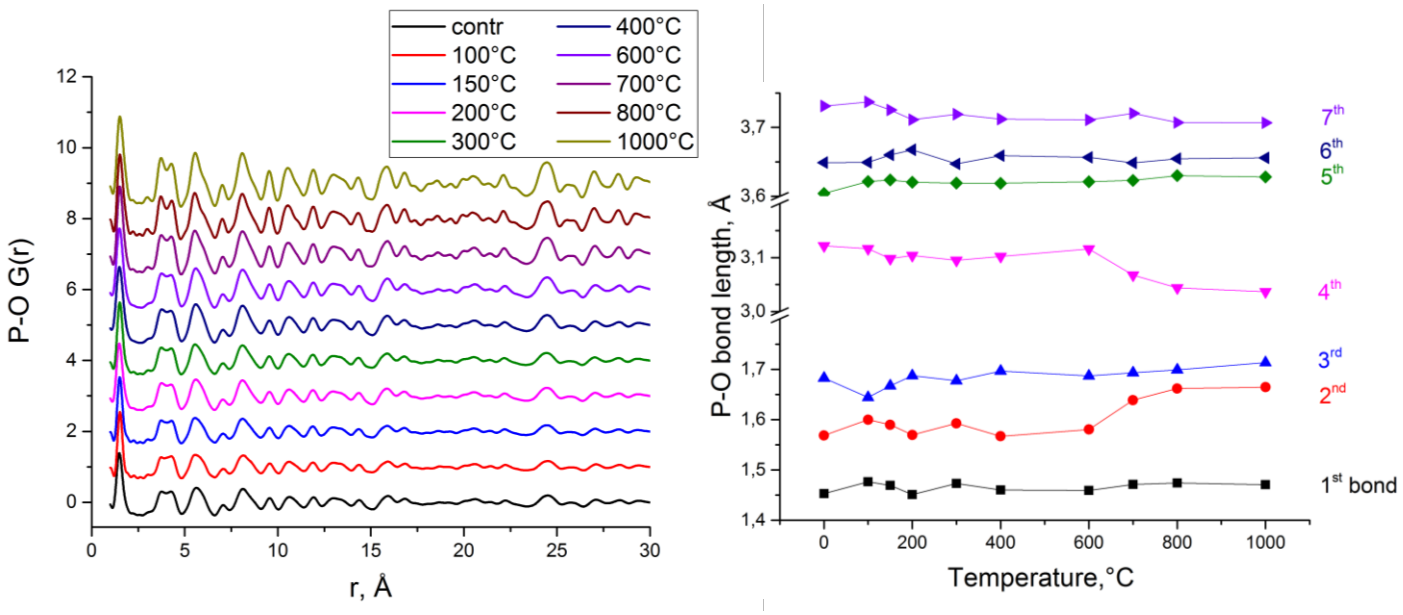

Figure 3.56. P-O atomic bond. Left: Evolution of partial PDFs with temperature. Right: Bond lengths vs temperature (each color shows a particular bond length between the *1st* to *7th* pair of P-O atoms).

In order to study the bond lengths distribution with temperature, it is important to mention that one should concentrate on bond lengths that give highest contribution into total *G(r)*, which are, in our case, Ca and O atoms since differences in P-P bond length cannot be appropriately resolved.

Ca-Ca *G(r)* undergoes a clear change after 600 °C, and eventually, atomic bonds get stabilized at 1000 °C at new values (grey areas in Fig. 3.57). But the most interesting is the behavior of Ca-O bonds. An average decrease is observed with temperature.

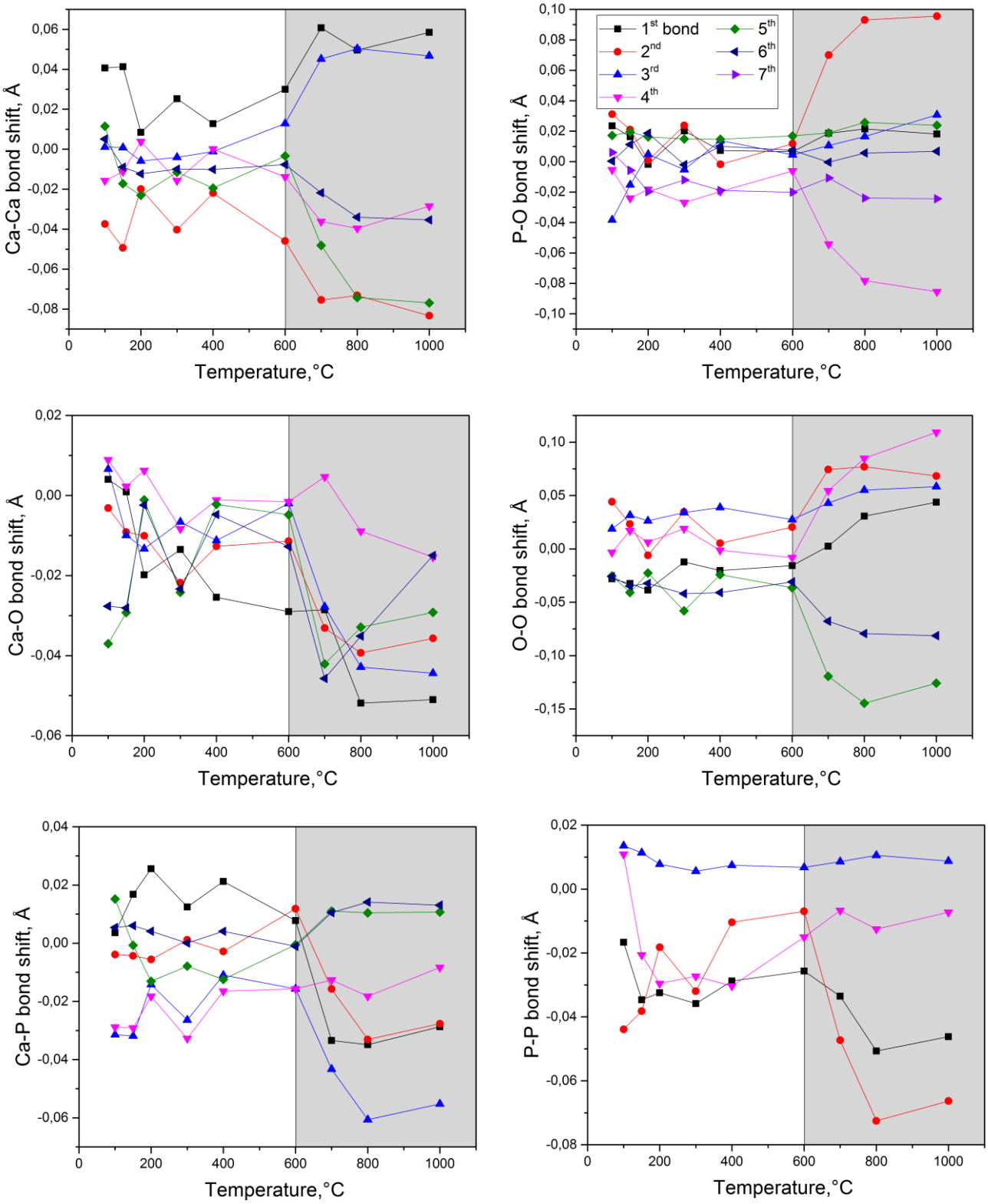

Figure 3.57. Bond length shifts from positions of control sample vs temperature. Each color shows a particular bond length (from *1st* to *7th* atoms pair) as indicated for the P-O bond shift.

Overall, from 700 °C, all bond lengths reach a plateau in a very striking manner, clearly signifying the occurrence of a structural transition (lattice energy is minimized). This effect can be better observed by plotting the bond lengths shifts from the position of control sample as is done in Fig. 3.57. Moreover, the evolution of all bond lengths below 600 °C is very disordered (non monotonic), before reaching a neat evolution toward the high temperature structure. This disorganized evolution is a clear indication of the complex modifications that bone tissue undergoes when heated at temperatures lower than 600 °C, in contrary to the absence of modifications that was concluded from Rietveld and other classical XRD methods. However, it is not clear if such subtle changes of the order of 0.02 Å are significant. Previous refinements indeed only showed a trend in lattice parameters and volume evolution vs temperature and the PDF analysis, therefore, could bring additional information.

Many debates exist about the possibility of co-existence of both crystalline and amorphous mineral phases in bone at control state [195,196]. A new model [169] was recently proposed implying the amorphous calcium phosphate layer surrounding crystalline hydroxyapatite. PDF analysis is, in principle, a perfect tool to verify existence of amorphous phase besides classical hydroxyapatite phase.

First of all, the hydroxyapatite structure obtained after modeling describes very well the experimental *G(r)* profile for the control sample (Fig. 3.58) and there is no need for a second phase for improving the fit as it was tested by the multiple phase model including both crystalline and amorphous calcium phosphate (the model resulted in 0% amorphous phase content). Nevertheless, we compared our data to an artificially synthesized amorphous calcium phosphate PDF profile (which is the phase expected to be present in bone by some authors) that was measured by another group (A. Fernandez-Martinez et. al, ISTER, Grenoble) at synchrotron ID15B beamline, ESRF.

The amorphous calcium phosphate (ACP) *G(r)* was calculated and refined with PDFgui starting from the same initial hydroxyapatite structure [64] used for bone fit, reducing the domain size to 6 Å. However, the stoichiometry of ACP data differs from hydroxyapatite as can be seen in Fig. 3.58: the first peak of ACP that corresponds to P-O bond lengths has higher intensity than the second one (Ca-O bond lengths) contrary to what is observed in hydroxyapatite. The stoichiometry is, therefore, expected to be between $CaPO_4$ and CaP_2O_4. In order to improve our model, the hydroxyapatite structure used for the fit was chosen to be Ca-deficient (with Ca vacancies) enabling the satisfactory fit of ACP data to be achieved. The scale factor obtained from this fit was used in order to normalize the ACP and bone data for

comparison as shown in Fig. 3.58. Assuming that distinguishable amount (few volume percent) of ACP was present in bone structure, the difference curve between bone data and hydroxyapatite fit (pink curve in Fig. 3.58) would be equivalent in shape (not in intensity) to the ACP curve (blue curve) which is not what is observed. Therefore, the PDF analysis, unlike

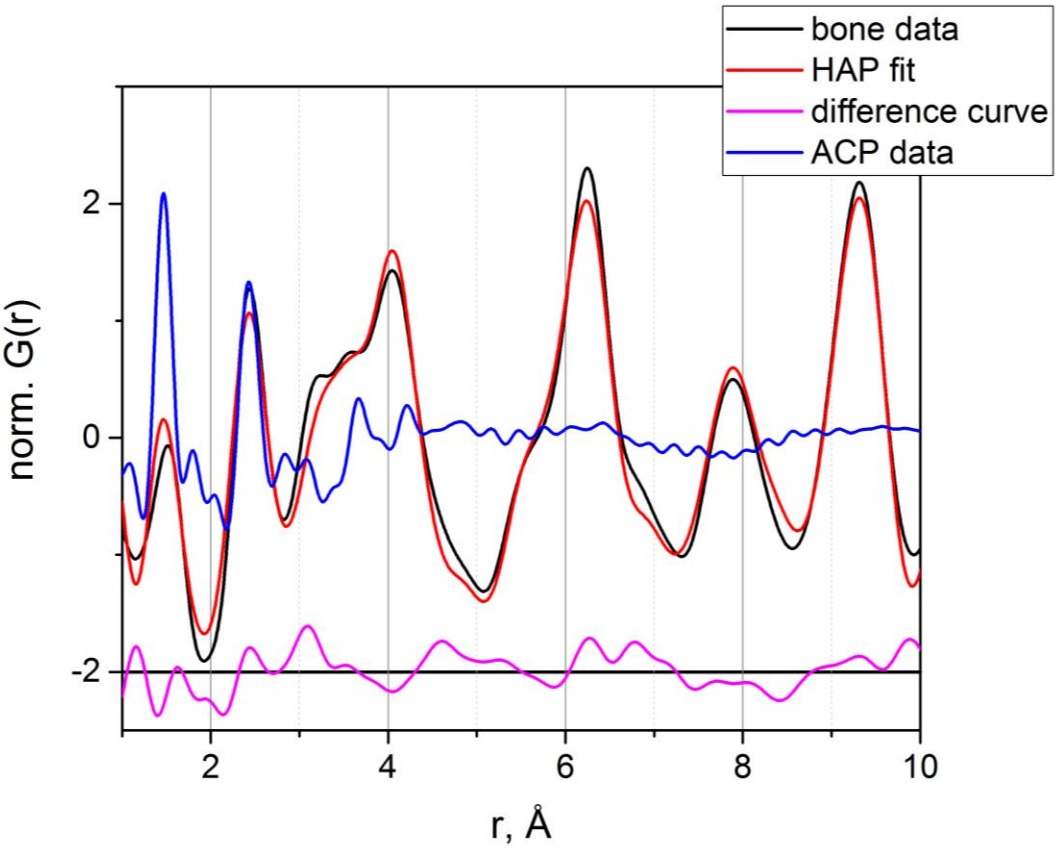

Rietveld, enables to draw the conclusion that within these experimental conditions no amorphous phase is observed or its quantity is too low to be distinguished.

Figure 3.58. The control sample *G(r)* with its model fit superimposed with experimentally obtained amorphous calcium phosphate *G(r).*

4.3.5. PDF analysis of pathological bone

Human pathological bone sections of 100μm thickness including control (CT1), fluorosis (Fluo1), hyperparathyroidism (HPT1, HPT2) and osteopetrosis (OPT1) diffraction patterns were recorded at ID11 beamline (ESRF) in a scanning mode with the energy of 78.25(78) keV (λ=0.158 Å), beam diameter of 10 μm, 10 μm step size and sample to detector distance of 100 mm. The detector (Frelon with 45.85 x 45.85 μm^2 (H x V) and 2048 x 2048 binning) was shifted horizontally to 1/3 of detector length in order to record high-*q*s. This allowed the *q*-range to extend to q_{max}=245 nm^{-1} despite the fact that some texture effects information was lost.

CeO_2 powder in 100 µm capillary and empty capillary were measured for calibration; data was masked for beamstop and detector dead pixels, corrected for beam decay, flat-field, spatial distortions and dark current.

The experimental resolution function parameters such as Q_{damp} and Q_{broad} were refined by calculating the PDF of CeO_2 and its fit to the model structure [197]. The refinement scheme consisted of scale factor, delta, lattice parameters and temperature factors refinement resulting in the following values of Q_{damp}=*0.0534*, Q_{broad} =0.01 with *rw*=0.21. These values were used for the refinement of pathological bone samples.

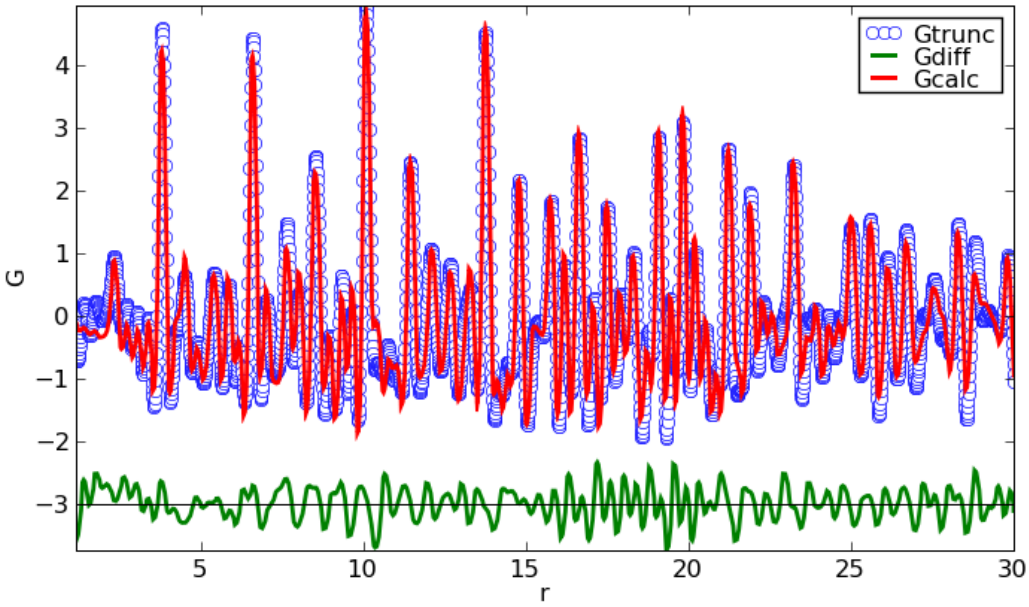

Figure 3.59. Experimental resolution function parameters refinement from crystalline CeO_2 PDF fit.

The measured pathological bone sample set profiles were radially integrated and PDF profiles were calculated for each scanning position by PDFgetX3 with r_{poly} = 0.9, $q_{maxinst}$ = 19 Å^{-1}, q_{min} = 1.2 Å^{-1} and q_{max} = 19.0 Å^{-1}.

Several masks were then built for elimination of the resin positions and for calculation of average PDF profiles for each sample. Optical (a) and polarized light (b) micrographs are shown for control (Fig. 3.60) and Fluo1 sample (Fig. 3.61) with indication of the scan position. Information about the rest of samples can be found in Appendix 5. The integrated intensity maps (c) of *I (q)* from 0 to 30 nm^{-1} are plotted with two masks: a conservative bone mask (d), used for calculation of sample average PDF profile, and an intermediate mask (e), that contains

data close to Haversian canals and external parts of trabeculae, and combined with the conservative bone mask it was used for the position-resolved study.

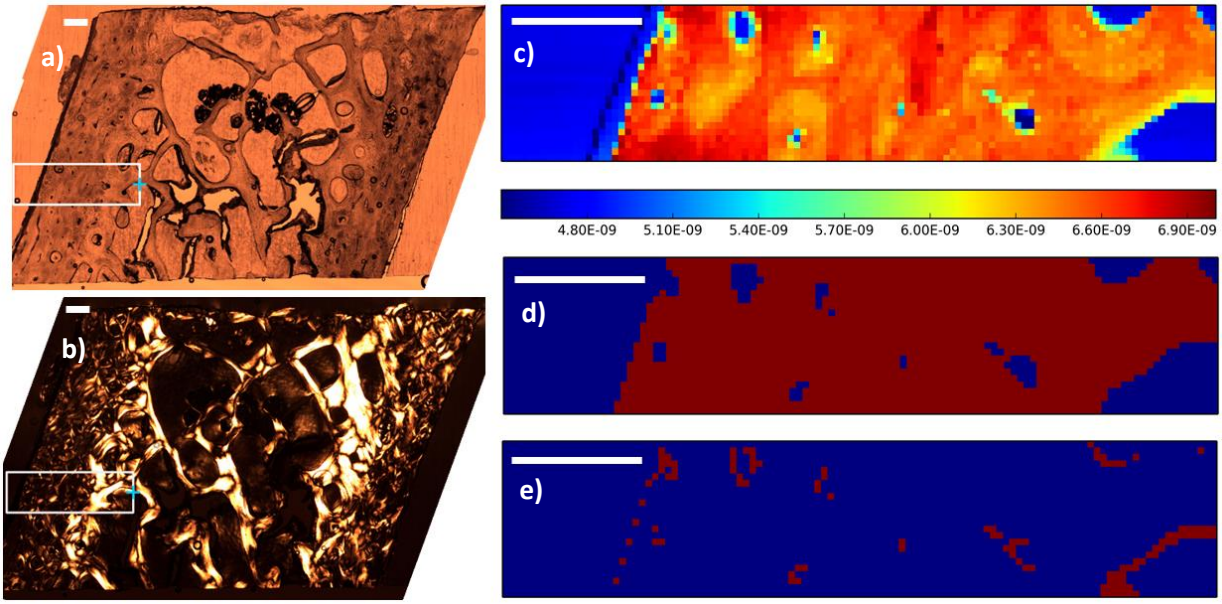

Figure 3.60. Control sample (CT1): a) optical micrograph and b) polarized light micrograph with indication of scanning area, c) integrated intensity map, d) conservative bone mask, e) intermediate bone mask. Scale bar: 200 µm.

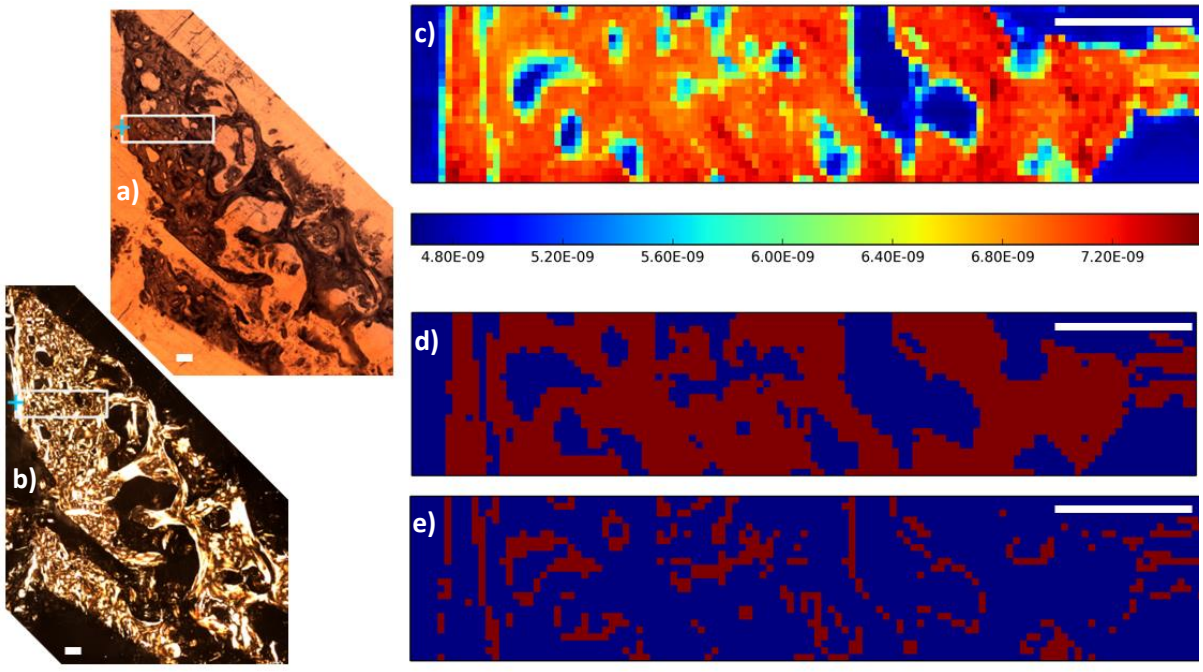

Figure 3.61. Fluorosis sample (Fluo1): a) optical micrograph and b) polarized light micrograph with indication of scanning area, c) integrated intensity map, d) conservative bone mask, e) intermediate bone mask. Scale bar: 200 µm.

4.3.5.1. Average PDF profiles of pathological bone

Thereby, PDF profiles were averaged for each sample using the conservative bone mask such as in Fig. 3.60d and Fig. 3.61d. The average PDF profile of the control sample was first compared to the control sample of the heated bone set measured in powder diffraction mode with laboratory source (see sub-chapter 3.3.4) as shown in Fig. 3.62 where several differences can be observed. Synchrotron measured profile has better low-*r* resolution as it is well seen at 3-4 Å peak in Fig. 3.62. At higher *r*, an overall peaks position shift is observed, which is inherent to the sample, indicating a change in mineral phase lattice parameters. An extra peak at 2 Å of the black curve comes from the *S(q)* corrections high *q* and is not related to the structure.

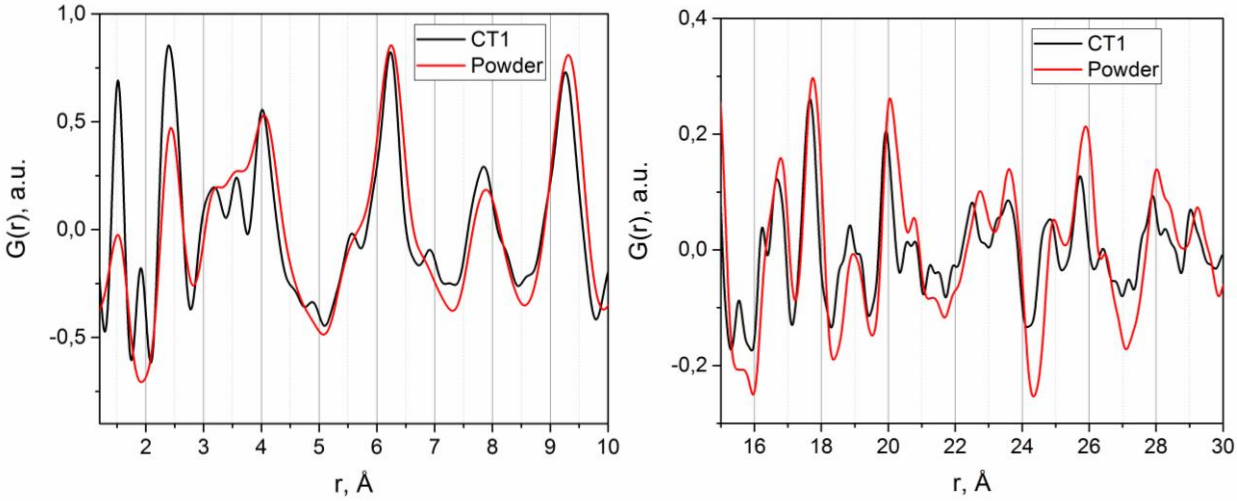

Figure 3.62. Comparison of control samples PDF profiles at different *r*-ranges measured in powder diffraction mode with laboratory source (red curve) and in scanning mode with synchrotron 10 µm diameter source.

The average *G(r)* profiles for five samples (CT1, Fluo1, HPT1, HPT2 and OPT1) are plotted in Fig. 3.63 at different *r*-ranges. It is clear that first several peaks (up to 4 Å) that correspond to first coordination sphere bond lengths of Ca-O and P-O (Fig. 3.64, right) are perfectly equivalent for all samples while at higher *r* many differences in both peak positions and width is observed as is shown in Fig. 3.64, left. This may indicate lattice parameters changes that will be refined in the following. The extension of *G(r)* oscillations at high-*r* is slightly different: the coherence length (or domain size) is higher for Fluo1 and HPT1 compared to the control sample.

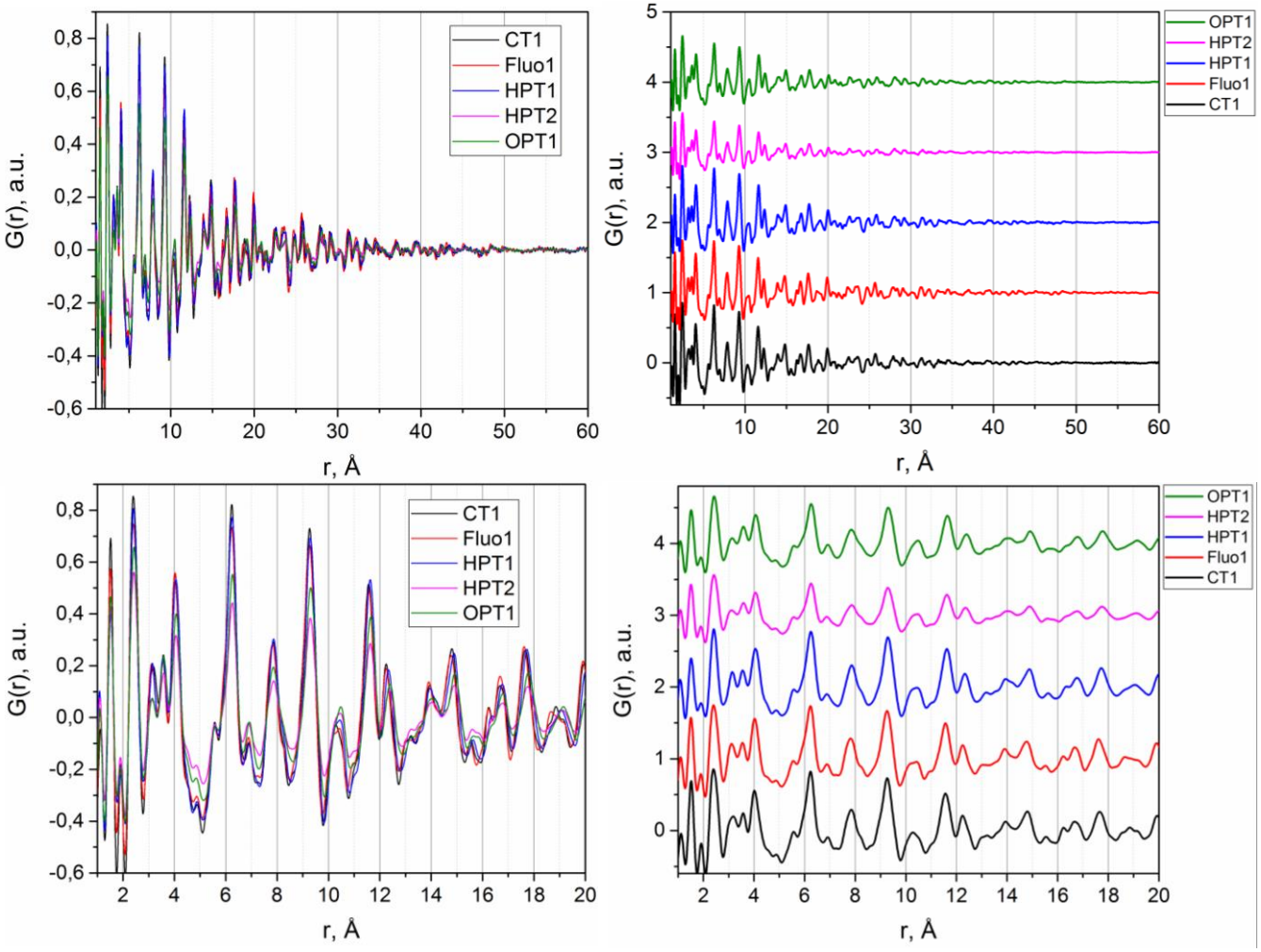

Figure 3.63. Average PDF profiles for pathological sample set (CT1, Fluo1, HPT1, HPT2 and OPT1) at different *r*-ranges. Left: no offset. Right: with offset.

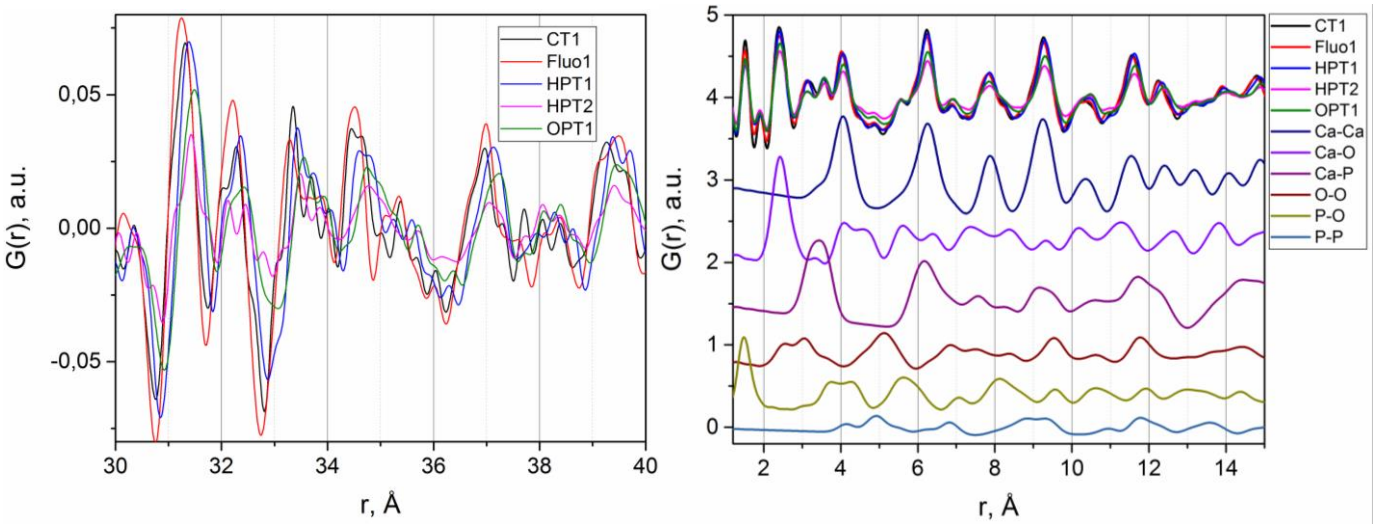

Figure 3.64. Average PDF profiles of pathological sample at high-*r* (left) and partial PDF contributions of the control sample to the total *G(r)* (all *G(r)* are represented).

The PDF refinement was done by PDFgui software for averaged profiles of the pathological sample set. The structure file for refinement was chosen to be the same as for ACOM-TEM and heated bone PDF analysis [64]. The experimental resolution function parameters (Q_{damp} and Q_{broad}) refined for CeO_2 etalon were fixed.

The refinement scheme was chosen to be as following for each PDF profile:

1) scale factor;
2) delta;
3) spdiameter;
4) *a* and *b* lattice parameters;
5) *c* lattice parameter;
6) nine parameters for isotropic thermal factors.

Examples of fit are shown in Fig. 3.65 for CT1 and Fluo1 sample (other samples are shown in Appendix 5). The resulting *rw* factors range from 0.21 to 0.28 which is considered as a reliable fit.

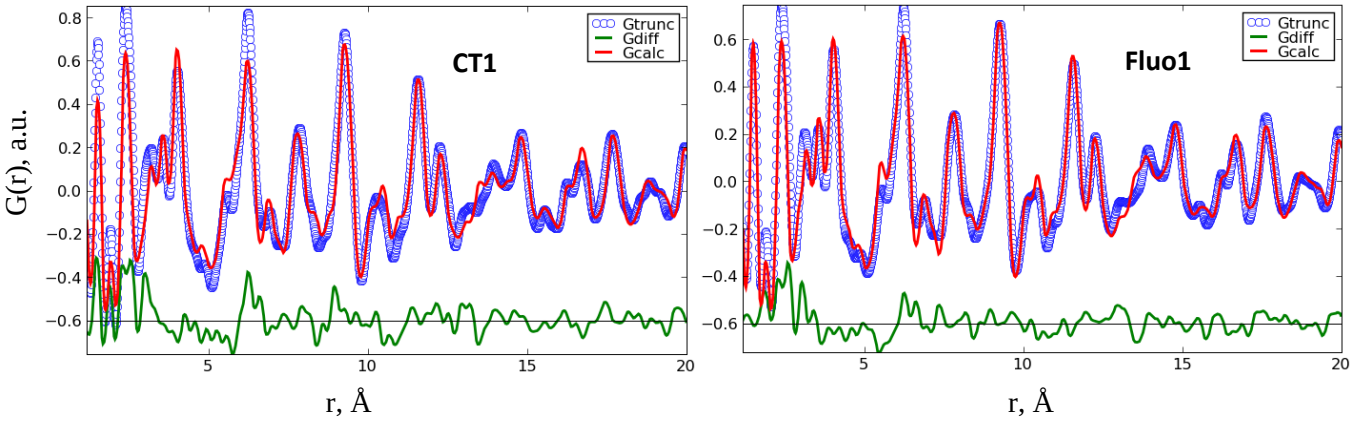

Figure 3.65. PDFgui refinement for CT1 and Fluo1 samples: blue – experimental profile, red – fit, green – difference curve.

The refined lattice parameters *a*=*b* and *c* for four samples (Control, Fluo1, HPT1 and OPT1) are shown in Fig. 3.66. A decrease in both *a* and *c* parameters is observed for bone affected by fluorosis and an increase is seen for hyperparathyroidism and osteopetrosis. The spdiameter which is attributed to the domain size in spherical approximation diminishes strongly for the osteopetrosis sample, slightly for the fluorosis case and is increases for hyperparathyroidism as shown in Fig. 3.67.

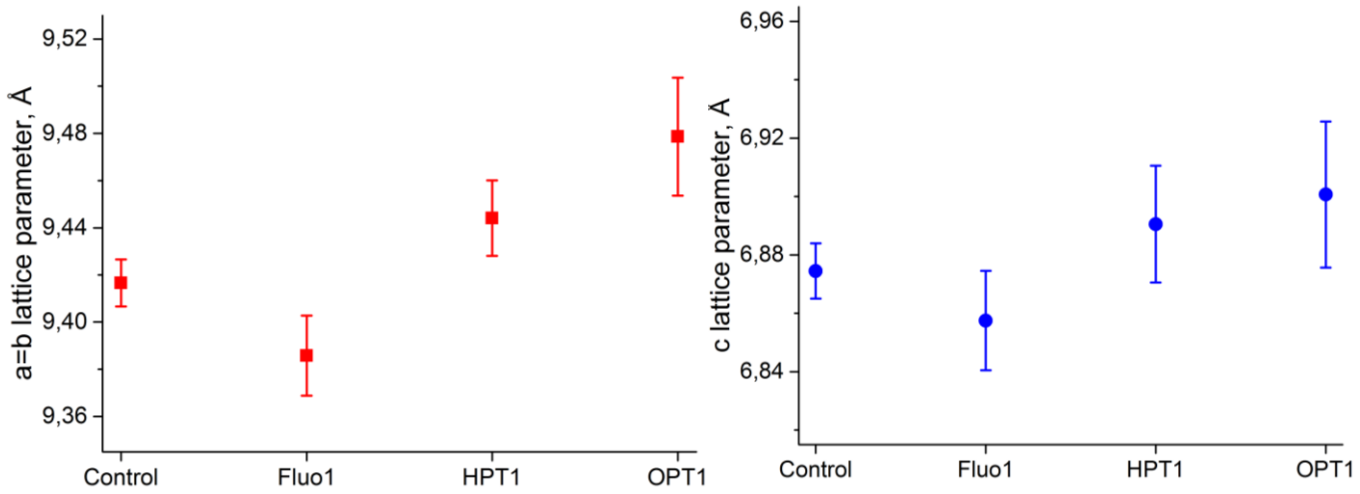

Figure 3.66. Lattice parameters refinement for pathological bone sample set indicating a decrease for Fluo1 and increase for HPT1 and OPT1.

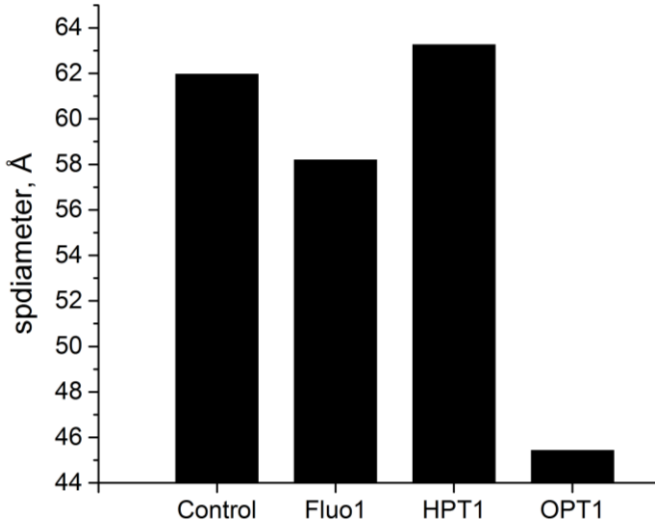

Figure 3.67. The spdiameter refinement for pathological bone sample set.

4.3.5.2. Position-resolved PDF of pathological bone

The advantage of the scanning mode in recording the diffraction patterns for PDF analysis not only decreases the illumination volume but also allows position-resolved bone characterization.

In order to address the heterogeneity of the sample and the need of position-resolved measurements, *G(r)* for each sample was analyzed by fitting four selected peaks at each scanning position at different *r*-extensions: 1.5, 2.4, 11.5 and 17.6 Å (that are shown with red arrows in Fig. 3.68) with a Gaussian (first two) and an asymmetric Gaussian functions (last

two) depending on the peak shape. Therefore, the maps indicating peaks position, intensity and FWHM were obtained by applying the mask that combines both conservative bone mask (Fig. 3.60d) and intermediate mask (Fig. 3.60e) to filter the data coming from the resin.

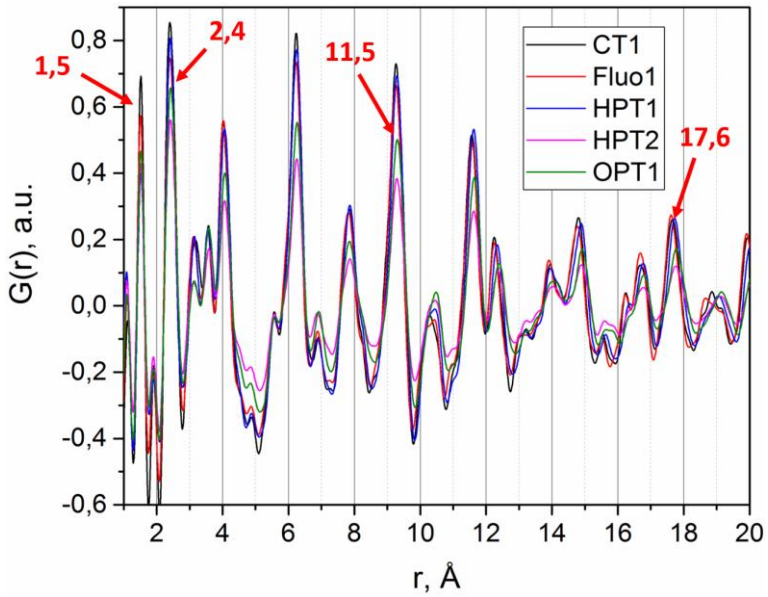

Figure 3.68. Averaged bone *G(r)* profiles for pathological sample set with indication of four selected peaks for fitting for position-resolved study.

The example of position, intensity and FWHM maps for 1.5, 2.4, 11.5 and 17.6 Å peaks of the control sample are drawn in Fig. 3.69 and Fig. 3.70, equivalent maps are constructed for pathological samples and are shown in Appendix 5. The first peak of 1.5 Å corresponds to first coordination sphere P-O bond lengths as shown in Fig. 3.55 and Fig. 3.64 (right). As indicated by quite homogeneous colors, no differences in peak position and width are observed for the control sample (which is not the case for HPT1 and OPT1). However, the peak at 2.4 Å, indicating the first coordination sphere of Ca-O bond lengths, shows a shift in peak position of 0.03 Å between trabecular bone part and mid-cortical and a difference in FWHM of 0.1 Å.

The same tendency is observed for other samples depending on scan position. At higher *r*, peaks encode too many bond length contributions but their position shifts indicate lattice parameters differences of the local structure from the average structure. The 11.5 Å peak does not show much discrepancies for most samples except for HPT1. The 17.6 Å peak shows the position shifts of 0.1 Å gradually moving from one sample side to another (see Fig. 3.70) for control as well as for Fluo1 and OPT1 samples. Quantitative changes should be further refined in terms of lattice parameter shifts by PDF modeling.

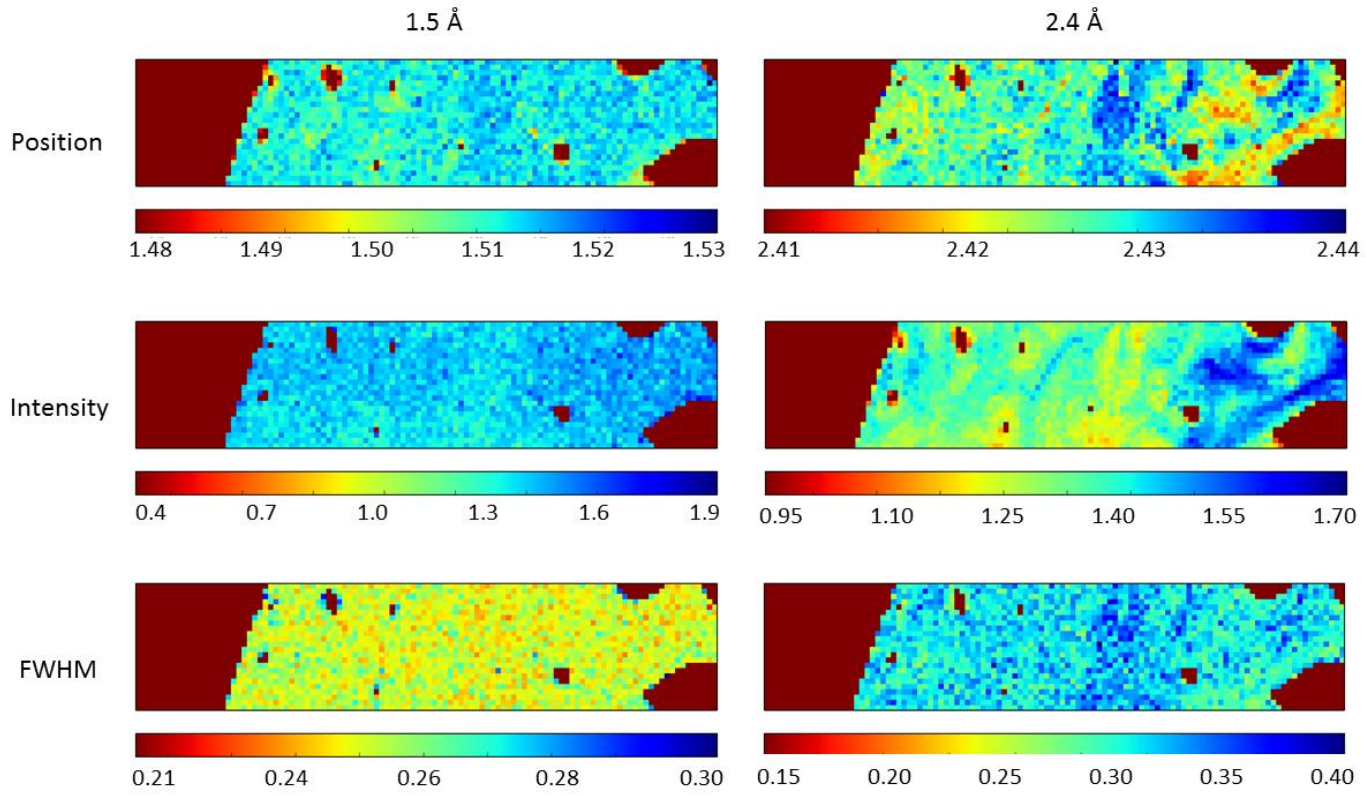

Figure 3.69. Position, intensity and FWHM of *1.5* and *2.4 Å* peaks for the control sample.

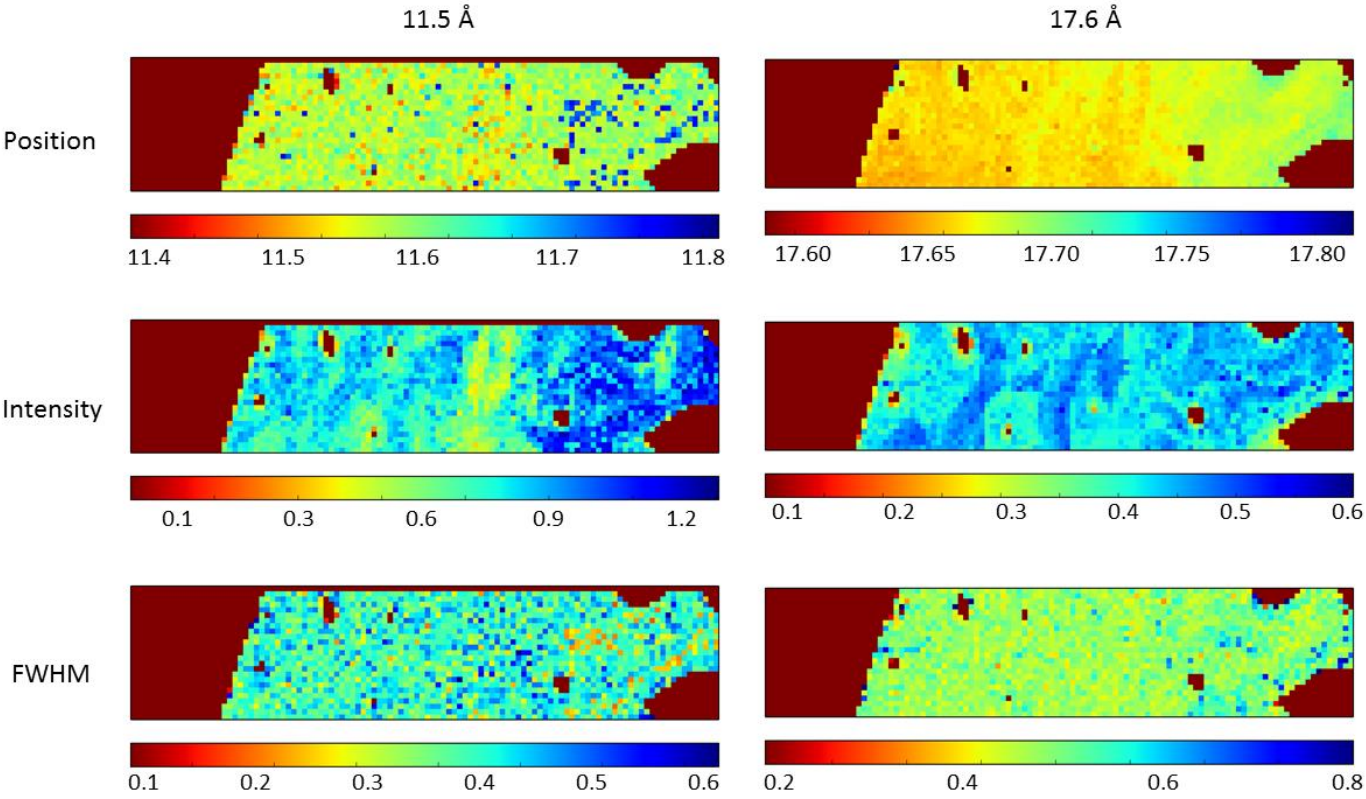

Figure 3.70. Position, intensity and FWHM of *11.5* and *17.6 Å* peaks for the control sample.

It is clear from current results that position-resolved PDF analysis is required. However, a tool for large dataset multipurpose PDF fit is currently not available and is under development by S. Billinge group (Columbia University, USA).

Discussion and perspectives

The foremost goal of the current work lies in understanding how the mineral structure of bone tissue is organized at different length scales. Relatively new methods currently in development for materials science analysis, such as CXDI, ACOM-TEM and PDF analysis, were used to characterize bone mineral phase.

CXDI is a powerful technique for high resolution 3D visualization; however, its use remains very challenging for biological materials, particularly with respect to sample preparation: sample size is defined by the coherence beam region size and is currently limited to isolated samples of around 5 µm in diameter. The reconstruction algorithm is robust and provides successful reconstructions when all experimental requirements are fulfilled (sample size, isolation, scattering power, etc.). However, the averaging of selected reconstructions based on error metrics value [149] is advised for visualization purposes.

The first application of CXDI to dentin tissue provided spatial resolution of the order of 20-50 nm that allowed nanoporosity and the collagen periodicity to be observed. However, the differences in mineral contrast at different locations are not significant to consider CXDI a viable future tool for mineralization studies. Overall, for very heterogeneous hierarchical biological materials such as bone and dentin, application of CXDI due to the small sample size requirement may present difficulties to include the histological relevance. Application of FIB or UV laser cutter in the final step of sample preparation is therefore required allowing attributing the obtained results to the precise location of the ultramicrotomy slice within the tissue. Such sample size limitation makes CXDI perfectly suited for nanocrystals, core-shell structures, nano-objects, etc. Yet, in order that CXDI becomes significant in the field of biological materials, the semiautomatic sample preparation, measuring and analysis tools should be developed. Improving the detector properties (pixel size and area), the source coherence and brilliance will be a step forward in terms of spatial resolution and field of view that draws strong perspectives for individual bone nanocrystals visualization.

Overall, CXDI provides complementary information to other methods at few micrometers field of view and with 20-50 nm resolution. Compared to nanotomography, it shows significantly better resolution but lacks in field of view. For example, a number of papers reported the trabecular bone organization with the resolution of the order of 10 µm and a field of view of few cm [198–200], the resolution of 1 µm with a field of view of few mm [201] and, at last, the 300 nm voxel size with 600 µm field of view [202].

The other coherent imaging technique, ptychography, is a strongly progressing tool based on oversampling the object reciprocal space by scanning it with a nanobeam in overlapping configuration and simultaneously reconstructing the beam profile and object in real space [203,204]. This partially allows overcoming the problem of limited sample size; however, the instrumental stability becomes crucial. The experimental setup required to focus an X-ray nanobeam for scanning experiment is much more complex than for CXDI, and any slight drift during scanning can introduce artefacts in the reconstruction procedure. In collaboration with B. Weinhausen at ID13 (ESRF), ptychography experiments were performed on bovine bone sections of 100 nm thickness prepared by ultramicrotomy as described in Chapter 2. Several successful reconstructions were obtained indicating slight mineral contrast change near lacuna-canaliculi network compared to other bone regions. The new development in quantitative interior ptychographic nanotomography is based on two measurements: the classical nanobeam scanning tomography of a small inner part of the sample and the low exposure overview scan of the whole sample volume [205]. It allows combining the high resolution advantage of ptychography (up to 10 nm voxel size) and the relatively large field of view and quantitative measures of the classical scanning diffraction.

Historically for investigation of individual nanocrystals, TEM was the tool of choice. The sub-angstrom resolution is currently achieved with the state-of-the-art double corrected Titan microscopes. However, the sample preparation is very difficult (especially for mineralized tissues). Both insights, relative high resolution and structure-phase information, are combined in ACOM-TEM where the sample is scanned with a beam of the order of 2 nm diameter in the diffraction mode and the template matching algorithm allows reconstructing the orientation maps. The nanocrystal orientation, organization, phase, symmetry and ionic substitutions were accessed by ACOM-TEM in bone for the first time. This tool is proven to be ideal for the study of bone tissue with crystal size larger than in a control state as in some pathological cases such as fluorosis.

Some improvements can be made in the fast camera resolution that would allow analysis beyond crystal orientation mapping. PDF analysis based on scanning electron diffraction has a great potential due to much smaller illumination volume [206]. Smaller beam size would provide an advantage in resolution after overcoming problems with beam convergence.

Cryo-ultramicrotomy in combination with cryo-TEM may slightly improve the bone sample quality and reduce the radiation damage risks. Environmental TEM may also provide a unique possibility of looking at the bone sample without dehydration and fixation in the state the closest to native, however, with a loss in resolution.

In addition, current developments in electron tomography [13] and atom probe tomography [207] offer 3D information at high spatial and elemental resolution despite very specific FIB sample preparation schemes including the protective layer deposition and beam current fine tuning.

PDF analysis was also applied to bone, to the best of our knowledge, for the first time. Bone structure and subtle local chemistry deviations from the average structure were investigated for the heated bone sample set. Its power in pathological bone cases is confirmed and illustrated.

Bone is known to give a highly overlapping X-ray diffraction profile with large broadening of peaks. The Rietveld method allows taking into account peaks broadening and overlapping in the refinement process. An alternative solution is offered by PDF analysis where those profiles are analyzed in real space.

However, there are several advantages and disadvantages of the two methods that have to be considered. If the diffraction correlation domain of the measured material extends far, Rietveld will provide a decent refinement, and there is no real need for PDF analysis. Otherwise, if correlation domains are small, Rietveld will fail, but PDF analysis will allow dealing with such structures. However, if comparison or parallel investigation of both large and small correlation domain structures are required, PDF analysis offers the possibility of such complex study.

In addition, fitting of different parts of $G(r)$ profile, i.e. at different r extensions, to the model structure allows investigating local deviations from the average structure. Another

advantage of PDF is that even noisy laboratory source profiles with poor statistics will be suitable for PDF refinement, while Rietveld will fail to describe the overlapping peaks.

Nevertheless, Rietveld refinement allows taking into account anisotropy whereas the current implementations of PDF analysis using available software is based on spherical approximation. In addition, Rietveld permits the strain determination, while in PDF analysis the stain information is encoded within atomic thermal factors.

Three new techniques were applied to bone tissue multi-scale characterization: TEM-ACOM and PDF for the first time to bone and CXDI for the first time to both dentin and mammal bone. The complementarity of these methods was shown covering the wide range of hierarchical length scales: from micrometer scale with tens of nm resolution with CXDI to sub-angstrom scale with PDF analysis.

The use of CXDI, ACOM-TEM and PDF eventually gave us information that is summarized below.

From CXDI, we investigated micrometer field of view with 20 nm resolution, observed for the first time collagen banding pattern in mammal samples. We also shed the light on the existence of collagen-apatite porosity that was not, to the best of our knowledge, evidenced before.

ACOM-TEM provides the single crystal investigation with atomic resolution over a field of view of around 400 nm. It enables the characterization of crystals orientation, space group, and deviation from the model hydroxyapatite structure in addition to lattice parameters, ionic substitution, apatite stoichiometry and chemical composition. This first application of ACOM-TEM on bone enabled clarification on various debates on the phases and phase transitions that take place in bone upon heating.

Eventually, PDF gives insight into the domain size, lattice parameters and bond lengths as well as classical Rietveld refinement in the case that the sample exhibits good crystallinity, but leading to different results otherwise. We therefore obtained new information on the control sample, bones heated at temperatures lower than 600 °C, when detecting such subtle changes was not expected by the community. Moreover, it allows an investigation of the disorder present in the system, enabling to draw the conclusion that in our experimental conditions, no amorphous domains could be identified. The first promising investigation of pathological bones with PDF analysis, both in average PDF and in scanning mode, allowed

identification of sub-atomic scale characteristics that differ between pathologies and, even more striking, depending on the histological location.

It is well known that the structural organization of bones is relevant on very different length scales. We investigated samples from their sub-angstrom arrangement taking into account chemical composition, through individual crystal organization (one crystal with respect to the next) to their micrometer organization with nanometer resolution, i.e. nanoporosity structure within the tissue.

We demonstrated that differences can be characterized with these three techniques on heated bone, of interest in archeology, anthropology and forensic science. The domain size increase, structural phase variation, improvement in crystallinity, lattice parameters deviations, the collagen denaturation before 300 °C, chaotic changes in atomic bonds between 100 and 600 °C followed by rapid stabilization from 700 °C are observed in heated bone. Furthermore, we report the evolution in individual crystal organization by the recrystallization mechanism followed by the formation of large crystal clusters and overall homogenization at the micrometer scale with an increase in nanoporosity volume.

For pathological bone tissue, it is expected that differences are present from the micrometer to individual crystal organization scales. We validated CXDI and ACOM-TEM application for bone and dentin tissue, and gathering of the nanostructural information from the pathological sample set can be further performed. Moreover, we were able to demonstrate using PDF analysis on the pathological sample set that structural differences, depending on the pathology, appear already at the sub-angstrom organization scale. We therefore propose advanced and complex but valuable new tools for bio-medical studies.

These results show promising perspectives in understanding the nanostructural characteristics of bone tissue and identifying key structural markers of pathological human bone, providing possible future development of new diagnostic and pharmaceutical tools. The multiscale characterization scheme described in current work can be easily applied to other biomaterial such as antler or fish bone as well as to a broad range of nanostructured materials.

Appendix 1. Sample preparation supplementary information

A.1.1. Detailed embedding protocols

PMMA embedding:

I. Fixation: at least 10 days in ethanol 70%. Can be longer especially for cortical bone depending on sample volume.
II. Dehydration: 48 hours in ethanol 100%.
III. Substitution: 48 hours in methylcyclohexane (not more).
IV. Impregnation and inclusion:
    - Purify methyl methacrylate (MMA) with aluminium oxide (Al_2O_3 grains). Add ~75 ml of Al_2O_3 grains into 1 *l* of MMA and stir for 15 min. Then filter MMA with the solid filter or teflon filter of 0.2 µm porosity. The glass dishes and cringes have to be used because MMA dissolves plastics. Repeat 3 times.
    - Mix 80% of purified MMA with 20% of dibutyl phthalate. The resulting solution is called MMA1. Keep samples in MMA1 for at least 5 days for cortical bone (48 hours min for trabecular) at 4°C. The pre-prepared MMA1 solution can be stored in the fridge.
    - Mix MMA1 with 1 gr percent of benzoyl peroxide (just before the process). The resulting solution is called MMA2. Keep samples in MMA2 for at least 3 days (cortical), 2 days (trabecular) at 4°C.
    - Mix MMA with 2 gr percent of benzoyl peroxide (just before the process) = MMA3. Keep samples in MMA3 for at least 3 days (cortical), 2 days (trabecular) at 4°C.
    - For inclusion, fill samples with MMA3 in glass bottles with covers or in PTFE flat embedding molds. In the second case ACLAR film has to be used to provide oxygen free solidification. The mold is covered with the

corresponding size of ACLAR film slowly starting from the corner to all the mold. In this way bubbles formation under the film can be avoided. Keep samples at 32°C for 48 hours. Temperature has to be well controlled at 32°C or slightly less to prevent bubbles formation.

Epon embedding:

I. Fixation:
- 1 volume of glutaraldehyde of 4%;
- 1 volume of cacodylate of 0.2M. Adjust pH to 7.4. Leave for 2 hours maximum at 4°C.

II. Washing:
- 1 volume sucrose of 0.4M;
- 1 volume cacodylate of 0.2M; pH=7.4. Make two baths of 1 hour and then one bath overnight at 4°C. Rinse in distilled water.

III. Dehydration:
- 30 min in ethanol 30%;
- 30 min in ethanol 50%;
- 30 min in ethanol 70%;
- 30 min in ethanol 95%;
- three baths of 30 min in ethanol 100%.

IV. Substitution:
- two baths of 1 hour in 50% propylene oxide in ethanol;
- 1 hour in 100% propylene oxide.

V. Impregnation:

To prepare Epon solution EmBed-812 Embedding kit from EMS was used. For hard tissues, as bone, Epon B solution is prepared in the following proportion: EMBed-812: 20 ml; DDSA: 9 ml; NMA: 12 ml; accelerator DMP-30: 0.62-0.82 ml.

Prior to measuring and mixing, the resin and anhydrides should be warmed to 60°C to reduce their viscosity. First, EMBed-812 is well mixed with DDSA and NMA and accelerator is added in the end (it will change the color of the solution). Mixing is imperative to be able to achieve uniform blocks.

- bath overnight in 50% Epon without accelerator in propylene oxide;

- 1 day in Epon 100% without accelerator (change the bath 3 times during a day);
- bath overnight in Epon 100% with accelerator (DMP-30).

In all impregnation stages, eppendorf centrifuge should be used.

VI. Inclusion: in Epon 100% with accelerator. Pour small quantity of the mixture into flat embedding mold and cure in the oven for 15 min. Then, position the samples in the mold, cover them with resin and cure for 48 hours at 60°C.

LR white embedding:

I. Dehydration:
- 30 min in ethanol 30%;
- 30 min in ethanol 50%;
- 60 min in ethanol 70%;
- 60 min in ethanol 85%;
- 60 min in ethanol 95%;
- 60 min in ethanol 100%;
- 120 min in ethanol 100%;
- overnight in ethanol 100%.

II. Impregnation: should be done in sealed glass bottles in centrifuge. In this protocol LR white is used without accelerator.
- 120 min in 80% of absolute ethanol in 20% of LR white;
- 120 min in 60% of absolute ethanol in 20% of LR white;
- 120 min in 40% of absolute ethanol in 20% of LR white;
- 120 min in 20% of absolute ethanol in 20% of LR white;
- overnight in LR white 100% at 4°C;
- 8 hours in LR white 100% at 4°C;
- overnight in LR white 100% at 4°C.

III. Inclusion:

The molds (gelatin capsules or PTFE flat embedding molds) are filled with the resin. The samples are then positioned in the molds. Molds are overfilled with resin and covered with capsule covers or ACLAR film to block access to oxygen in the way that no air bubbles are created. Cure samples for 4 days at 60°C.

Epofix embedding:

Epofix embedding kit from Struers is used. Mix 15 ml of resin and 2 ml of hardener (or equivalent) by avoiding as much as possible bubbles formation. Pour it into plastic molds that contain samples. Put them under dynamical vacuum in the desiccator for 10 min, enabling the bubbles created in the resin to move to the mold surface. Keep it then closed under vacuum for the solidification time of 8 hour at room temperature.

A.1.2. Ultramicrotomy cutting

First, sample is trimmed by hand under the loop with the metallic blade to achieve flat cubic shaped surface of 1x1 mm^2. The second step of trimming is done with the use of trim diamond knife (Fig. A.1.).

Figure A.1. Diamond knifes used in ultramicrotomy. From left to right: trimming knife, histo (semi-thin sections 10 um -150 nm), ultra 35° (ultrathin sections 100-10 nm).

The optimal trimming scheme is shown in Fig. A.2 and is described as:

1. First, trim the sample surface with the front facet (step 1 in Fig. A.2). Mark the original sample angular position.
2. Turn the sample to +20° and shift the knife on the left in the way that its right side cut the sample (step 2 in Fig. A.2). Trim until the all sample side is cut.
3. Turn the sample to -40° (-20° from original position) and shift the knife correspondingly to the right and cut until all side is cut (step 3 in Fig. A.2).
4. Turn the sample back to starting position.
5. Turn the sample to +90° and cut the future pyramid top side (step 4 in Fig. A.2).

6. Shift the knife on the left side and cut the future pyramid bottom side (step 5 in Fig. A.2).
7. At last, turn the sample to starting position and finish the sample surface (again) with the front facet (step 1 in Fig. A.2).
8. Check by the knife motors the geometry of the resulting trapezoidal pyramid. The correct distances are: bottom side: 400 µm; top side: 100 µm, height: 330 µm. This is the maximum area; in some cases the trapezia should be decreased (by keeping the size ratio constant with a min of 5 µm for the top side). If the sizes are too large, repeat the necessary steps above until correct dimensions are achieved.

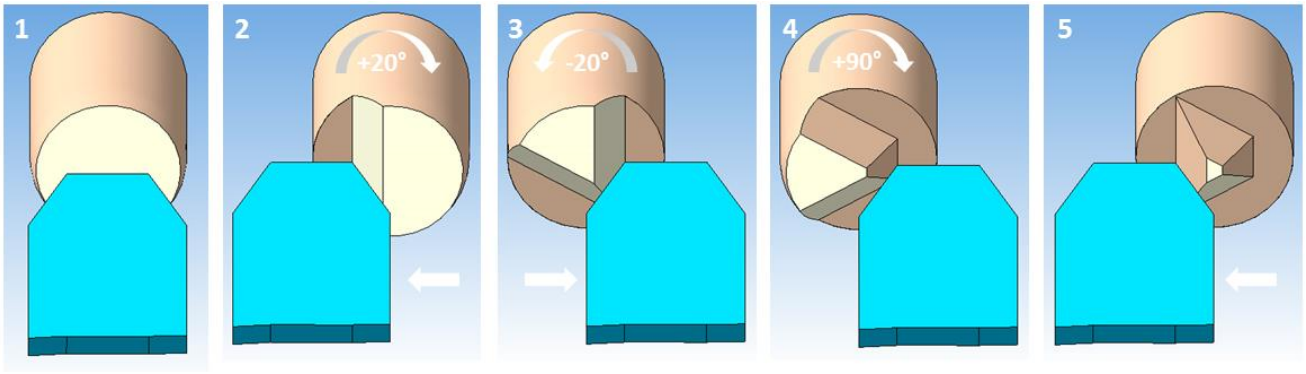

Figure A.2. Trimming scheme for achieving the pyramid with the trapezoid shape face: 1) trim the sample surface with the front facet; 2) trim first trapezoid pyramid side with the right knife edge; 3) trim second first trapezoid pyramid side with the left knife edge; 4) trim up pyramid side with the left knife edge; 5) trim bottom pyramid side with the right knife edge. All angles shown are relative to initial angular position.

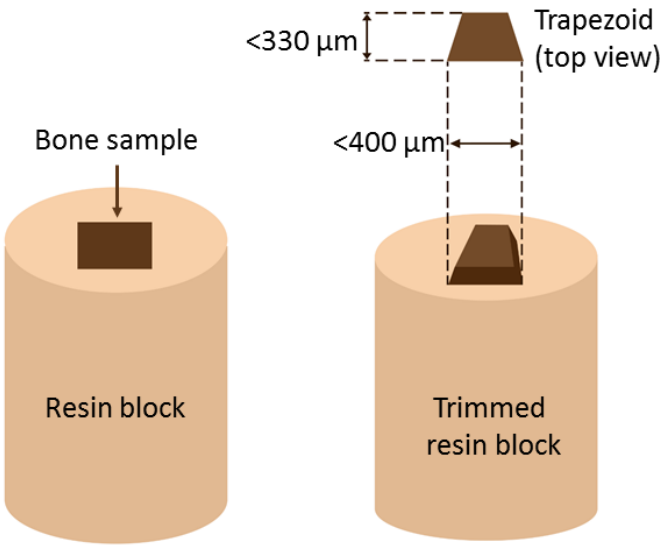

Figure A.3. View of the sample before and after trimming with the trapezoid dimensions.

Before starting trimming after any change in sample angle or knife position, set correct start and end position of the specimen arm. The optimal advance for trimming bone tissue with trim 45 diamond knife is 1 µm and the speed is 100 mm/s

After the trimming is complete, change the knife to histo (Fig. A.1.) and follow the following steps:

1. Set the clearance angle on the knife stage to the value advised by the knife in specification.
2. Bring the knife close to the block so that you can see both the block face and the knife edge with a binocular of the ultramicrotome. Focus the binocular on the knife edge.
3. Align the block face with the knife edge.

   Proper alignment of knife and specimen block is critical for successful sectioning and requires practice and patience [208]. You can change angles and positions of your block and knife using the knobs on the microtome. First, the parallel sides of the trapezoid block face are oriented parallel to the knife edge (see Fig. A.4, front view). Subsequently, the surface of the block face must be oriented parallel to the knife edge in both vertical and horizontal directions (Fig. A.4, top and side view).

   The proper alignment is judged by observing the reflection of the knife edge on the block face. The width of the reflection represents the distance between the knife and the block face. If the knife and the block face are parallel to each other, the reflection should have the same thickness across the block face (Fig. A.4, top view) and the same thickness should be maintained when the block moves past the knife edge (Fig. A.4, side view). When reflection disappears - the knife and block face are in contact (or almost in contact). The reflection may appear somewhat different depending on the specific knife and resin that is used.

4. Set the set the correct start and end position of the specimen arm, the advance (1 µm) and the retrieving speed (“fast”).
5. Fill up the knife boat with fresh distilled water (with the slight overfill in the way that water covers fully all knife edge). Swipe the surface of the water with Parafilm piece to remove any dust particles.

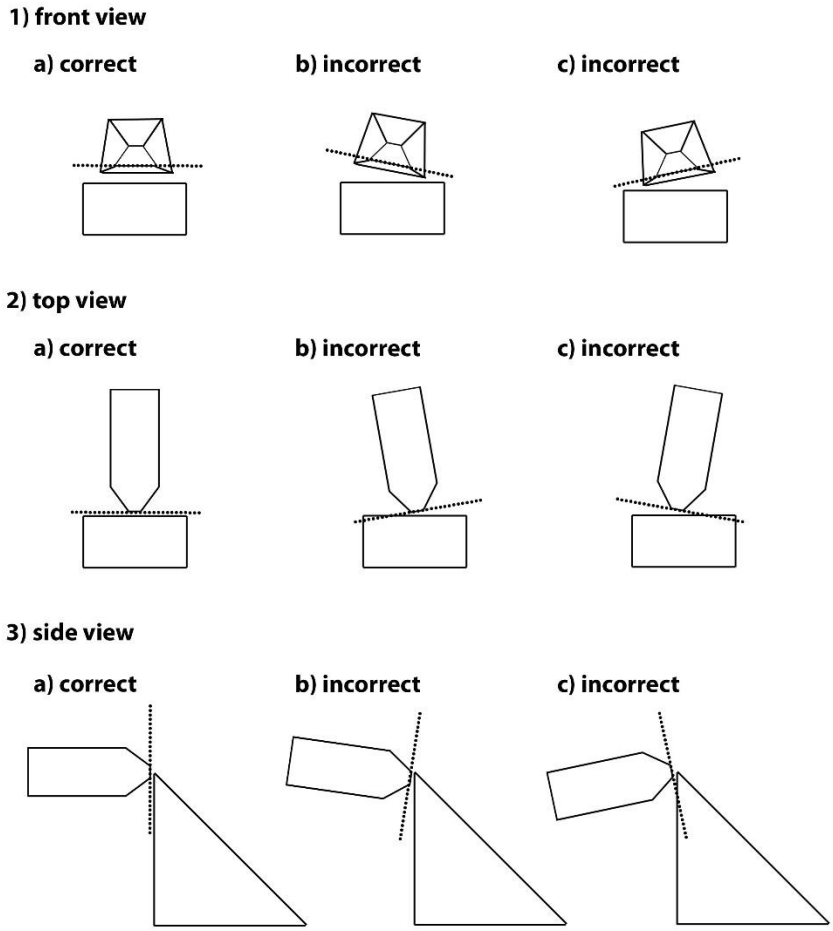

Figure A.4. Aligning the resin block and knife for thin sectioning. Possible correct and incorrect positions of the block with respect to the knife edge in all three dimensions [208]. Advance the block face towards the knife and observe the reflection of the knife edge getting thinner and thinner. Use the 1µm advance once you get very close to the knife edge.

6. Adjust the water amount to the correct level. The general rule is to overfill the bath first and to slowly suck the water out until the uniform non-transparent silvery surface is observed in the whole water bath.

   This works for all resin types described before, except for Epon for which the water bath should be greatly overfilled. Note that water level should be checked frequently as it will naturally become lower due to evaporation. The correct water level is essential to seeing the interference colors of your sections (see below). Improper water levels can cause sectioning problems.
7. Launch an automatic cut and look for the first section. The first section will be most likely incomplete so wait until the knife cuts the entire sample surface and stop cutting.

8. Swipe the surface of the water again with Parafilm piece to remove all incomplete and broken pieces. Repeat from 7.
9. Continue the automatic cutting. The sections will float on the surface of water due to surface tension forming the ribbon (Fig. A.5).

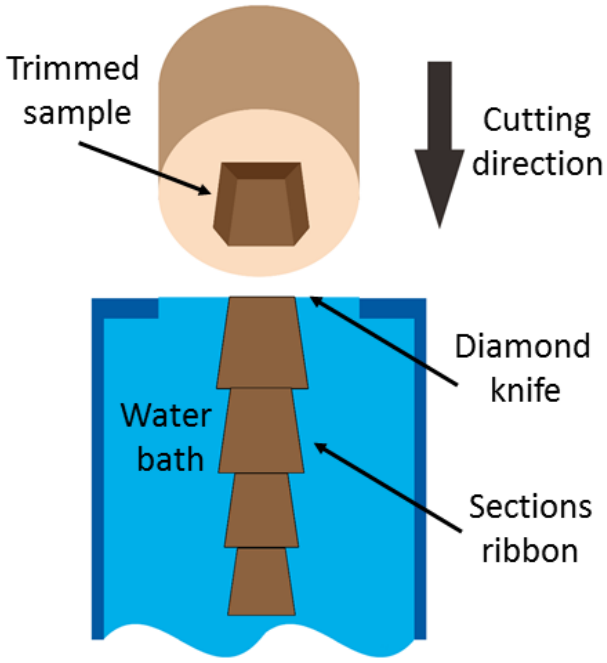

Figure A.5. Ribbon formation while sectioning with ultramicrotomy.

Although the ultramicrotome has a section thickness control, the accurate thickness of the sections can be determined from interference colors. By illuminating the floating section with white light, the reflections from the top section surface and water surface will interfere for a wavelength that depends on the section thickness ($\lambda = 2dsin\theta$). The interference card (Fig. A.6), given by Leica, provides the calibration of the section thickness as function of color.

In the case of histological 1 µm sections, the color will appear white but for the cutting of ultrathin sections, the verification of thickness according to the diagram is mandatory.

10. Sections collecting. The sections/ribbons can be moved to different regions of the reservoir with an eyelash manipulator (eyelash or fine hair glued onto a wooden stick). Sections must be moved away from the knife edge and can be collected from water reservoir with a PERFECT LOOP as described in Fig. A.7. Samples are collected and placed at the pre-cleaned glass slides and dried in air (covered by a petri dish to slow

down the dehydration process). Tissue cutting with histo knife is necessary in order to prepare the surface for cutting with more sensitive ultra knife.

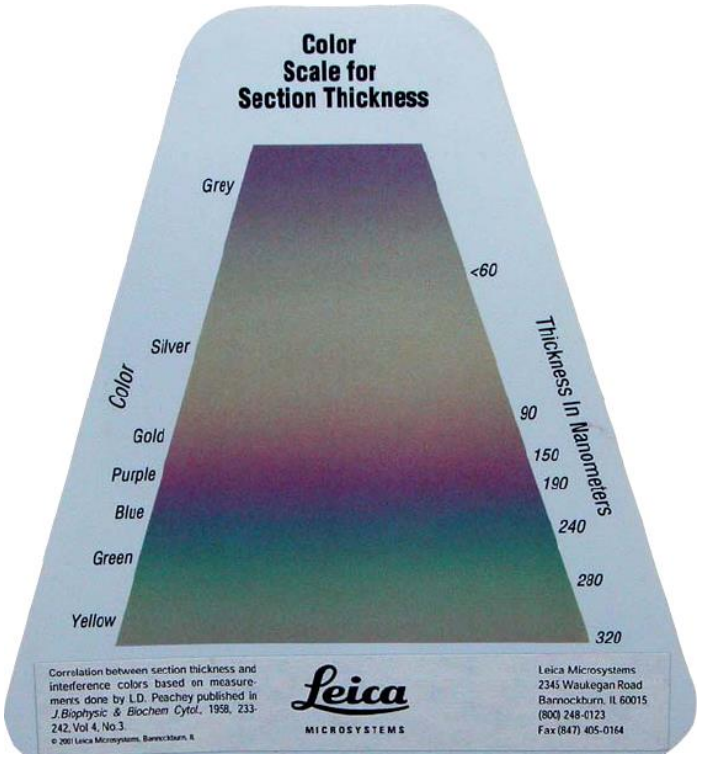

Figure A.6. Color/thickness diagram for determination of the slices thickness from Leica.

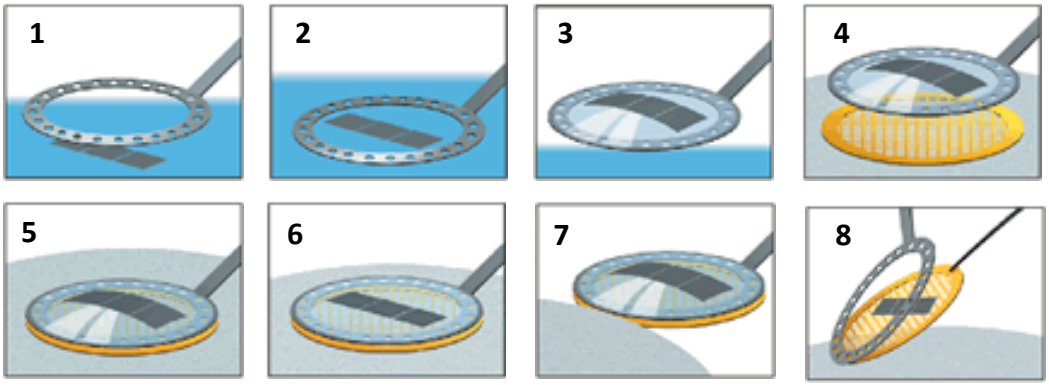

Figure A.7. Procedure of sections transporting with SUPER LOOP [209]: 1) center the loop above the sections; 2) slowly lower the loop over the sections and touch the water; 3). gently lift up the loop with the sections in a droplet of water; 4) lower the loop onto a grid and lift up again; 5) the grid holds to the loop by surface tension; 6) lower the loop to the filter paper to remove water; 7) for coated grids touch with filter paper to remove water; 8) separate the grid from the loop with an eyelash if needed.

11. The knife has to be changed to ultra 35. In order to end the use of a specific knife the precise procedure has to be followed. Swipe the surface of the water again with Parafilm piece to remove all floating sections. Suck away the water from the knife reservoir. Wash the bath with distilled water.
12. Cleaning the knife is mandatory in order to avoid the quick degradation of its cutting capacity.
    - Remount the diamond knife securely in the ultramicrotome knife stage.
    - Take a polystyrene cleaning stick and using a clean razor blade, bevel it to an angle of approximately 60°.
    - Clean the stick into 100% ethanol and shake off the excess.
    - Pass the stick over the diamond knife edge without applying pressure so that it just cuts the polystyrene (Fig. A.8.).
    - Make one sweep across the knife.
    - Make a second cleaning pass in the other direction. If necessary repeat the procedure until the edge is clean [111].

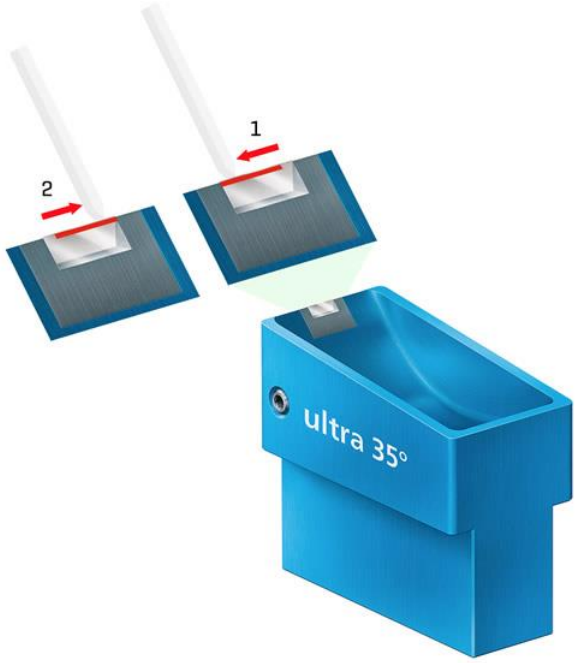

Figure A.8. Scheme of diamond knife cleaning procedure with polystyrene cleaning stick [111].

13. Set ultra 35 knife. Repeat p. 1-10 with choosing 40-70 nm thickness for TEM study and 5-15 mm/s speed depending on the resin used for embedding. The optimal speed for bone in LR white was 5 mm/s, in Epon - 15 mm/s, for PMMA - 8 mm/s.
14. Prepare grids by cleaning them in acetone 100%, drying and discharging with glow discharge cleaning system such as PELCO easiGlow™ by Ted Pella Inc. This has to be done maximum 10 min before placing the sections on the grid. Then place the grids on a sheet of filter paper.
15. Transport the sections using PERFECT LOOP on the grid in a way that the filter paper sucks the water through the grid allowing the sticking of the sections on the grid.
16. Clean ultra 35 knife as it is describe in p. 12-13.

Appendix 2. Synchrotron radiation

A.2.1. Synchrotron source

A **synchrotron** is an extremely powerful source of X-rays. These are produced by highly energetic electrons moving in a large circle in the synchrotron. The entire world of synchrotron science depends on one physical phenomenon: when a moving electron changes direction, it emits energy. When the electron is moving fast enough, the emitted energy is at X-ray wavelength.

A synchrotron machine accelerates electrons to extremely high energy and then make them change direction periodically. The resulting X-rays are emitted as dozens of thin beams, each directed toward a beamline next to the accelerator. The machine operates day and night, with periodic short and long-term shutdowns for maintenance. More than 40 synchrotron light sources have been built around the world.

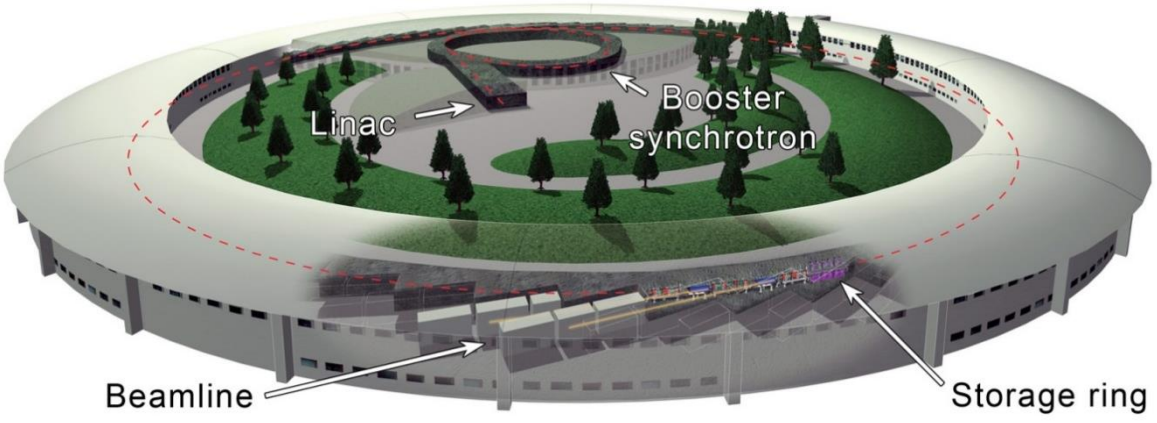

Figure A.2.1. Scheme of the synchrotron at ESRF (Grenoble, France) with its principle components [148].

The diffraction measurements for CXDI, SAXS and PDF analysis of the present work were performed at a third-generation synchrotron facility – the European Synchrotron Radiation Facility (ESRF) in Grenoble, France.

Every synchrotron consists of the following parts: Linac, Booster, Storage ring and Beamlines (as shown in Fig. A.2.1).

In the **Linac,** the electrons for the storage ring are produced in an electron gun - a device similar to cathode ray tubes. These electrons are packed in “bunches” and then accelerated to 200 million electron-volts, enough for injection into the booster synchrotron.

The Booster is a 300-meter-long pre-accelerator where the electrons are accelerated to an energy of 6 billion electron-volts (6 GeV) before being injected into the storage ring. The booster synchrotron only works a few times a day for a few minutes, when the storage ring is refilled. Every 50 milliseconds, it can send a bunch of 6 GeV electrons into to the storage ring.

The **Storage ring** is a tube 844 meters in circumference where the electrons circle for hours close to the speed of light. The tube is maintained at very low pressure (around 10-9 mbar). As the electrons travel around in the ring, they pass through different types of magnets (see below) and in the process produce X-rays. Units called RF cavities resupply the energy electrons have emitted as X-rays.

The X-ray beams emitted by the electrons are directed toward "**Beamlines**" that surround the storage ring in the experimental hall. Each beamline is designed for use with a specific technique or for a specific type of research. Experiments run throughout the day and night. Within the experiment hall, a beamline consists of an optics cabin, an experimental cabin, and a control cabin, aligned in a row (Fig. A.2.2).

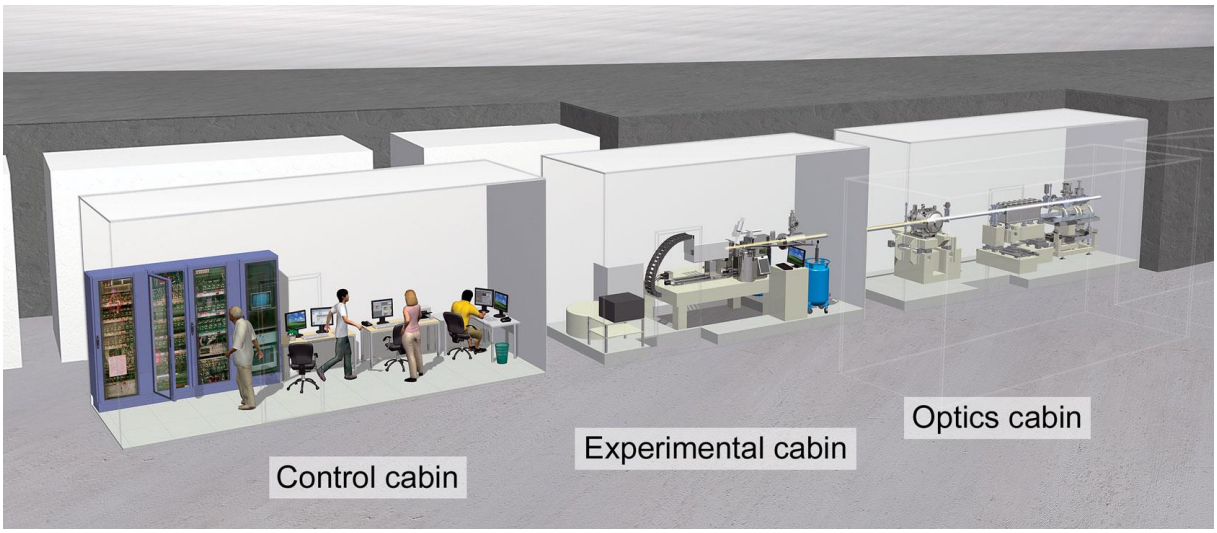

Figure A.2.2. The beamline principal scheme [148].

In ESRF, currently 43 different beamlines are producing top level scientific research (Fig. A.2.3) [148].

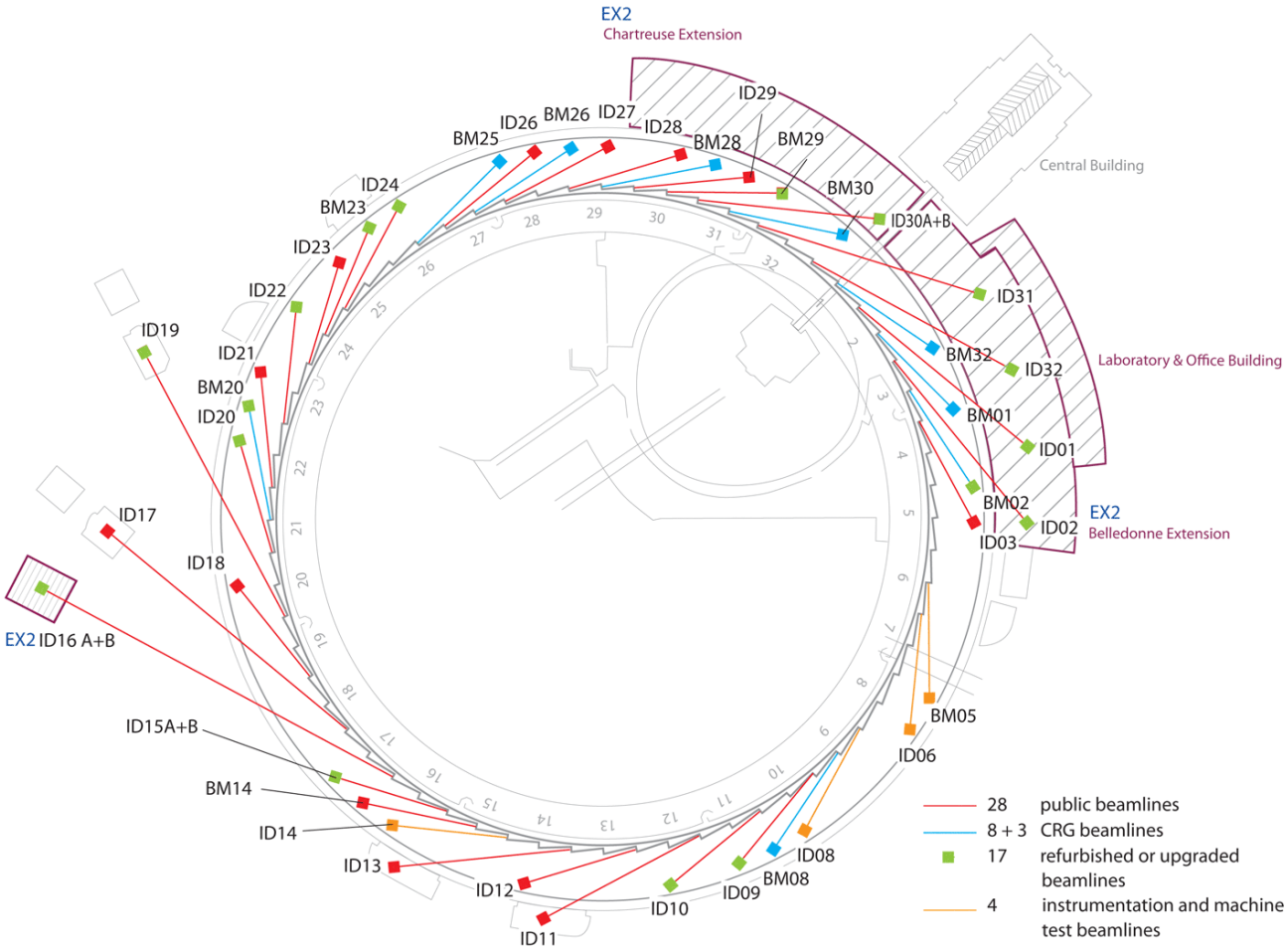

Figure A.2.3. Representation of the accessible ESRF beamlines in 2015 [148].

A.2.2. Magnets in the storage ring

The storage ring at ESRF includes 32 straight and 32 curved sections in alternating order. In each curved section, two large bending magnets force the path of the electrons into a racetrack-shaped orbit 844 meters in circumference. In each straight section, several focusing magnets ensure that the electrons remain close to their ideal orbital path. The straight sections also host the undulators, where the intense beams of X-rays are produced.

The three main insertion devices are bending magnets, wigglers and undulators providing different focusing and, as a result, brilliance of the radiation.

The simplest insertion device is a bending magnet (Fig. A.2.4). The main function of which is to bend the electrons into their racetrack orbit. However, as the electrons are deflected

from their straight path when passing through these magnets, they emit a spray of X-rays tangentially to the plane of the electron beam. The synchrotron light from a bending magnet covers a wide and continuous spectrum, from microwaves to hard X-rays, and it is much less focused, or brilliant, than the fine beam of X-rays from other insertion devices.

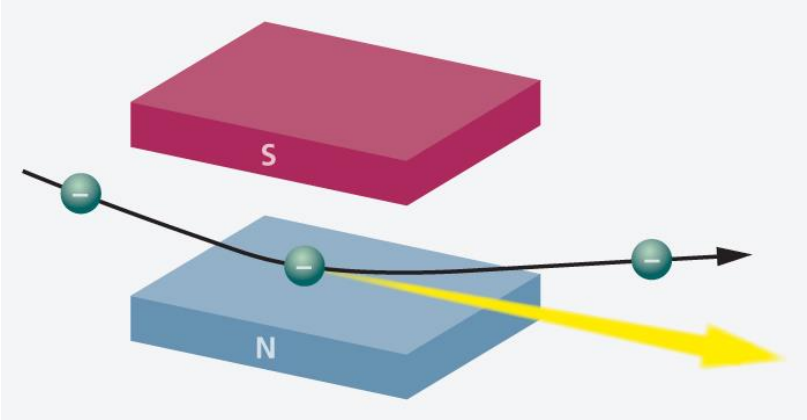

Figure A.2.4. Bending magnet scheme.

An **undulator** (Fig. A.2.5) is an insertion device from high-energy physics and usually part of a larger installation, a synchrotron storage ring. It consists of a periodic structure of dipole magnets. The static magnetic field is alternating along the length of the undulator with a wavelength λ_u. Electrons traversing the periodic magnet structure are forced to undergo oscillations and thus to radiate energy. The radiation produced in an undulator is very intense and concentrated in narrow energy bands in the spectrum. It is also collimated on the orbit plane of the electrons.

For the characteristics of undulators, one uses the dimensionless parameter, K:

$$K = \frac{eB\lambda_u}{2\pi\beta m_e c} \tag{A-1}$$

where e is the particle charge, B is the magnetic field, $\beta = v/c$, v – speed of particle, c is the speed of light, m_e – the electron rest mass, $\gamma = \frac{1}{\sqrt{1-\beta^2}}$.

The K-Factor determines the energy of radiation produced. For $K \ll 1$, the oscillation amplitude of the motion is small and the radiation displays interference patterns which lead to narrow energy bands. If $K \gg 1$, the oscillation amplitude is bigger and the radiation contributions from each field period sum up independently, leading to a broad energy spectrum. In this regime of fields, the device is no longer called an undulator; it is called a **wiggler**. Wiggler radiation is

also generated from a periodic magnet structure, but in the strong magnetic field limit where in at least one plane the angular excursions are significantly greater than the natural radiation cone.

Figure A.2.5. Principal scheme of the undulator: 1 - magnets, 2 - electron beam, 3 - synchrotron radiation, λ_u. - undulator wavelength.

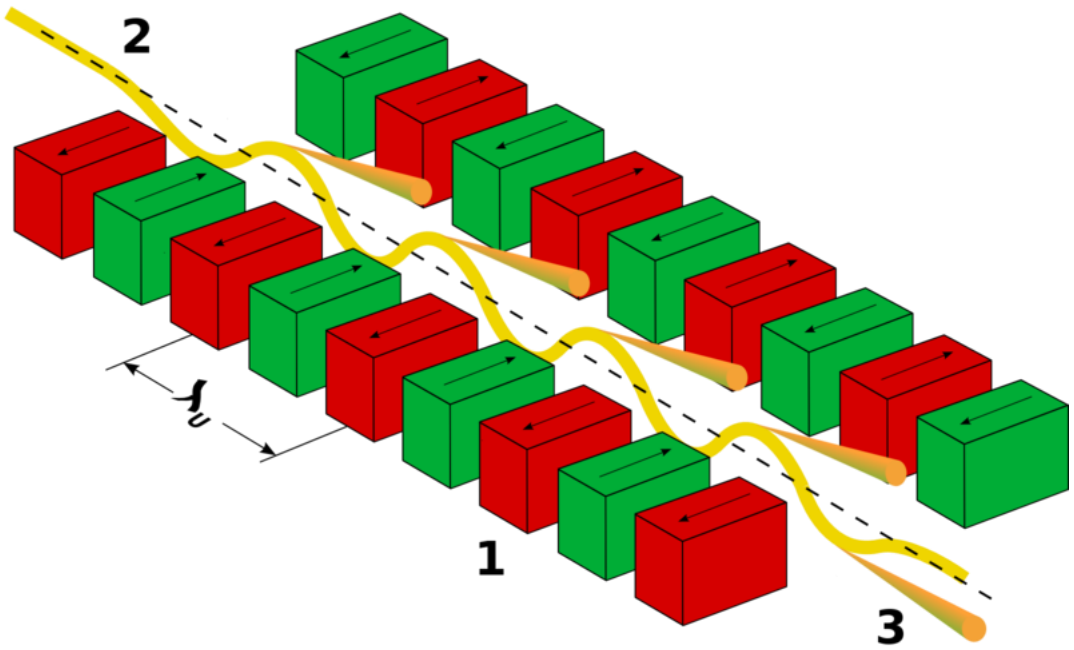

Undulators can provide several orders of magnitude higher flux than a simple bending magnet and as such are in high demand at synchrotron radiation facilities. For an undulator with N periods, the brightness can be up to N^2 more than a bending magnet (see Fig. A.2.6). The difference in the performance of these devices arises from differences in the maximum angles of the electron oscillations in the horizontal plane: K is around 20 for a wiggler, and 1 for an undulator.

The polarization of the emitted radiation can be controlled by using permanent magnets to induce different periodic electron trajectories through the undulator. If the oscillations are confined to a plane, the radiation will be linearly polarized. If the oscillation trajectory is helical, the radiation will be circularly polarized.

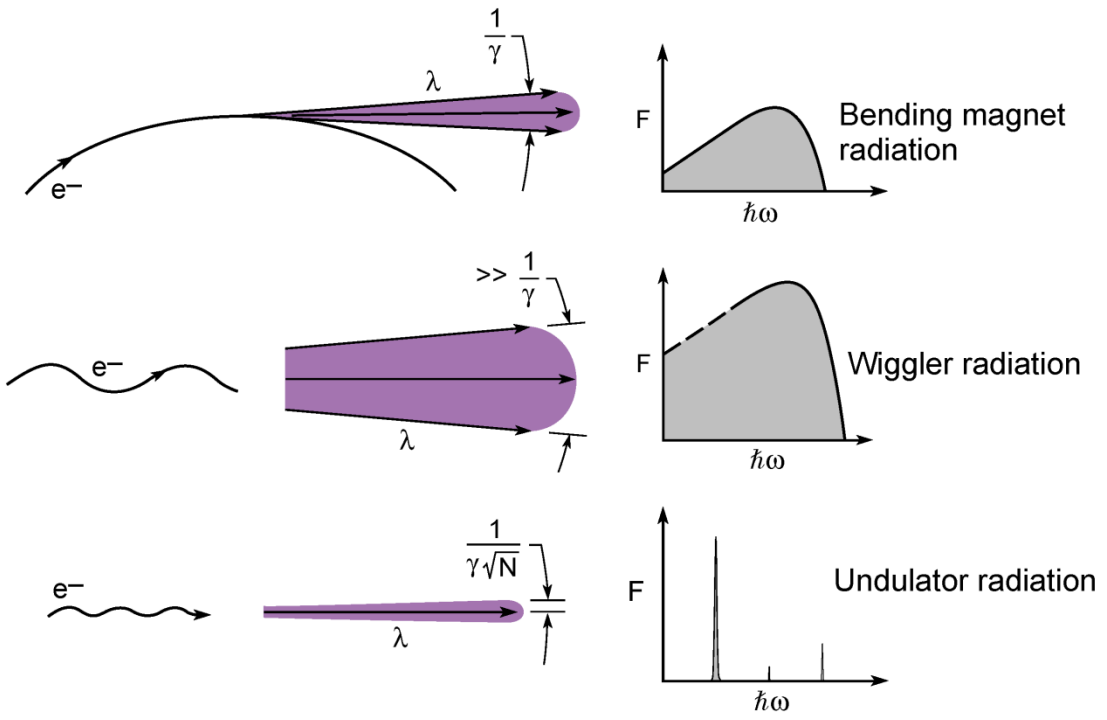

Figure A.2.6. Synchrotron radiation emitted by the three kind of insertion devices and their radiation spectra [119].

The three types of insertion devices give rise to different emittance and radiation spectra, as shown in Fig. A.2.6.

The radiation spectrum of bending magnet radiation is very broad, analogous to a "white light" X-ray light bulb. The emission angle is typically $\frac{1}{\gamma}$ where γ is the Lorentz contraction factor (see [119] for more details).

The frequency spread of undulator radiation can be very narrow, and the radiation can be extremely bright and partially coherent, under certain circumstances. The characteristic emission angle is narrowed by a factor of $\sqrt{N}$ (where N is the number of magnetic periods, typically of the order of 100).

The characteristic emission angle for wiggler radiation is higher than the natural $\frac{1}{\gamma}$ radiation cone. The radiation that is generated gives peaks at higher photon energies and is more abundant (higher photon flux and more power). Its radiation spectrum is very broad, similar to that of the bending magnet. Although more power is radiated, wiggler radiation is less bright because of the substantially increased radiation cone.

A.2.3. Properties of synchrotron radiation: brilliance and coherence

When comparing X-ray sources, an important measure of quality of the source is called **brilliance** [210]. Brilliance takes into account:

- number of photons produced per second;
- the angular divergence of the photons, or how fast the beam spreads out;
- the cross-sectional area of the beam;
- the photons falling within a bandwidth (BW) of 0.1% of the central wavelength or frequency.

The resulting formula is:

$$Brilliance = \frac{photons}{second \cdot mrad^2 \cdot mm^2 \cdot 0.1\%\, BW} \quad \text{(A-2)}$$

The greater the brilliance, the more photons of a given wavelength and direction are concentrated on a spot per unit of time. In most X-ray literature, the units for brilliance appear as: photons/s/mm^2/mrad^2/0.1%BW.

A.2.4. X-ray focusing optics

Optical lenses (from glass or plastic) work effectively since their refractive index deviates considerably from unity, and this produces a significant change in the direction of light propagation at the air–lens interface. In addition, they are transparent and hardly any losses take place in transmitting the beam through the lens.

The refraction at an interface also occurs for X-rays, but there are two basic differences from the case of visible light: the deviation in the index of refraction from unity is very small, of order 10^{-5}; and the refractive index is less than one, not greater than one as it is for visible light. This implies that the shape of a converging X-ray lens must be the same as that of a diverging optical lens. One consequence of the refractive index in the X-ray region being close to unity is that the focal length of a single lens would be of order 100 m [210]. Several types of modern X-ray optics used for this study will be described.

Compound refractive lens (CRL) is a series of individual lenses arranged in a linear array in order to achieve focusing of X-rays in the energy range of 2-150 keV. With a series of single lenses, the combined focal length may be reduced in proportion to the number of lenses,

as shown in Fig. A.2.7 [211]. To minimize the absorption, the lens must be made from a material such as aluminum, beryllium, or lithium.

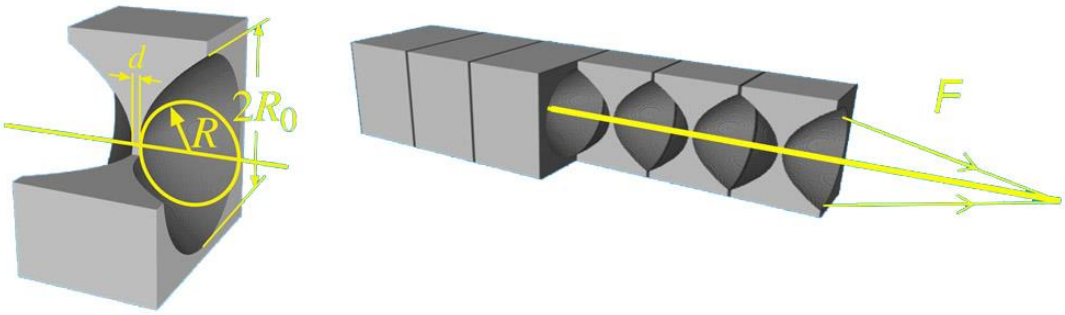

Figure A.2.7. Parabolic compound refractive transfocator. Left: A single refractive lens illustrating the rotational symmetry about the optical axis. Right: A compound refractive lens with six elements (three lenses are shown cut in half). Putting N lenses in line reduces the focal length by a factor of N with respect to a single lens. F - focal length, R - radius of the parabola apex, d - spacing [212].

Kirkpatrick-Baez-optics (**KB-mirrors**) [213] consist of two mirrors. If for example, the surface of the first mirror is aligned horizontally, the second mirror is aligned vertically (Fig. A.2.8). In order to achieve a common focal point, both mirrors have to be elliptically curved in a way such that the horizontal focus line of the first mirror and the vertical focus line of the second mirror coincide in the same plane. The curvature of the mirrors is realized by sophisticated and highly precise mechanics, allowing for focal spot diameters in the 50 nm range. The quality of the focal spot image of the X-ray source worsens rapidly, with the source point getting larger.

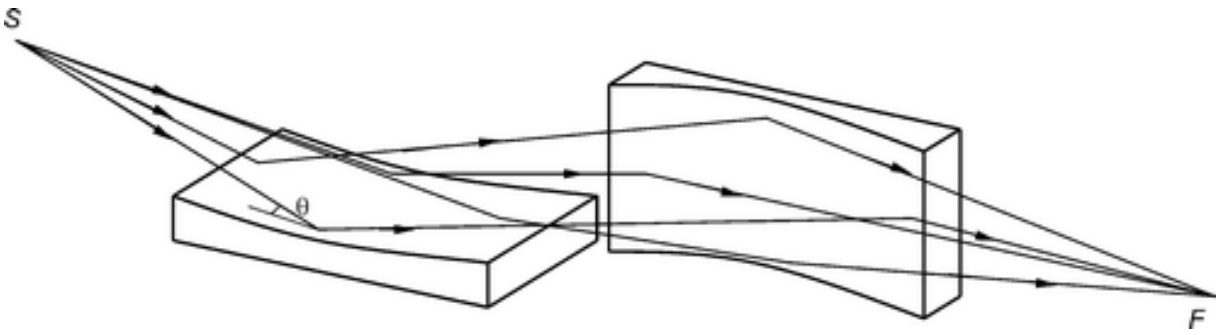

Figure A.2.8. Two-mirror Kirkpatrick–Baez system: *S* - source; *θ* - mirror incidence angle; *F* - focal length [214].

Appendix 3. EDX spectra for heated bone series

An extensive data including all temperature for EDX analysis on heated bone sample set is presented. Each image includes:

a) Large field of view bright field image in TEM mode for the region selection;
b) Bright field image in TEM mode of the scan position;
c) Bright field images in EDX mode before the first scanning frame;
d) Bright field images in EDX mode before the last scanning frame;
e) C elemental map;
f) O elemental maps;
g) P elemental maps;
h) Ca elemental map;
i) EDX spectra.

1000 °C

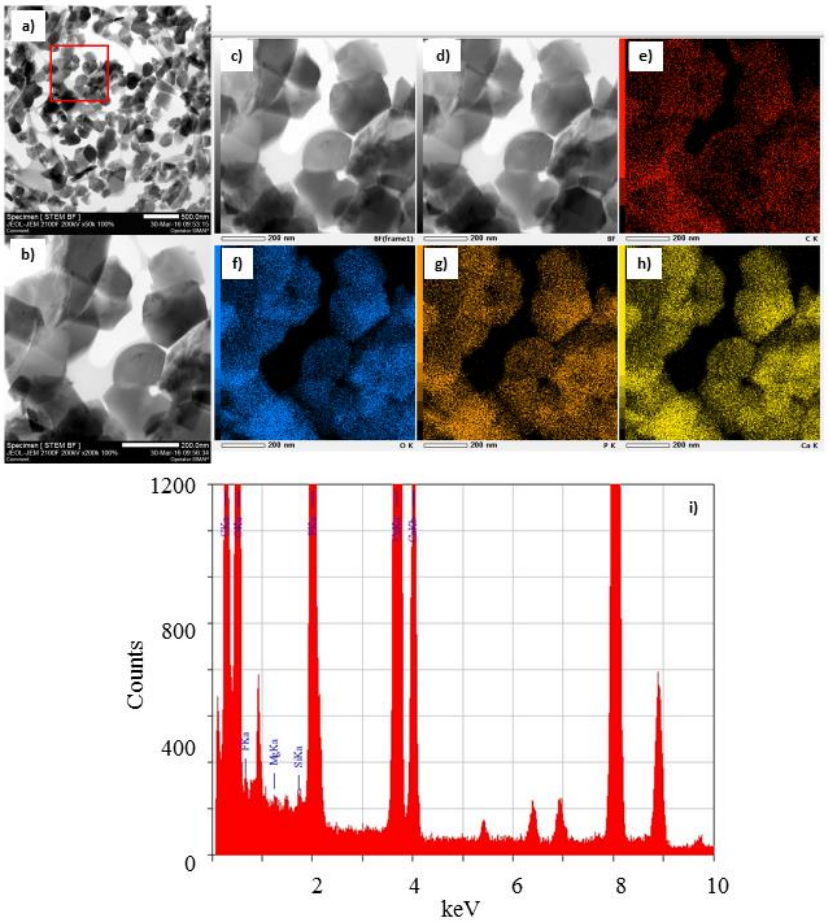

Figure A.3.1. Scanning EDX of the 1000 °C bone sample.

700 °C

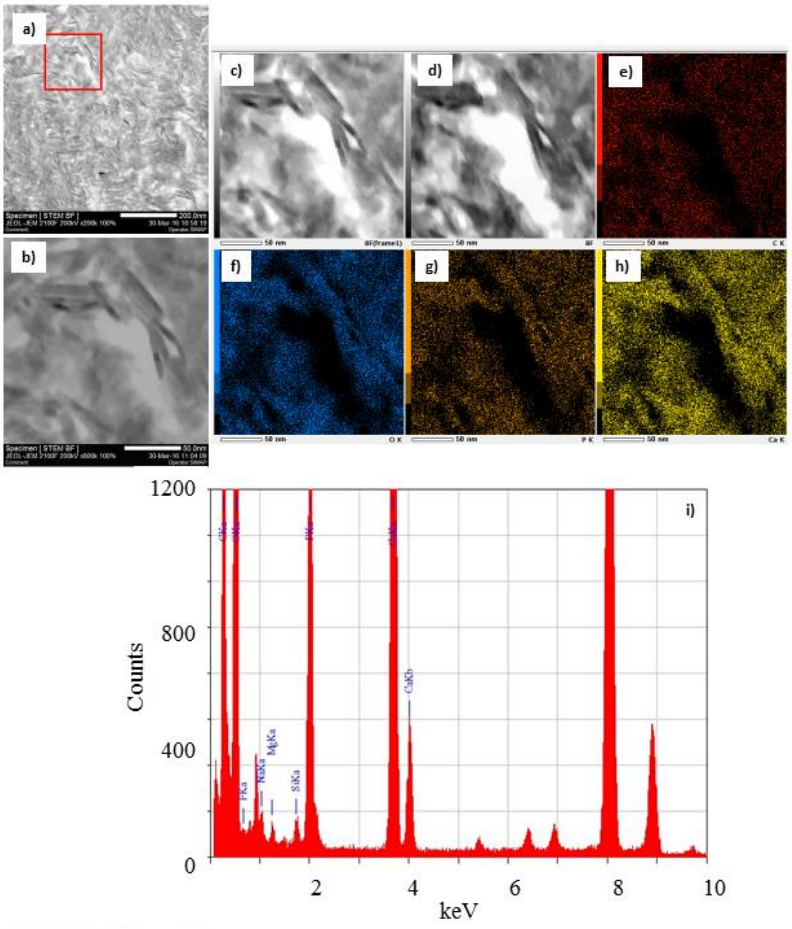

600 °C

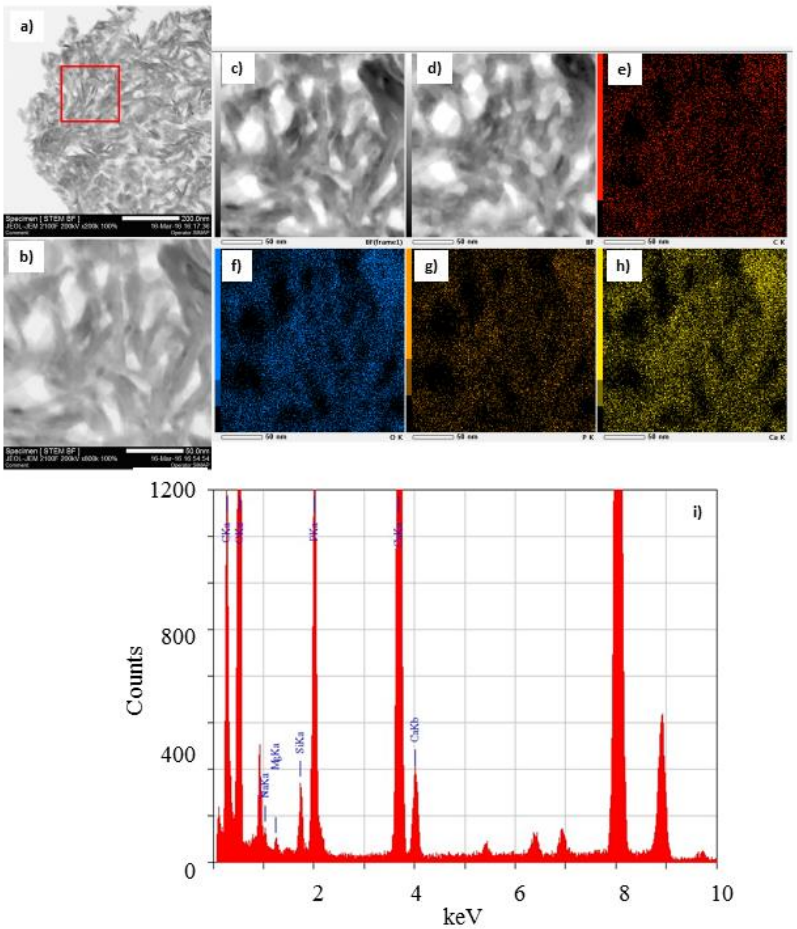

Figure A.3.2. Scanning EDX of the 700 °C and 600 °C bone samples.

400 °C

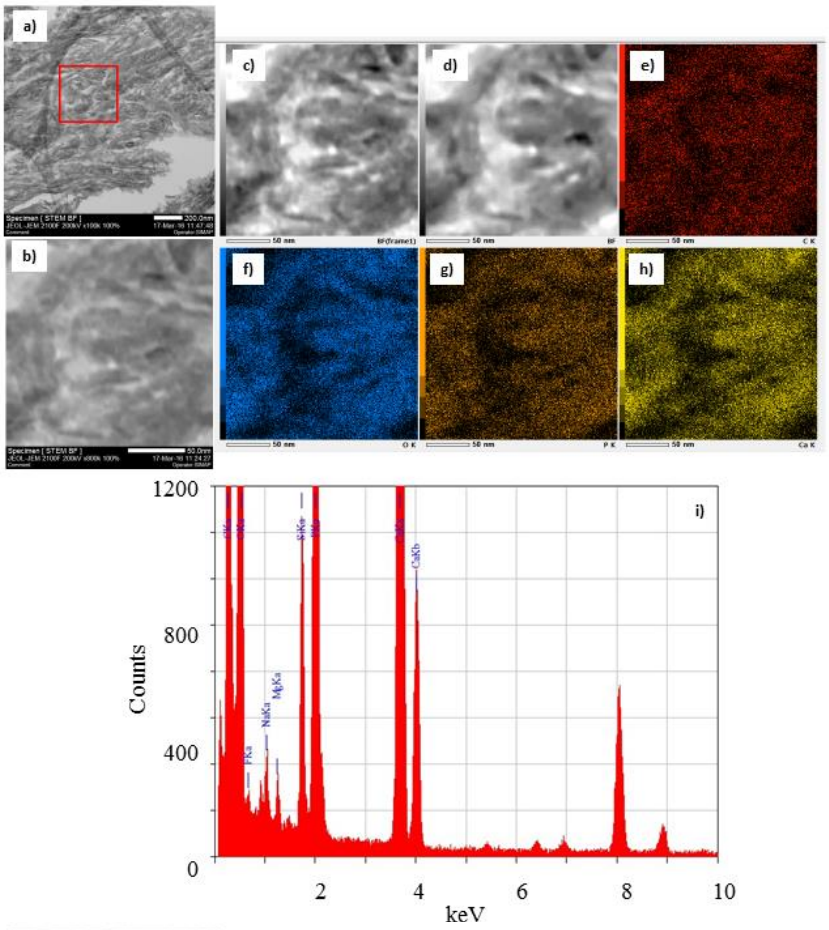

300 °C

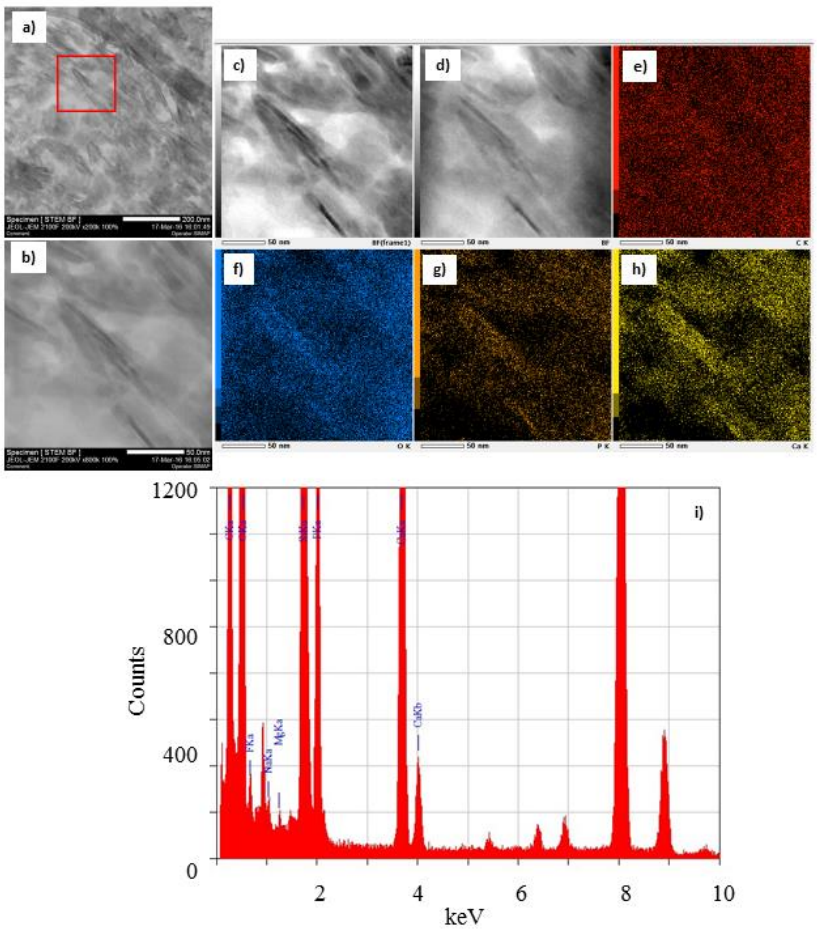

Figure A.3.3. Scanning EDX of the 400 °C and 300 °C bone samples.

200 °C

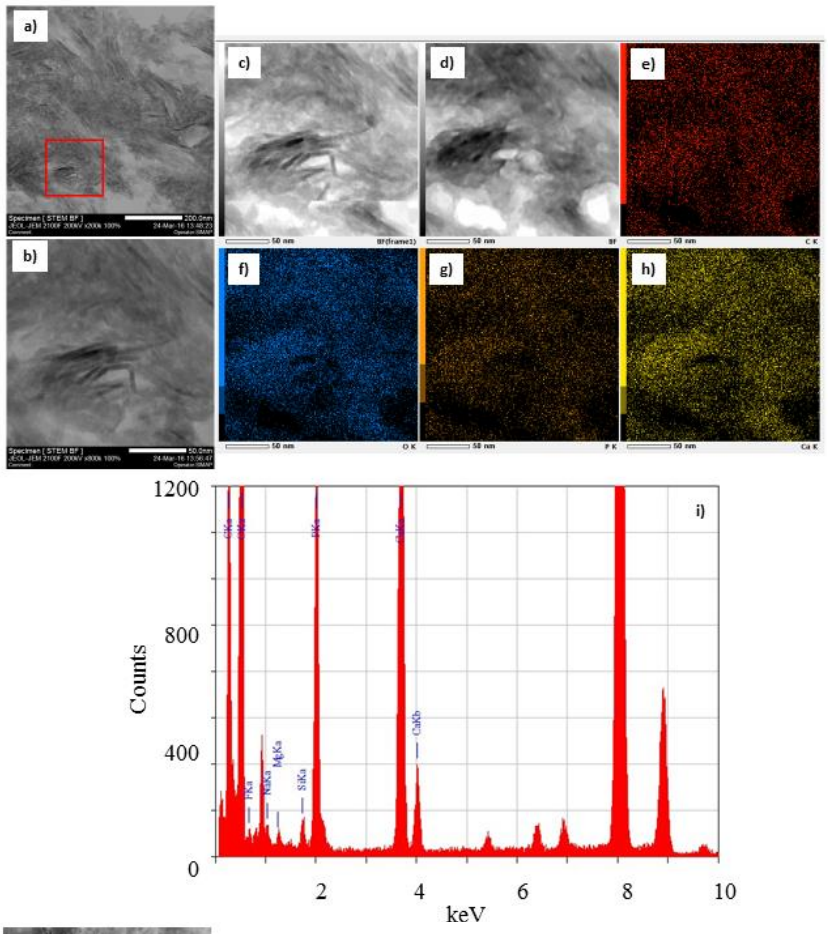

100 °C

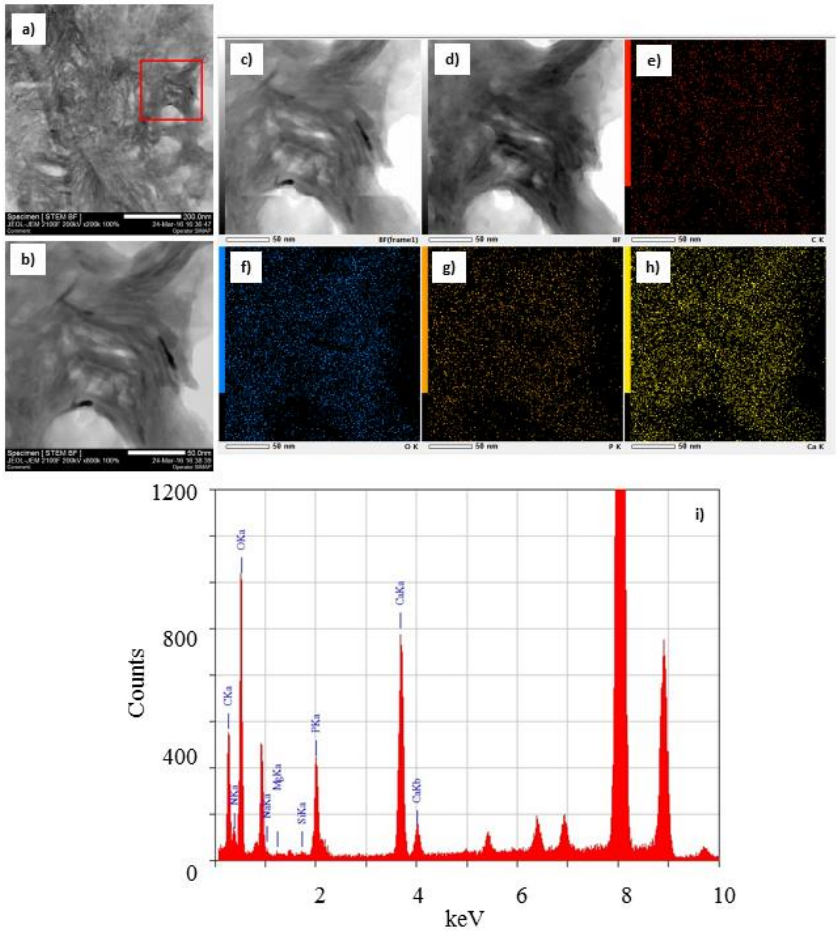

Figure A.3.4. Scanning EDX of the 200 °C and 100 °C bone samples.

Control

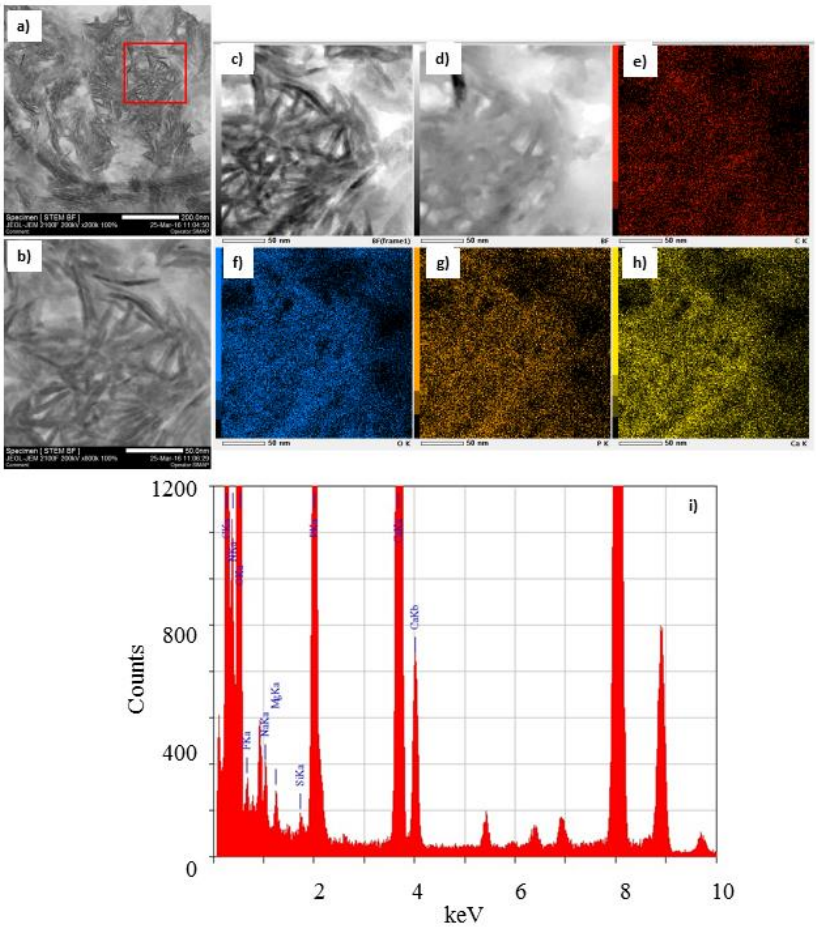

Figure A.3.5. Scanning EDX of the control bone sample.

Appendix 4. Heated bone Rietveld and PDF analysis supplementary information

A.4.1. Rietveld refinement results for heated bone

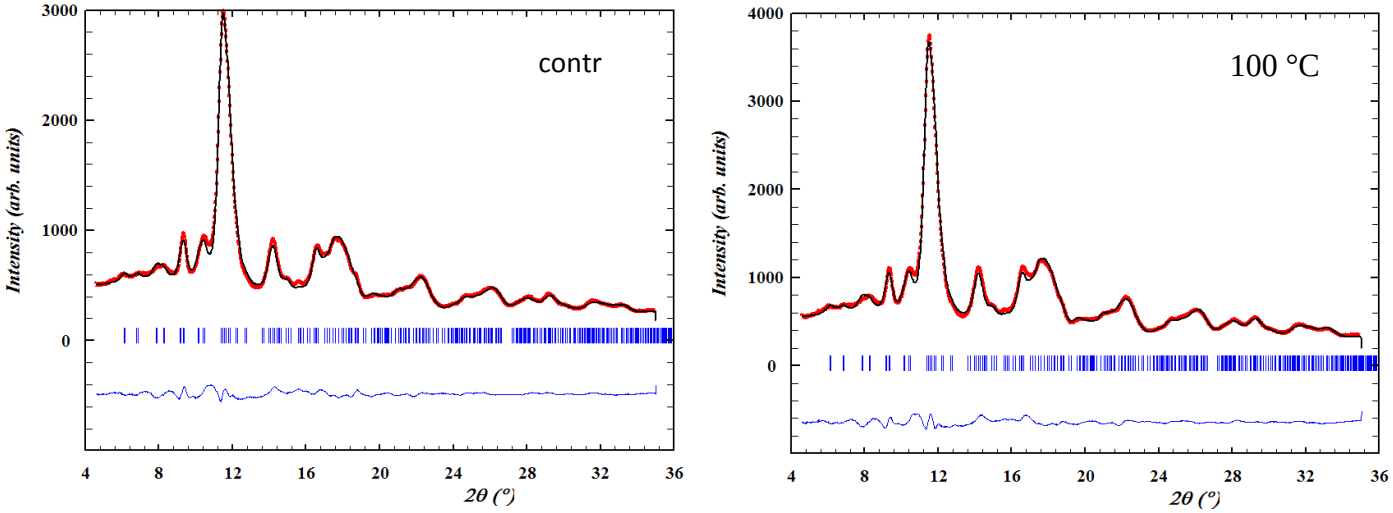

Figure A.4.1. Rietveld-refined diffraction patterns for the control and 100 °C samples. Black - experimental data, red - fit result, blue - misfit function.

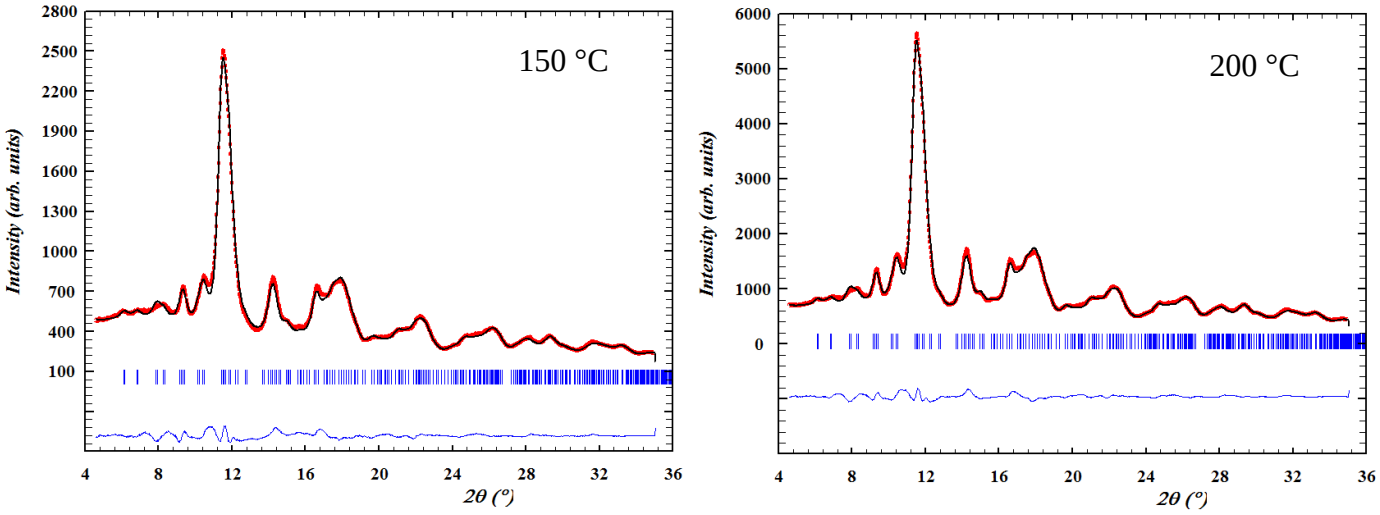

Figure A.4.2. Rietveld-refined diffraction patterns for the 150 °C and 200 °C samples. Black - experimental data, red - fit result, blue - misfit function.

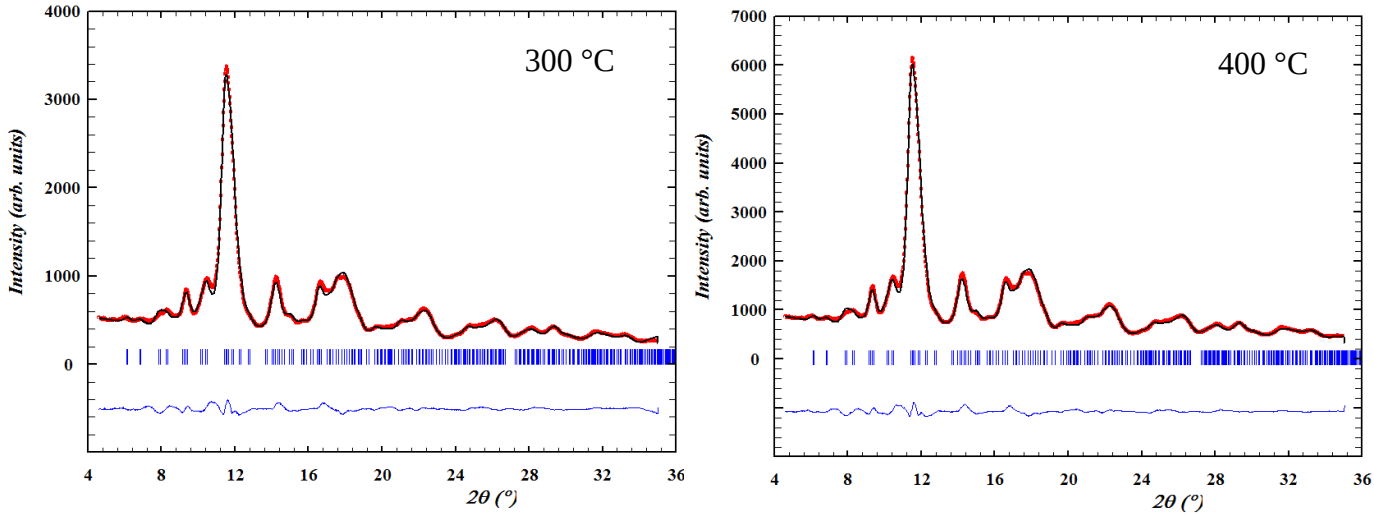

Figure A.4.3. Rietveld-refined diffraction patterns for the 300 °C and 400 °C samples. Black - experimental data, red - fit result, blue - misfit function.

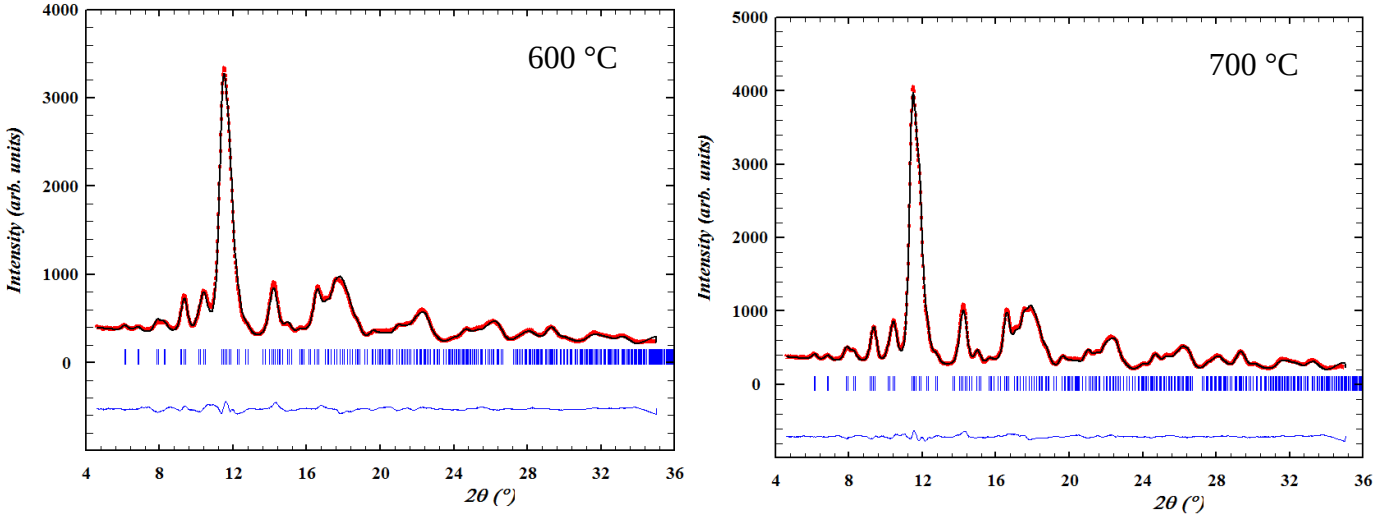

Figure A.4.4. Rietveld-refined diffraction patterns for the 600 °C and 700 °C samples. Black - experimental data, red - fit result, blue - misfit function.

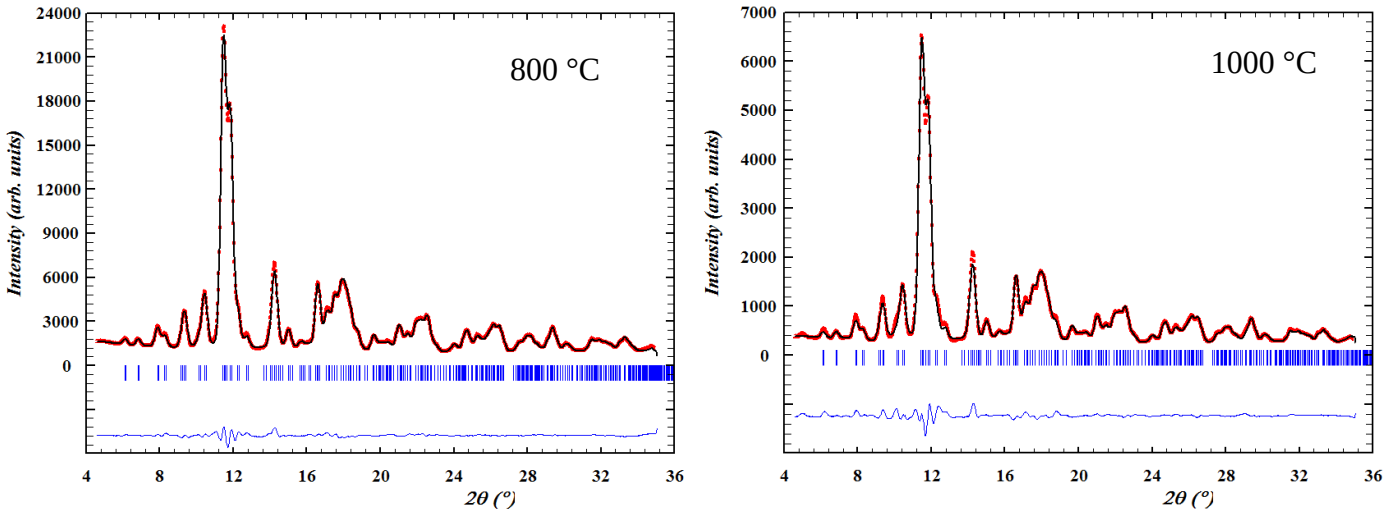

Figure A.4.5. Rietveld-refined diffraction patterns for the 800 °C and 1000 °C samples. Black - experimental data, red - fit result, blue - misfit function.

A.4.2. PDF refinement results for heated bone

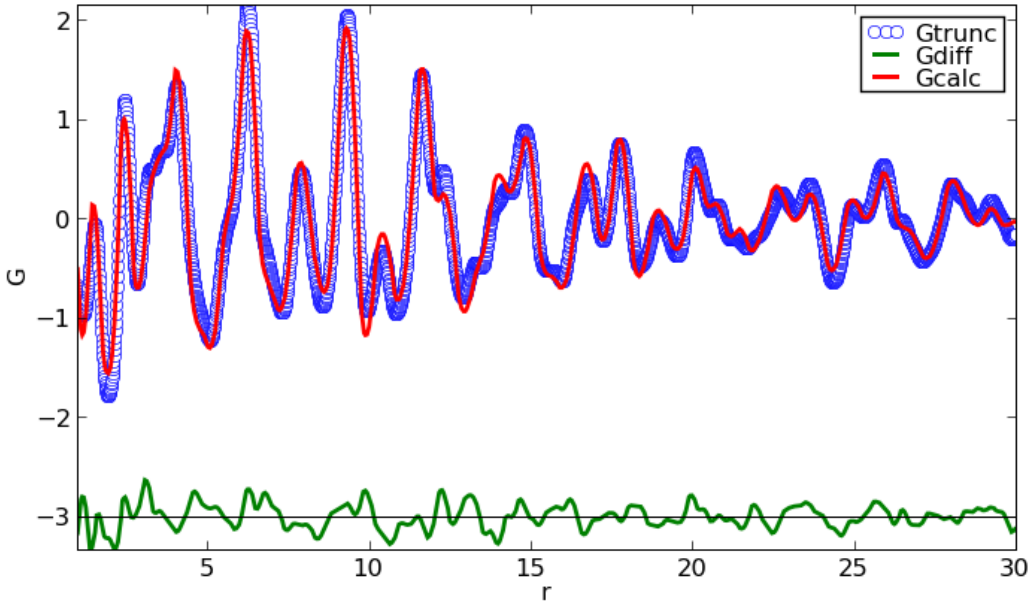

Figure A.4.6. PDFgui fit for the control sample. Blue circles: experimental PDF; red curve: modelled PDF; green: misfit function.

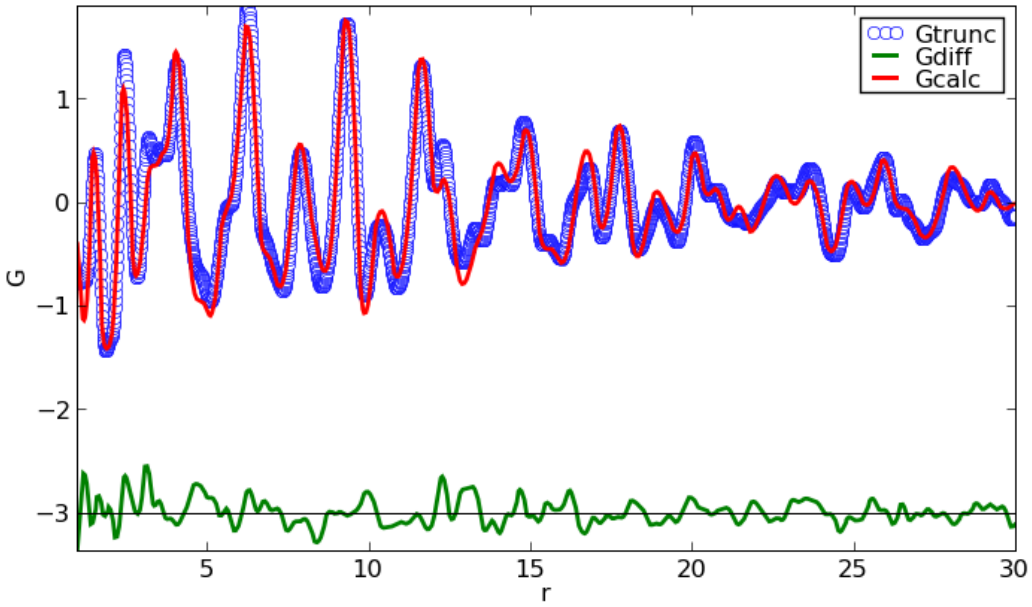

Figure A.4.7. PDFgui fit for the 100°C sample. Blue circles: experimental PDF; red curve: modelled PDF; green: misfit function.

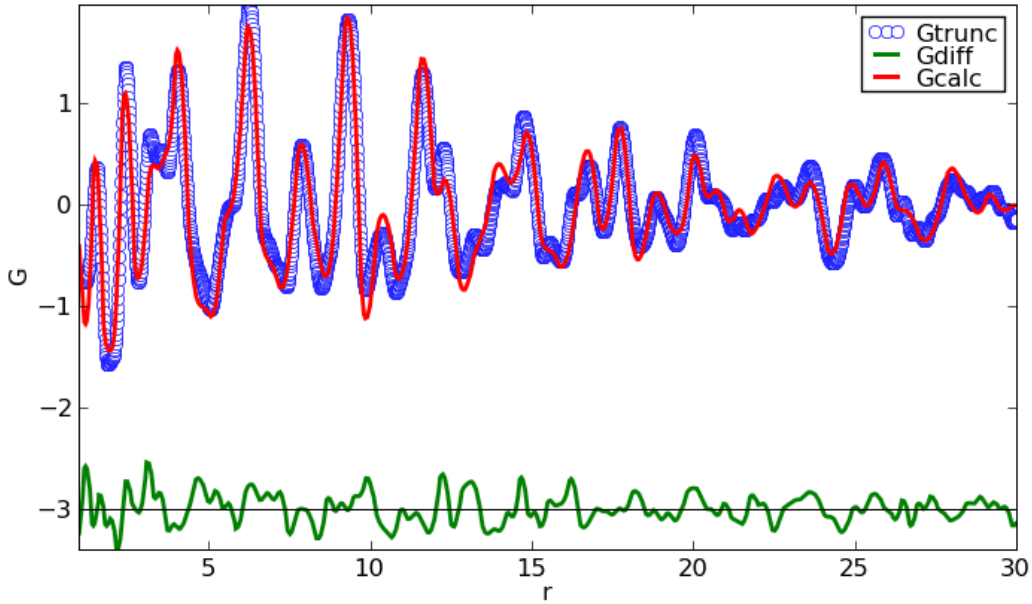

Figure A.4.8. PDFgui fit for the 150°C sample. Blue circles: experimental PDF; red curve: modelled PDF; green: misfit function.

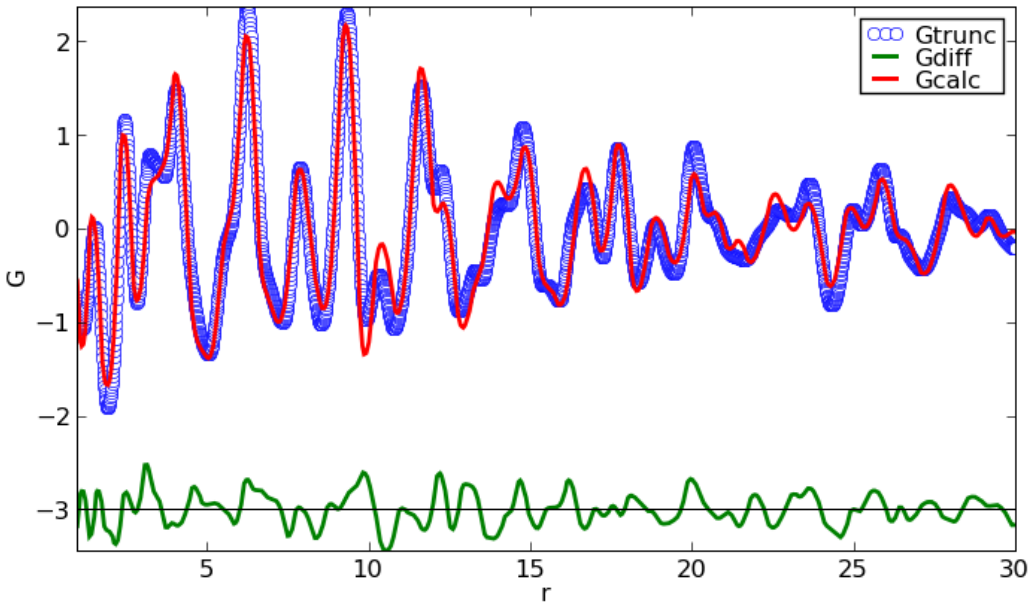

Figure A.4.9. PDFgui fit for the 200°C sample. Blue circles: experimental PDF; red curve: modelled PDF; green: misfit function.

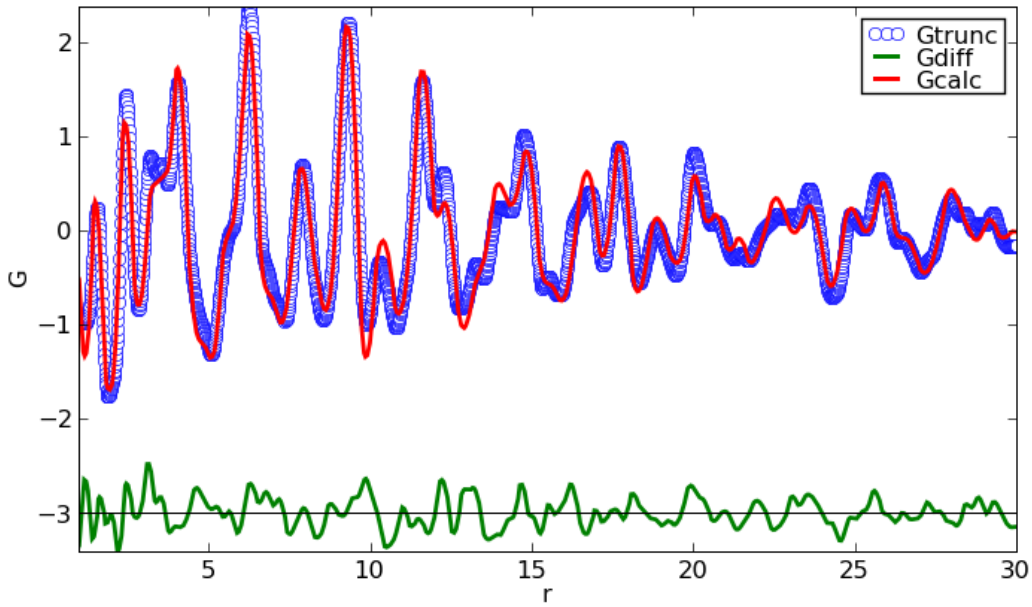

Figure A.4.10. PDFgui fit for the 300°C sample. Blue circles: experimental PDF; red curve: modelled PDF; green: misfit function.

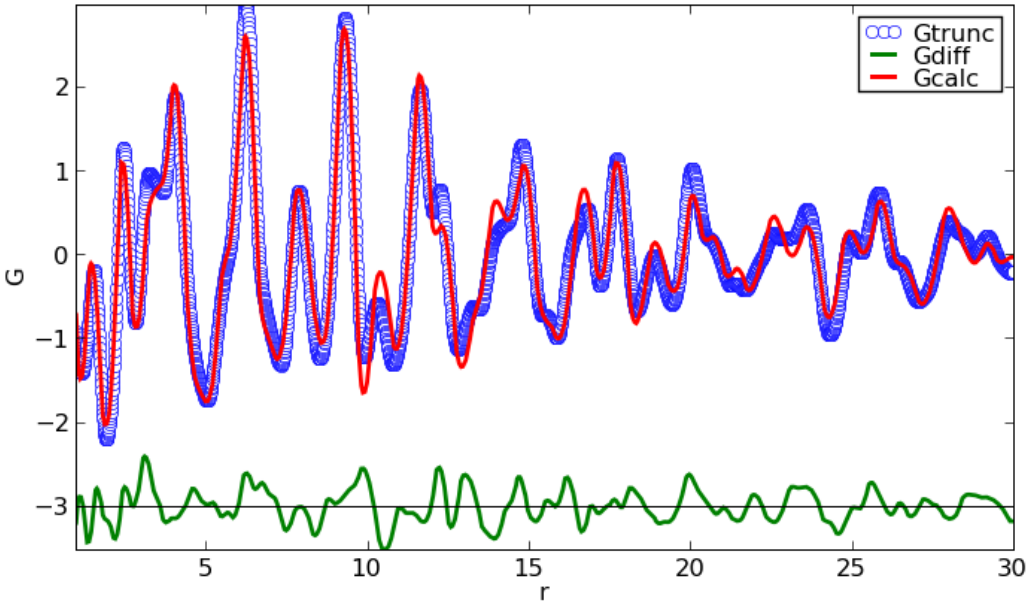

Figure A.4.11. PDFgui fit for the 400°C sample. Blue circles: experimental PDF; red curve: modelled PDF; green: misfit function.

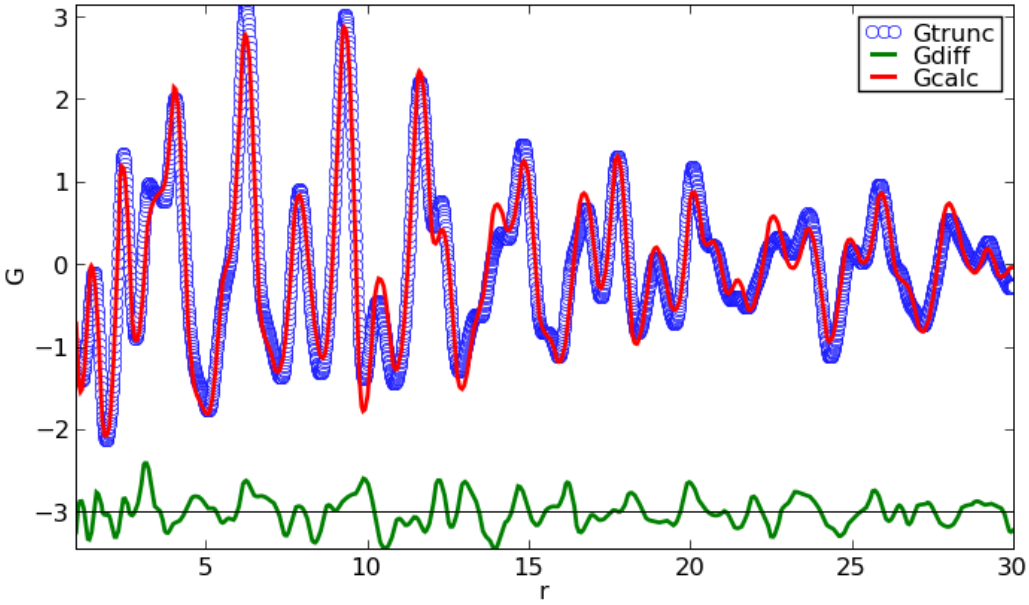

Figure A.4.12. PDFgui fit for the 600°C sample. Blue circles: experimental PDF; red curve: modelled PDF; green: misfit function.

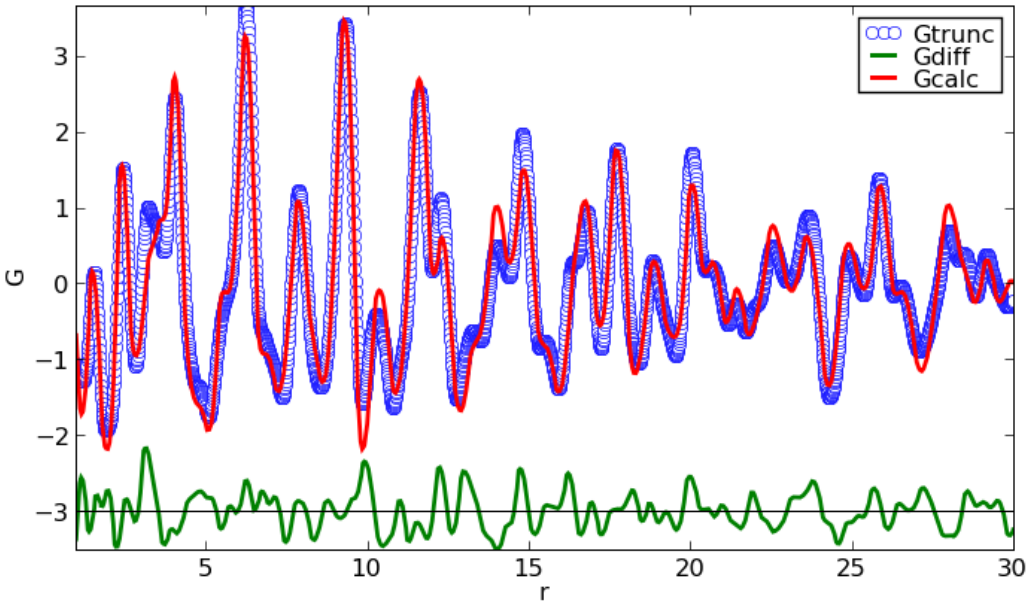

Figure A.4.13. PDFgui fit for the 700°C sample. Blue circles: experimental PDF; red curve: modelled PDF; green: misfit function.

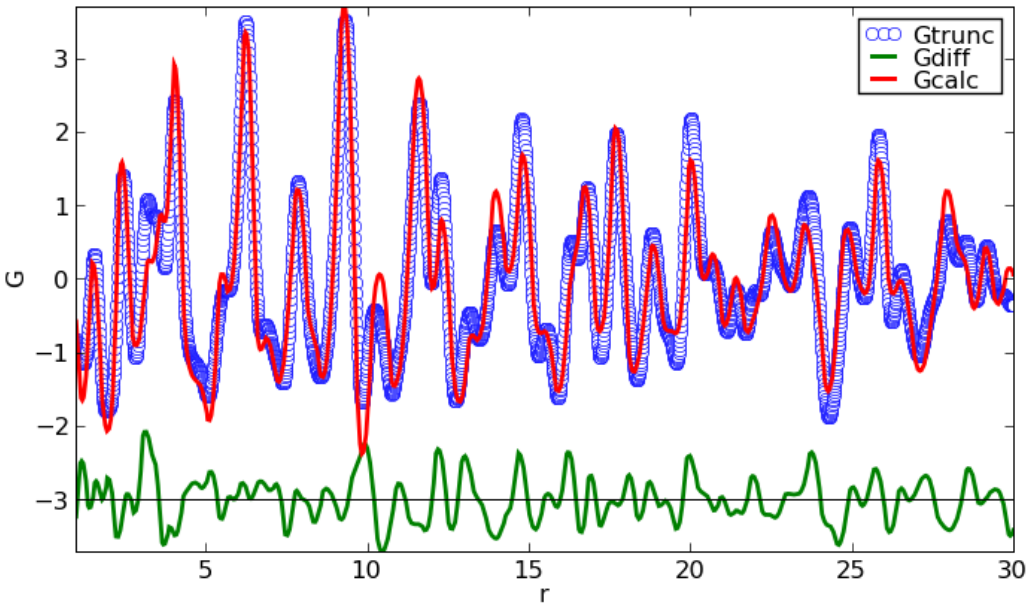

Figure A.4.14. PDFgui fit for the 800°C sample. Blue circles: experimental PDF; red curve: modelled PDF; green: misfit function.

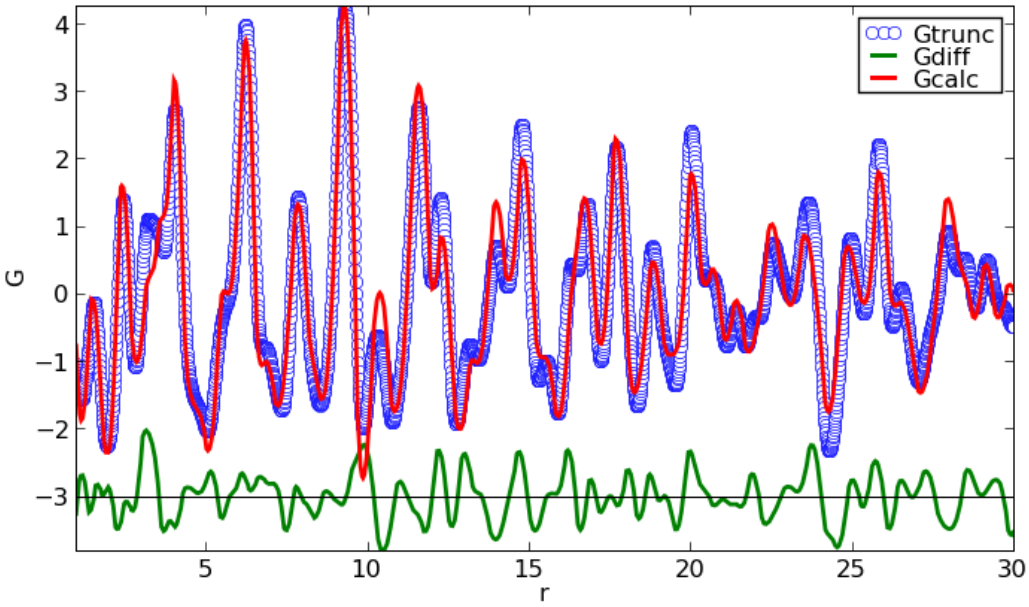

Figure A.4.15. PDFgui fit for the 1000°C sample. Blue circles: experimental PDF; red curve: modelled PDF; green: misfit function.

A.4.3. Partial PDF of heated bone

The plots for all six atomic bonds partial PDFs (Ca-Ca, Ca-O, Ca-P, P-O, O-O and P-P) evolution upon heating are represented in Fig. A.4.16 with the offset of *+1* for the display.

The bond lengths were also calculated from the resulting model structures for each heating temperature and for each of Ca-Ca, Ca-O, Ca-P, P-O, O-O and P-P pairs up to 5 Å. The temperature dependence of first 4 to 7 bond lengths for each atomic pair is represented in Fig. A.4.17 by different colors.

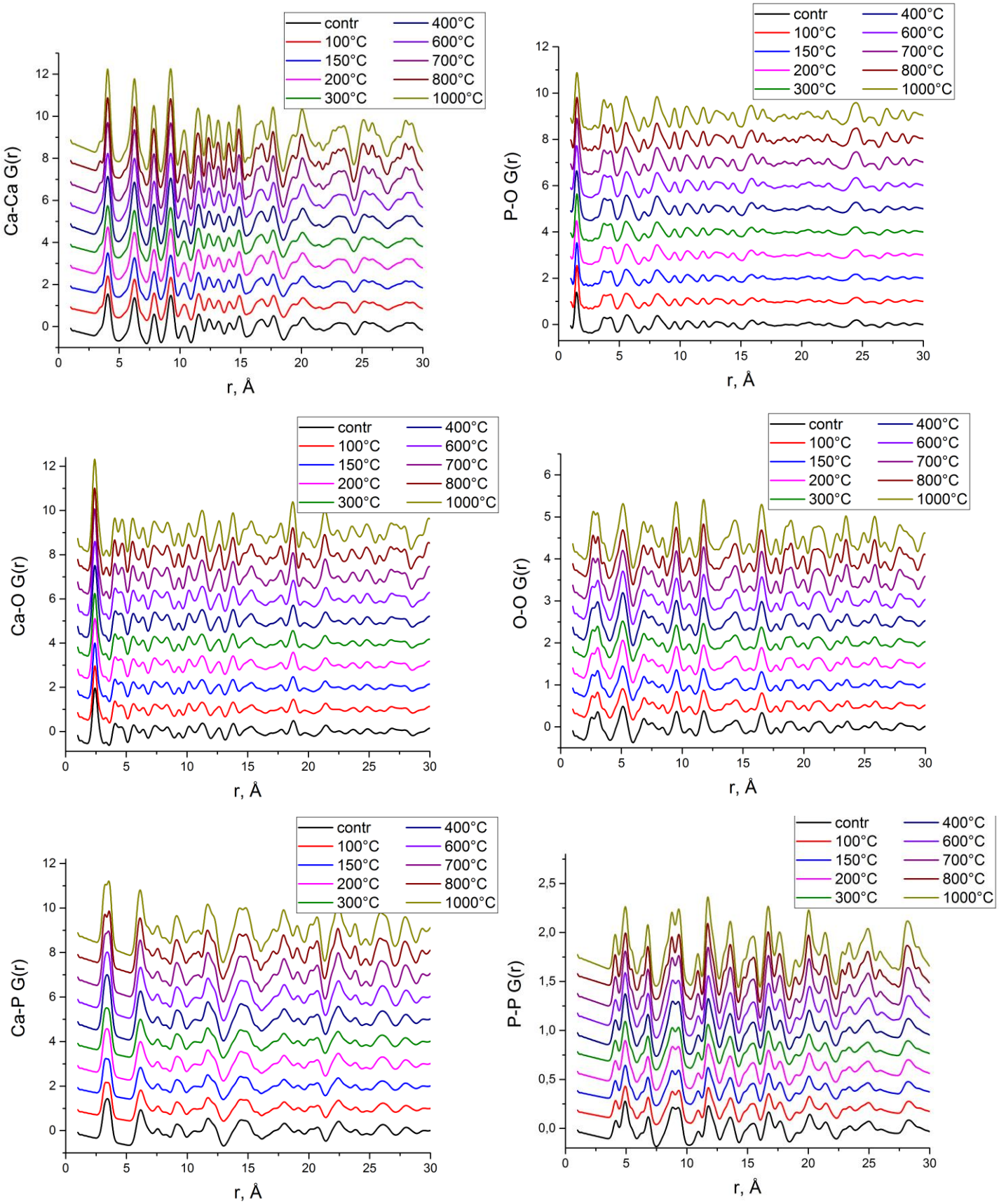

Figure A.4.16. Evolution of partial PDFs with temperature for 6 pairs of atomic bonds (Ca-Ca, P-P, O-O, Ca-O, P-O and Ca-P pairs). Offset *+1* is used for clarity.

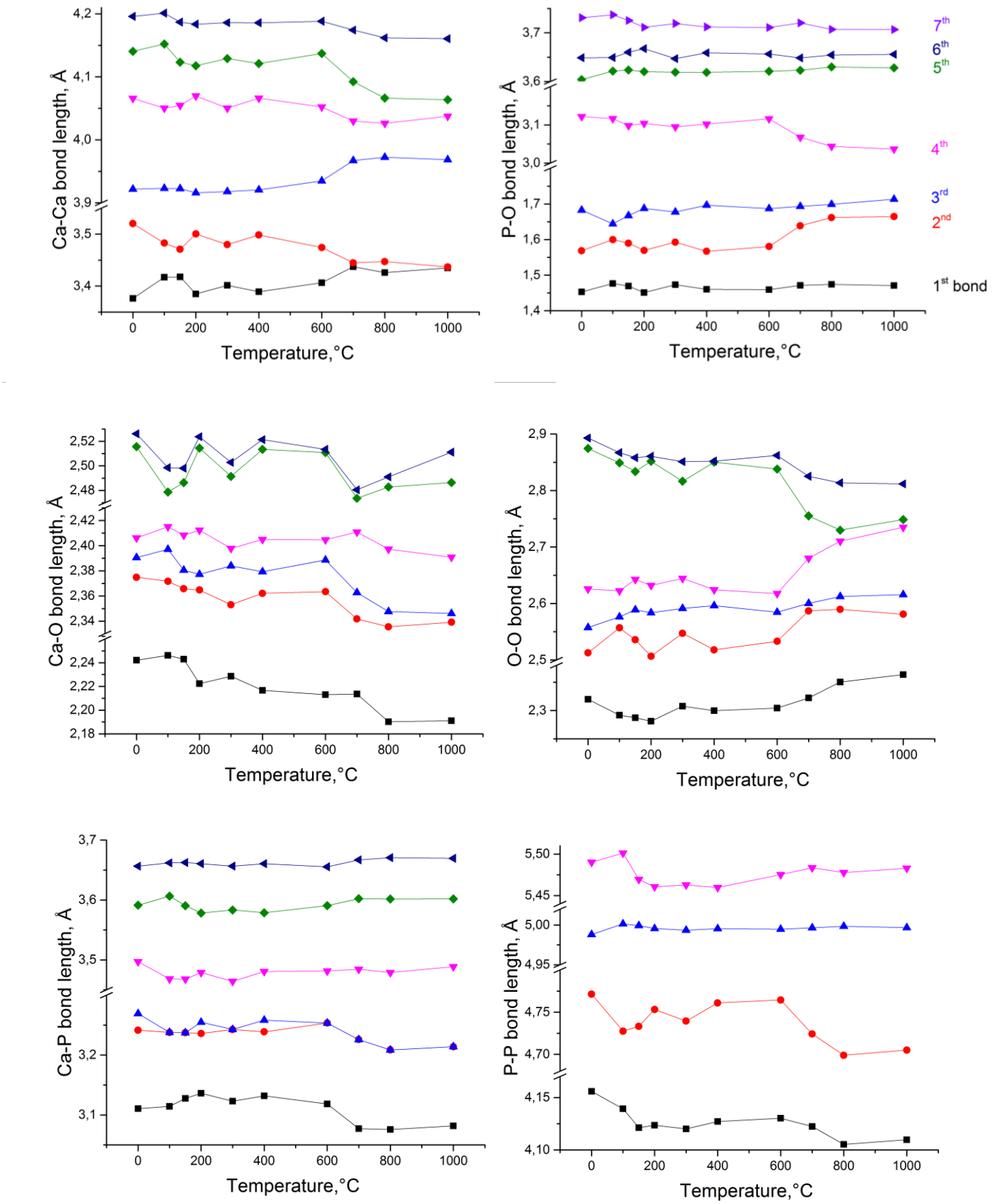

Figure A.4.17. Bond lengths vs temperature (each color shows a particular bond length between the *1st* to *7th* pair as signified for P-O pair).

Appendix 5. PDF analysis of pathological bone supplementary information

A.5.1. Pathological bone scan selection and masks

In the current section the scans for pathological bone PDF analysis are shown in Fig. A.5.1. – Fig. A.5.5. The optical micrograph (a) and polarized light micrograph (b) of the whole sample with the indication of the scan area are represented on the left side of figures. The right side contains the integrated intensity map of *I (q)* profiles (c) with conservative (d) and intermediate (e) bone masks used for average pathological bone PDF analysis and position resolved-study, respectively.

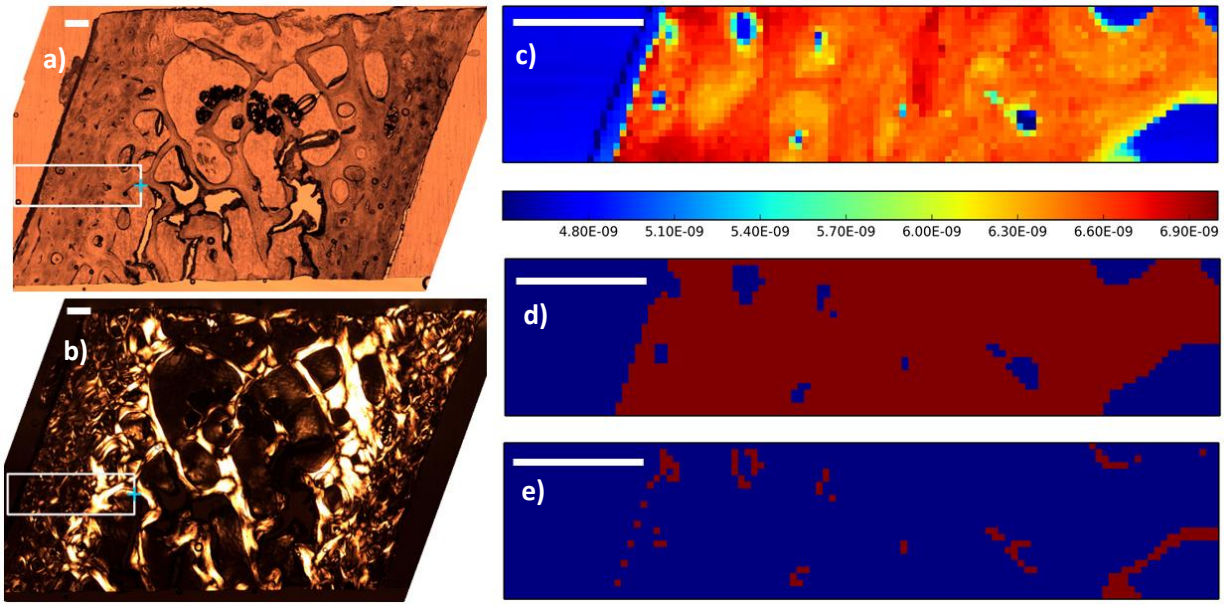

Figure A.5.1. Control sample (CT1): a) optical micrograph and b) polarized light micrograph with indication of scanning area, c) integrated intensity map, d) conservative bone mask and e) intermediate bone mask. Scale bar: 200 μm.

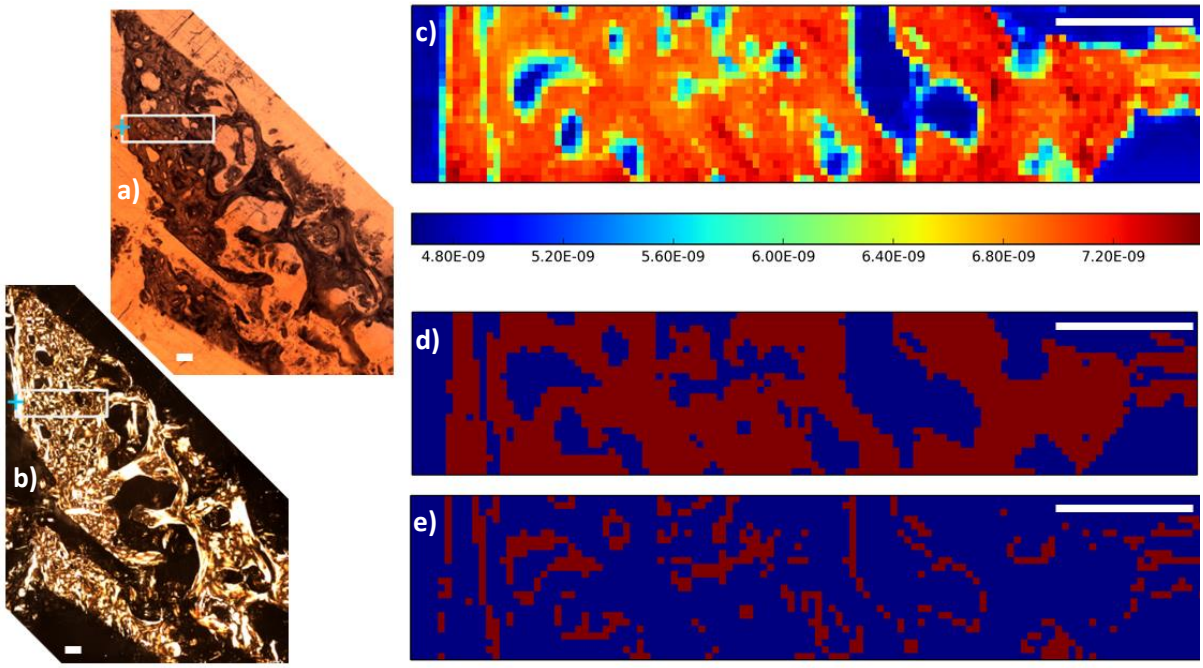

Figure A.5.2. Fluorosis sample (Fluo1): a) optical micrograph and b) polarized light micrograph with indication of scanning area, c) integrated intensity map, d) conservative bone mask and e) intermediate bone mask. Scale bar: 200 µm.

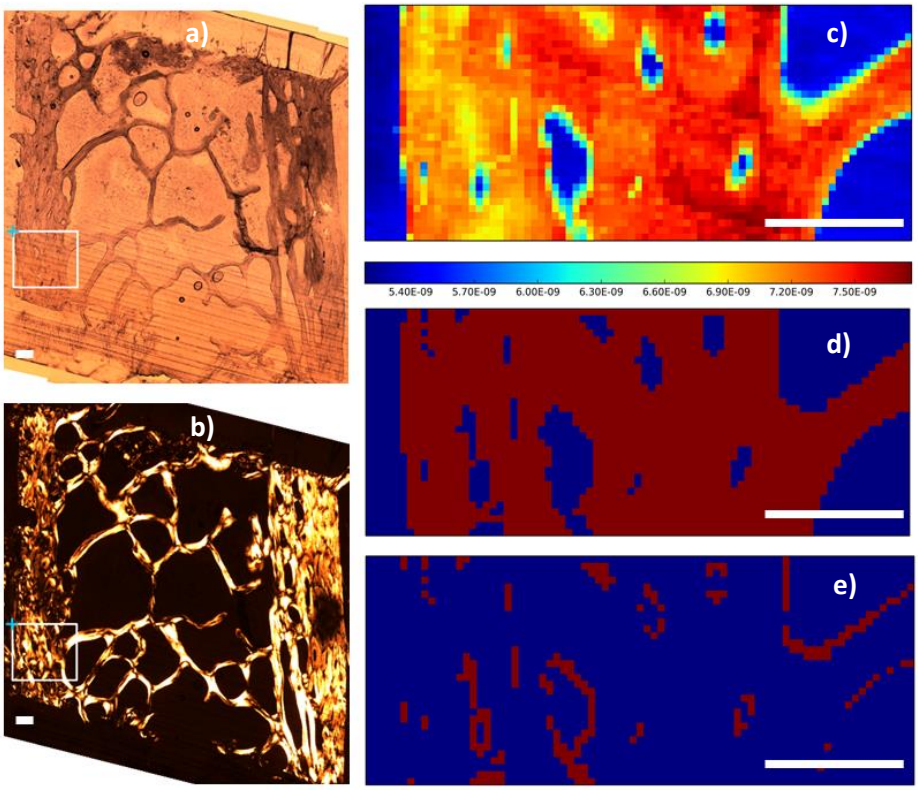

Figure A.5.3. Hyperparathyroidism sample (HPT1): a) optical micrograph and b) polarized light micrograph with indication of scanning area, c) integrated intensity map, d) conservative bone mask and e) intermediate bone mask. Scale bar: 200 µm.

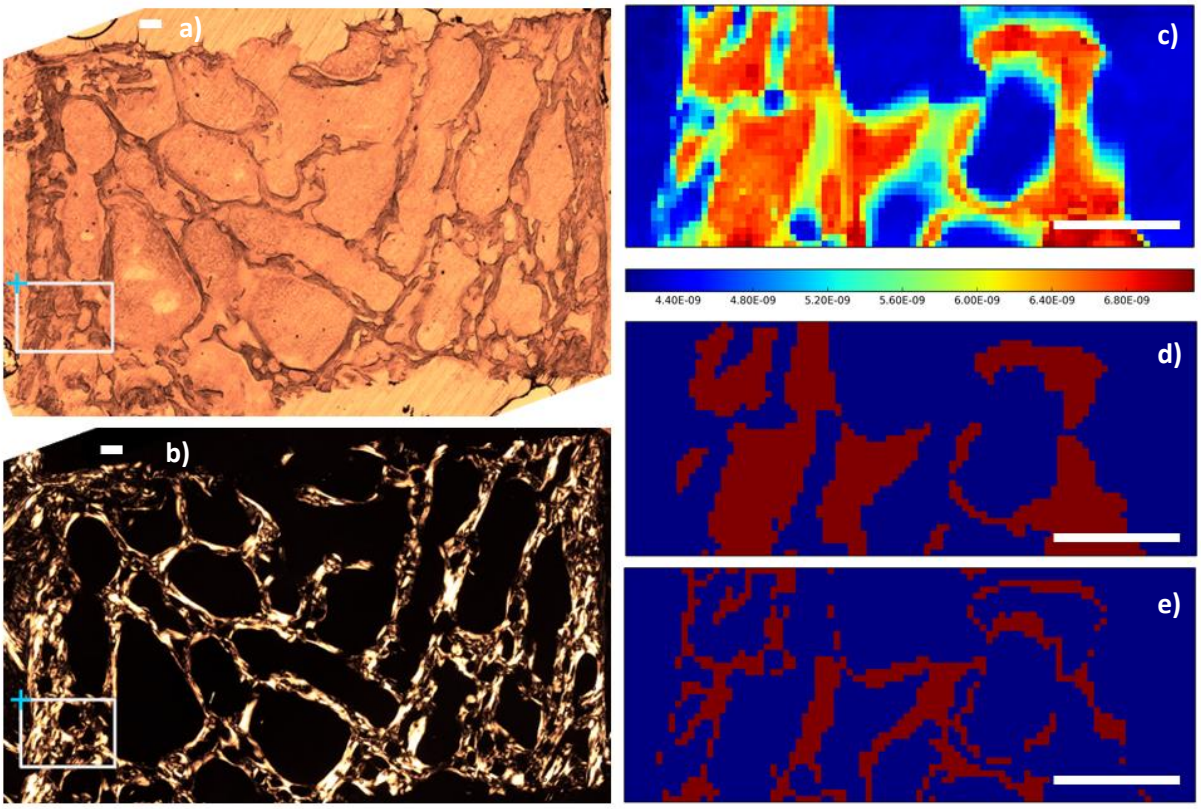

Figure A.5.4. Hyperparathyroidism sample (HPT2): a) optical micrograph and b) polarized light micrograph with indication of scanning area, c) integrated intensity map, d) conservative bone mask and e) intermediate bone mask. Scale bar: 200 µm.

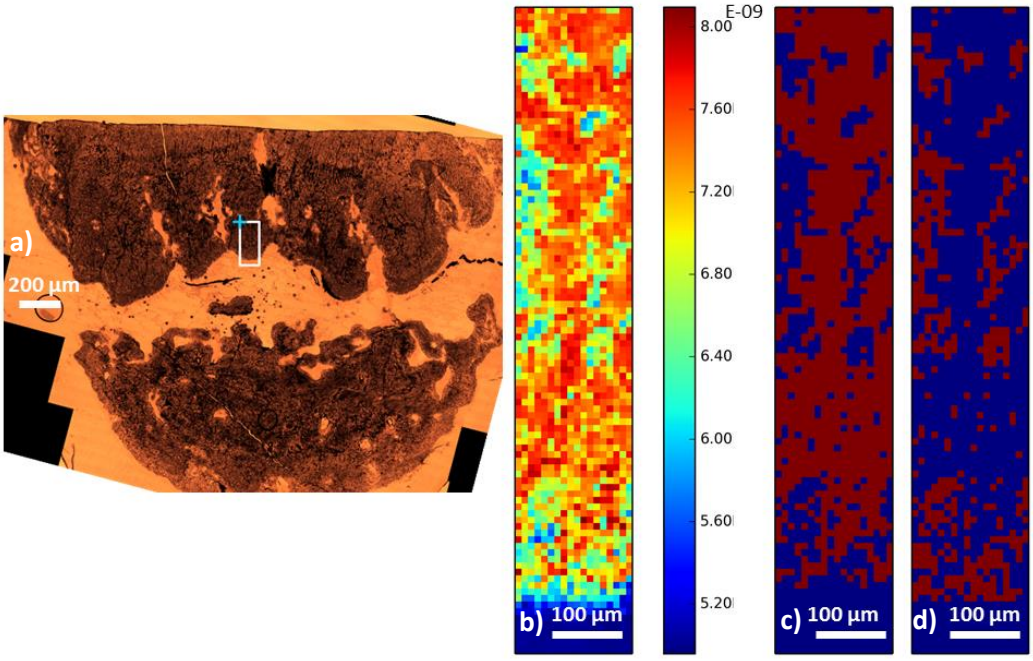

Figure A.5.5. Osteopetrosis sample (OPT1): a) optical micrograph with indication of scanning area, c) integrated intensity map, d) conservative bone mask and e) intermediate bone mask.

A.5.2. Average pathological bone PDF fit

PDF refinement for the average profiles of pathological bone set are show on Fig. A.5.6 – Fig. A.5.10.

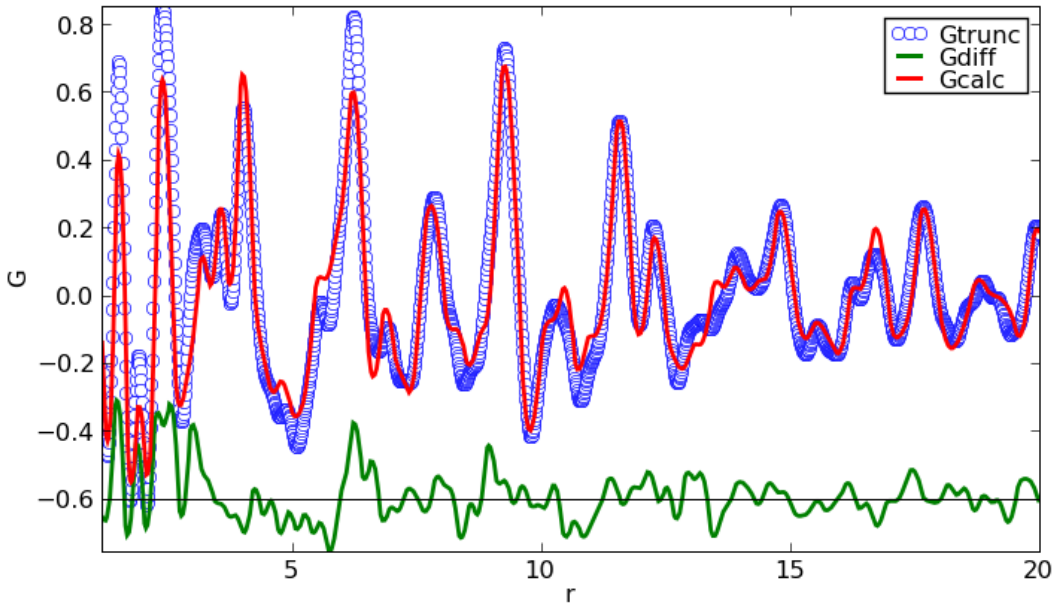

Figure A.5.6. PDFgui refinement for the control sample (CT1): blue – experimental profile, red – fit, green – difference curve.

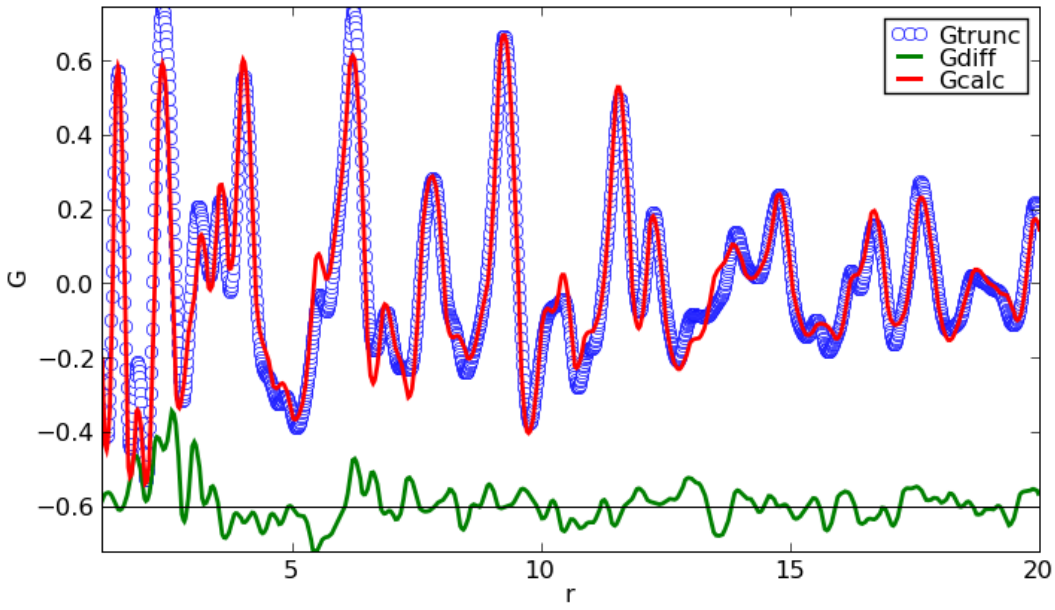

Figure A.5.7. PDFgui refinement for the fluorosis sample (Fluo1): blue – experimental profile, red – fit, green – difference curve.

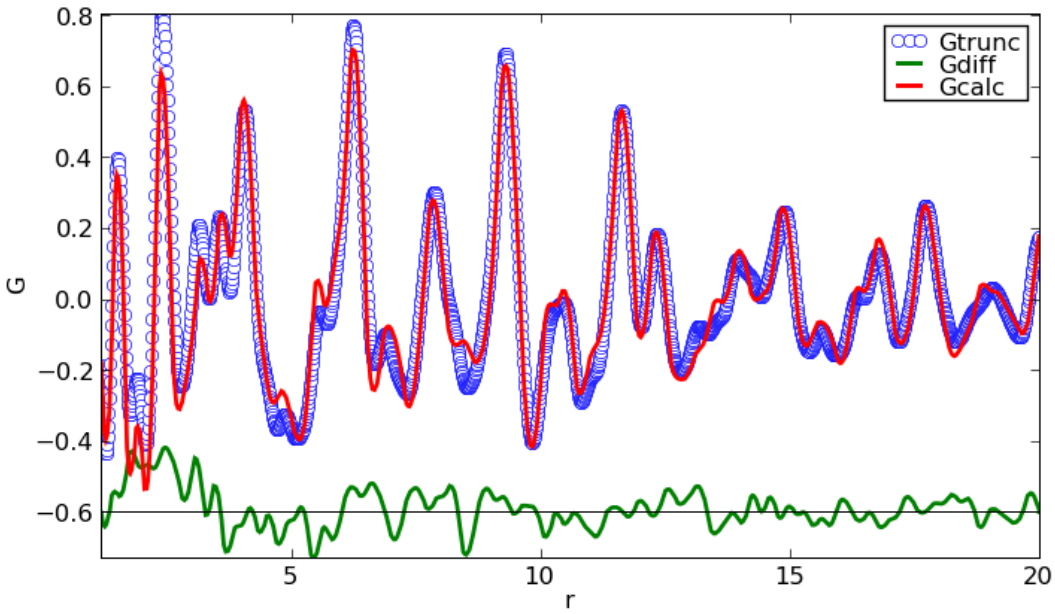

Figure A.5.8. PDFgui refinement for the hyperparathyroidism sample (HPT1): blue – experimental profile, red – fit, green – difference curve.

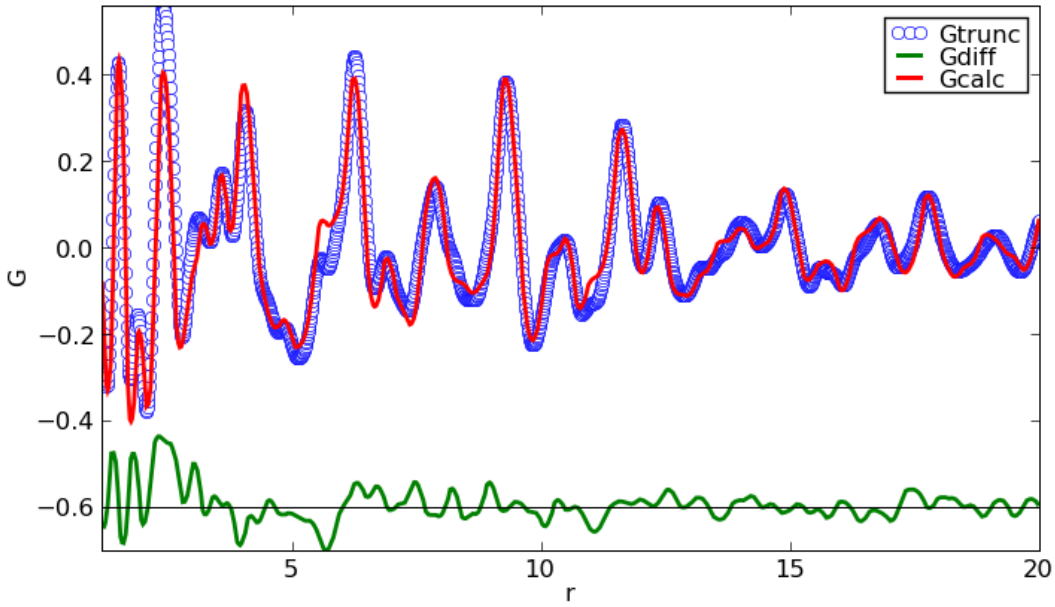

Figure A.5.9. PDFgui refinement for the hyperparathyroidism sample (HPT2): blue – experimental profile, red – fit, green – difference curve.

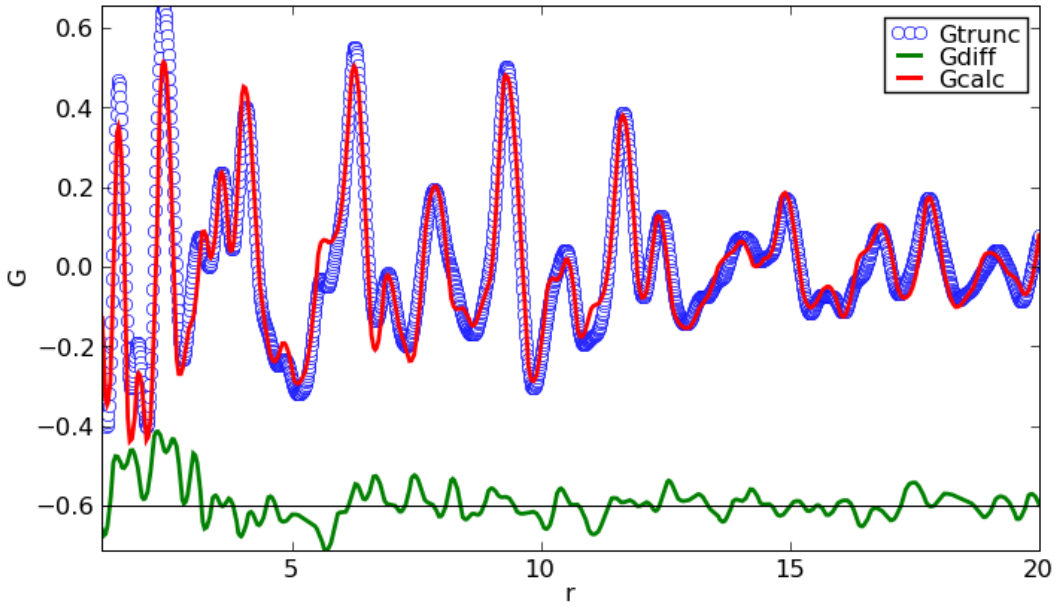

Figure A.5.10. PDFgui refinement for the osteopetrosis sample (HPT1): blue – experimental profile, red – fit, green – difference curve.

A.5.3. Position-resolved pathological bone four peaks fit

The *G(r)* for each of pathological samples were analyzed by fitting four selected peaks at each scanning position at different r-extensions: 1.5, 2.4, 11.5 and 17.6 with a Gaussian (first two) and an asymmetric Gaussian functions (last two) depending on the peak shape.

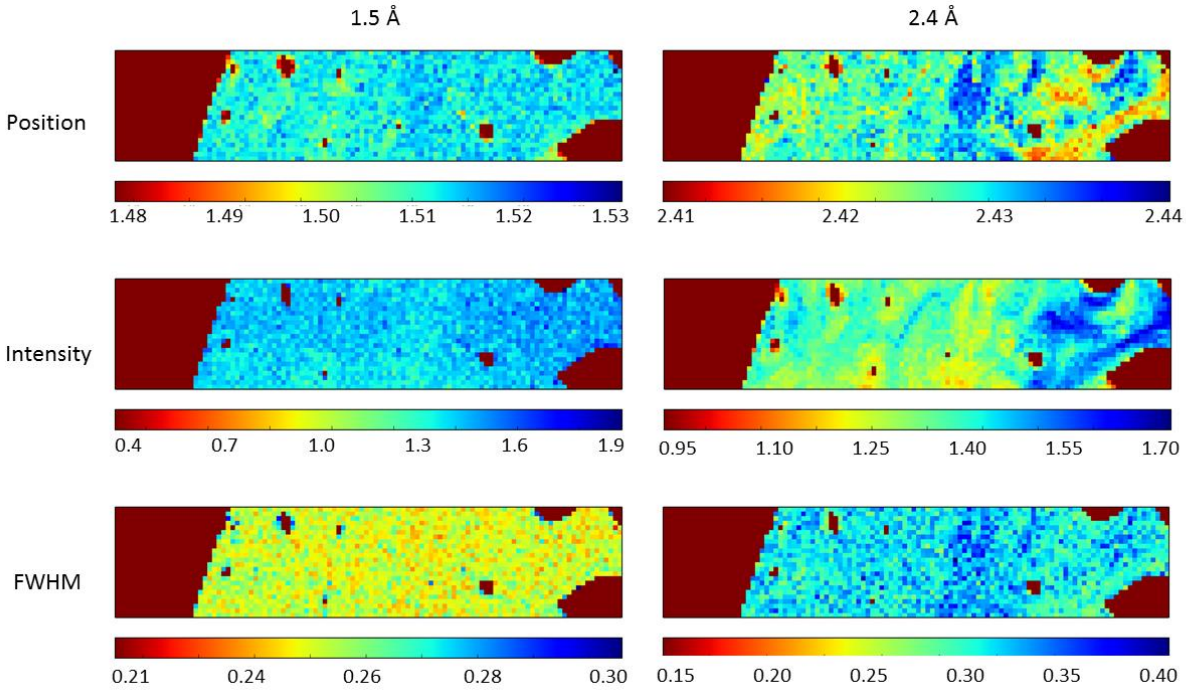

Figure A.5.11. Position, intensity and FWHM of *1.5* and *2.4 Å* peaks for CT1 sample.

The peaks position, intensity and FWHM maps are obtained by applying the mask that combines both conservative bone mask and intermediate mask to filter the data coming from the resin and plotted in Fig. A.5.11 – Fig. A.5.18

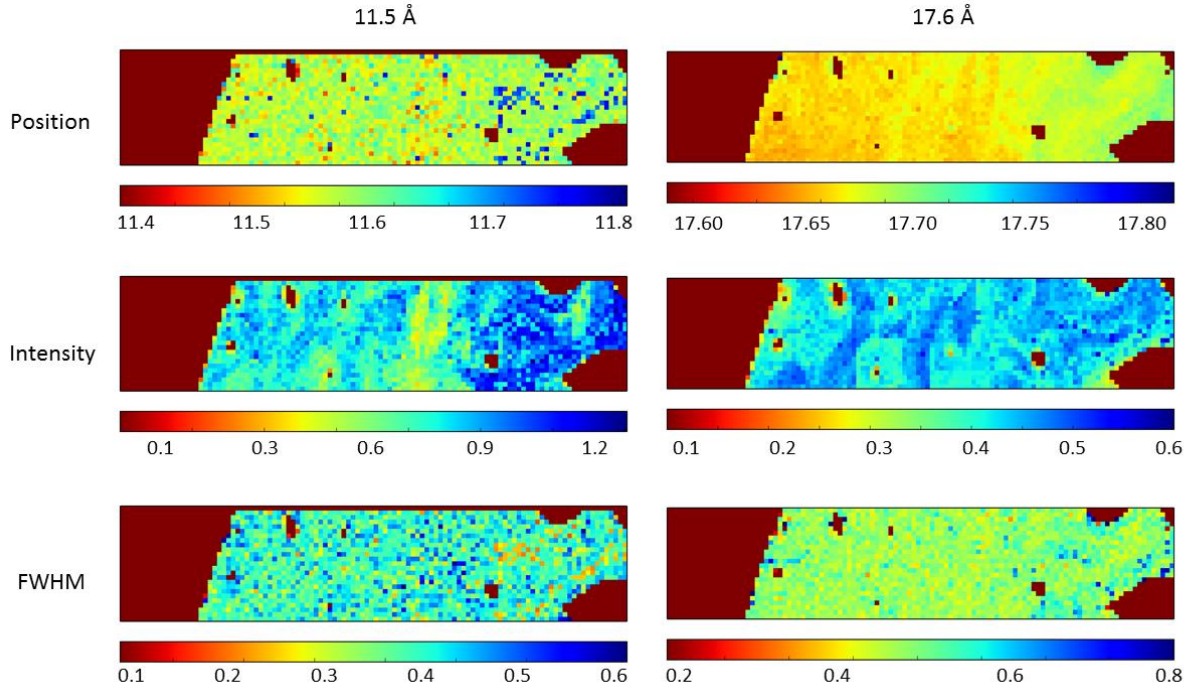

Figure A.5.12. Position, intensity and FWHM of *11.5* and *17.6 Å* peaks for CT1 sample.

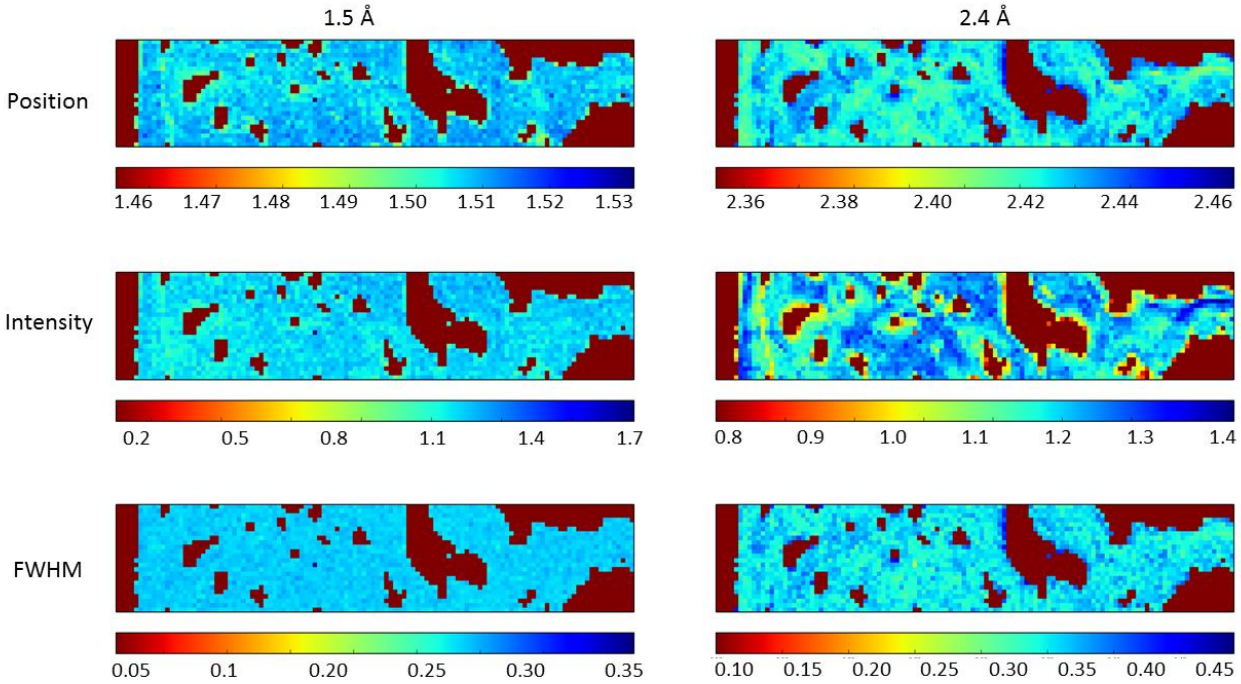

Figure A.5.13. Position, intensity and FWHM of *1.5* and *2.4 Å* peaks for Fluo1 sample.

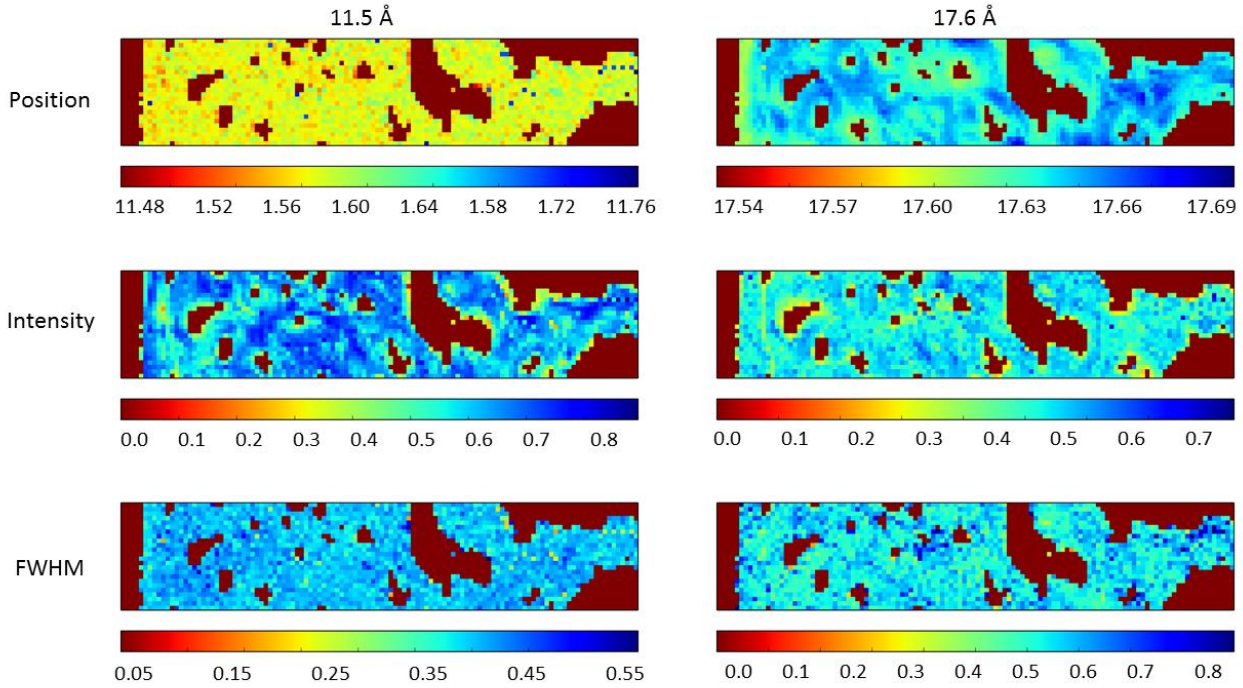

Figure A.5.14. Position, intensity and FWHM of *11.5* and *17.6 Å* peaks for Fluo1 sample.

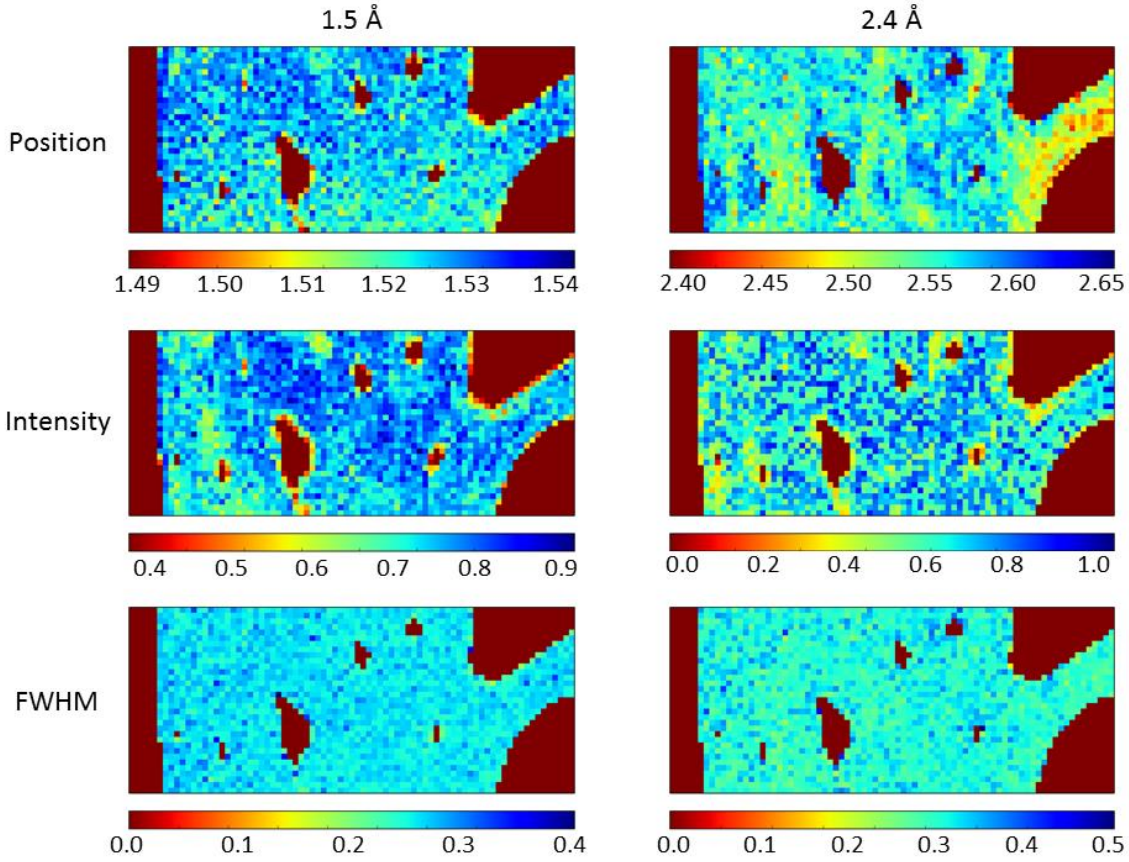

Figure A.5.15. Position, intensity and FWHM of *1.5* and *2.4 Å* peaks for HPT1 sample.

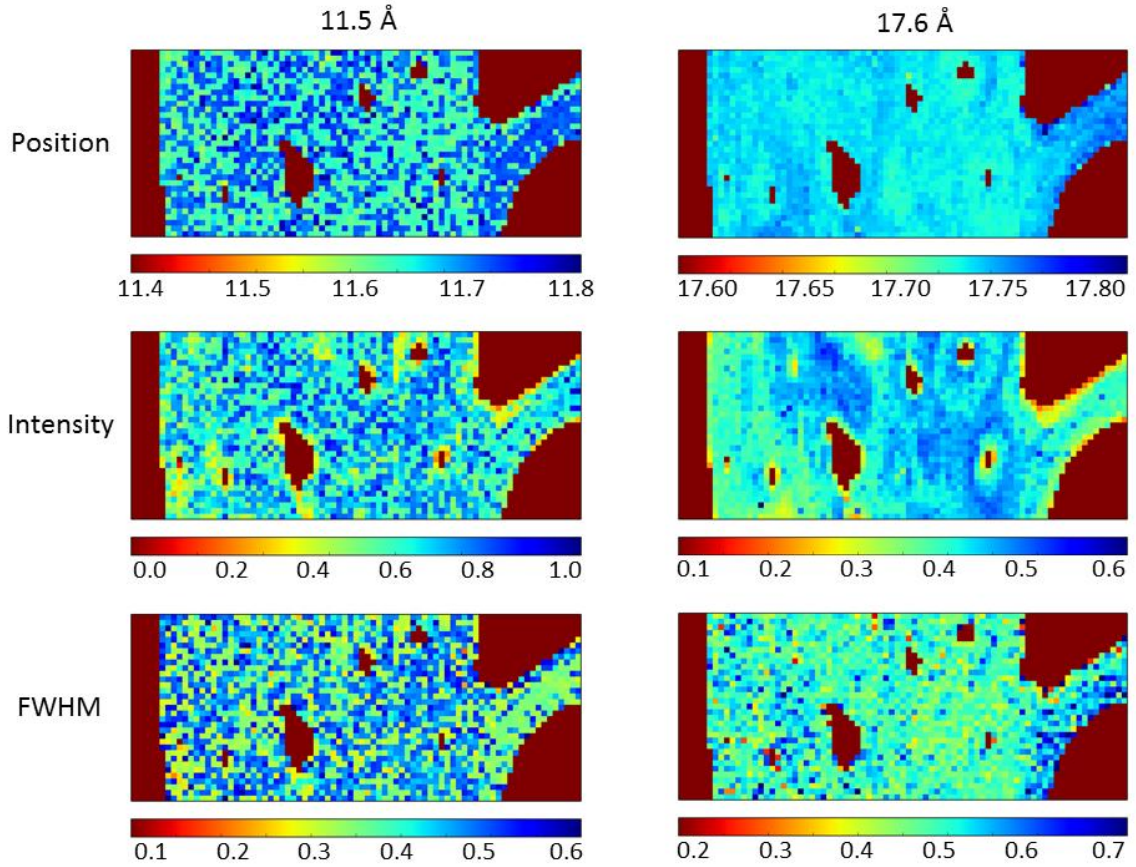

Figure A.5.16. Position, intensity and FWHM of *11.5* and *17.6 Å* peaks for HPT1 sample.

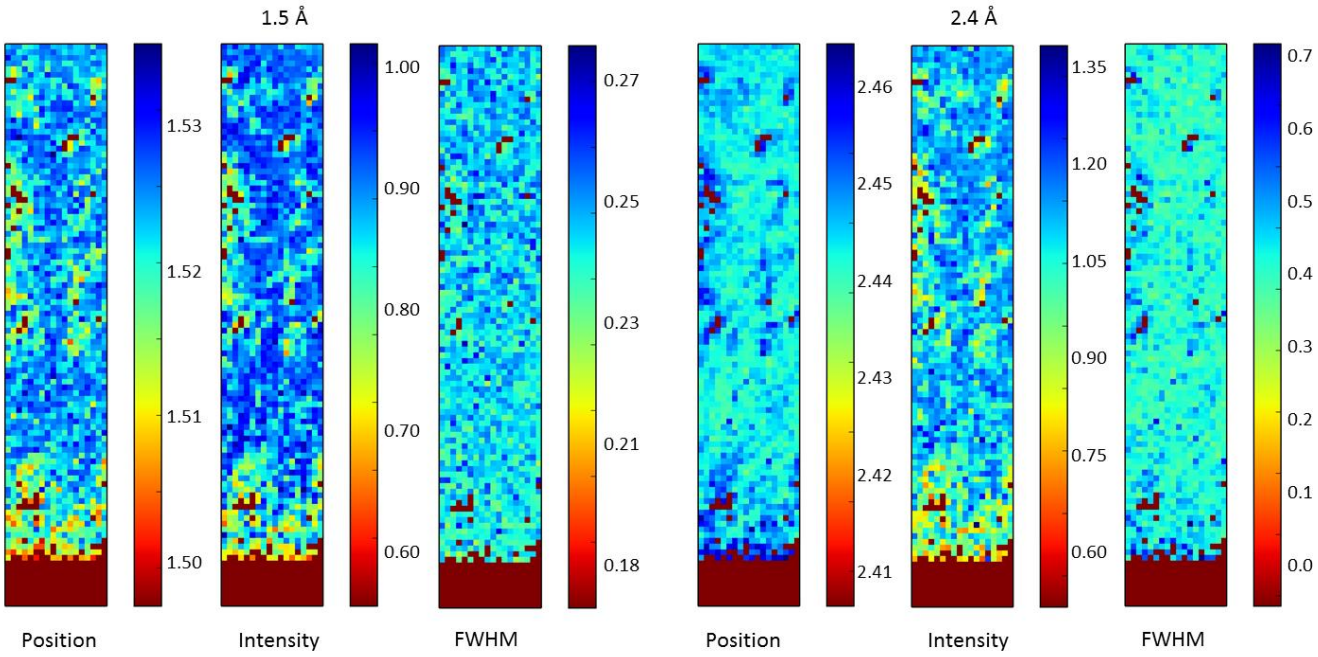

Figure A.5.17. Position, intensity and FWHM of *1.5* (left) and *2.4 Å* (right) peaks for OPT1 sample.

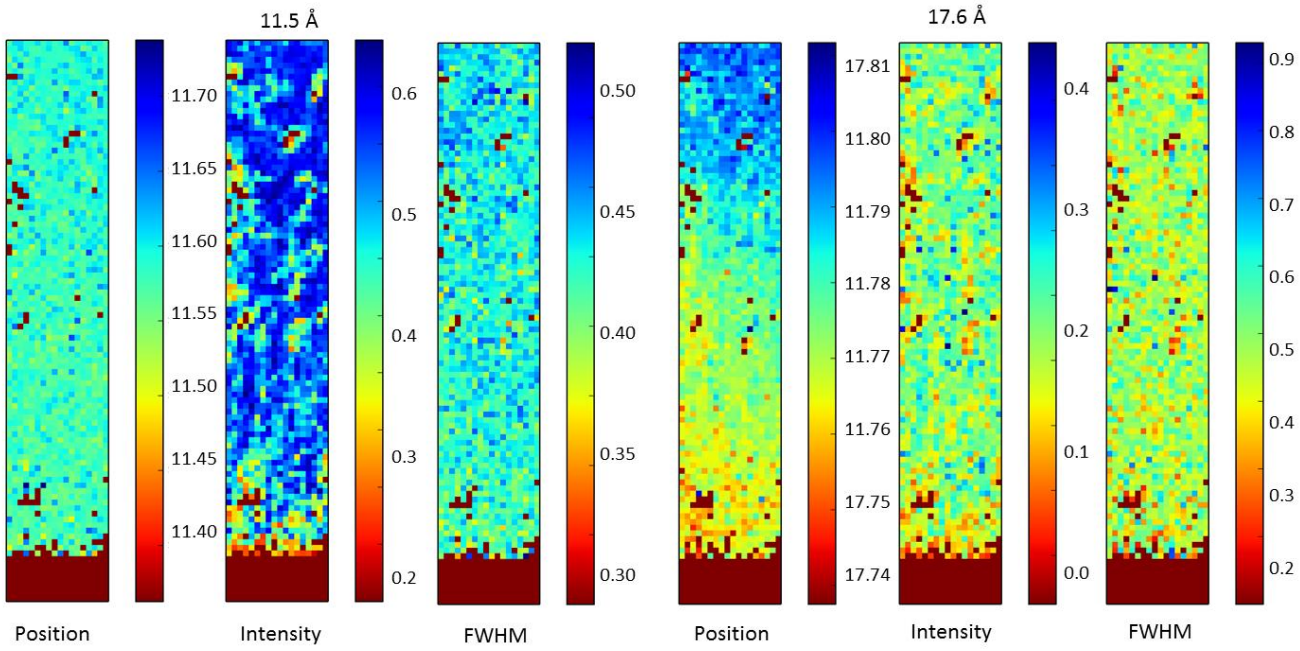

Figure A.5.18. Position, intensity and FWHM of *11.5* (left) and *17.6 Å* (right) peaks for OTP1 sample.

References

1. Fogelman, I. & Blake, G. M. Different approaches to bone densitometry. *J. Nucl. Med.* **41,** 2015–25 (2000).

2. Lochmüller, E.-M., Lill, C. A., Kuhn, V., Schneider, E. & Eckstein, F. Radius Bone Strength in Bending, Compression, and Falling and Its Correlation With Clinical Densitometry at Multiple Sites. *J. Bone Miner. Res.* **17,** 1629–1638 (2002).

3. Schuit, S. *et al.* Fracture incidence and association with bone mineral density in elderly men and women: the Rotterdam Study. *Bone* **34,** 195–202 (2004).

4. Camacho, N. P. *et al.* The Material Basis for Reduced Mechanical Properties in oim Mice Bones. *J. Bone Miner. Res.* **14,** 264–272 (1999).

5. de Jong, W. F. Le substance minerale dans le os. *Recl. des Trav. Chim. des Pays-Bas,* 445–450 (1926).

6. Handschin, R. G. & Stern, W. B. X-ray diffraction studies on the lattice perfection of human bone apatite (Crista Iliaca). *Bone* **16,** S355–S363 (1995).

7. Schroer, C. G. *et al.* Hard x-ray nanoprobe based on refractive x-ray lenses. *Appl. Phys. Lett.* **87,** 124103 (2005).

8. Wagermaier, W. *et al.* Scanning texture analysis of lamellar bone using microbeam synchrotron X-ray radiation. *J. Appl. Crystallogr.* **40,** 115–120 (2007).

9. Granke, M. *et al.* Microfibril Orientation Dominates the Microelastic Properties of Human Bone Tissue at the Lamellar Length Scale. *PLoS One* **8,** (2013).

10. McNally, E. A., Schwarcz, H. P., Botton, G. A. & Arsenault, A. L. A Model for the Ultrastructure of Bone Based on Electron Microscopy of Ion-Milled Sections. *PLoS One* **7,** e29258 (2012).

11. Xin, R., Leng, Y. & Wang, N. HRTEM Study of the Mineral Phases in Human Cortical

Bone. *Adv. Eng. Mater.* **12,** B552–B557 (2010).

12. Boyde, A. in *Bone Research Protocols* 365–400 (Humana Press, 2012). doi:10.1007/978-1-61779-415-5_24

13. Grandfield, K. *et al.* Visualizing biointerfaces in three dimensions: electron tomography of the bone-hydroxyapatite interface. *J. R. Soc. Interface* **7,** 1497–1501 (2010).

14. Eppell, S. J., Tong, W., Katz, J. L., Kuhn, L. & Glimcher, M. J. Shape and size of isolated bone mineralites measured using atomic force microscopy. *J. Orthop. Res.* **19,** 1027–34 (2001).

15. Paschalis, E. P., Betts, F., DiCarlo, E., Mendelsohn, R. & Boskey, A. L. FTIR Microspectroscopic Analysis of Human Iliac Crest Biopsies from Untreated Osteoporotic Bone. *Calcif. Tissue Int.* **61,** 487–492 (1997).

16. Freeman, J. J., Wopenka, B., Silva, M. J. & Pasteris, J. D. Raman Spectroscopic Detection of Changes in Bioapatite in Mouse Femora as a Function of Age and In Vitro Fluoride Treatment. *Calcif. Tissue Int.* **68,** 156–162 (2001).

17. Benno, N., Brian, M. & Joachim, M. *Biomechanics and Biology of Movement*. (Human Kinetics, 2000).

18. Boskey, A. L. & Coleman, R. Aging and Bone. *J. Dent. Res.* **89,** 1333–1348 (2010).

19. Donnelly, E., Meredith, D. S., Nguyen, J. T. & Boskey, A. L. Bone tissue composition varies across anatomic sites in the proximal femur and the iliac crest. *J. Orthop. Res.* **30,** 700–706 (2012).

20. Gregson, C. L. *et al.* Analysis of body composition in individuals with high bone mass reveals a marked increase in fat mass in women but not men. *J. Clin. Endocrinol. Metab.* **98,** 818–828 (2013).

21. Leslie, W. D. Ethnic Differences in Bone Mass—Clinical Implications. *J. Clin. Endocrinol. Metab.* **97,** 4329–4340 (2012).

22. Boskey, A. & Mendelsohn, R. Infrared analysis of bone in health and disease. *J. Biomed. Opt.* **10,** 031102 (2005).

23. Weiner, S. & Wagner, H. D. The Material Bone: Structure-Mechanical Function Relations. *Annu. Rev. Mater. Sci.* **28,** 271–298 (1998).

24. Weiner, S. & Traub, W. Bone structure: from angstroms to microns. *FASEB J.* **6,** 879–85 (1992).

25. Rho, J. Y., Kuhn-Spearing, L. & Zioupos, P. Mechanical properties and the hierarchical structure of bone. *Med. Eng. Phys.* **20,** 92–102 (1998).

26. Caeiro, J. R., González, P. & Guede, D. Biomechanics and bone (& II): Trials in different hierarchical levels of bone and alternative tools for the determination of bone strength. *Rev. Osteoporos. y Metab. Miner.* **5,** 99–108 (2013).

27. Hoffler, C., McCreadie, B., Smith, E. & Goldstein, S. in *Mechanical Testing of Bone and the Bone-Implant Interface* 133–150 (2000).

28. Bensen, C. & An, Y. in *Mechanical Testing of Bone and the Bone-Implant Interface* 87–101 (CRC Press, 1999). doi:10.1201/9781420073560.ch5

29. Steele, G. D. & Bramblett, C. A. *The Anatomy and Biology of the Human Skeleton*. (Texas A&M University Press, 1988).

30. Cavendish, M. *Mammal anatomy: an illustrated guide*. (Cavendish Square Publishing, 2010).

31. Mescher, A. *Junqueira's Basic Histology Text and Atlas*. *McGraw Hill Medical* (2010). doi:10.1097/00005768-199905001-01645

32. McCloskey, C. & Furnival, T. Structure of bone and implant materials. (2006). Available at: http://www.doitpoms.ac.uk/tlplib/bones/index.php.

33. Hollister, S. Introduction to Biosolid Mechanics: Chapter 9: Bone Structure-Function. Available at: http://www.umich.edu/~bme332/ch9bone/bme332bone.htm.

34. Bureau, M. N., Legoux, J.-G. & Denault, J. Implantable biomimetic prosthetic bone. (2013).

35. Rho, J. Y., Ashman, R. B. & Turner, C. H. Young's modulus of trabecular and cortical bone material: Ultrasonic and microtensile measurements. *J. Biomech.* **26,** 111–119 (1993).

36. Mallonee, J. Types of Bone Cells. Available at: http://study.com/academy/lesson/types-of-bone-cells.html.

37. Currey, J. D. *Bones: structure and mechanics*. *Journal of Physics: Conference Series*

(Princeton University Press, 2002).

38. Safadi, F. F. *et al.* in *Bone Pathology* 1–50 (Humana Press, 2009). doi:10.1007/978-1-59745-347-9_1

39. Giraud-Guille, M. M. Twisted plywood architecture of collagen fibrils in human compact bone osteons. *Calcif. Tissue Int.* **42,** 167–180 (1988).

40. Wagermaier, W. *et al.* Spiral twisting of fiber orientation inside bone lamellae. *Biointerphases* **1,** 1 (2006).

41. Wess, T. J. in *Collagen: Structure and Mechanics* 49–80 (2008). doi:10.1007/978-0-387-73906-9_3

42. Fratzl, P. in *Collagen* 506 (Springer US). doi:10.1007/978-0-387-73906-9_1

43. Cui, F. Z., Li, Y. & Ge, J. Self-assembly of mineralized collagen composites. *Materials Science and Engineering R: Reports* **57,** 1–27 (2007).

44. Fratzl, P. & Weinkamer, R. Nature's hierarchical materials. *Progress in Materials Science* **52,** 1263–1334 (2007).

45. Facca, S. *et al.* Active multilayered capsules for in vivo bone formation. *Proc. Natl. Acad. Sci. U. S. A.* **107,** 3406–11 (2010).

46. Hulmes, D. J. S. in *Collagen: Structure and Mechanics* 15–47 (2008). doi:10.1007/978-0-387-73906-9_2

47. Ziv, V. & Weiner, S. Bone crystal sizes: a comparison of transmission electron microscopic and X-ray diffraction line width broadening techniques. *Connect. Tissue Res.* **30,** 165–175 (1994).

48. Kuhn-Spearing, L. T., Rey, C., Kim, H. M. & Glimcher, M. J. in *Synthesis and processing of nanocrystalline powder* (ed. Bourell, D. l) 206 (1996).

49. Glimcher, M. J. in *Metabolic bone disease* (eds. Avioli, L. V & Krane, S. M.) 23–50 (Academic Press, 1997).

50. Boskey, A. Bone mineral crystal size. *Osteoporos. Int.* **14,** 16–21 (2003).

51. Vetter, U., Eanes, E. D., Kopp, J. B., Termine, J. D. & Robey, P. G. Changes in apatite crystal size in bones of patients with osteogenesis imperfecta. *Calcif. Tissue Int.* **49,** 248–

250 (1991).

52. Lodish, H; Berk, A; Zipursky, S. L. et al. in *Molecular Cell Biology* (ed. Freeman, J. J.) (2000).

53. Bella, J., Eaton, M., Brodsky, B. & Berman, H. M. Crystal and molecular structure of a collagen-like peptide at 1.9 A resolution. *Science (80-.).* **266,** 75–81 (1994).

54. Berisio, R., Vitagliano, L., Mazzarella, L. & Zagari, A. Crystal structure of the collagen triple helix model [(Pro-Pro-Gly)(10)](3). *Protein Sci.* **11,** 262–70 (2002).

55. Shoulders, M. D. & Raines, R. T. Collagen Structure and Stability. *Annu Rev Biochem* **78,** 929–958 (2010).

56. Farlay, D. & Boivin, G. in *Osteoporosis* (InTech, 2012). doi:10.5772/29091

57. Rey, C., Combes, C., Drouet, C. & Glimcher, M. J. Bone mineral: update on chemical composition and structure. *Osteoporos. Int.* **20,** 1013–1021 (2009).

58. Chen, P.-Y., Toroian, D., Price, P. A. & McKittrick, J. Minerals Form a Continuum Phase in Mature Cancellous Bone. *Calcif. Tissue Int.* **88,** 351–361 (2011).

59. Landis, W. J., Song, M. J., Leith, A., McEwen, L. & McEwen, B. F. Mineral and Organic Matrix Interaction in Normally Calcifying Tendon Visualized in Three Dimensions by High-Voltage Electron Microscopic Tomography and Graphic Image Reconstruction. *J. Struct. Biol.* **110,** 39–54 (1993).

60. Landis, W. J. *et al.* Mineralization of Collagen May Occur on Fibril Surfaces: Evidence from Conventional and High-Voltage Electron Microscopy and Three-Dimensional Imaging. *J. Struct. Biol.* **117,** 24–35 (1996).

61. Landis, W. J., Hodgens, K. J., Arena, J., Song, M. J. & McEwen, B. F. Structural relations between collagen and mineral in bone as determined by high voltage electron microscopic tomography. *Microsc. Res. Tech.* **33,** 192–202 (1996).

62. Jäger, I. & Fratzl, P. Mineralized Collagen Fibrils: A Mechanical Model with a Staggered Arrangement of Mineral Particles. *Biophys. J.* **79,** 1737–1746 (2000).

63. Roseberry, H. H., Hastings, A. B. & Morse, J. K. X-ray analysis of bone and teeth. *J. Biol. Chem.* 395–407 (1931).

64. Hughes, J. M., Cameron, M. & Crowley, K. D. Structural variations in natural F, OH,

and Cl apatites. *Am. Mineral.* **74,** 870–876 (1989).

65. Elliott, J. C., Mackie, P. E. & Young, R. a. Monoclinic hydroxyapatite. *Science* **180,** 1055–1057 (1973).

66. Hughes, J. M. & Rakovan, J. The Crystal Structure of Apatite, Ca5(PO4)3(F,OH,Cl). *Rev. Mineral. Geochemistry* **48,** 1–12 (2002).

67. Slepko, A. & Demkov, A. A. Hydroxyapatite: Vibrational spectra and monoclinic to hexagonal phase transition. *J. Appl. Phys.* **117,** 074701 (2015).

68. Corno, M., Busco, C., Civalleri, B. & Ugliengo, P. Periodic ab initio study of structural and vibrational features of hexagonal hydroxyapatite Ca10(PO4)6(OH)2. *Phys. Chem. Chem. Phys.* **8,** 2464–2472 (2006).

69. Ma, G. & Liu, X. Y. Hydroxyapatite: Hexagonal or monoclinic? *Cryst. Growth Des.* **9,** 2991–2994 (2009).

70. Ikoma, T., Yamazaki, A., Nakamura, S. & Masaru, A. Phase Transition of Monoclinic Hydroxyapatite. *Netsu Sokutei* **25,** 141–149 (1998).

71. Suda, H., Yashima, M., Kakihana, M. & Al., E. Monoclinic - Hexagonal Phase Transition in Hydroxyapatite Studied by X-ray Powder Diffraction and Differential Scanning Calorimeter Techniques. *J. Phys. Chem.* **99,** 6752–6754 (1995).

72. Wopenka, B. & Pasteris, J. D. A mineralogical perspective on the apatite in bone. in *Materials Science and Engineering C* **25,** 131–143 (2005).

73. Gourrier, A. *et al.* Scanning small-angle X-ray scattering analysis of the size and organization of the mineral nanoparticles in fluorotic bone using a stack of cards model. *J. Appl. Crystallogr.* **43,** 1385–1392 (2010).

74. Everett, E. T. Fluoride's Effects on the Formation of Teeth and Bones, and the Influence of Genetics. *J. Dent. Res.* **90,** 552–560 (2011).

75. Laurencin, D. *et al.* Magnesium incorporation into hydroxyapatite. *Biomaterials* **32,** 1826–1837 (2011).

76. Rude, R. K. & Gruber, H. E. Magnesium deficiency and osteoporosis: animal and human observations. *J. Nutr. Biochem.* **15,** 710–716 (2004).

77. Luoma, H. The role of magnesium in the aetiology and prevention of caries: some new

findings and implications. *Magnesium research : official organ of the International Society for the Development of Research on Magnesium* **1,** 223–230 (1988).

78. McConnell, D. & Gruner, J. W. The problem of the carbonate-apatites. III. Carbonate-apatite from Magnet Cove, Arkansas. *Am. Minerol.* **25,** 157–168 (1940).

79. Vallet-Regi, M. & Arcos, D. in *Nanoceramics in Clinical Use: From Materials to Applications* 1–29 (RSC Publishing, 2015). doi:10.1039/9781782622550-00001

80. Elliott, J. C. Structure and chemistry of the apatites and other calcium orthophosphates. *Studies in Inorganic Chemistry Volume* **18,** (Elsevier, 1994).

81. Antonakos, A., Liarokapis, E. & Leventouri, T. Micro-Raman and FTIR studies of synthetic and natural apatites. *Biomaterials* **28,** 3043–3054 (2007).

82. Termine, J. D., Eanes, E. D., Greenfield, D. J., Nylen, M. U. & Harper, R. a. Hydrazine-deproteinated bone mineral. Physical and chemical properties. *Calcif. Tissue Res.* **12,** 73–90 (1973).

83. Cazalbou, S., Combes, C., Eichert, D. & Rey, C. Adaptative physico-chemistry of bio-related calcium phosphates. *J. Mater. Chem.* **14,** 2148–2153 (2004).

84. Pàmies, P. Bone's bridged layers. *Nat. Mater.* **13,** 428–428 (2014).

85. Duer, M. & Veis, A. Bone mineralization: Water brings order. *Nat. Mater.* **12,** 1081–1082 (2013).

86. Muschler, G. F., Raut, V. P., Patterson, T. E., Wenke, J. C. & Hollinger, J. O. The Design and Use of Animal Models for Translational Research in Bone Tissue Engineering and Regenerative Medicine. *Tissue Eng. Part B Rev.* **16,** 123–145 (2010).

87. Pearce, A. I., Richards, R. G., Milz, S., Schneider, E. & Pearce, S. G. Animal models for implant biomaterial research in bone: A review. *European Cells and Materials* **13,** 1–10 (2007).

88. Aerssens, J., Boonen, S., Lowet, G. & Dequeker, J. Interspecies Differences in Bone Composition, Density, and Quality: Potential Implications for in Vivo Bone Research 1. *Endocrinology* **139,** 663–670 (1998).

89. Viateau, V., Logeart-Avramoglou, D., Guillemin, G. & Petite, H. in *Sourcebook of Models for Biomedical Research* 725–736 (Humana Press, 2008). doi:10.1007/978-1-

59745-285-4_74

90. Smith, J. W. Collagen fibre patterns in mammalian bone. *J. Anat.* **94,** 329–344 (1960).

91. Liebschner, M. A. K. Biomechanical considerations of animal models used in tissue engineering of bone. *Biomaterials* **25,** 1697–1714 (2004).

92. Rogers, J., Weidmann, S. M. & Parkinson, A. Studies on the Skeletal Tissues. II. The collagen content of bones from rabbits, oxen, and humans. *Biochem. J.* **50,** 537–542 (1951).

93. Greenwood, C., Rogers, K., Beckett, S. & Clement, J. Initial observations of dynamically heated bone. *Cryst. Res. Technol.* **48,** 1073–1082 (2013).

94. LeGeros, R. Z., Bonel, G. & Legros, R. Types of 'H2O' in human enamel and in precipitated apatites. *Calcif. Tissue Res.* **26,** 111–118 (1978).

95. Rogers, K. D. & Daniels, P. An X-ray diffraction study of the effects of heat treatment on bone mineral microstructure. *Biomaterials* **23,** 2577–2585 (2002).

96. Hiller, J. C., Thompson, T. J. U., Evison, M. P., Chamberlain, A. T. & Wess, T. J. Bone mineral change during experimental heating: An X-ray scattering investigation. *Biomaterials* **24,** 5091–5097 (2003).

97. Piga, G., Malgosa, A., Thompson, T. J. U. & Enzo, S. A new calibration of the XRD technique for the study of archaeological burned human remains. *J. Archaeol. Sci.* **35,** 2171–2178 (2008).

98. Nakano, T., Umakoshi, Y. & Tokumura, A. Variation in crystallinity of hydroxyapatite and the related calcium phosphates by mechanical grinding and subsequent heat treatment. *Metall. Mater. Trans. A* **33,** 521–528 (2002).

99. Beckett, S., Rogers, K. D. & Clement, J. G. Inter-species variation in bone mineral behavior upon heating. *J. Forensic Sci.* **56,** 571–579 (2011).

100. Mostafa, N. Y. & Brown, P. W. Computer simulation of stoichiometric hydroxyapatite: Structure and substitutions. *J. Phys. Chem. Solids* **68,** 431–437 (2007).

101. Ren, F., Leng, Y., Xin, R. & Ge, X. Synthesis, characterization and ab initio simulation of magnesium-substituted hydroxyapatite. *Acta Biomater.* **6,** 2787–2796 (2010).

102. Murugan, R., Rao, K. P. & Sampath Kumar, T. S. Heat-deproteinated xenogeneic bone

from slaughterhouse waste: Physico-chemical properties. *Bull. Mater. Sci.* **26,** 523–528 (2003).

103. Albers-Schonberg, H. Roentgenbilder einer seltenen Knochennerkrankung. *Munch Med Wochenschr* **51,** 365 (1904).

104. Stark, Z. & Savarirayan, R. Osteopetrosis. *Orphanet J. Rare Dis.* **4,** 5 (2009).

105. Boskey, A. Mineral changes in osteopetrosis. *Crit Rev Eukaryot Gene Expr* **13,** 109–116 (2003).

106. Rolighed, L., Rejnmark, L. & Christiansen, P. Bone involvement in primary hyperparathyroidism and changes after parathyroidectomy. *Eur. Endocrinol.* **10,** 84–87 (2014).

107. Mosekilde, L. Primary hyperparathyroidism and the skeleton. *Clinical Endocrinology* **69,** 1–19 (2008).

108. Krishnamachari, K. Skeletal fluorosis in humans: a review of recent progress in the understanding of the disease. *Process Food Nutr. Sci.* **10,** 279–314 (1986).

109. Yildiz, M., Akdoğan, M., Tamer, N. & Oral, B. Bone mineral density of the spine and femur in early postmenopausal Turkish women with endemic skeletal fluorosis. *Calcif. Tissue Int.* **72,** 689–693 (2003).

110. Leica. Ultramicrotomes & Cryo-Ultramicrotomes. Available at: http://www.leica-microsystems.com.

111. DiATOME Diamond Knives. Available at: https://www.diatomeknives.com/.

112. Guide to Sectioning on the Reichert-Jung Ultracut E Ultramicrotome Shannon Modla BioImaging Center Delaware Biotechnology Institute.

113. Bravais, A. Mémoire sur les systèmes formés par les points distribués régulièrement sur un plan ou dans l'espace. *J. Ec. Polytech* **19,** 1–128 (1850).

114. Kittel, C. *Introduction to Solid State Physics*. *John Wiley and Sons, Inc., New York***,** (2004).

115. Ashcroft, N. W. & Mermin, N. D. *Solid State Physics*. *Solid State Physics* **2,** (1976).

116. Verezhak, M. Aperiodic self-assembled materials by inelastic synchrotron and neutron

scattering. (University of Rennes 1, 2011).

117. Egami, T. & Billinge, S. J. . *Underneath the Bragg Peaks. Materials Today* **6,** (2003).

118. van Smaalen, S. *Incommensurate crystallography*. (OUP Oxford, 2002).

119. Attwood, D. *Soft X-Rays and Extreme Ultraviolet Radiation. Principles and Applications* (Cambridge University Press, 2013).

120. Livet, F. & Sutton, M. X-ray coherent scattering in metal physics. *Comptes Rendus Physique* **13,** 227–236 (2012).

121. Kakudo, M. & Kasai, N. *X-ray diffraction by polymers*. (Elsevier, 1972).

122. Myers, P. *Introductory Solid State Physics*. (CRC Press, 2002).

123. Abbe, E. Beiträge zur Theorie des Mikroskops und der mikroskopischen Wahrnehmung. *Arch. für Mikroskopische Anat.* **9,** 413–418 (1873).

124. Porter, A. B. On the diffraction theory of microscopic vision. *Philos. Mag.* **11,** 154–156 (1906).

125. Willig, K. I. *et al.* Nanoscale resolution in GFP-based microscopy. *Nat. Methods* **3,** 721–3 (2006).

126. Betzig, E. *et al.* Imaging intracellular fluorescent proteins at nanometer resolution. *Science* **313,** 1642–1645 (2006).

127. Rietveld, H. M. Line profiles of neutron powder-diffraction peaks for structure refinement. *Acta Crystallogr.* **22,** 151–152 (1967).

128. Rietveld, H. M. A profile refinement method for nuclear and magnetic structures. *J. Appl. Crystallogr.* **2,** 65–71 (1969).

129. Young, R. The Rietveld Method. *International Union of Crystallography Oxford Science Publications* 312 (1993). doi:10.1017/CBO9781107415324.004

130. Will, G. Powder diffraction: The rietveld method and the two stage method to determine and refine crystal structures from powder diffraction data. Powder Diffraction: The Rietveld Method and the Two Stage Method to Determine and Refine Crystal Structures from Powder Diffraction Data (2006). doi:10.1007/3-540-27986-5

131. McCusker, L. B., Von Dreele, R. B., Cox, D. E., Louër, D. & Scardi, P. Rietveld

refinement guidelines. *J. Appl. Crystallogr.* **32,** 36–50 (1999).

132. Bordet, P. Local structure studies using the pair distribution function. *Neutrons Mater. Sci.* **104,** (2015).

133. Qiu, X., Thompson, J. W. & Billinge, S. J. L. PDFgetX2: A GUI-driven program to obtain the pair distribution function from X-ray powder diffraction data. *J. Appl. Crystallogr.* **37,** 678 (2004).

134. Farrow, C. L. *et al.* PDFfit2 and PDFgui: computer programs for studying nanostructure in crystals. *J. Phys. Condens. Matter* **19,** 335219 (2007).

135. Juhás, P., Farrow, C. L., Yang, X., Knox, K. R. & Billinge, S. J. L. Complex modeling: A strategy and software program for combining multiple information sources to solve ill posed structure and nanostructure inverse problems. *Acta Crystallogr. Sect. A Found. Adv.* **71,** 562–568 (2015).

136. Proffen, T. & Billinge, S. J. L. PDFFIT, a program for full profile structural refinement of the atomic pair distribution function. *J. Appl. Crystallogr.* **32,** 572–575 (1999).

137. Proffen, T. & Neder, R. B. DISCUS : a program for diffuse scattering and defect-structure simulation. *J. Appl. Crystallogr.* **30,** 171–175 (1997).

138. Krayzman, V. *et al.* A combined fit of total scattering and extended X-ray absorption fine structure data for local-structure determination in crystalline materials. *J. Appl. Crystallogr.* **42,** 867–877 (2009).

139. Sayre, D. Prospects for long-wavelength X-ray microscopy and diffraction. in *Lecture Notes in Physics, Vol. 112, Imaging Processes and Coherence in Physics* 229–235 (1980). doi:10.1007/3-540-09727-9

140. Martínez, M. Crystallography-Cristalografia. (2011). Available at: http://www.xtal.iqfr.csic.es/Cristalografia.

141. Miao, J., Charalambous, P., Kirz, J. & Sayre, D. Extending the methodology of X-ray crystallography to allow imaging of micrometre-sized non-crystalline specimens. *Nature* **400,** 342–344 (1999).

142. Chushkin, Y. & Zontone, F. Upsampling speckle patterns for coherent X-ray diffraction imaging. *J. Appl. Crystallogr.* **46,** 319–323 (2013).

143. Fienup, J. R. Phase retrieval algorithms: a comparison. *Appl. Opt.* **21,** 2758–2769 (1982).

144. Fienup, J. R. & Wackerman, C. C. Phase-retrieval stagnation problems and solutions. *J. Opt. Soc. Am. A* **3,** 1897–1907 (1986).

145. Köhl, M., Minkevich, A. A. & Baumbach, T. Improved success rate and stability for phase retrieval by including randomized overrelaxation in the hybrid input output algorithm. *Opt. Express* **20,** 17093 (2012).

146. Williams, G., Pfeifer, M., Vartanyants, I. & Robinson, I. Effectiveness of iterative algorithms in recovering phase in the presence of noise. *Acta Crystallogr. Sect. A Found. Crystallogr.* **63,** 36–42 (2007).

147. Duisenberg, A. J. M., Kroon-Batenburg, L. M. J. & Schreurs, A. M. M. An intensity evaluation method: EVAL-14. *J. Appl. Crystallogr.* **36,** 220–229 (2003).

148. Synchrotron Science. Available at: http://www.esrf.eu/about/synchrotron-science.

149. Fienup, J. R. Invariant error metrics for image reconstruction. *Appl. Opt.* **36,** 8352–8357 (1997).

150. Goldstein, J. *et al.* Scanning Electron Microscopy and X-ray Microanalysis. Scanning Electron Microscopy **1,** (2003).

151. Rauch, E. F. & Véron, M. Automated crystal orientation and phase mapping in TEM. *Mater. Charact.* **98,** 1–9 (2014).

152. Rauch, E. F. & Dupuy, L. Rapid spot diffraction patterns idendification through template matching. *Arch. Metall. Mater.* **55,** 87–99 (2005).

153. Schwarzer, R. A. & Zaefferer, S. An Inexpensive CCD Camera System for the Recording and On-Line Interpretation of TEM Kikuchi Patterns. *Mater. Sci. Forum* **157-162,** 189–194 (1994).

154. Vincent, R. & Midgley, P. A. Double conical beam-rocking system for measurement of integrated electron diffraction intensities. *Ultramicroscopy* **53,** 271–282 (1994).

155. Rauch, E. F. *et al.* Automated nanocrystal orientation and phase mapping in the transmission electron microscope on the basis of precession electron diffraction. *Zeitschrift für Krist.* **225,** (2010).

156. Cardoso, L., Fritton, S. P., Gailani, G., Benalla, M. & Cowin, S. C. A review of recent

advances in the assessment of bone porosity, permeability, and interstitial fluid flow. *J. Biomech.* **46,** 253–265 (2012).

157. Cowin, S. C. Bone poroelasticity. *Journal of Biomechanics* **32,** 217–238 (1999).

158. Palacio-Mancheno, P. E., Larriera, A. I., Doty, S. B., Cardoso, L. & Fritton, S. P. 3D assessment of cortical bone porosity and tissue mineral density using high-resolution μcT: Effects of resolution and threshold method. *J. Bone Miner. Res.* **29,** 142–150 (2014).

159. Sharma, D. *et al.* Alterations in the osteocyte lacunar-canalicular microenvironment due to estrogen deficiency. *Bone* **51,** 488–497 (2012).

160. Hannah, K. M., Thomas, C. D. L., Clement, J. G., De Carlo, F. & Peele, A. G. Bimodal distribution of osteocyte lacunar size in the human femoral cortex as revealed by micro-CT. *Bone* **47,** 866–871 (2010).

161. Wang, L., Ciani, C., Doty, S. B. & Fritton, S. P. Delineating bone's interstitial fluid pathway in vivo. *Bone* **34,** 499–509 (2004).

162. Nyman, J. S. *et al.* The influence of water removal on the strength and toughness of cortical bone. *J. Biomech.* **39,** 931–938 (2006).

163. Piekarski, K. & Munro, M. Transport mechanism operating between blood supply and osteocytes in long bones. *Nature* **269,** 80–82 (1977).

164. Fritton, S. P. & Weinbaum, S. Fluid and Solute Transport in Bone: Flow-Induced Mechanotransduction. *Annu. Rev. Fluid Mech.* **41,** 347–374 (2009).

165. Lan Levengood, S. K. *et al.* Multiscale osteointegration as a new paradigm for the design of calcium phosphate scaffolds for bone regeneration. *Biomaterials* **31,** 3552–3563 (2010).

166. Tovar, N. *et al.* The physicochemical characterization and in vivo response of micro/nanoporous bioactive ceramic particulate bone graft materials. *Mater. Sci. Eng. C* **43,** 472–480 (2014).

167. Wang, S., Kowal, T. J., Marei, M. K., Falk, M. M. & Jain, H. Nanoporosity significantly enhances the biological performance of engineered glass tissue scaffolds. *Tissue Eng. Part A* **19,** 1632–40 (2013).

168. Jones, J. R. New trends in bioactive scaffolds: The importance of nanostructure. *J. Eur. Ceram. Soc.* **29,** 1275–1281 (2009).

169. Forien, J.-B. *et al.* Water-Mediated Collagen and Mineral Nanoparticle Interactions Guide Functional Deformation of Human Tooth Dentin. *Chem. Mater.* **28,** 3416–3427 (2016).

170. Cuesta, F. B. de la *et al.* Collagen imaged by Coherent X-ray Diffraction: towards a complementary tool to conventional scanning SAXS. *J. Phys. Conf. Ser.* **247,** 012004 (2010).

171. Berenguer, F. *et al.* Coherent X-ray imaging of collagen fibril distributions within intact tendons. *Biophys. J.* **106,** 459–466 (2014).

172. Jiang, H. *et al.* Nanoscale imaging of mineral crystals inside biological composite materials using X-ray diffraction microscopy. *Phys. Rev. Lett.* **100,** (2008).

173. Chushkin, Y. *et al.* Three-dimensional coherent diffractive imaging on non-periodic specimens at the ESRF beamline ID10. *J. Synchrotron Radiat.* **21,** 594–599 (2014).

174. Vennat, E., Bogicevic, C., Fleureau, J. M. & Degrange, M. Demineralized dentin 3D porosity and pore size distribution using mercury porosimetry. *Dent. Mater.* **25,** 729–735 (2009).

175. Chadefaux, C. & Reiche, I. Archaeological Bone from Macro- to Nanoscale: Heat-Induced Modifications at Low Temperatures. *J. Nano Res.* **8,** 157–172 (2009).

176. Schofield, P. F., Knight, K. S. & van der Houwen, J. A. M. The role of hydrogen bonding in the thermal expansion and dehydration of brushite, di-calcium phosphate dihydrate. *Phys. Chem. Miner.* **31,** 606–626 (2004).

177. Catti, M., Ferraris, G. & Filhol, A. Hydrogen bonding in the crystalline state. CaHPO4 (monetite), P1 or P1? A novel neutron diffraction study. *Acta Crystallogr. Sect. B Struct. Crystallogr. Cryst. Chem.* **33,** 1223–1229 (1977).

178. Sugiyama, K. & Tokonami, M. Structure and crystal chemistry of a dense polymorph of tricalcium phosphate Ca3 (PO4)2: A host to accommodate large lithophile elements in the earth's mantle. *Phys. Chem. Miner.* **15,** 125–130 (1987).

179. Calvo C, G. R. The crystal structure of whitlockite from the Palermo quarry. *Am.*

Mineral. **60,** 120–133 (1975).

180. Fleet, M. E. & Liu, X. Coupled substitution of type A and B carbonate in sodium-bearing apatite. *Biomaterials* **28,** 916–926 (2007).

181. Fleet, M. E. Infrared spectra of carbonate apatites: ν2-Region bands. *Biomaterials* **30,** 1473–1481 (2009).

182. Penel, G., Leroy, G., Rey, C. & Bres, E. MicroRaman spectral study of the PO4 and CO3 vibrational modes in synthetic and biological apatites. *Calcif. Tissue Int.* **63,** 475–481 (1998).

183. Suetsugu, Y., Shimoya, I. & Tanaka, J. Configuration of Carbonate Ions in Apatite Structure Determined by Polarized Infrared Spectroscopy. *J. Am. Ceram. Soc.* **81,** 746–748 (1998).

184. Schramm, D. U., Terra, J., Rossi, A. M. & Ellis, D. E. Configuration of CO2- radicals in γ-irradiated A-type carbonated apatites: Theory and experimental EPR and ENDOR studies. *Phys. Rev. B* **63,** 024107 (2000).

185. Suetsugu, Y., Takahashi, Y., Okamura, F. P. & Tanaka, J. Structure Analysis of A-Type Carbonate Apatite by a Single-Crystal X-Ray Diffraction Method. *J. Solid State Chem.* **155,** 292–297 (2000).

186. Elliott, J. in *Rev. in Mineral. & Geochem.* (eds. Kohn, M., Rakovan, J. & Hughes, J.) 427–453 (Mineral Soc Amer, 2002).

187. LeGeros, R. Z. Calcium Phosphates in Demineralization/Remineralization Processes. *J. Clin. Dent.* **10,** 65–73 (1999).

188. El Feki, H., Michel Savariault, J., Ben Salah, A. & Jemal, M. Sodium and carbonate distribution in substituted calcium hydroxyapatite. *Solid State Sci.* **2,** 577–586 (2000).

189. Bauer, M. & Klee, W. E. Induced ferrielectricity in chlorapatite. *Zeitschrift für Krist. - Cryst. Mater.* **206,** (1993).

190. Comodi, P., Liu, Y. & Frezzotti, M. L. Structural and vibrational behaviour of fluorapatite with pressure. Part II: In situ micro-Raman spectroscopic investigation. *Phys. Chem. Miner.* **28,** 225–231 (2001).

191. Bigi, A., Falini, G., Gazzano, M., Roveri, N. & Tedesco, E. Structural refinements of

strontium substituted hydroxylapatites. *Mater. Sci. Forum* **278-2,** 814–819 (1998).

192. Meneghini, C., Dalconi, M. C., Nuzzo, S., Mobilio, S. & Wenk, R. H. Rietveld refinement on x-ray diffraction patterns of bioapatite in human fetal bones. *Biophys. J.* **84,** 2021–2029 (2003).

193. Miculescu, F. *et al.* Cortical bone as resource for producing biomimetic materials for clinical use. *Dig. J. Nanomater. Biostructures* **7,** 1667–1677 (2012).

194. Team, F. FullProf Suite. (2006). Available at: https://www.ill.eu/sites/fullprof/.

195. Termine, J. D. & Posner, A. S. Infrared analysis of rat bone: age dependency of amorphous and crystalline mineral fractions. *Science (80-.).* **153,** 1523–1525 (1966).

196. Glimcher, M. J., Bonar, L. C., Grynpas, M. D., Landis, W. J. & Roufosse, A. H. Recent studies of bone mineral: Is the amorphous calcium phosphate theory valid? *J. Cryst. Growth* **53,** 100–119 (1981).

197. Wyckoff, R. W. G. *Crystal Structures*. *Science* **1,** (1963).

198. Chappard, C. *et al.* Comparison of synchrotron radiation and conventional x-ray microcomputed tomography for assessing trabecular bone microarchitecture of human femoral heads. *Med. Phys.* **33,** 3568–3577 (2006).

199. Bousson, V. *et al.* Cortical bone in the human femoral neck: three-dimensional appearance and porosity using synchrotron radiation. *J. Bone Miner. Res.* **19,** 794–801 (2004).

200. Nuzzo, S., Peyrin, F., Cloetens, P., Baruchel, J. & Boivin, G. Quantification of the degree of mineralization of bone in three dimensions using synchrotron radiation microtomography. *Med. Phys.* **29,** 2672–2681 (2002).

201. Pacureanu, A., Langer, M., Boller, E., Tafforeau, P. & Peyrin, F. Nanoscale imaging of the bone cell network with synchrotron X-ray tomography: optimization of acquisition setup. *Med. Phys.* **39,** 2229–38 (2012).

202. Salomé, M. *et al.* A synchrotron radiation microtomography system for the analysis of trabecular bone samples. *Med. Phys.* **26,** 2194–2204 (1999).

203. Hegerl, R. & Hoppe, W. Dynamische Theorie der Kristallstrukturanalyse durch Elektronenbeugung im inhomogenen Primärstrahlwellenfeld. *Ber. Bunsenges. phys.*

Chem. **74,** 1148–1154 (1970).

204. Dierolf, M. *et al.* Ptychographic X-ray computed tomography at the nanoscale. *Nature* **467,** 436–439 (2010).

205. Guizar-Sicairos, M. *et al.* Quantitative interior x-ray nanotomography by a hybrid imaging technique. *Optica* **2,** 259 (2015).

206. Gorelik, T. E., Schmidt, M. U., Kolb, U. & Billinge, S. J. L. Total-Scattering Pair-Distribution Function of Organic Material from Powder Electron Diffraction Data. *Microsc. Microanal.* **21,** 459–471 (2015).

207. Gordon, L. M., Tran, L. & Joester, D. Atom Probe Tomography of Apatites and Bone-Type Mineralized Tissues. *ACS Nano* (2012). doi:10.1021/nn3049957

208. Choat, B., Jansen, S. & Prychid, C. Preparation of Material for TEM Examination. *Prometheus Wiki* (2011).

209. Specimen Preparation and Embedding Supplies. Available at: https://www.emsdiasum.com/microscopy/products/preparation/ultramicrotomy.aspx.

210. Als-Nielsen, J. & McMorrow, D. *Elements of Modern X-ray Physics: Second Edition* (2011). doi:10.1002/9781119998365

211. Snigirev, A., Kohn, V., Snigireva, I. & Lengeler, B. A compound refractive lens for focusing high-energy X-rays. *Nature* **384,** 49–51 (1996).

212. Snigirev, A. A. Refractive lenses allow compact, precision focusing of x-rays. *SPIE Newsroom* (2011). doi:10.1117/2.1201108.003688

213. Kirkpatrick, P. & Baez, A. V. Formation of optical images by X-rays. *J. Opt. Soc. Am.* **38,** 766–774 (1948).

214. Snigireva, I. & Snigirev, A. X-Ray microanalytical techniques based on synchrotron radiation. *J. Environ. Monit.* **8,** 33–42 (2006).